



HAL
open science

Synthèse par ALD et caractérisation de couches extractrices d'électrons pour application dans les cellules solaires à base de pérovskite

Olivier Fournier

► To cite this version:

Olivier Fournier. Synthèse par ALD et caractérisation de couches extractrices d'électrons pour application dans les cellules solaires à base de pérovskite. Matériaux. Université Paris sciences et lettres, 2021. Français. NNT : 2021UPSLC025 . tel-03724070

HAL Id: tel-03724070

<https://pastel.hal.science/tel-03724070>

Submitted on 15 Jul 2022

HAL is a multi-disciplinary open access archive for the deposit and dissemination of scientific research documents, whether they are published or not. The documents may come from teaching and research institutions in France or abroad, or from public or private research centers.

L'archive ouverte pluridisciplinaire **HAL**, est destinée au dépôt et à la diffusion de documents scientifiques de niveau recherche, publiés ou non, émanant des établissements d'enseignement et de recherche français ou étrangers, des laboratoires publics ou privés.

THÈSE DE DOCTORAT
DE L'UNIVERSITÉ PSL

Préparée à l'Ecole Nationale Supérieure de Chimie de Paris

**Synthèse par ALD et caractérisation de couches
extractrices d'électrons pour application dans les cellules
solaires à base de pérovskite**

Soutenue par

Olivier FOURNIER

Le 19 Juillet 2021

École doctorale n°397

**Physique et chimie des
matériaux**

Spécialité

**Physique et chimie des
matériaux**

Composition du jury :

Emmanuelle DELEPORTE Professeur, ENS Paris-Saclay	<i>Présidente Rapporteuse</i>
Thomas RIEDL Professor, University of Wuppertal	<i>Rapporteur</i>
Zhuoying CHEN Chargée de recherche, ESPCI	<i>Examinatrice</i>
Giulia GRANCINI Professor, University of Pavia	<i>Examinatrice</i>
Peter REISS Chercheur CEA, CEA Grenoble	<i>Examineur</i>
Laurent LOMBEZ Chargé de recherche, INSA Toulouse	<i>Directeur de thèse</i>

*Even when the dark comes crashing through
When you need a friend to carry you
And when you're broken on the ground
You will be found*

*So let the sun come streaming in
'Cause you'll reach up and you'll rise again
Lift your head and look around
You will be found*

You Will Be Found, *Dear Evan Hansen*,
Benj Pasek & Justin Paul

Acknowledgements - Remerciements

La thèse apparaît bien souvent comme une aventure solitaire, ce qui – dans une certaine mesure – est justifié. Cependant une expérience de thésard ne serait pas grand chose sans toutes les personnes qui de près ou de loin permettent de rester à flots et d’avancer tant d’un point de vue professionnel et scientifique que personnel. Il est donc grand temps, alors que cette aventure se termine, de procéder aux remerciements qui, bien qu’attendus par la tradition, n’en restent pas moins sincères. Je tiens par avance à m’excuser si quelqu’un est oublié : aussi certain qu’il est difficile de stabiliser une pérovskite, cette section ne sera pas exhaustive !

Mes premiers remerciements vont à mon encadrement, le trio de choc constitué de Laurent Lombez, Jean Rousset et Nathanaelle Schneider. Durant ces trois années, ils m’ont fait confiance pour travailler sur ce sujet épineux mais ô combien intéressant à l’interface entre l’ALD, les pérovskites et la luminescence. A leur contact, j’ai beaucoup appris sur des thématiques variées allant de la chimie de surfaces au mapping de fonction de collecte en passant par le double canard électrochimique, toujours dans une rigueur scientifique non dénuée d’humour et de légèreté quand le besoin s’en faisait ressentir.

Je remercie tout d’abord Laurent pour avoir accepté de diriger ces travaux. Malgré le tournant très ”chimie” qu’a pris cette thèse et ton grand retour dans le Sud, tu es toujours resté très disponible et d’excellent conseil. Je te remercie d’avoir partagé tes connaissances et bonnes pratiques en matière d’optique, de PL et de science des matériaux en général. Tu as aussi réussi l’exploit de me mettre au cross-fit sur les bords de la Seine (et ce n’était pas gagné d’avance !).

Vient ensuite le tour de mon voisin d’un temps, Jean, chef de projet hors pair. Entre les galères Candlelight, les conseils sur les recettes de pâtes à l’aubergine ou les meilleures adresses de la cité phocéenne, la vénerie, les pérovskites, l’avenir, l’électrochimie, les ”petites molécules”, les nouvelles orientations de la thèse ... on en a écumé des sujets de discussion ! Je ne compte pas les vendredis soir où tu venais aux nouvelles, réussissant toujours à voir le bon côté des choses, même dans des batchs dont le potentiel était parfois (souvent ?) bien, bien caché. Cet enthousiasme contagieux a été d’un grand secours pendant les ”bas” de la thèse, et sait rendre la plus banale des réunions un très bon moment ! En fin de compte, je pense que tu as réussi ton défi, ouvrir un physicien (de formation) aux joies et plaisirs de la chimie.

Cette initiation à la chimie doit aussi beaucoup à Nathanaelle, ambassadrice de l'ALD s'il en est une. Des grains de sable témoignent encore de ma lecture assidue du "Techniques de l'Ingénieur" spécial ALD que tu m'avais donné à l'issue des premiers entretiens ! Un grand merci pour avoir facilité de nombreuses collaborations et discussions avec des laboratoires et des équipes extérieures à l'IPVF, et ainsi participé à l'enrichissement scientifique de mon expérience de thèse. Ton entrain et ta capacité à t'intéresser à tous les sujets, y compris ceux dont tu étais moins familière (pérovskite, PL, règle de trois ...), m'ont aussi aidé à avancer. Enfin, je ne peux pas passer sous silence l'investissement et la réactivité sans faille dont tu as fait particulièrement preuve à la fin de cette aventure (bonjour la charge mentale !).

Au risque de me répéter, je tiens à souligner encore une fois collectivement la disponibilité, l'écoute et la confiance dont vous avez fait preuve envers moi pendant ces dernières années. Je me considère extrêmement chanceux de vous avoir eus comme encadrants, ce fut un réel plaisir de travailler avec vous !

Cette thèse n'aurait pas pu se faire non plus sans les efforts conjoints d'EDF et de l'UMR IRDEP, puis IPVF. Je tiens en particulier à remercier Matthieu Versavel et Jean-Christophe Gault de m'avoir accepté à EFESE, puis Cédric Guérard et Stéphanie Muller d'avoir continué à encadrer les activités du groupe technologies solaires.

Je suis également très reconnaissant envers les membres du jury qui, malgré un emploi du temps très serré, ont trouvé le temps de relire ma thèse et d'évaluer le travail effectué durant ces trois années (plus quelques mois). Je souhaite remercier particulièrement Emmanuelle Deleporte pour avoir accepté la double casquette de rapportrice et de présidente de jury.

J'ai aussi eu la chance pendant ces travaux de thèse de travailler avec trois autres laboratoires à l'occasion de collaborations. Merci à Elizabeth Blanquet, Arnaud Mantoux, Alexandre Crisci et Elise Garel de m'avoir accueilli quelques jours au Simap et de m'avoir permis de travailler sur mes premiers dépôts ALD. Je remercie aussi chaleureusement François Ozanam qui a pris le temps de m'initier au difficile art de polir des prismes de Si, de prendre des mesures propres de FTIR et surtout de les interpréter au LPMC. Un grand merci enfin à Muriel Bouttemy et Davina Messou pour toutes les analyses XPS que vous avez faites à l'ILV, et la patience que vous avez eue avec des échantillons pas toujours faciles à analyser ! En parlant d'ILV, je glisse aussi un remerciement à Solène qui a toujours pris le temps pour discuter XPS, états d'âme et j'en passe.

Merci aussi à Mireille pour son aide précieuse dans les (nombreuses) tâches administratives qui jalonnent l'expérience de thèse, ainsi qu'à Hakima Si-Bachir et Didier Journaux, notamment dans les dernières semaines de la thèse.

A l'IRDEP puis à l'IPVF, j'ai été entouré de personnes passionnantes auprès desquelles j'ai pu apprendre sur de nombreux sujets, toujours dans la bonne humeur, et sans qui ce travail n'aurait jamais pu aboutir. Durant mes années à l'IPVF, j'ai eu la chance de travailler avec trois "communautés" dont les réunions ont ponctué mes semaines.

Le lundi c'était carac/laser/bâtiment F avec Laurent, Daniel O., Jean-François, Baptiste, Daniel S., Marie, Mahyar, Géraud, Thomas, Alexandra, Amaury ...

autour de discussions passionnées sur la physique des semiconducteurs. Je remercie aussi Adrien pour m'avoir enseigné comment apprivoiser l'hyperspectrale et la TR-FLIM, Stefania pour avoir partagé les heures de désespoir quand on se rend compte que, décidément, l'imagerie de PL, c'est pas si évident, Guillaume et Jean-Baptiste pour les avoir entraînés sur le chemin tortueux (l'impasse ?) de la PL(V) pulsée sur pérovskite.

Le mardi prenait une coloration plus chimie, avec la réunion des aficionados de l'ALD durant laquelle pour combler l'attente des gaz spéciaux, on discutait cycles, croissance, marquage de substrat avec Nathanaelle, Frédérique, Simone, Paul-Alexis, André ... Merci spécialement à Damien et Thomas pour leur aide précieuse pendant le développement et le dépôt des couches ALD. Il en faut de la patience pour veiller une croissance de matériau plus lente encore que la dérive des continents !

Pour conclure la semaine venait la grand-messe du projet F/programme II. Je me souviendrai longtemps des introductions enflammées de Jean, ainsi que des nombreux résultats qui ont été discutés dans l'intimité relative de la trentaine de participants réguliers à cette réunion. Je remercie Amelle d'avoir formé un novice à l'art subtil de la synthèse de pérovskite, Aurélien pour ses conseils en manip, Sébastien d'avoir supporté mes questions, Marion, Sam pour ses sauvetages récurrents de l'évap d'Au, Régis pour le complexe réglage des simus, Thomas, Philip pour les discussions sur le greffage, Philippe pour les simulations DFT, Stéphanie ... Un immense merci en particulier à Armelle pour les nombreuses heures passées dans les laboratoires de chimie à élaborer les cellules pérovskite et pour la patience avec laquelle elle accueillait (avec le sourire) mes plans de manip colorés qui arrivaient (souvent) à la dernière minute et qui changeaient (encore plus souvent) à la dernière seconde. Merci enfin à Claire pour son travail effectué sur le greffage de molécules, j'espère que le stage a été instructif !

Une pensée pour l'énorme effort fourni par l'équipe de choc de Sophie et Valérie pendant le redémarrage des labos. Parlant de labos, merci à Julie, Frédérique, Nicolas L. et Nicolas V. pour leur investissement en temps que chefs de pôle. J'en profite pour remercier Nicolas L. pour la bonne discussion que nous avons eue avec Jean qui a lancé le chapitre du greffage des acides phosphoniques.

Plus généralement, je remercie tous les habitants de l'IPVF d'avoir contribué à une atmosphère de recherche stimulante et agréable à la fois (cf. les traditionnelles bières au Guichet) ! J'ai ici une pensée particulière pour mes co du 2B.B13 : Charlene, Harold, Karolien, Jonathan, Baljeet, Dhanu, Jung-Eun, Romaric, Cécile, Kathy, Rafael, Caterin, Christian, Maria, Capucine, Anatole ... J'en retiendrai pêle-mêle les Scrabbles au tableau, les sessions musique ("*We're soaring*" ...), les discussions plus ou moins philosophiques ...

Le sel de la vie de thésard réside aussi beaucoup dans les liens qui se forment entre les thésards des différentes générations. Ma condition physique et mentale leur doit beaucoup, pour le meilleur – les tentatives de cross-fit le long de la Seine, les entraînements sérieux au semi marathon, la découverte de l'escalade – comme pour le pire – les déclamations publiques en langue étrangère, les entraînements sérieux au levé de coude aux Grands Voisins, la découverte de la délirium. Ce sont surtout de longues discussions au détour d'une bière, d'un bout de chemin, d'un concert de Jain ou d'un coin de bureau sur la pluie, le beau temps, l'avenir, la

société, et qui j'en suis convaincu m'ont beaucoup fait mûrir sur ces sujets (surtout la météo). Merci aux "vieux thésards" d'avoir montré la voie, pour leurs conseils avisés qui permettent de naviguer entre les écueils (notamment administratifs !) de la thèse, pour les trucs et astuces de manips ... Je pense particulièrement à Charlène, Harold, Valentin, Mishael, Fabien, Adrien, Louis, Romaric, Cécile. Merci aux Tuches et à mes deux *sister-ships* de thèse : Sophie, Arpit, Margot, Anatole et Emilie pour ces bons moments passés à l'IPVF, en labo, à la cafet autour d'un mot fléché ou d'une déprime du mercredi, rapidement compensée par les séances découverte du quatrième art sur les flancs de Montmartre ("*Voitures !*") ou du septième art entre "collègues". Je pense évidemment aussi à celles et ceux qui continuent à progresser le long du chemin tortueux de la thèse: Paul-Alexis, Salim, Marie, Javid, Thomas, Alexandre, Guillaume, Capucine, Bérangère ... Je n'ai pas envie de vous souhaiter bon courage, mais plutôt bonne continuation et profitez à fond de cette expérience unique qu'est la thèse. Je vous remercie aussi d'avoir apporté un souffle nouveau dans le train-train routinier qui a tendance à s'installer trop rapidement, et de m'avoir introduit aux charmes de la cité massicoise.

Bien qu'il me semble improbable d'avoir réussi à fournir un manuscrit d'une parfaite limpidité et exempt de typo et autres fautes d'orthographe, le travail de relecture acharné de quelques personnes m'a permis d'en corriger un certain nombre de défauts. Pour le temps consacré à relire, rectifier, suggérer, discuter de tout ou partie de ce manuscrit, je remercie du fond du coeur Nathanaelle, Laurent, Jean, Muriel, Valentin, Anatole, Guillaume et Margot.

Un grand merci aussi à mes amis *extra-labo* de s'être occupé de préserver ma vie sociale, qui peut rapidement se retrouver en voie d'extinction en thèse. Je pense en particulier à mes comparses de la maison du bonheur, les balances, les amis de Bob : Apo, Tim, Camille, Vianney, Chloé, Baudue et Matthieu qui ont été présents au jour le jour entre bons petits plats, parties de coinche ou de Munchkin acharnées, et soirées endiablées. Vous avez rendu les confinements (et la rédaction) bien plus doux ! Je n'oublie pas celles et ceux que j'ai vus plus ou moins souvent, avec toujours beaucoup de plaisir : les sigmas, les angoumoisins, les X ... ou que j'ai pris plaisir à rencontrer (coucou les habitués des repas coloc !). Je n'ai pas forcément réussi à vous expliquer avec clarté le sujet de mes recherches ("*Et du coup tu trouves ?*", "*Mais en fait tu fais pousser des panneaux PV ?*"), mais si le coeur vous en dit, ce manuscrit devrait vous éclairer un peu sur le sujet.

L'adage dit qu'il faut garder le(s) meilleur(s) pour la fin. Je suis infiniment reconnaissant envers mes parents de m'avoir toujours encouragé et permis de faire les études qui m'ont amené ici aujourd'hui. Je remercie évidemment aussi mes frères et soeurs pour les exemples qu'ils sont, ainsi que les valeurs ajoutées qui ont chacune su apporter leur caractère à cette composition familiale. Merci donc à ma famille qui est un appui sur lequel je peux toujours compter, pour les moments heureux comme pour les plus difficiles. Je nous souhaite de continuer longtemps à rester disponibles les uns pour les autres. Je suis fier de vous !

Alors que ces remerciements touchent à leur fin, j'espère que vous prendrez autant de plaisir à lire les pages qui suivent que j'en ai pris (non pas à les écrire mais) à vivre cette aventure !

List of Figures

I.1	Projected energy mix for various sectors according to the IEA net zero emission scenario.	2
I.2	Projection of ITRPV on the solar PV module market.	4
1.1	Irradiance spectra of the solar radiation.	8
1.2	Schematic of the photon/matter interaction in a semiconductor. . .	10
1.3	Schematic of the different recombination pathways in a semiconductor. . .	11
1.4	Ultimate PV parameters of a single junction function of the band gap of the absorber.	15
1.5	Simplified one diode electrical model of a realistic solar cell.	17
1.6	Phase transition of perovskite materials.	21
1.7	Absorption coefficient of MAPbI ₃	22
1.8	Variation of the absorption coefficient in MAPb(Br _x I _{1-x}) ₃	24
1.9	Schematic representation of the different perovskite solar cell architectures.	27
1.10	Example of interface-dependant properties of the perovskite.	29
1.11	Schematic representation of an ALD cycle	34
1.12	Properties of an ALD process	35
1.13	Examples of evolution of the representation of the ALD process. . .	36
1.14	Evolution of the ALD process.	39
1.15	Various applications of the ALD process.	41
1.16	Schematic of the Beneq TFS-200 reactor	44
1.17	Schematic of the combination operation mode	45
2.1	QCM data of ALD-TiO ₂	51
2.2	Properties of ALD-TiO ₂ processes	52
2.3	XPS of ALD-TiO ₂ thin films	54
2.4	Properties of the ALD-TiO ₂ thin films with the H ₂ O/TTIP process	56
2.5	Properties of the ALD-TiO ₂ thin films with the H ₂ O ₂ /TTIP process	57
2.6	QCM data of ALD-SnO ₂	62
2.7	Properties of ALD-SnO ₂ processes	63
2.8	XPS of ALD-SnO ₂ thin films	65
2.9	Properties of the ALD-SnO _x films.	67
2.10	Properties of the ALD-SnO ₂ films.	68
2.11	Hyperspectral imager setup.	71
2.12	Transmission of the collection branch of the hyperspectral imager	73

LIST OF FIGURES

2.13 Influence of the shape of the absorption coefficient on the PL emission.	75
2.14 Influence of the fitting parameters on the PL spectrum.	76
3.1 XRR analysis of annealed ALD-TiO ₂ thin films function of the annealing temperature	84
3.2 GI-XRD analysis of ALD-TiO ₂ thin films function of the annealing temperature.	86
3.3 Optical properties of ALD-TiO ₂ thin films function of the annealing temperature.	88
3.4 Cyclic voltametry of compact TiO ₂ layers function of the thickness and of the annealing temperature.	90
3.5 Homogeneity of the ALD-TiO ₂ and SP-TiO ₂	92
3.6 Morphology of the perovskite on SP- and ALD-TiO ₂	94
3.7 Microstructure of the perovskite on SP- and ALD-TiO ₂	95
3.8 Normalized PV parameters function of the thickness of the ALD-TiO ₂ layer.	97
3.9 Transmission of ALD TiO ₂ thin films and related integrated current density.	100
3.10 Sketch of the cell architecture for the comparison of SP- and ALD-TiO ₂ .	100
3.11 Comparison of the PV parameters of cells based on SP- and ALD-TiO ₂ .	102
3.12 MPPT and EQE of the best batch comparing cells using SP- and ALD-TiO ₂	103
3.13 SSPL spectra and PLQY of perovskite on SP-TiO ₂ and ALD-TiO ₂ .	105
3.14 Integration of c-TiO ₂ in planar devices.	107
4.1 XRR analysis of annealed ALD-SnO ₂ thin films function of the annealing temperature.	113
4.2 GI-XRD analysis of ALD-SnO ₂ thin films function of the annealing temperature.	114
4.3 Optical properties of ALD-SnO ₂ thin films function of the annealing temperature.	115
4.4 Cyclic voltamograms of annealed SnO ₂ thin films function of the thickness and of the annealing temperature	117
4.5 Sketch of the cell architecture for the study on the effect of the annealing and deposition temperatures of SnO ₂ in full devices. . .	118
4.6 PV parameters function of the deposition and annealing temperatures of the ALD-SnO ₂ layer.	119
4.7 Sketch of the cell architecture for the study on the effect of the addition of PCBM on SnO ₂ in full devices.	122
4.8 IV curves of cells deposited on SnO ₂ , SnO ₂ /PCBM and PCBM. . .	123
4.9 Violation of the shifting approximation on ALD-SnO ₂	125
4.10 Wettability issue of the perovksite ink on PCBM.	126
4.11 Wettability test of the perovksite ink on various substrates.	128
4.12 SEM micrographs of perovskite deposited on various substrates. . .	129
4.13 IV curves of cells deposited on PCBM ₅ and DMF-stat.	130
4.14 Sketch of the cell architecture for the study on the effect of the thickness of ALD-SnO ₂ in full devices.	131

LIST OF FIGURES

4.15	PV parameters function of the thickness of the ALD-SnO ₂ layer.	131
5.1	Main properties of ALD-ZnO process and thin film.	137
5.2	Schematic representation of the different binding modes of a phosphonic acid derivative onto a metal oxide layer.	139
5.3	Grafting process as used in this work	142
5.4	Static contact angle of ZnO modified by phosphonic acid derivatives	145
5.5	Evidences of the degradation of ZnO-ref in a solvent, and of the modification of the surface by 2-AEPA.	146
5.6	High resolution XPS spectra of modified ZnO	149
5.7	Normalized HR XPS spectra of P 2p and F 1s photopeaks for the grafted molecules and 4-FBzPA powder.	150
5.8	ATR-FTIR spectra of ZnO-AEPA, ZnO-ABzPA and ZnO-FBzPA.	151
5.9	Relative depth profiles of the elements of the grafted layers.	154
5.10	Organization of the different molecules on top of ZnO	155
5.11	Evolution of N 1s and P 2p photopeaks with the immersion time in a solution of 2-AEPA.	156
5.12	SEM micrographs of a triple cation perovskite on top of modified surfaces.	158
5.13	Diffraction pattern of AEPA-pvk and Ref-pvk.	159
5.14	Angle dependent GI-XRD of Ref-pvk and AEPA-pvk	160
5.15	Sketch of the cell architecture for the study on ZnO modification.	162
5.16	J-V characteristic of complete photovoltaic devices made on Ref-pvk, AEPA-pvk and FBzPA-pvk substrates.	163
A.1	Basic features of a cyclic voltammogram.	201
A.2	Morphology of the perovskite on SP- and ALD-TiO ₂	203
A.3	DFT simulation of the FTIR spectra of the free molecules.	206
A.4	Transmission of Ref-pvk and AEPA-pvk.	206
R.1	Projection du mix énergétique par secteur d'activité d'après le scénario de l'IEA Net Zero Emission.	209
R.2	Projection de l'ITRPV sur le marché des modules solaires.	211
R.3	Résumé du chapitre 1.	213
R.4	Résumé du chapitre 3.	216
R.5	Résumé du chapitre 4.	217
R.6	Résumé du chapitre 5.	218

List of Tables

1.1	Typical compositions and performances of different PSC architectures	28
2.1	Properties of ALD-TiO ₂ processes and materials	49
2.2	Properties of the ALD precursors used at IPVF for the synthesis of SnO ₂ and TiO ₂ .	50
2.3	Composition of the ALD-TiO ₂ thin films	54
2.4	Properties of ALD-SnO ₂ processes and materials	60
3.1	Fitted parameters of the XRR data of annealed ALD-TiO ₂	85
3.2	PV parameters function of the thickness of ALD-TiO ₂	98
3.3	Photovoltaic parameters of the best performing cells made on ALD-TiO ₂ and SP-TiO ₂	101
4.1	Fitted parameters of the XRR data of annealed ALD-SnO ₂	112
4.2	PV parameters function of the annealing and deposition temperatures of ALD-SnO ₂	121
4.3	PV parameters of the best performing cells deposited on SnO ₂ , SnO ₂ /PCBM and PCBM	124
4.4	Experimental protocol for the wettability study of perovskite on PCBM	127
4.5	PV parameters of the best performing cells depending on the thickness of ALD-SnO ₂	132
5.1	Basic properties of 2-AEPA, 4-ABzPA and 4-FBzPA	141
5.2	Composition and deposition conditions of the samples modified by phosphonic acid derivatives.	144
5.3	Binding energy (eV) positions of the different contributions used to fit the core level spectra (XPS analysis)	147
5.4	Positions of the vibration modes extracted from the different FTIR spectra of ZnO-AEPA, ZnO-ABzPA and ZnO-FBzPA.	152
5.5	Photovoltaic parameters of the best performing cells made on Ref-pvk, AEPA-pvk and FBzPA-pvk substrates	162
A.1	PL fitted parameters	204
A.2	Comparison of the PV parameters of cells based on SP- and ALD-TiO ₂	205

List of symbols and abbreviations

List of abbreviations

(AS-, S-, PE-)	(Area selective, spatial, plasma-enhanced) atomic layer deposition
ALD	
ALE	Atomic layer etching
AM	Air-mass
ATR-FTIR	Attenuated total reflection Fourier transform infrared spectroscopy
BE	Binding energy
BSE	Back-scattered electrons
BSG	Borosilicate glass
CBD	Chemical bath deposition
CCUS	Carbon capture, utilization and storage
CIGS	Copper indium gallium selenide
CVD	Chemical vapor deposition
DFT	Density functional theory
DOS	Density of states
DRAM	Dynamic random access memory
DSSC	Dye sensitized solar cell
EL	Electroluminescence
ETL	Electron transport layer
GDP	Gross domestic product
GPC	Growth per cycle
HOMO	Highest occupied molecular orbit
HTL	Hole transport layer
IEA	International Energy Agency
IPCC	International Panel on Climate Change
IPVF	Institut Photovoltaïque d'Île-de-France
IR	Infrared

ITRPV	International road-map for PV
LCOE	Levelized cost of electricity
LED	Light emitting diode
LUMO	Lowest unoccupied molecular orbit
MAD	Median absolute deviation
MLD	Molecular layer deposition
MOSFET	Metal-oxide-semiconductor field effect transistor
MPP(T)	Maximum power point (tracking)
NA	Numerical aperture
NZE	Net zero emission
OSC	Organic solar cell
PCE	Power conversion efficiency
PL	Photoluminescence
PLQY	Photoluminescence quantum yield
PSC	Perovskite solar cell
PV	Photovoltaics
PVD	Physical vapor deposition
QCM	Quartz crystal microbalance
QFLS	Quasi-Fermi level splitting
RH	Relative humidity
SAM	Self assembled monolayer
SCE	Saturated calomel electrode
SEM	Scanning electron microscopy
SLG	Sodalime glass
SP	Spray-pyrolysis
SRH	Shockley-Read-Hall
SSPL	Steady state PL
T-BAG	Tethering by aggregation and growth
TCO	Transparent conductive oxide
TRPL	Time-resolved PL
(AR-)XPS	(Angle-resolved) X-ray photoelectron spectroscopy
(GI-)XRD	(Grazing-incidence) X-ray diffraction
XRR	X-ray reflectivity

List of chemicals

2-AEPA	2-aminoethylphosphonic acid
4-ABzPA	4-aminobenzylphosphonic acid
4-FBzPA	4-fluorobenzylphosphonic acid

DEZ	Diethylzinc
FA	Formammidinium
FK209	Tris(2-(1H-pyrazol-1-yl)-4-tert-butylpyridine)cobalt(III) tribis(trifluoromethane)sulfonimide
FTO	Fluor-doped tin oxide
IPA	Propan-2-ol
ITO	Indium-tin oxide
Li-TFSI	Lithium bis(trifluoromethanesulfonyl)imide
MA	Methylammonium
PCBM	6,6-phenyl-C ₆₁ -butyric acid methyl ester
PMMA	Poly(methyl methacrylate)
PTAA	Poly(triaryl amine)
Spiro-OMeTAD	2,2',7,7'-tetrakis[N,N-di(4-methoxyphenyl)amino]-9,9'-spirobifluorene
TAA	Titanium(IV) diisopropoxide bis(acetylacetonate)
^t Bp	Tert-butyl pyridine
TDMASn	Tetrakis(dimethylamino) Sn
TDMAT	Tetrakis(dimethylamino) Ti
TTIP	Ti tetra(isopropoxide)

List of symbols

α	Absorption coefficient
α_{id}	Ideal absorption coefficient (quadratic DOS)
$\Delta\mu$	Quasi-Fermi level splitting
$\delta\lambda$	Spectral resolution of the volume Bragg grating
η	Efficiency
$\eta_{n,p}$	Electrochemical potential of electrons, holes
γ	Energy broadening parameter (Katahara model for absorption)
$\Gamma(x)$	Euler gamma function
λ	Wavelength
$\lambda_{Cu,K\alpha 1}$	Wavelength of the $K_{\alpha 1}$ radiation of Cu
$\mu_{n,p}$	Mobility of electrons, holes
$\tilde{\mu}_{n,p}$	Chemical potential of electrons, holes
ϕ	Electrostatic potential
$\Phi_{abs}^{ex}, \Phi_{abs,0}$	Excitation irradiance, excitation irradiance in the dark (black body emission of the surrounding)
Φ_{BB}	Black-body irradiance
$\Phi_{em}, \Phi_{em,0}$	Emitted irradiance, emitted irradiance in the dark

List of symbols and abbreviations

Φ_{gen}^{max}	Flux of photogenerated carriers in the radiative limit
ρ	Density
σ	Stefan-Boltzmann constant
$\tau_{n,p}$	Carrier lifetime of electrons, holes
θ	Parameter describing the decay of the tail states distribution (Katahara model for absorption)
Ω_{coll}	Collection solid angle
$a(E)$	Absorptivity
B	Broadening parameter
c	Speed of light
d	Thickness of the absorber
d_{SE}	Earth-Sun mean distance
$D_{n,p}$	Diffusion coefficient of electrons, holes
E	Energy
\mathcal{E}	Electrostatic field
e	Thickness of the film (XRR)
$\dot{E}_{BB}, \dot{E}_C, \dot{E}_S$	Energy flux of a black body, the PV converter, the Sun
E_1	Typical energy (Katahara model for absorption)
E_F	Fermi level
$E_{FC, FV}$	Quasi-Fermi level of electrons, holes
E_γ	Energy of a photon
E_t	Energy level of a trap state
$E_{C,V}$	Energy position of the conduction band, the valence band
E_{el}	Electric energy
E_g	Band gap
EQE_{LED}	External quantum efficiency of a device working as an LED
EQE_{PV}	External quantum efficiency of a device working as a solar cell
$f_{C,V}$	Occupation factor of the conduction band, the valence band
$f_{e,h}$	Distribution of electrons, holes
FF	Fill factor
$F_{n,p}$	Free energy of electrons, holes
$G_{n,p}$	Generation rate of electrons, holes
h	Planck constant
I, I_d	Hyperspectral cube, hyperspectral cube in the dark
I_{abs}	Calibrated hyperspectral cube in absolute units
I_{EL}	Electroluminescence emission
I_λ	Sun irradiance at the top of the atmosphere.
I_{las}	Laser intensity (for hyperspectral calibration)
I_{raw}	Counts on the CCD camera

List of symbols and abbreviations

I_{rec}	Rectified counts on the CCD camera
I_{ref}	Reference spectrum (for hyperspectral calibration)
I_{trans}	Transmitted spectrum (for the hyperspectral calibration)
J	Current density
J_0	Dark diode current
J_{rad}	Current density in the radiative limit
J_{SC}	Short current density
J_{SC}^{ideal}	Ideal short circuit current density
K	Shape factor
$K_{A1,A2}$	Auger recombination coefficients
k_B	Boltzmann constant
L	Mean crystallite size
M	Molecular weight
N	Number of particles
n	Number of ligands exchanged in an ALD reaction; number of ALD cycles
n, p	Density of electrons, holes
n^0, p^0	Density of electrons, holes at thermal equilibrium
N_A	Avogadro's number
$N_{C,V}$	Effective density of states of the conduction band, the valence band
n_{id}	Diode ideality factor
$n_{photons}$	Number of photons (for the hyperspectral calibration)
P_{las}	Power of the laser (for the hyperspectral calibration)
P_{sat}	Saturating vapor pressure
PCE	Power conversion efficiency
q	Elementary charge
R_{aug}	Auger recombination rate
R_{ctp}	Counts to photon conversion ratio (for the hyperspectral calibration)
R_{eh}	Radiative recombination coefficient
R_{rad}	Radiative recombination rate
R_S	Series resistance
R_{SH}	Shunt resistance
R_{SRH}	Shockley-Read-Hall recombination rate
r_{sun}	Radius of the Sun
$R_{surf,n,p}$	Surface recombination rate of electrons, holes
R_{trans}	Correcting factor for the transmission (for the hyperspectral calibration)
R_X	Atomic radius of element X
$R_{n,p}$	Recombination rate for electrons, holes

List of symbols and abbreviations

$\dot{S}_{BB}, \dot{S}_C,$	Entropy flux of a black body, the PV converter, the Sun, created
\dot{S}_S, \dot{S}_G	entropy flux
S_{px}	Size of a pixel (for the hyperspectral calibration)
T	Temperature
T	Transmission
t	Tolerance factor
T_{dep}	Deposition temperature
t_{exp}	Exposure time (for the hyperspectral calibration)
t_i	Duration of an ALD step
T_{source}	Temperature of the ALD source
T_A, T_C, T_S	Temperature of the ambient, the PV converter, the Sun
V	Voltage
$v_{n,p}^{rec}$	Surface recombination velocity of electrons, holes
V_{OC}	Open circuit voltage
V_{OC}^{rad}	Radiative limit for the V_{OC}
\dot{W}	Thermodynamic work flux
W_{el}	Electrical work
z	Zenith angle

Contents

Acknowledgements - Remerciements	v
List of Figures	ix
List of Tables	xii
List of symbols and abbreviations	xiii
Introduction	1
1 General introduction	7
1.1 Physics of solar cells	7
1.1.1 Black body emission and solar spectrum	7
1.1.2 Generation, quasi equilibrium and quasi Fermi level splitting	8
1.1.3 Recombination pathways of carriers	10
1.1.4 Thermodynamic limits of the photovoltaic conversion	13
1.1.5 Relation with the operation of realistic devices.	16
1.2 Perovskite solar cells	18
1.2.1 The genesis of perovskite solar cells	18
1.2.2 Properties of halide perovskite	19
1.2.3 Architecture of a perovskite solar cell	25
1.2.4 Challenges and opportunities of perovskite solar cells	30
1.3 Atomic layer deposition	33
1.3.1 Description of an ALD process	33
1.3.2 Strengths and limitations of the technique	40
1.3.3 A brief history of ALD	41
1.3.4 Presentation of the Beneq TFS-200 ALD reactor	43
1.3.5 Conclusion	46
2 Methods and processes	47
2.1 Development of TiO ₂ by ALD	47
2.1.1 Introduction	47
2.1.2 Choice, transport and reactivity of the precursors	49
2.1.3 Properties of the ALD process	51
2.1.4 Properties of the as-deposited ALD-TiO ₂ thin films	53
2.1.5 Conclusions on the development of ALD-TiO ₂	58

2.2	Development of SnO ₂ by ALD	58
2.2.1	Introduction	58
2.2.2	Choice, transport and reactivity of the precursors	61
2.2.3	Properties of the ALD process	63
2.2.4	Properties of the as-deposited ALD-SnO ₂ thin films	64
2.2.5	Conclusion on the deposition of ALD-SnO ₂	69
2.3	Photoluminescence imaging	69
2.3.1	Motivations	69
2.3.2	Absolute SSPL on a hyperspectral imager: experimental setup and calibration procedure	71
2.4	Conclusion	77
3	Optimization and integration of ALD-TiO₂ in perovskite solar cells	79
3.1	Motivations	79
3.1.1	Previous uses of TiO ₂ in perovskite solar cells	79
3.1.2	Potential benefits of ALD versus spray pyrolysis (SP) deposition of TiO ₂ for perovskite solar cells	80
3.2	Influence of post-annealing treatments on ALD-TiO ₂ thin films properties	83
3.2.1	Structural changes	83
3.2.2	Optical properties of the ALD-TiO ₂ thin films	87
3.2.3	Characterization of the blocking ability of the ALD-TiO ₂ thin films	89
3.2.4	Conclusions on the effect of the annealing on ALD-TiO ₂	90
3.3	Comparison of the homogeneity of the TiO ₂ thin films deposited by ALD and by SP	91
3.4	Integration of ALD-TiO ₂ layers as compact ETL in perovskite solar cells	93
3.4.1	Properties of the perovskite deposited on a c-TiO ₂ / mp-TiO ₂ bilayer	93
3.4.2	Optimization of the thickness of the ALD-TiO ₂ compact layer	96
3.4.3	PV performances of cells based on the two deposition methods	101
3.4.4	Photoluminescence imaging of half cells	104
3.4.5	Integration into planar devices	105
3.5	Conclusion	106
4	Optimization and integration of ALD-SnO₂ in perovskite solar cells	109
4.1	Motivation	109
4.1.1	SnO ₂ in PSC: an efficient oxide in planar structures	109
4.1.2	ALD-SnO ₂ in PSC	110
4.2	Influence of post-annealing treatments on ALD-SnO ₂ thin films properties	111
4.2.1	Structural properties	111
4.2.2	Optical properties of the ALD-SnO ₂ thin films	114

4.2.3	Characterization of the blocking abilities of the ALD-SnO ₂ thin films	116
4.2.4	Conclusions on the annealing study	116
4.3	Integration of ALD-SnO ₂ layers in planar perovskite solar cells . .	118
4.3.1	Influence of the deposition temperature and of the annealing temperature	118
4.3.2	Passivation with PCBM	122
4.3.3	Thickness study	130
4.4	Conclusion	132
5	Modification of ALD-ZnO with phosphonic acid derivatives	135
5.1	Motivation	135
5.1.1	The versatility of ZnO	135
5.1.2	Issues with the integration of ZnO in perovskite solar cells .	135
5.2	Properties of the ALD-ZnO	136
5.2.1	Properties of the ALD-ZnO process	136
5.2.2	Properties of the ALD-ZnO thin films	136
5.3	Modification of the ZnO surface with phosphonic acid derivatives (organophosphonates)	138
5.3.1	Rationale behind the design of the molecules	138
5.3.2	Description of the grafting process	141
5.4	Characterization of the grafted layer	143
5.4.1	Assessment of the presence of the molecules on the surface	144
5.4.2	Characterization of the chemical environment of the surface	146
5.4.3	Organization of the molecules on the surface	153
5.5	Influence of the grafting on the properties of the absorber and on the complete solar cells	157
5.5.1	Effect of ZnO modification on the perovskite thin film . . .	157
5.5.2	Integration in complete PV devices	161
5.6	Conclusion	163
	General conclusion and perspectives	165
C.1	Development of ALD materials	165
C.2	Integration of ALD-TiO ₂	166
C.3	Integration of ALD-SnO ₂	167
C.4	Passivation of the ZnO/perovskite interface	168
C.5	Bottlenecks to the quick development of new perovskite solar cell architectures	169
C.6	Perspectives	170
	References	172
	Appendix	198
A.1	Experimental	198
A.1.1	Device preparation	198
A.1.2	Characterization techniques	199
A.2	Additional information on characterization techniques	200
A.2.1	Principle of the cyclic voltametry	200

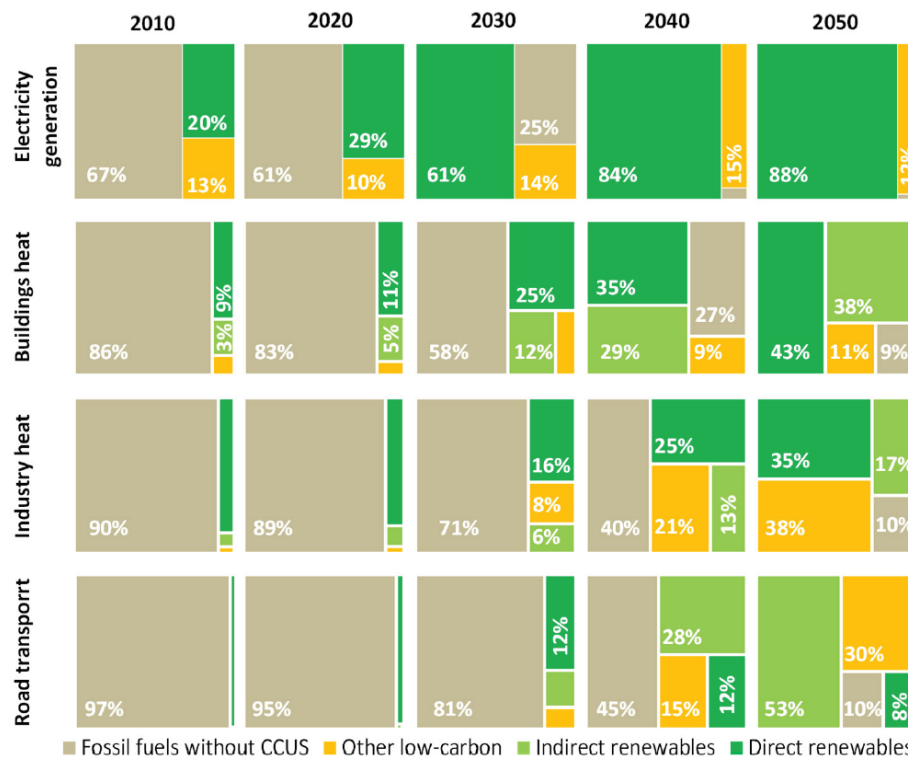
A.2.2	Statistical analysis of the distribution of the perovskite grain size	202
A.3	Additional experimental data	204
A.3.1	Fitting parameters of the PL spectra	204
A.3.2	Mean PV parameters of the cells based on ALD-TiO ₂ and SP-TiO ₂	205
A.3.3	FTIR spectra of the free molecules	206
A.3.4	Transmission spectra of Ref-pvk and AEPA-pvk	206
A.4	List of conferences and publications	207
A.4.1	List of publications	207
A.4.2	List of international conferences	207
A.4.3	List of national conferences	207
Résumé des travaux de thèse		208

Introduction

During the last 50 years – and fostered by the publication of several reports (such as Meadows and Rome (1972)) – the concept of energy transition (or energy crisis) has gained importance in the politic sphere, as well as in the public opinion in reaction to the consecutive oil crisis and more recently to the increasing amount of reports and studies pointing at the global impact of the modern, fossil fuels-based economy on the environment. After several years of investigation and arguments, it is now admitted that the observed climate change characterized by a gradual increase of the global temperature (hence the misleading name of "global warming") is of anthropogenic nature, according to a large consensus in the scientific community (Cook et al. (2016)).

Anthropogenic climate change not only acts at the obvious climatic scale with the increase of extreme climatic events (such as heat waves, droughts, wild fires, storms ... Stott (2016)) or the accelerated melting of the cryosphere (Pörtner et al. (2019)). It also affects broader social and environmental matters. For instance, the impact of climate change on social inequalities is a persistent issue at the global scale (between countries) and at the local scale (within a country; Islam and Winkel (2017)). The global awareness of the intricate issues related to climate change has raised. Among other things, it has been met on the government side with the organization of the annual United Nations Climate Change Conference, or the constitution of the Intergovernmental Panel on Climate Change (IPCC). The multiplication of initiatives – such as actions and reporting by non-governmental organizations, or the organization of environment protests (recently: Fridays for Future or climate marches) – also show the increasing civilian interest on this matter. These unprecedented common efforts underline the urge to address the issues related to climate change.

The IPCC reports regularly on diverse topics related to climate change and provides advice and recommendations for the policy makers. It produced in 2018 the "special report on global warming of 1.5 °C" which describes the consequences of an increase of the global temperature by 1.5 °C along with the necessary steps to limit the temperature increase to 1.5 °C. A major finding is that following a business as usual scenario, this target would be exceeded before 2050. Following the target set by the Paris agreements in 2015 – whereby the countries agreed to "achieve a balance between anthropogenic emissions by sources and removals by sinks of greenhouse gases in the second-half of the century" – would also not be sufficient and would lead to an increase of 3 °C by 2100. Limiting the temperature



IEA. All rights reserved.

Figure I.1: Fuel shares in total energy use in selected applications in the net zero emission scenario. Notes: Indirect renewables = use of electricity and district heat produced by renewables. Other low-carbon = nuclear power, facilities equipped with CCUS, and low-carbon hydrogen and hydrogen-based fuels. Adapted from IEA (2021).

increase to 1.5 °C would essentially require to reduce the net emission of CO₂ and reach net zero emission by 2050.

This ambitious – yet crucial – target implies to reevaluate the way the production and the use of energy are conceived. In preparation of the 26th Conference of Parties of the United Nations Framework Convention on Climate Change, the International Energy Agency (IEA) provided a roadmap indicating the actions and policies to undertake in order to actually meet the net zero emission (NZE) target by 2050 (IEA (2021)). Interestingly, the report explicitly fosters an immediate decline in the investments in fossil fuels to limit their usage to the bare necessity, in combination with carbon capture, utilization and storage (CCUS). The NZE scenario revolves around several pillars: the increase of the energy efficiency, the change in the behaviors and the development of the electrification, of renewables, of hydrogen-based technologies, of bioenergy and of CCUS. The former three pillars would incidentally support a decrease of the total energy consumption from 412 EJ (1 EJ = 10¹⁸ J) in 2020 to 344 EJ in 2050, hence an average annual growth rate of -0.6%/year. This decrease of the energy consumption would not necessarily impede

the growth of the gross domestic product (GDP) (even if alternative scenarii are discussed elsewhere in the degrowth framework (Kallis et al. (2018))) because of a concomitant decrease of the energy intensity (seen as the amount of energy necessary to create 1 point of GDP). A key aspect of the NZE lies in the shift in the current paradigm of the energy generation with a gradual transfer from a fossil fuels-based generation to a renewable generation of the energy in all sectors as shown in [Figure I.1](#). The share of renewable energies in the energy mix in the NZE is planned to grow from 29% in 2020 up to 88% in 2050, mostly driven by the increase of the capacity of solar photovoltaic (PV) and wind power plants. To meet these challenging objectives, the annual installed capacities have to be multiplied by 5 and 3 respectively in 2030 compared to the capacities installed in 2020 (from 134 GW in 2020 up to 630 GW in 2030 for solar PV, from 114 GW in 2020 up to 390 GW in 2030 for wind), and remain at this level until 2050.

Solar PV has the potential to compete with current conventional and renewable energy sources and hence match these expectations. The penetration of PV in the energy market is currently driven by large net capacity additions in China, in the US and in Europe, accounting for more than 50% of the added capacity (IEA (2020)). Additional markets (especially in India and in the Middle East) are expected to develop and contribute to the increase of the annual installed capacity. However, the development of solar PV still highly depends on the local regulation and policies. A recent report from the U.S. Energy Information Administration shows that solar PV generation is among the most economically attractive energy sources, second only to geothermal generation (EIA (2021)), with an average levelized cost of electricity (LCOE) of 30.43 2020-USD per MWh for resources entering service in 2026 at utility scale (including tax credit). Such low LCOEs can be achieved owing to the ever-decreasing module sales price as the cumulative module shipment increases. The learning curve is presented in [Figure I.2.a](#). The learning rate of 23.8% until 2006 has increased up to 40% since 2006, which further promotes the acceleration of the integration of solar PV in the world energy mix. Decreasing the costs of PV owing to mass production savings is a way to make PV more attractive. Another way to do so is to increase the efficiency of the modules, hence increasing the potential power output per surface unit. According to the previsions of the 12th edition of the international roadmap for PV (ITRPV), the PV market will still be strongly dominated by Si cells based on diffused and passivated p-n junctions (PERC/PERL/PERT/TOPCON), still accounting for more than 70% of the market share in 2031 ([Figure I.2.b](#)). Depending on the considered Si technology, the current module efficiencies in mass production vary from 21% to 24%, and are expected to cap at 25.5% efficiency by 2031 ([Figure I.2.c](#)). An alternative way of increasing module efficiencies is to develop tandem technologies. These kinds of modules consist in different solar cells stacked on top of each other, with the objective of harvesting the solar radiation in a more effective way. The reader is referred to H. Li and Wei Zhang (2020) for further details on this matter. ITRPV anticipates the introduction of tandem solar cells on the market as soon as 2023, with a starting efficiency of about 25.5%, increasing to more than 28% in 2031 (+12% relative increase compared to Si monojunctions) ([Figure I.2.d](#)). According to ITRPV predictions, all promising industrial tandem technologies rely on a perovskite-based top cell (Fisher et al. (2021)). Other solutions based on large

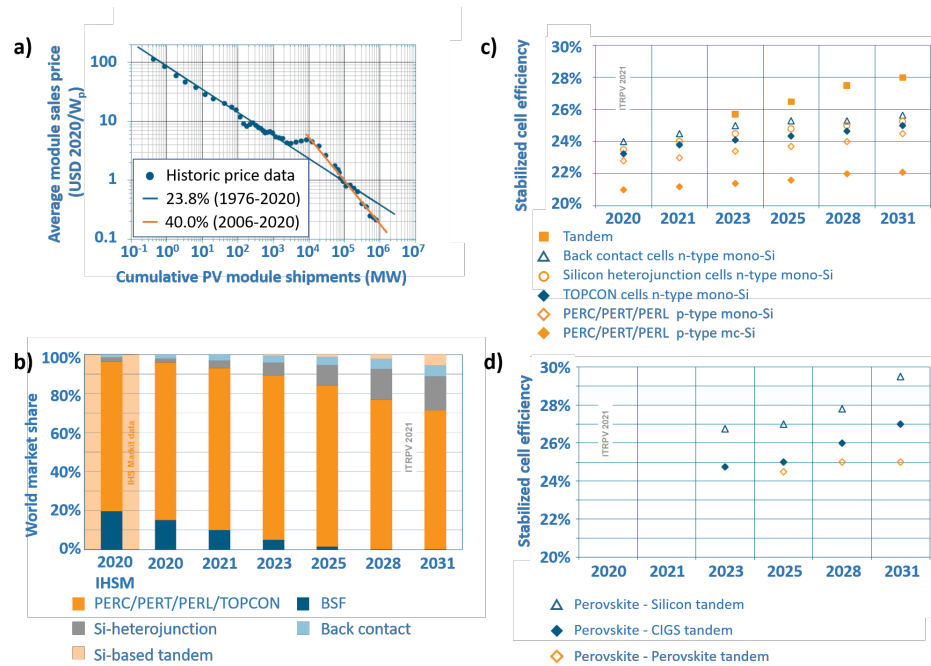


Figure I.2: Projection of ITRPV on the solar PV module market. a) Learning curve of the PV module sales price with the cumulative PV module shipment. b) Predicted composition of the PV module market in terms of technology. c) Predicted efficiencies of mass-production PV modules depending on the technology. d) Predicted efficiencies of mass-production PV modules for various tandem technologies. Adapted from Fisher et al. (2021)

band gap CuInGaSe₂ (CIGS) or III-V technologies on silicon are being developed at lab scale but still lack power conversion efficiency or economic profitability.

Perovskite solar cells are a groundbreaking thin film PV technology whose development has been extremely fast: the efficiency of lab-scale cells has first been reported in 2009 at 3.8% (Kojima et al. (2009)), and has since then steadily increased to reach 25.5% in 2021 (J. Jeong et al. (2021)). The development of industrial scale production of perovskite modules (in tandem or single junction configurations) has quickly followed, supported by the emergence of dedicated start ups (Oxford PV, Saule Technology ...) and recent massive investments of PV manufacturers (\$15 million raised by GCL for the development of a mass production line; *GCL's fund raising* (2021)). This class of material is based on a hybrid organic-inorganic chemistry and encompasses a large variety of materials. Their expedient opto-electrical properties can be tuned depending on the desired application, ranging from small band gap cells for flexible single junctions to large band gap cells for tandem top cells. Perovskite solar cells can be developed at low temperatures (typically <200 °C) by a large variety of processes, and display an interesting tolerance to defects. Apart from these formidable assets, a number of issues have still to be settled to exploit this technology at its full potential. The major challenges consist in:

- (i) the further optimization of the cells architecture to achieve even higher efficiencies (theoretical limit around 30%, depending on the composition of the perovskite);
- (ii) minimizing the losses during the transition from lab-scale cells to commercial modules;
- (iii) ensuring the stability of the cells to match the normative expectations.

This dissertation will focus on the synthesis and on the characterization of a constitutive layer of a perovskite solar cell (PSC) referred to as the electron transport layer (ETL, or n-type selective contact). This layer is usually a wide band gap oxide or a semiconducting organic layer. The former one will mostly be addressed here. Atomic layer deposition (ALD) has been chosen to synthesize these selective contacts. It displays several assets in regard of the aforementioned challenges: ALD is a deposition technique which is already used at an industrial scale (helping in the resolution of challenge (ii)). It allows for the deposition in smooth conditions ($P \sim 1$ mbar, $T < 200$ °C) of very thin yet conformal layers with a possible sub-nanometer control on their thickness, while ensuring a good homogeneity of the layers. Moreover, the composition of the film can be finely controlled (helping toward challenges (i) and (iii)). The synthesis (ALD and completion of the cell) and most of the characterization of the cells have been performed at the Institut Photovoltaïque d'Île-de-France (IPVF, Palaiseau, France). Additional characterizations have been made at the Institut Lavoisier de Versailles (Versailles, France) and at the Laboratoire de Physique de la Matière Condensée (Palaiseau, France).

First, some elements of context are provided in [Chapter 1](#) in order to understand the general framework of the dissertation. Relevant figures of merit of the photovoltaic conversion are derived from thermodynamic considerations and basic condensed matter physics. Theoretical limits are also discussed. This general introduction addresses in more details the specific properties of a perovskite absorber, the basic architectures of a perovskite solar cell, along with the strengths and limitations of this technology. A section is dedicated to the principle of ALD and presents the essential features of an ALD process as well as the specificity of the ALD reactor Beneq TFS-200 which is used for all ALD processes in this dissertation.

[Chapter 2](#) focuses on the description of key processes and of an original characterization tool. The developments of SnO₂ and of TiO₂ by ALD at IPVF are reported. The variations of major characteristics of the as-deposited materials are investigated depending on the set A/B of molecular precursors used (A = tetrakis(dimethylamino)Sn(IV), tetra(isopropoxide)Ti(IV); B = H₂O, H₂O₂), on the deposition temperature and on the thickness of the film (*i.e.* on the number of ALD cycles). This chapter also briefly presents the basics on steady state photoluminescence measurements using a hyperspectral imager. This characterization tool has been devised in A. Delamarre's thesis (Delamarre (2013)), and uses a quite unique way of determining spatially-resolved optoelectronic properties of an absorber owing to absolutely calibrated photoluminescence 3D spectra (two spatial dimensions, one spectral dimension).

Chapter 3 delves into the integration of ALD-TiO₂ in a classic mesoporous perovskite architecture. The usual compact TiO₂ layer deposited by spray pyrolysis (SP-TiO₂) is substituted by a compact ALD-TiO₂ layer, while keeping the rest of the process identical. First, the change of properties of ALD-TiO₂ upon annealing in air is analyzed. In order to assess the potential benefits of ALD in terms of upscale, the relative homogeneity of SP-TiO₂ and ALD-TiO₂ on a large scale substrate is discussed. The integration of ALD-TiO₂ in complete devices and its thickness optimization are presented and compared to the IPVF baseline devices. Finally, the interest of the mesoporous scaffold is addressed.

Chapter 4 focuses on the synthesis of planar perovskite devices integrating the ALD-SnO₂ as electron transport layer. The influence of an annealing step in air after ALD on the properties of the film is discussed. The integration and the optimization of complete devices based on ALD-SnO₂ are then reported. The optimization process encompasses a study on the thickness of the SnO₂ film, on its deposition temperature and on its annealing temperature. The opportunity of increasing the efficiency of the cells by combining the inorganic SnO₂ with an additional organic layer is presented.

Chapter 5 reports on the integration of ALD-ZnO in perovskite devices. To counteract the well-known reactivity of perovskite with ZnO, the grafting of three phosphonic acid derivatives is examined. A thorough study based on surface sensitive characterization methods such as (angle-resolved) X-ray photoelectron spectroscopy (XPS) and attenuated total reflection Fourier transform infrared spectroscopy (ATR-FTIR) allows to identify the grafting modes and structures of the different molecules. The effect of the grafting on the properties of the perovskite deposited on top of the molecules are assessed and gives information on the chemical passivation abilities of the chosen molecules. Finally, complete devices with these modified ALD-ZnO layers are presented.

Chapter 1

General introduction

1.1 Physics of solar cells

Photovoltaic devices are used to harvest the energy of the solar radiation and convert it into electricity. This conversion was first experimentally described by E. Becquerel (Becquerel (1839)) and its theoretical framework has been developed in the course of the XXth century. This section discusses useful notions regarding these devices able to convert the radiation of the Sun into useful electric work. Starting from thermodynamics principles, basic concepts of charge carriers generation and recombination are presented. The ultimate performances of a single junction in the radiative limit are derived and the operation of a more realistic device is briefly discussed.

1.1.1 Black body emission and solar spectrum

The radiation emitted by the Sun can be reasonably described by a black body emission as described by Planck's law at $T_S = 5800$ K.

$$\Phi_{BB}(\lambda, T) = \frac{2hc^2}{\lambda^5} \frac{1}{e^{\frac{hc}{\lambda k_B T}} - 1} \quad (1.1)$$

where Φ_{BB} is the spectral radiance in $\text{J m}^{-2} \text{s}^{-1} \text{m}^{-1} \text{sr}^{-1}$, h is Planck's constant, c the speed of light in vacuum, k_B the Boltzmann constant and T the surface temperature of the black body. Supposing a lambertian emission (Lambert (1760)) and taking into account the quadratic decay of an isotropic radiation, the irradiance reaching the top of the atmosphere is given by $I_\lambda(\lambda, T) = \pi \Phi_{BB}(\lambda, T) \cdot \left(\frac{r_{Sun}}{d_{SE}}\right)^2$ where r_{Sun} is the radius of the Sun and d_{SE} is the Sun-Earth distance (equal to one astronomical unit). A total irradiance of about 1300 W m^{-2} reaches the top of the atmosphere. Part of the spectrum is filtered due to the absorption and scattering by the atmospheric gases (mostly by H_2O , CO_2 , O_2 , O_3 and NO_x). This modification of the solar spectrum depends on the length of the optical path in the atmosphere. The air mass (AM) defines the length of the optical path in the atmosphere at normal incidence, and AM1.0 spectrum is the solar spectrum filtered

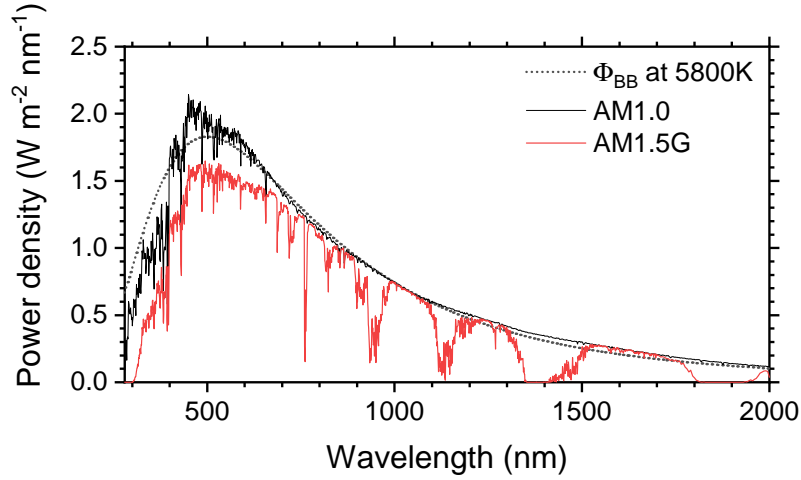


Figure 1.1: Irradiance spectrum of the solar radiation at the top of the atmosphere (AM1.0) and standardized AM1.5G spectrum. The black body radiation at 5800 K is added in dotted line.

by one AM. Similarly, the AMX spectrum is defined as the solar spectrum for an optical path of X air masses and is related to the zenith angle of the Sun z by $z = \cos^{-1}(1/X)$. AM0 spectrum can be used to name the solar spectrum at the top of the atmosphere. In photovoltaics, the standardized solar spectrum is the AM1.5G (G for global, taking into account direct and diffuse light), corresponding to the solar spectrum at the surface of Earth with $z = 48.2^\circ$, and with an incident power of 1000 W m^{-2} . This is representative of the annual irradiance at temperate latitudes. The different spectra (AM0, AM1.5G and the black body radiation) are presented in [Figure 1.1](#).

1.1.2 Generation, quasi equilibrium and quasi Fermi level splitting

An important feature of a semiconductor is its band gap E_g . It consists of a range of forbidden energy states in the material defined by the difference of the conduction band minimum (E_C) and the valence band maximum (E_V). The electrons in the valence band are localized and participate in the cohesion of the lattice while electrons in the conduction band can freely move in the semiconductor and participate in the conductivity of the material. Transitions from the valence band to the conduction band (and vice-versa) can occur but require (or release) an energy $E > E_g$. When an electron leaves the valence band, it creates a quasi-particle named hole of opposite charge. At thermal equilibrium, the distribution of electrons follows a Fermi-Dirac statistic characterized by its Fermi energy E_F :

$$f_e(E) = \frac{1}{e^{\frac{E-E_F}{k_B T}} + 1} \quad (1.2)$$

The distribution of holes can be defined similarly and both Fermi energies are equal at equilibrium. The densities of free carriers n (electrons) and p (holes) are determined as the convolution of the Fermi-Dirac statistic with the density of states (DOS) of the conduction and valence bands respectively.

Under illumination, the semiconductor absorbs the radiation with an energy $E > E_g$, described in [Figure 1.2](#) (step 1). With this energy gain, an electron-hole pair is created (an electron of the valence band is promoted to the conduction band, step 2). The higher the energy of the radiation, the higher the kinetic energy of the photogenerated carriers is. They rapidly lose energy by interaction with the lattice (emission of phonons of energy ~ 10 meV) until they reach the bottom of the conduction band or the top of the valence band (step 3). This relaxation called thermalization is fast within the bands (on the order of the ps) because of the continuum of accessible energy states. Specific recombination pathways are responsible for the recombination of an electron at the bottom of the conduction band and a hole of the top of the valence band. They occur on larger timescales and are detailed in [section 1.1.3](#) (step 4). After the fast thermalization, the populations of electrons in the conduction band and of holes in the valence band reach a quasi-equilibrium state and can hence be described by a Fermi-Dirac statistic. However, since both populations have simultaneously increased, a single Fermi energy is not enough to describe the system; distinct quasi-Fermi levels for electrons E_{FC} and for holes E_{FV} are introduced (Würfel (2005)), defined by the distribution of electrons f_e and holes f_h :

$$f_e(E) = \frac{1}{e^{\frac{E-E_{FC}}{k_B T}} + 1} \quad ; \quad f_h(E) = \frac{1}{e^{\frac{E-E_{FV}}{k_B T}} + 1} \quad (1.3)$$

In the Boltzmann approximation valid for $E_C - E_{FC} > 3k_B T$ and $E_V - E_{FV} > 3k_B T$, the quasi Fermi levels can be expressed as:

$$E_{FC} = E_C - k_B T \ln \left(\frac{N_C}{n} \right) \quad (1.4a)$$

$$E_{FV} = E_V + k_B T \ln \left(\frac{N_V}{p} \right) \quad (1.4b)$$

where N_C and N_V are the effective density of state of the conduction band and of the valence band. Note the [Equation \(1.4\)](#) resembles two Nernst equations with standard potentials E_C and E_V .

Work can be produced from the solar cell by extracting the electrons and the holes before they are able to recombine. The accessible energy can be determined by thermodynamic considerations. Würfel derived the variation in free energy dF resulting from the variation in the number of free carriers dN (Würfel (1982)).

$$dF = dF_n + dF_p = (\eta_n + \eta_p)dN = ([\tilde{\mu}_n - q\phi] + [\tilde{\mu}_p + q\phi]) dN \quad (1.5)$$

where n and p subscripts refer to electrons and holes, η is the electrochemical potential, $\tilde{\mu}$ is the chemical potential, q is the elementary charge and ϕ is the electrostatic potential. Further derivations allow to identify the electrochemical

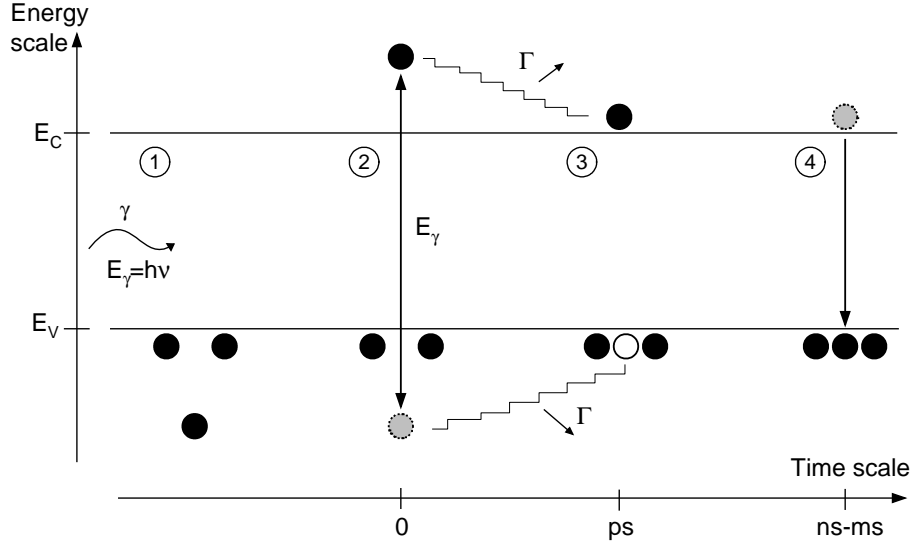


Figure 1.2: Schematic of the photon/matter interaction in a semiconductor. Upon absorption of a photon γ of energy $E_\gamma > E_g$ (step 1) an electron hole-pair is generated (step 2). The populations of electrons and holes thermalize to the band edges by interaction with the lattice, emitting phonons Γ (step 3). At longer time scales, electrons and holes recombine (step 4).

potential to the quasi-Fermi levels defined earlier:

$$\frac{dF}{dN} = \eta_n + \eta_p = E_{FC} - E_{FV} = \Delta\mu \quad (1.6)$$

where the quasi Fermi level splitting $\Delta\mu$ is introduced. Hence the amount of work which can be extracted from a solar cell is directly related to the number of carriers which can be extracted and to their quasi-Fermi level splitting (QFLS). The electrical energy provided by the solar cell can also be written as a function of the external voltage V : $dE_{el} = V \cdot qdN$. By identification with Equation (1.6), it comes $qV = \Delta\mu$. Using Equation (1.4), V and $\Delta\mu$ can be expressed as function of properties of the semiconductor:

$$qV = \Delta\mu = E_g - k_B T \ln \left(\frac{N_C N_V}{np} \right) \quad (1.7)$$

Equation (1.7) underlines the relation between the external voltage of the cell, the band gap energy of the absorber and the density of the photogenerated charge carriers.

1.1.3 Recombination pathways of carriers

After the thermalization step of a semiconductor under illumination, the populations of electrons and holes are in thermal equilibrium with the lattice (the same T characterizes both populations) and in equilibrium within each band (Fermi

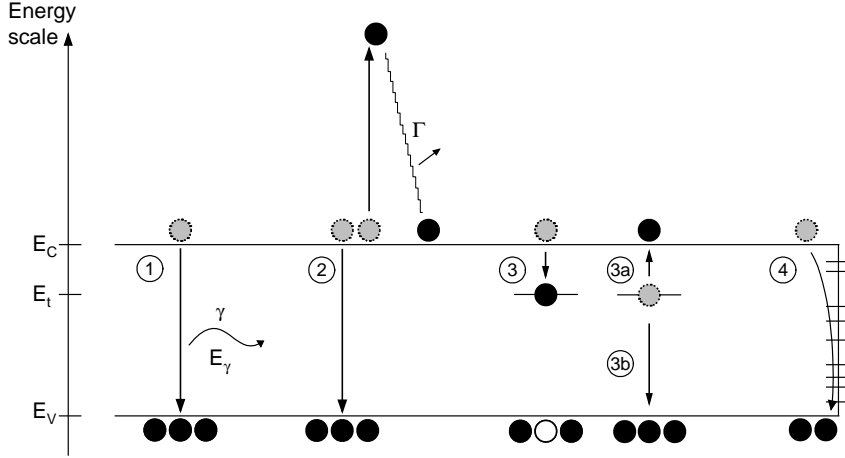


Figure 1.3: Schematic of the different recombination pathways in a semiconductor: 1) radiative recombination resulting in the emission of a photon γ . 2) Auger recombination involving an extra free electron. 3) Trap-assisted bulk recombination through a trap state localized at energy E_t . The trapped charge can either escape the trap (3a) or recombine (3b). 4) Surface recombination through a continuous distribution of interfacial states.

Dirac statistic applies for both populations); however the system is not in equilibrium with the ambient radiation ($\Delta\mu \neq 0$). From this quasi-equilibrium state, the system can relax to equilibrium using different pathways which are classified here as radiative recombinations and non-radiative recombinations, summarized in [Figure 1.3](#). Recombination rates can be defined to include the recombinations in the continuity equation which governs the charge carrier dynamics:

$$\frac{\partial n}{\partial t}(x) = G_n(x) - R_n(x) + D_n \frac{\partial^2 n}{\partial x^2} + \mu_n \frac{\partial(n\mathcal{E})}{\partial x} \quad (1.8a)$$

$$\frac{\partial p}{\partial t}(x) = G_p(x) - R_p(x) + D_p \frac{\partial^2 p}{\partial x^2} - \mu_p \frac{\partial(p\mathcal{E})}{\partial x} \quad (1.8b)$$

where $G(x)$ and $R(x)$ gather the generation and recombination rates, D is the diffusion coefficient, μ is the mobility and \mathcal{E} is the local electrostatic field. Further details on the derivation of the continuity equation can be found in other references ([Würfel \(2005\)](#)).

1.1.3.1 Radiative recombinations

During a radiative recombination ([Figure 1.3.1](#)) an electron from the conduction band and a hole from the valence band recombine by emitting a photon of energy E . The radiative recombinations are responsible for the emission spectrum of a semiconductor. The spectral irradiance of a semiconductor is given by the Lasher-

Stern-Würfel equation (Roosbroeck and W. Shockley (1954); William Shockley and Queisser (1961); Lasher and Stern (1964); Würfel (1982)).

$$\Phi_{em}(E, T, \Delta\mu) = \frac{2}{h^3 c^2} \frac{E^2 a(E)}{\exp\left(\frac{E - \Delta\mu}{k_B T}\right) - 1} \quad (1.9)$$

where Φ_{em} is the spectral irradiance by unit of solid angle in $\text{ph m}^{-2} \text{s}^{-1} \text{J}^{-1} \text{sr}^{-1}$ and $a(E)$ is the absorptance of the semiconductor. The semiconductor can only absorb light at energies higher than the band gap, so that $a(E) \sim 1$ for $E > E_g$ and $a(E) \sim 0$ for $E < E_g$. The absorption around the band gap is governed by the band structure near the band edges and is quite sensitive to sub-band gap states. A comprehensive model for the absorption is discussed in [section 2.3.2.3](#). At thermal equilibrium ($\Delta\mu = 0$), the emission spectrum corresponds to that of a black body radiation described in [Equation \(1.1\)](#) for energies higher than the band gap. This kind of emission is thus sometimes referred to as a grey-body emission. Out of thermal equilibrium (for instance if the semiconductor is pumped by a light bias – photoluminescence, PL – or an electric bias – electroluminescence, EL), the QFLS modifies the emission spectrum. For a non-degenerated semiconductor in low injection regime, $E - \Delta\mu \gg k_B T$ if $E > E_g$. The Boltzman approximation can be applied, and [Equation \(1.9\)](#) can be approximated by:

$$\Phi_{em}(E, T, \Delta\mu) \approx \Phi_{em}(E, T, \Delta\mu = 0) \cdot \exp\left(\frac{\Delta\mu}{k_B T}\right) \quad (1.10)$$

[Equation \(1.10\)](#) shows that under injection, the luminescence of the absorber scales exponentially with the QFLS, which provides a sensitive tool to investigate the QFLS and the absorption properties of a film as discussed in [chapter 2.3](#).

The radiative recombination rate has been derived by Roosbroeck and Shockley from the detailed balance principle applied to the spontaneous absorption and emission (Roosbroeck and W. Shockley (1954)):

$$R_{rad} = R_{eh}(np - n^0 p^0) \quad (1.11)$$

where R_{eh} is the bulk radiative recombination rate, and n^0 and p^0 are the carrier densities at equilibrium.

1.1.3.2 Non-radiative recombinations

Diverse types of non-radiative recombinations can occur either within the bulk of the material or at the interfaces.

Auger recombination ([Figure 1.3.2](#)) is a type of bulk recombination based on the Auger effect (Meitner (1922); Auger (1923)) which can be described by the rate equation:

$$R_{aug}(x) = K_{A1} \cdot n(np - n^0 p^0) + K_{A2} \cdot p(np - n^0 p^0) \quad (1.12)$$

This process involves three particles: an electron-hole pair and a free electron (rate K_{A1}) or hole (rate K_{A2}). The energy released by the recombination of the electron-hole pair is transferred to the free carrier which accesses states of higher energy

in its band. Since the process relies on the interaction between three particles, it is less probable than the other recombinations presented here and requires high carrier densities to have an influence on the recombination dynamics. It is for instance a well known phenomenon in Si solar cells limiting the ultimate carrier lifetime, but it remains negligible in perovskite solar cells under usual operation conditions (low and moderate injection regimes, Q. Lin et al. (2018)).

Trap-assisted recombinations (Figure 1.3.3) have been formalized by W. Shockley, W.T. Read and R.N. Hall (SRH) (W. Shockley and Read (1952); R. N. Hall (1952)). These traps can be for instance impurities or imperfections in the lattice. As an example, a free electron gets trapped in a localized state at an energy level in the band gap, emitting a photon or multiple phonons. It can from there either be released in the conduction band (step 3a) or recombine with a hole of the valence band (step 3b). For an impurity (recombination center) located at an energy level E_t , the rate equation is written:

$$R_{trap} = \frac{np - n^0 p^0}{\tau_n(n + n_1) + \tau_p(p + n_2)} \quad (1.13)$$

where τ_n (τ_p) is the lifetime of an electron (a hole) in the conduction band (valence band) if all impurities are filled with holes (with electrons), $n_1 = N_C \exp[-(E_C - E_t)/k_B T]$ and $n_2 = N_V \exp(-(E_t - E_V)/k_B T)$. The lifetime can be expressed function of the density of the impurities and of their capture cross-section (Würfel (2005)). Traps located in the middle of the gap (deep traps) are more active recombination centers than the one located close to a band edge (shallow traps) (Würfel (2005)). It can be intuitively understood: the shallower the trap, the easier it is for the trapped charge to escape it (due to thermal motion) before it recombines. Hence, midgap defects are especially detrimental and should be avoided.

Finally, non-radiative recombinations occur at the surface of the absorber (Figure 1.3.4). The recombination process is similar to the one described in the SRH recombination, *i.e.* assisted by states inside the band gap. Due to the often chaotic chemistry of the surfaces (adsorbed species, disruption of the crystalline lattice ...), the surface trap states are hard to precisely characterize and constitute a continuum of states inside the gap. A practical formalization of this recombination pathway consists in the introduction of a surface recombination velocity v^{rec} such that the surface recombination rate is written:

$$R_{surf,n} = v_n^{rec} n \quad (1.14a)$$

$$R_{surf,p} = v_p^{rec} p \quad (1.14b)$$

Surface recombinations are treated as boundary conditions in Equation (1.8) ($D_n \partial n / \partial x = R_{surf,n}$ and $D_p \partial p / \partial x = R_{surf,p}$ at the boundaries).

1.1.4 Thermodynamic limits of the photovoltaic conversion

1.1.4.1 Ultimate performances of the photovoltaic conversion

The maximal efficiency for the conversion of solar energy into electrical energy can be estimated from thermodynamic considerations (De Vos and Pauwels (1981);

Würfel (2005)). A perfect converter is regarded as a black body absorber at temperature T_C which exchanges energy and entropy currents with the Sun (absorbed currents \dot{E}_S , \dot{S}_S , emitted current \dot{E}_C , \dot{S}_C) and work current \dot{W} with its surrounding at ambient temperature T_A . An additional term $\dot{S}_G \geq 0$ accounts for the created entropy flux according to the second law of thermodynamics. The application of the first and second laws of thermodynamics allows to write:

$$\dot{E}_S - \dot{E}_C = T_A \cdot (-\dot{S}_G + \dot{S}_S - \dot{S}_C) - \dot{W} \quad (1.15)$$

The converter is assumed to be able to absorb the radiation of the Sun with creation of entropy while preserving a temperature $T_C < T_S$ ($\dot{S}_G = 0$, reversible process). This assumption is disputable but sets the best-case scenario for the photovoltaic conversion. The entropy and energy currents of a black-body at temperature T are given by (Würfel (2005)):

$$\dot{E}_{BB} = \sigma T^4 \quad (1.16a)$$

$$\dot{S}_{BB} = \frac{4}{3} \sigma T^3 \quad (1.16b)$$

where σ is the Stefan-Boltzmann constant. Considering that the Sun and the converter behave as black-bodies at T_S and T_C , the efficiency of the photovoltaic conversion reads:

$$\eta = -\frac{\dot{W}}{\dot{E}_S} = 1 - \frac{4 T_A}{3 T_S} - \left(\frac{T_C}{T_S}\right)^4 \left(1 - \frac{4 T_A}{3 T_C}\right) \quad (1.17)$$

It reaches its maximum value for $T_C = T_A$ for which $\eta = 93.3\%$ also known as the Landsberg limit. It sets the thermodynamic upper bound for any photovoltaic conversion. Landsberg limit could theoretically be approached with a device composed of an infinity of monochromatic absorbers. The tandem technology is based on this principle, distributing the absorption of the solar spectrum over several absorbers (in practice between two and four of them) in order to increase the power conversion efficiency of the system. Perovskite solar cells as presented in this manuscript are expected to enable the industrialization of such devices.

1.1.4.2 Radiative limit of a single junction solar cell

In this manuscript, the focus is put on the synthesis of single junction solar cells, whose ultimate operation conditions differ from the one described by the Landsberg limit. Ultimate PV parameters at various operation points of such devices can nevertheless be determined to compare real-life devices with.

Under illumination with a spectral photon flux Φ_{abs}^{ex} , the maximum flux of photo-generated carriers per illuminated area unit Φ_{gen}^{max} is determined by the band gap of the material:

$$\Phi_{gen}^{max} = \int_{E_g}^{\infty} \Phi_{abs}^{ex}(E) dE \quad (1.18)$$

where Φ_{abs}^{ex} is in $\text{ph s}^{-1} \text{eV}^{-1}$. Equation (1.18) supposes (i) a perfect transmission of the light from the external medium to the absorber, (ii) a perfect step absorptance

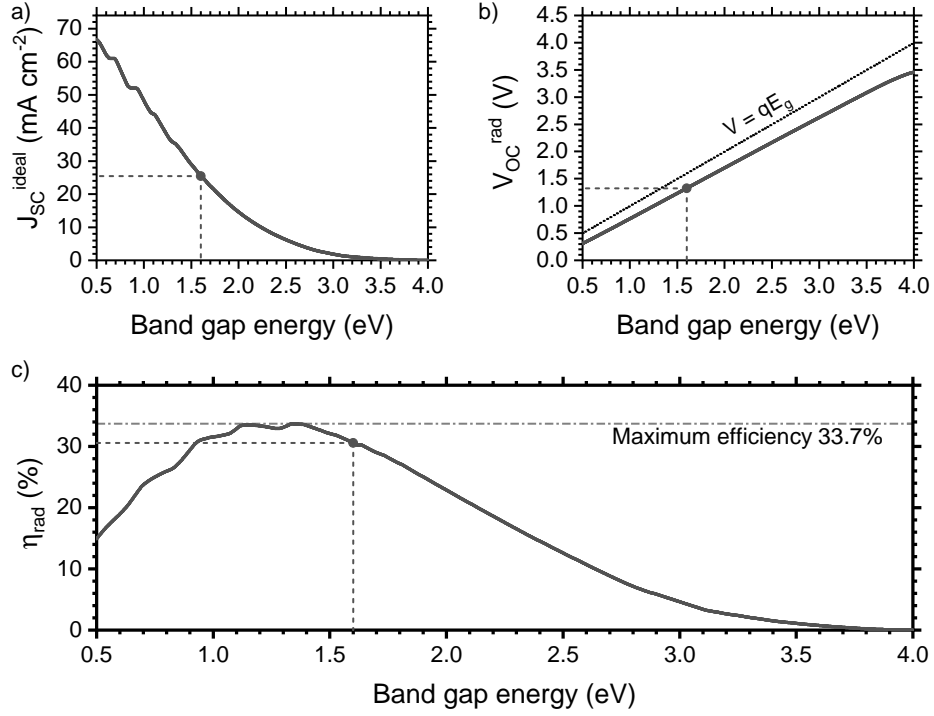


Figure 1.4: Ultimate PV parameters of a single junction function of the band gap of the absorber under AM1.5G spectrum: a) ideal J_{SC} , b) V_{OC} in the radiative limit, c) ultimate power conversion efficiency (PCE) of a single junction. The parameters for an absorber with a band gap at 1.6 eV are indicated.

of the semiconductor $a(E) = 1$ if $E > E_g$, $a(E) = 0$ otherwise, (iii) a one-for-one conversion of impinging photon to an electron-hole pair. At ideal short circuit conditions, the electron hole pairs are separated and the free carriers are extracted towards the external circuit by the mean of selective contacts without any loss. The maximum short-circuit current density can then be written:

$$J_{SC}^{ideal} = q\Phi_{gen}^{max} = q \int_{E_g}^{\infty} \Phi_{abs}^{ex}(E) dE \quad (1.19)$$

The variation of the short circuit current density function of the band gap of the absorber under AM1.5G is presented in Figure 1.4.a. As expected, the lower the band gap is, the higher the achievable short circuit current density. For a semiconductor with a band gap of 1.6 eV, $J_{SC}^{ideal} = 25.48 \text{ mA cm}^{-2}$.

As mentioned in section 1.1.3, the semiconductor at thermal equilibrium with its surrounding at temperature T emits a grey-body radiation which can be written for each energy $\Phi_{em,0}(E, T) = a(E)\Phi_{BB}(E, T)$. Because of the equilibrium, the absorbed and emitted fluxes are equal $\Phi_{abs,0} = \Phi_{em,0}$. Under illumination (Φ_{abs}^{ex}), this emission is enhanced by a factor $\exp(\Delta\mu/k_B T)$. Supposing that only radiative

recombinations occur (radiative limit), the net radiative current density is given by:

$$J_{rad} = q(\Phi_{abs} - \Phi_{em}) \quad (1.20a)$$

$$= q \left((\Phi_{abs,0} + \Phi_{abs}^{ex}) - \exp\left(\frac{\Delta\mu}{k_B T}\right) \Phi_{0,em} \right) \quad (1.20b)$$

$$= J_{SC}^{ideal} - q\Phi_{0,em} \left(\exp\left(\frac{\Delta\mu}{k_B T}\right) - 1 \right) \quad (1.20c)$$

Remembering that the QFLS is related to the external voltage (Equation (1.7)), the radiative limit of the open circuit voltage can be calculated setting $J_{rad} = 0$ which yields:

$$V_{OC}^{rad} = \frac{k_B T}{q} \ln \left(\frac{J_{SC}^{ideal}}{q\Phi_{0,em}} + 1 \right) \quad (1.21)$$

The variation of V_{OC}^{rad} function of the band gap of the semiconductor for an AM1.5G illumination spectrum is reported in Figure 1.4.b. For a band gap of 1.6 eV, $V_{OC}^{rad} = 1.33$ V. The optimal fill factor in the radiative limit can be estimated from the V_{OC} as follows: $FF = 1 - k_B T / (qV_{OC})$, which yields a fill factor of 98%.

Electric work can be expressed as $W_{el} = JV$. In both situations presented before, no work can be extracted from the cell because there is no potential difference (short-circuit) or no current flowing (open-circuit). The maximum power point is hence located somewhere in between these two operation points. The maximum power conversion efficiency can be determined as:

$$\eta_{rad} = \frac{J_{rad}(V_{mpp}) \cdot V_{mpp}}{\Phi_{abs}^{ex}} \quad (1.22)$$

where V_{mpp} is such that $d\eta/dV(V_{mpp}) = 0$. MPP stands for maximum power point. The variation of η_{rad} with the band gap of the semiconductor under AM1.5G is displayed in Figure 1.4.c. A maximum power conversion efficiency (PCE) of 33.7% can be achieved for a band gap of 1.34 eV. For a semiconductor with a band gap of 1.6 eV, the maximum PCE is 30.6%. A similar derivation was first proposed by W. Shockley and H.J. Queisser in 1961 (William Shockley and Queisser (1961)).

1.1.5 Relation with the operation of realistic devices.

In reality, the PV parameters of single junctions are lower than the ideal case derived in the previous section. Because of additional non-radiative recombination pathways, the conversion of an incoming photon into an electron in the external circuit is not unity. It is represented by the spectral external quantum efficiency (EQEPV, electrons out/photons in) and Equation (1.18) becomes:

$$J_{SC} = q \int_0^{\infty} EQEPV(E) \Phi_{abs}^{ex}(E) dE \quad (1.23)$$

The external quantum efficiency takes into account the optical losses of photons, the absorption of the absorber, as well as the losses of charge carriers due to

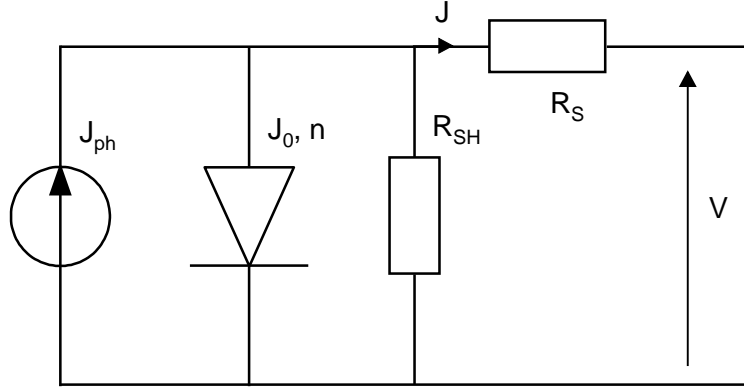


Figure 1.5: Simplified one diode electrical model of a realistic solar cell.

non-radiative recombinations. Uwe Rau (2007) derived two reciprocity relations for PV solar cells which allow to estimate the non-radiative losses of a solar cell from PL and EL measurements:

$$I_{EL}(E) = EQE_{PV}(E)\Phi_{BB}(E) \left(\exp\left(\frac{qV}{k_B T}\right) - 1 \right) \quad (1.24a)$$

$$\Delta V_{OC} = V_{OC}^{rad} - V_{OC} = -\frac{k_B T}{q} \ln(EQE_{LED}) \quad (1.24b)$$

where EQE_{LED} is the external quantum efficiency of a light emitting diode (LED, photons out/electrons in). Equation (1.24b) can also be re-written in terms in terms of photoluminescence quantum yield (PLQY, photons out/photons in) as showed by Ross (1967):

$$\Delta V_{OC} = -\frac{k_B T}{q} \ln(PLQY) \quad (1.25)$$

Usually the behavior of a solar cell is modeled by the electric schematic presented in Figure 1.5 and is governed by the following equation:

$$J(V) = J_{ph}(V) - J_0 \left(\exp\left(\frac{q(V + JR_S)}{n_{id} k_B T}\right) - 1 \right) - \frac{V + JR_S}{R_{SH}} \quad (1.26)$$

This diode equation can be seen as an extension of the Equation (1.20) derived in the ideal radiative limit. Two resistance terms R_S (series resistance) and R_{SH} (shunt resistance) have been added to account for the ohmic losses due to the transport of the carriers (R_S) and for the recombinations via shunt paths in the solar cell (R_{SH}). The ideality factor n_{id} indicates the kind of recombinations occurring in the absorber. R. Scheer and H.W. Schock derived the value of n_{id} for different recombination processes (Scheer and Schock (2011)). Usually, $n_{id} \sim 1$ indicates that the majority recombinations are the band-to-band radiative recombinations (as

in Equation (1.20)) whereas $n_{id} \sim 2$ indicates SRH-dominated recombinations. The dark current density J_0 is related to the grey-body emission of the semiconductor at thermal equilibrium. Finally, the photo current can depend on the voltage which is sometimes referred to as the violation of the shifting approximation (Robinson et al. (1994)). It mirrors the fact that the charge collection efficiency can depend on the voltage which can be explained for instance by interface recombinations or photocurrent barriers. It can also be caused by shunt pathways appearing in secondary phases under illumination, by a large series resistance or by the saturation of SRH recombinations (Scheer and Schock (2011)).

1.2 Perovskite solar cells

1.2.1 The genesis of perovskite solar cells

1.2.1.1 Perovskite materials

Discovered in 1839 by G. Rose (Rose (1840)), the perovskite structure describes a large class of materials characterized by a similar chemical composition ABX_3 (more on this in section 1.2.2.1). Silicate perovskite materials ((Mg,Fe)SiO₃ or CaSiO₃) are a major constituent of the lower parts of Earth's mantle (Murakami et al. (2012)). A recent study identified more than 90,000 potential combination of perovskite materials - most of which have not been studied in practice (Filip and Giustino (2018)). Based on the same structure than the natural silicate perovskite, synthetic inorganic oxide perovskite materials have been developed and used in various research areas such as electrocatalysis, photocatalysis, photovoltaics (W.-J. Yin et al. (2019)), optics, capacitors (Dimos and Mueller (1998)) ... Organic-inorganic perovskite were first reported in the late 1970s and gained interest in the research community from the 1990s onward and have been used in thin film field effect transistors, LEDs and laser cavities (Zhengzheng Liu et al. (2020)).

1.2.1.2 Halide perovskite

In 2009, the group of T. Miyasaka used for the first time a hybrid organic-inorganic halide perovskite material (CH₃NH₃PbX₃, X = I or Br) as the absorber material in a dye sensitized solar cell (DSSC) and reached a power conversion efficiency of 3.8% (Kojima et al. (2009)). The perovskite material was immersed in a corrosive liquid electrolyte – acting as hole selective contact – which lowered substantially its stability. Major breakthroughs occurred in 2012 in the group of H. Snaith (M. M. Lee et al. (2012)) and M. Graetzel (H.-S. Kim et al. (2012)). A solid hole transport layer is used in lieu of the electrolyte, which solved partly the issue of stability of the perovskite materials. At the same time, the perovskite quantum dots sensitizing the mesoporous TiO₂ in previous architectures were replaced by a thin film of perovskite, thanks to the superior opto-electrical properties of the perovskite (absorption and transport properties). It required a challenging control of the nucleation of the layer (Soto-Montero et al. (2020)). These changes in the architecture of the cell distinguish this technology from the DSSCs. As absorbers, organometallic trihalide perovskite feature exceptional optoelectronic performances and the PV community has shown a growing interest towards them in the past

ten years going from only 10.9% in 2012 to certified 25.5% in 2021 (J. Jeong et al. (2021)). The easy processing pathways and large emulation of the scientific community on this topic augur a bright future for perovskite solar cells which in less than 10 years already compete with longer-established and longer-studied technologies at lab scale (Si, CIGS, CdTe, ...).

1.2.1.3 Industrialization perspectives

Because of the versatility of perovskite materials and their projected low environmental impact, perovskite solar cells are considered as a promising technology from an industrial point of view. Even though the stability of perovskite cells has been an issue in the early stages of the development of the technology, companies recently claimed that viable solutions are being developed to allow for an upcoming commercialization of perovskite modules withstanding stability standards. For instance Oxford PV, founded by H. Snaith back in 2010, has recently announced performances approaching 30% on 1 cm² perovskite-on-silicon tandem solar cells (*Oxford PV* (2021)). Their CEO, F. Averdung, expects their perovskite-on-silicon tandem modules to enter the PV market by early 2022. According to the 12th edition of ITRPV, the tandem solar cells are expected to enter the market by 2023 (Fisher et al. (2021)). Major companies in the renewable area such as the German Meyer Burger or the Chinese GoldWind recently invested in Oxford PV, underlining the trust and interest of well-established industrial actors in this technology. Other actors such as Saule Technology, Toshiba or Microquanta Semiconductor participate in this race for the industrialization of perovskite solar modules (integrated in tandem architectures or as single junctions *e.g.* on flexible substrates). Recently, the giant of PV modules manufacturer GCL raised over \$15 million for the development of a 100 MW mass-production line of perovskite solar cells (*GCL's fund raising* (2021)).

1.2.2 Properties of halide perovskite

This section focuses on reporting the main structural and optoelectrical properties of hybride halide perovskite. This set of material used for solar cell applications encompasses a large variety of compositions, hence a large variety of properties. The focus is first put on the archetypal CH₃NH₃PbI₃ which is subject of a large part of theoretical studies on halide perovskite. The discussion is then extended to other commonly used compositions in photovoltaic devices. Finally, the properties of the specific composition used in this dissertation are addressed.

1.2.2.1 Structural properties

A perovskite material refers to a material having a similar crystalline structure as the historical CaTiO₃ formalized as ABX₃. In the case of organometallic trihalide perovskite, the A species is a monovalent organic cation (most representative cations being methylammonium CH₃NH₃⁺ – MA⁺ or formamidinium CH₂(NH₂)₂⁺ – FA⁺), the B species is a divalent metallic cation (usually Pb²⁺ or Sn²⁺) and X is a halogen (Cl⁻, Br⁻ or I⁻). An alkali metal (Cs⁺, Rb⁺, K⁺) can also be added in the mixture in the A site for composition engineering purposes. The ideal crystalline structure

has a cubic symmetry, in which the A cation is 12-fold coordinated to the X halogen of the inorganic octahedral cages BX_6 (Figure 1.6). V. Goldschmidt devised an empirical rule which predicts stable compositions of perovskite-like materials at room temperature (Equation (1.27)):

$$0.813 < t = \frac{R_A + R_B}{\sqrt{2}(R_A + R_X)} < 1.107 \quad (1.27)$$

where R_X is the atomic radius of species X (Goldschmidt (1926)). t can be seen as the ratio of the atomic radii in a close-packed perovskite structure ($t = 1$).

With decreasing temperature, the perovskite transitions from the cubic phase (α -phase) to a tetragonal or hexagonal phase (β - and δ -phase respectively) and finally an orthorhombic phase (γ -phase) – typical transition temperatures are given in Figure 1.6.a. In cubic, tetragonal and orthorhombic symmetries, the octahedra share corners, while they share edges in the hexagonal symmetry (B. Kim et al. (2020)). The transition from cubic to tetragonal symmetries is characterized by alternate rotation of the octahedra around the c -axis, reducing the symmetry of the crystal. The transition from tetragonal to orthorhombic symmetry is characterized by the rotation of the octahedra in the same direction along the c -axis (Whitfield et al. (2016)).

The cohesion of the crystal relies on different mechanisms. The inorganic structure of BX_6 octahedra is supported by ionic bonding mixed to a lesser extent with covalent and van der Waals contributions (Egger et al. (2016)). These strong interactions cause the hybridization of electronic states of these ions. On the other hand, the organic cation is only weakly bound to the inorganic cage *via* hydrogen bonding. It does not participate in the electronic states close the band edges of the perovskite and has ultimately a structural role (as a scaffold to force the organization of corner-sharing BX_6) and an electrostatic role (charge compensation) (Brivio et al. (2014)). Due to the relative flexibility of the crystalline structure, the crystal can accommodate ions of non-ideal size ($t \neq 1$) and still preserve its cubic symmetry. The softness of the structure also explains the high ionic mobilities in the crystal, related to low activation energies for ion migration. For instance in $MAPbI_3$, activation energies for I^- , MA^+ and Pb^{2+} are reported between 0.08 and 0.58 eV, 0.46 and 1.12 eV, and 0.8 and 2.31 eV respectively, based on both theoretical predictions and experimental observations (Futscher et al. (2019)). As comparison, the activation energy for Si^0 self-diffusion has been found higher than 4.0 eV (by density functional theory, DFT), highlighting the "softness" of perovskite materials (Estreicher et al. (2011)). This ionic conduction is at the root of hysteresis phenomena observed in perovskite solar cells.

1.2.2.2 Optoelectronic properties of the archetypal $MAPbI_3$

The properties of $MAPbI_3$ have been extensively studied and serve as a basis of understanding for the properties of other hybrid organic-inorganic perovskite. It is reported to have an optical band gap around 1.55 eV and an excellent absorption coefficient (De Wolf et al. (2014)). Values up to $1 \times 10^5 \text{ cm}^{-1}$ have been measured by Fourier transform photocurrent spectroscopy measurement which is comparable

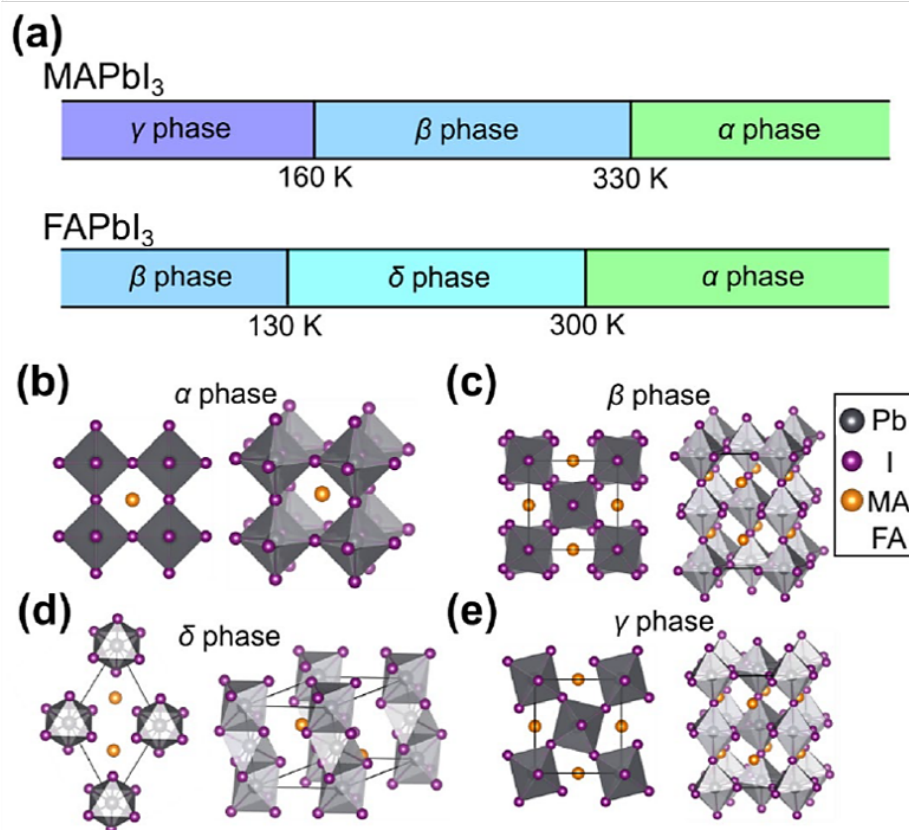


Figure 1.6: Phase transition of perovskite materials. a) Phase transition temperatures for MAPbI₃ and FAPbI₃. Crystal structure of a) the perovskite α -phase, b) the perovskite β -phase, c) the non-perovskite δ -phase and d) the perovskite γ -phase. The 2D view are taken along the c direction. Reproduced from B. Kim et al. (2020).

to GaAs (direct band gap) and almost two orders of magnitude higher than c-Si (indirect band gap) (Figure 1.7). Only a thin layer of absorber (sub-micrometric) is required to harvest most of the useful solar spectrum, justifying the use of perovskite in thin film solar cells configuration. As mentioned before, the band structure of MAPbI₃ close to the band edges is formed by the orbitals of the inorganic ions. The valence band maximum is composed of a mixture of Pb 6s and I 5p orbitals (rather anionic nature), while the conduction band minimum is composed of the Pb 6p orbitals (Egger et al. (2016)). The possible intra-atomic transitions between Pb 6s and Pb 6p orbitals have been advanced as an explanation to the high absorption coefficient observed in MAPbI₃ (Wan-Jian Yin et al. (2015)). The binding energy of excitons in MAPbI₃ is only of a few meV at room temperature (Miyata et al. (2015)). It is less than the thermal energy at room temperature (25 meV), which means that photogenerated charge carriers can be essentially considered as free carriers.

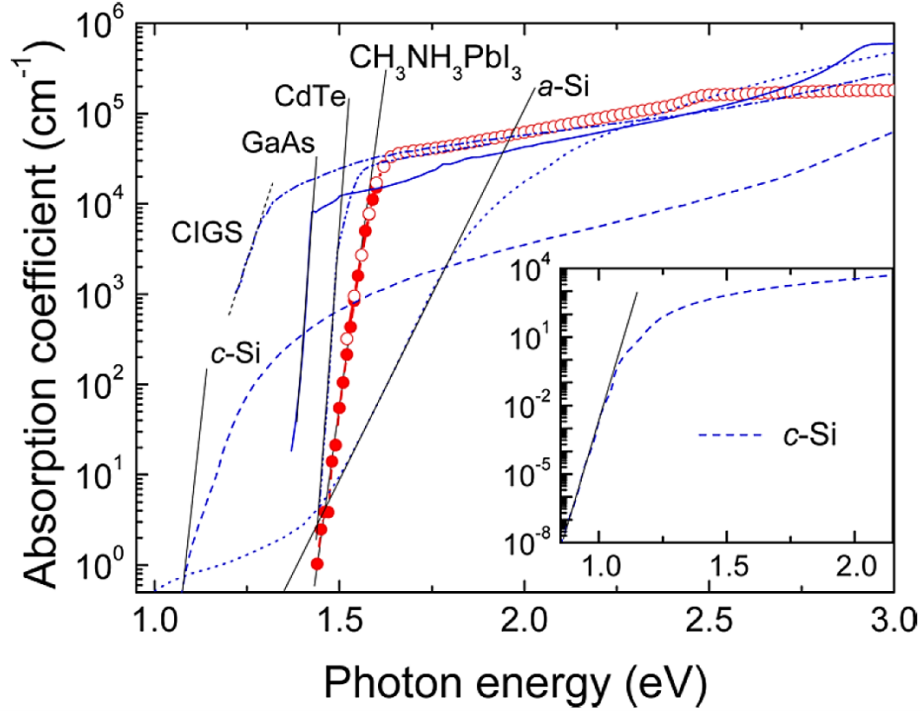


Figure 1.7: Effective absorption coefficient of a MAPbI_3 perovskite thin film compared with other typical photovoltaic materials, including amorphous silicon (a-Si), GaAs, CIGS, CdTe, and crystalline silicon (c-Si), all measured at room temperature. For clarity, the inset shows the data for c-Si down to low absorption values. Reproduced from De Wolf et al. (2014).

The generation and recombination mechanisms in perovskite absorbers have sparked a large interest and have been investigated by various methods (Wolff et al. (2019)). Radiative recombination rates measured in perovskite ($\sim 1 \times 10^{-10} \text{ cm}^{-3} \text{ s}^{-1}$ Bercegol et al. (2017)) are on par with those of III-V technologies (Markvart and Castañer (2018)). Large carrier lifetimes (above $1 \mu\text{s}$, deQuilettes et al. (2016)) have been reported. The mechanisms behind these high values are still subject to discussion (deQuilettes et al. (2019)). Part of the answer can be related to the sub-band gap states which can act as non-radiative recombination centers. In hybrid perovskite, shallow states have a lower formation energy than mid-gap states. As mentioned in section 1.1.3.2, this kind of defects are way less harmful to the carrier lifetime, explaining the large tolerance of perovskite absorbers to defects. The characteristic defect density for MAPbI_3 is reported around $1 \times 10^{16} \text{ cm}^{-3}$ (Bercegol, Ramos, Rebai, Guillemot, Ory, et al. (2018)). Other optical effects such as Rashba effect (T. Wang et al. (2017)) or photon recycling (Kirchartz et al. (2016)) can also explain the exceptional opto-electronic properties of perovskite absorbers. The long carrier lifetime makes up for the low mobilities observed in perovskite and diffusion lengths up to several μm are observed (Gong et al. (2019)), which is much more than the thickness usually needed to harvest most of the solar spectrum.

1.2.2.3 Alternative compositions

Apart from MAPbI₃, other compositions of perovskite have been investigated in the search for adaptability to diverse applications, enhanced performances and higher stability.

Pure compositions. Another usual composition of hybrid perovskite is FAPbI₃. This perovskite has a slightly lower band gap (around 1.50 eV, Sanjun Wang et al. (2020)) which approaches the ideal value for a single junction solar cell. It also has a high absorption coefficient and a sharp absorption onset comparable to those of MAPbI₃. The band structure near the band edges is also governed by the inorganic network, explaining the similar opto-electronic properties of MAPbI₃ and FAPbI₃ (Sanjun Wang et al. (2020)). Davies et al. (2018) however demonstrated with terahertz spectroscopy that the substitution of the A cation influences the temperature dependence of optoelectronic properties of the perovskite (exciton binding energy and carrier mobility). The most notable effect of this substitution affects the structural properties of the perovskite. The α -phase of FAPbI₃ is metastable at room temperature (transition from the perovskite α -phase to the non-perovskite γ -phase at 180 °C when T decreases) which is addressed by different strategies such as composition engineering of the perovskite material or of its interfaces (H. Chen et al. (2021)). Because of the higher activation energy of decomposition of FA⁺ compared to MA⁺, FAPbI₃ exhibits however a higher thermal stability than MAPbI₃. Thanks to a careful anion engineering, J. Jeong et al. (2021) recently claimed the world record efficiency for a PSC based on a FAPbI₃ absorber (25.6%, certified 25.2%). They also demonstrated a good stability of their cells (heat stability test of encapsulated devices: -10% relative efficiency after 1000 h at 60 °C and 20% relative humidity; operation stability test of encapsulated devices: -15% relative efficiency after 400 h at MPP, 1 sun illumination, under nitrogen atmosphere).

Other pure compositions are considered in the scientific community. Among them, inorganic formulations as CsPbX₃ are studied to achieve "all-inorganic" perovskite solar cells on a search for an increased stability (Xiang and Tress (2019)). Promising results have been obtained in this regard. All-inorganic cells based on CsPbBr₃ (with a carbon hole transport layer/electrode) have shown no sign of performance degradation after 3 month stored in humid air (> 80% relative humidity – RH) at ambient temperature (J. Liang et al. (2016)). They also exhibited a good resistance to extreme temperature cycles (from -22 °C to 100 °C) for 80 h. However, the efficiency of these kinds of solar cells are not yet up to the level of the hybrid perovskite-based technologies. Moreover, the photoactive α -phase of these kinds of compounds tend to be metastable at ambient temperature. Hence, compositional engineering is still being investigated to find easy and reliable ways of stabilizing the α -phase (Eperon et al. (2015)).

Mixed compositions. Perovskite materials well-suited for PV applications exist not only in "pure" compositions (in the sense that each site A, B and X is occupied by a single chemical element), but also in a large variety of "mixed" compositions, offering a tunable range of opto-electrical properties (Figure 1.8).

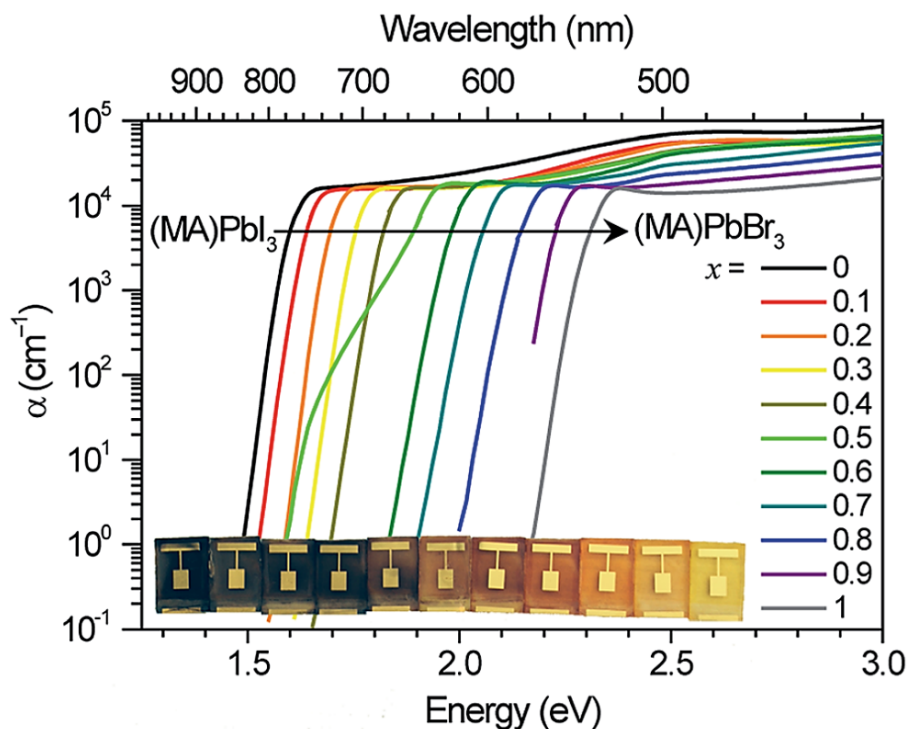


Figure 1.8: Absorption coefficient of $\text{MAPb}(\text{Br}_x\text{I}_{1-x})_3$ measured by diffuse spectral reflection and transmission measurements on thin films and photocurrent spectroscopy of solar cells. Inset: photograph of $\text{MAPb}(\text{Br}_x\text{I}_{1-x})_3$ photovoltaic devices from $x = 0$ to $x = 1$ (left to right). Reproduced from Hoke et al. (2015).

The partial substitution of the halogen anion X or of the metallic cation B have the most impact on the optoelectronic properties of the absorber, because the band structure close to the band edges is governed by the BX_3^- scaffold. For instance, beginning from the classic MAPbI_3 perovskite ($E_g = 1.53 \text{ eV}$), the band gap opens by replacing part of iodine by bromine, until the MAPbBr_3 composition is reached ($E_g = 2.3 \text{ eV}$) (Hoke et al. (2015)). Substituting lead by tin allows to reach narrower band gaps down to 1.2 eV (S. Gu et al. (2020)). On the other hand, changing the composition of the A site has a milder effect on the band gap of the material (FAPbI_3 : 1.50 eV , MAPbI_3 : 1.55 eV , CsPbI_3 : 1.73 eV).

However, these solid solutions are not unconditionally stable. The introduction of Sn^{2+} is hampered by the rapid oxidation of $\text{Sn}(\text{II})$ to $\text{Sn}(\text{IV})$. Solvent engineering or perovskite ink engineering have for instance been explored to mitigate this effect (X. Gu et al. (2013)). The solid solution $\text{MAPb}(\text{I}_x\text{Br}_{1-x})_3$ undergoes a photoinduced phase segregation into I-rich and Br-rich phases which can easily be observed on the photoluminescence spectra of the absorber for $x > 20\%$ (Slotcavage et al. (2016)). As a consequence, a large range of compositions are actually metastable and the gap can practically be tuned up to 1.7 eV for MA-based perovskite. The concentration

threshold at which this phase segregation is observed depends on the cation, hence the range of accessible band gap energies. In the case of FA-based (resp. Cs-based) perovskite, the maximum achievable band gap of a mixed I/Br composition is 1.6 eV (resp 1.9 eV) (Kegelmann (2019)). Alloying perovskite with different A cations can on the other hand increase the stability of the film. Triple cation perovskite including Cs have been intensively investigated and are a promising mixture to further stabilize the perovskite and increase the efficiency. The addition of Cs is responsible for an increase of the band gap (increasing from 1.57 eV to 1.61 eV for Cs concentration varying from 0 to 20% in $\text{Cs}_x(\text{MA}_{0.17}\text{FA}_{0.83})_{1-x}\text{Pb}(\text{I}_{0.83}\text{Br}_{0.17})_3$), of the exciton binding energy (from 8.0 meV to 10.1 meV) and a decrease of the tolerance factor. Upon opto-electrical optimization, $x = 5\%$ has been identified as the optimized Cs ratio in the perovskite. The addition of Cs up to 5% also increases the perovskite crystallinity, and its thermal stability (Saliba et al. (2016)). Finally, smaller elements – which are not expected to enter the perovskite lattice – such as rubidium have also been recently used in perovskite solar cells as additives. The addition of a small amount of Rb does not seem to change the band gap of the perovskite until 10% Rb is added and helps to stabilize the black photoactive phase of the perovskite (Turren-Cruz et al. (2018)). On a morphological point of view, Rb increases sensibly the grain size (from 70 nm without Rb to 381 nm with only 1% Rb).

1.2.2.4 Mixed perovskite used at IPVF

The composition of the absorber synthesized at IPVF and used throughout this dissertation is $\text{Cs}_{0.05}(\text{MA}_{0.17}\text{FA}_{0.83})_{0.95}\text{Pb}(\text{I}_{0.83}\text{Br}_{0.17})_3$ with 10% excess of PbI_2 (composition of the solution used for the spin coating deposition).

The perovskite crystallizes in the α -phase, and has an optical band gap of 1.6 eV. The transport properties of a perovskite film on a TiO_2 bilayer have been measured by photoluminescence (Bercegol, Ramos, Rebai, Guillemot, Ory, et al. (2018)). The radiative recombination rate has been determined at $1.2 \times 10^{-10} \text{ cm}^3 \text{ s}^{-1}$, the diffusion coefficient at $6 \times 10^{-3} \text{ cm}^2 \text{ s}^{-1}$, the trap density at $4.2 \times 10^{14} \text{ cm}^{-3}$, the diffusion length at 780 nm and the effective lifetime at 1.0 μs . These results are on par with the literature.

1.2.3 Architecture of a perovskite solar cell

1.2.3.1 Constitutive elements of a perovskite solar cell

The architecture of a PSC typically consists of the stack of five layers:

- The perovskite itself, which has the role of light absorber. Electron/hole pairs are photogenerated, separated and transported in this layer.
- The electron selective layer or electron transporting layer (ETL). It is responsible for extracting the photo-generated electrons from the perovskite and for blocking the holes in order to reduce the recombinations at the electrode surface.

- The hole selective layer or hole transporting layer (HTL). It is responsible for extracting the photo-generated holes from the perovskite and for blocking the electrons in order to reduce the recombinations at the electrode surface.
- Two electrodes, connected respectively to the ETL and to the HTL. They ensure the electrical connection between the solar cell and the external circuit. On the front side of the PSC, transparent conducting oxides (TCO) such as indium-doped tin oxide or fluorine-doped tin oxide are frequently used. In stand-alone PSC, Au or Ag are usually used as counter-electrode. For tandem applications, the back contact should be transparent imposing the use of a second TCO (H. H. Park (2021b)).

1.2.3.2 The different architectures of perovskite solar cells

Figure 1.9 presents the different architectures commonly used for PSCs.

Mesoporous architecture. The classic mesoporous architecture is inherited from DSSCs (Figure 1.9.a and Figure 1.9.b). A dense, pinhole-free n-type TiO_2 layer is deposited on the TCO (usually FTO) as a hole blocking layer. On top of it, a thicker mesoporous layer of TiO_2 is deposited and then infiltrated by the perovskite absorber. This allows for a large contact surface between the absorber and the ETL which was crucial for DSSC due to the small carrier life times in the dye. In perovskite solar cells, it helps to control the nucleation of the perovskite and is also reported to increase the exchange area (hence the extraction) between the perovskite and TiO_2 , even though this is not consensual. On top of the perovskite an HTL is deposited which historically consists in a thick layer of doped spiro-OMeTAD. This architecture sets the standard n-i-p architecture (referring to the doping of each layer by order of synthesis, the perovskite being labeled intrinsic out of convenience). Alternative architectures have also been studied based on different combinations of blocking layers and scaffolds (SnO_2 , AlO_x , ZrO_2 D. Wang et al. (2020); Y. Li et al. (2015)). Mesoporous p-i-n architectures are seldom reported in the literature (X. Yin et al. (2019)).

Planar architectures. Owing to the long diffusion length and the high absorption coefficient measured in perovskite, the mesoporous layer is not mandatory to ensure the good absorption of the incident light and the transport of the electrons from the absorber to the electrode (as it is in DSSCs). With the development of more appropriate extraction layers, new architectures were developed, called planar architectures (Figure 1.9.c and Figure 1.9.d). In this case, the perovskite is grown directly on the dense extraction layer, without any mesoporous scaffold. N-i-p and p-i-n architectures are equally investigated by the community. The selection of one architecture over the other often comes down to the selection of the ETL and HTL materials, and the constraints their synthesis implies.

For instance, a typical process for p-type NiO_x requires an annealing at $>250^\circ\text{C}$ (B. Zhang et al. (2020)). Since the perovskite is not stable at such high temperatures, NiO_x must be integrated in p-i-n configurations. Similarly, spin coated SnO_2 nanoparticles are usually annealed in air at 180°C , forcing the n-i-p architecture

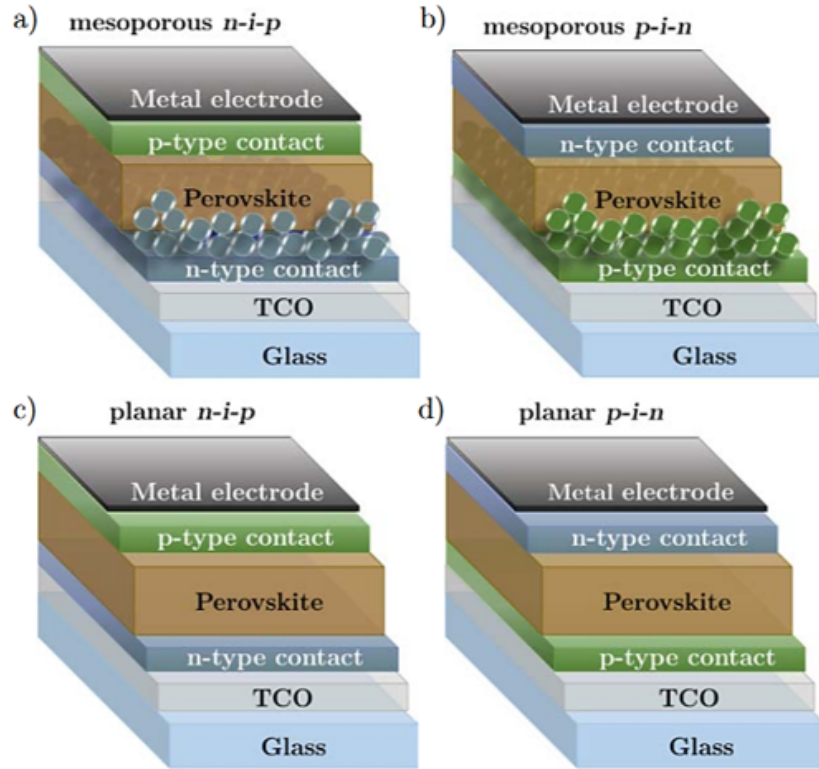


Figure 1.9: Schematic representations of the different perovskite solar cell architectures: a) $n-i-p$ mesoporous architecture, b) $p-i-n$ mesoporous architecture, c) $n-i-p$ planar architecture, and d) $p-i-n$ planar architecture. Reproduces from Kegelmann (2019).

(Saliba et al. (2018)). In tandem applications, matching the polarity of the top and bottom cells will also influence the choice of the cell structure. The planar architectures can usually be synthesized at lower temperatures than their mesoporous counterparts, enabling more resilient processes. A short summary of the characteristics and typical range of efficiencies of the best cells reported in the literature for each architecture is provided in [Table 1.1](#).

1.2.3.3 Requirements for the design of charge transport layers.

The role of charge transport layers is to promote the transport of a charge carrier while preventing the transport of the charge carrier of opposite sign. Owing to the respective n and p doping of the ETL and the HTL, they also participate in the charge transport by creating a built-in voltage across the stack. In order to efficiently act as a charge transport layer, a material should fulfill several requirements: (i) a good carrier mobility in order to minimize the electrical losses; (ii) a high transparency in the visible range to prevent parasitic absorption of the

Table 1.1: Typical compositions and performances of different PSC architectures. A typical reference achieving high efficiency is provided. (bl.) The material is used in a bilayer consisting in a compact and a mesoporous layer. (mp) The material is only used as a mesoporous scaffold. (*) SAM: self-assembled monolayer.

Architecture	ETL	HTL	Typical higher PCE	Reference
Mesoporous n-i-p	TiO ₂ (bl.), Al ₂ O ₃ (mp)	Spiro-OMeTAD, PTAA	> 25%	J. Jeong et al. (2021)
Mesoporous p-i-n	PCBM	NiO _x (mp)	~ 18 %	X. Yin et al. (2019)
Planar n-i-p	SnO ₂ , ZnO, TiO ₂	Spiro-OMeTAD, PTAA, CuSCN	> 21%	Liyang Yang et al. (2018)
Planar p-i-n	PCBM/BCP, C ₆₀ , SnO ₂	PEDOT:PSS, NiO _x , SAM(*)	> 20%	Al-Ashouri et al. (2019)

incident light, which is usually coupled with a high band gap; (iii) a good band alignment to promote the transport of one carrier (small band offset) and block the other one (large band offset); (iv) a chemical and structural compatibility with the perovskite absorber in order to limit its degradation; (v) a deposition process compatible with the perovskite (low temperature, solvent engineering ...).

1.2.3.4 The central question of interfaces.

Many reviews recently addressed the role of interfaces in perovskite solar cells and pointed out how important they are to improve the performances and the stability of the devices (Schulz et al. (2019); Aydin et al. (2019)). Irrespective of the chosen architecture, perovskite solar cells contain many interfaces between materials of diverse natures and functionalities (organic/inorganic materials, metal/semiconductor ...). Each interface has a large influence on the behavior of the complete stack whether is it seen from a chemical or a physical point of view.

The nature of the surface on which the perovskite is deposited affects the growth and the properties of the perovskite not only at the interface with the substrate but also in the bulk of the perovskite (Climent-Pascual et al. (2016)). XPS measurements performed on a film of MAPbI₃ also reveal a variation of the position of the Fermi level at the surface of the perovskite (presumably representative of the bulk of the perovskite) depending on the nature of the substrate. On n-type substrates, E_F is close to the conduction band minimum, while on p-doped substrates, E_F appears close to midgap (Figure 1.10.b Miller et al. (2014)). Hence the apparent doping of the perovskite deposited with the same precursor solution is affected by the doping type of the substrate, highlighting the influence of interfaces in the growth of the perovskite. The interfaces have also been pointed as favored recombination and degradation centers (Aydin et al. (2019)), caused mostly by

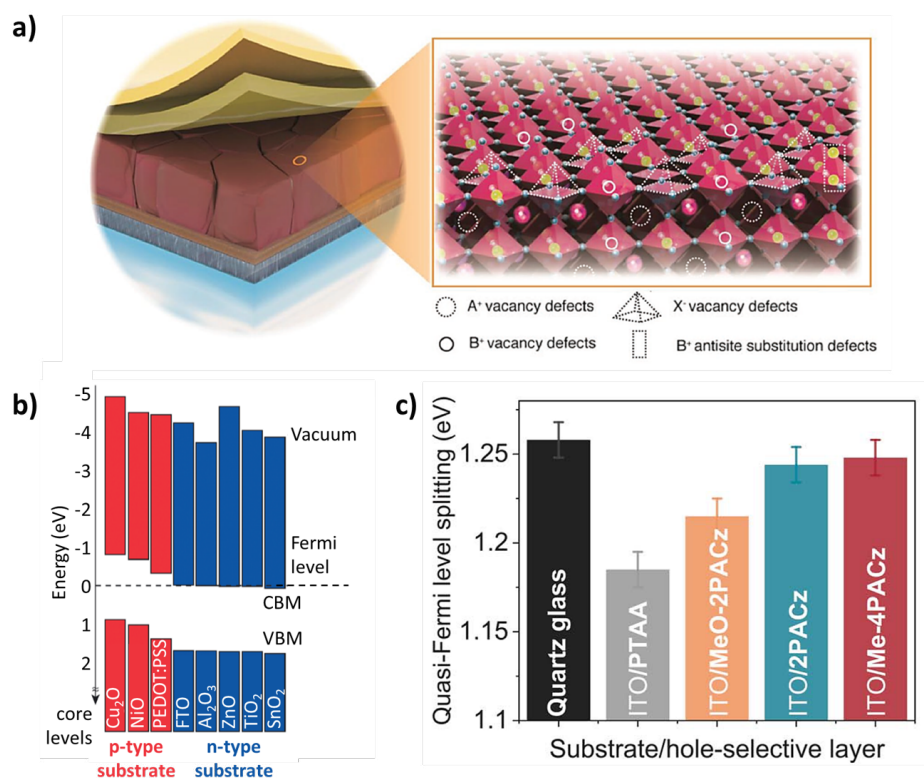


Figure 1.10: a) Schematic illustration of typical PSCs and detailed view of possible surface defects on perovskite crystals, *e.g.* interstitials, substitutional, and vacancies. Reproduced from Aydin et al. (2019). b) Band offset of MAPbI₃ films on various substrates with values for the VBM (valence band maximum) derived from a linear fit to band onset and vacuum level determined from XPS and values for the CBM (conduction band minimum) projected from a calculated band gap of 1.7 eV. Reproduced from Miller et al. (2014). c) Quasi-Fermi level splitting (QFLS) values of 1.68 eV band gap perovskite films on a bare glass substrate and different hole-selective layers on indium tin oxide. Error bars denote the global error of the evaluation method (~20 meV). Reproduced from Al-Ashouri et al. (2020).

point defects at the interface or by the disruption of the crystalline network on either side of the interface leaving reactive dangling bonds (Figure 1.10.a). For instance, an oxygen vacancy at the TiO₂ interface creates a deep trap state located at 0.75-1.18 eV below the conduction band (Pan et al. (2013)). Several strategies have been employed to reduce the detrimental non-radiative recombinations, including surface doping (Giordano et al. (2016)), multilayering (Cao et al. (2018)), chemical treatment of the surface (Xu Liu et al. (2018)), polymer capping (PMMA, POTO, deQuilettes et al. (2016)), addition of fullerene derivatives (Q. Dong et al. (2019)), of a 2D Ruddlesden-Popper perovskite (Sutanto et al. (2021)), of a thin dielectric layer (Koushik et al. (2017)), or modification of the perovskite ink to include Lewis base (Noel et al. (2014)). In order to achieve a monolithic perovskite/silicon tandem solar cell with a > 29%, Al-Ashouri et al. (2020) insist on the role of the extraction

layers (in this case the HTL) in the performance and stability of perovskite solar cells. The QFLS of the perovskite effectively varies depending on the substrate it is grown onto and gets closer to that of the perovskite on glass for the best performing HTL (Figure 1.10.c). As the need to solve passivation issues increases, the architectures are becoming more complex. The extraction layers often consist in a stack of different materials in order to take advantage of the benefits of one material while mitigating its weaknesses (Bush et al. (2017)).

As underlined by Schulz et al. (2019), the development and optimization of extracting layers has mostly relied on rudimental considerations and rather originate of phenomenological observations which are justified *a posteriori*. This can be explained by the difficulty to derive a consensual and consistent theoretical framework to explain the interplay between the different layers composing the perovskite solar cell, especially regarding the charge transport across the extraction layers. Hence, sometimes contradictory or ambiguous conclusions are drawn. As an example, steady state photoluminescence (SSPL) and time-resolved photoluminescence (TRPL) are often used to qualify the goodness of an extraction layer. A commonly reported observation is that the faster the decay and the lower the PL of the perovskite on a given extraction layer, the better the extraction layer (*e.g.* Azmi, Hadmojo, et al. (2018)). However, without a proper physical model, it is uncertain whether these observations originate indeed from an enhanced extraction of the carriers, or from a degradation of the quality of the bulk or of the interface of the perovskite which would increase the non-radiative recombinations. Specific and more thorough experimental procedures and physical models have hence been developed to properly answer these questions (Kirchartz et al. (2020)). In conclusion, interfaces are by many aspects a key element of the perovskite solar cells, yet still not completely understood.

1.2.4 Challenges and opportunities of perovskite solar cells

1.2.4.1 Hysteresis and peculiar transport phenomena

Perovskite solar cells under operating conditions display an unusual behavior compared to other solar technologies. A slow transient response to a variation of voltage is observed, which is best seen in the hysteretic behavior of the standard J–V characterization of the solar cells, *i.e.* the characteristics can be different depending on the scan direction (and scan rate) of the voltage sweep. The origin of this behavior has been long discussed and several hypothesis have been proposed: ion migration (Lopez-Varo et al. (2017)), polarization of ferroelectric domains, or trapping/detrapping mechanisms at the interfaces (Tress (2017)). A consensus has not been reached but in a general manner, improving the quality of the interface and reducing the interfacial trap density reduce the hysteresis by making the charge extraction field-independent (Habisreutinger et al. (2018)). For instance, the use of fullerene-derivatives in the charge extracting layer has been related to a substantial reduction of the hysteresis (Kegelmann et al. (2017)). Because of this hysteretic behavior, the performances of perovskite solar cells as determined by the standard J–V characterization are highly dependent on the measurement conditions, and new standards such as stabilized power output at maximum power point must be

applied to allow for fair comparison of the results (Khenkin et al. (2020)).

Due to the relative newness and the fast development of the hybride perovskite materials, the comprehension of the mechanisms governing the properties of the absorber (alone or integrated in a complete stack) progresses at a fast pace, but many grey areas still need to be elucidated. Building on the knowledge acquired from the use of halide perovskite in the end of the 1990s and in the 2000s, the material's properties have been examined by a large variety of structural characterizations (X-ray diffraction – XRD, and derivatives, ...), of chemical spectroscopy (XPS and derivatives, FTIR, ...), of optoelectrical characterization (PL, EL, impedance spectroscopy, photocurrent or photovoltage spectroscopy, ...) and of modeling at various scales (DFT, molecular dynamics ...) (D. Li et al. (2021); deQuilettes et al. (2019); Tailor et al. (2020)). Insights have been gained for instance in the control of the crystallization of the perovskite, in the comprehension of its electronic structure or of its optoelectronic properties (photon recycling, photonic transport ... Kirchartz et al. (2016); Bercegol et al. (2019)). However, there is still a lot of room for a better comprehension of the mechanisms at play in perovskite solar cells, especially on the influence of the substrates on the properties of the film (*e.g.* substrate-dependent intrinsic doping of the perovskite Miller et al. (2014)), on the self-healing mechanisms of perovskite (Cheng et al. (2021)) or on the transport properties of the stack (*e.g.* interpretation of PL spectra on full stack, Krückemeier et al. (2021)), and of complete modules.

1.2.4.2 Multiple stability issues

A central area of research is to ensure the stability of the perovskite cells and modules in order to match the stability requirements of the PV market. The sources of intrinsic instabilities are manifold: phase segregation of the perovskite alloys (Slotcavage et al. (2016)), high trap densities at the interfaces and at the grain boundaries (Y. Yang et al. (2020)) ... The absorber however is not the only source of intrinsic degradation of the performances: acid-base reactions can lead to the degradation of the organic cation (further discussed in [Chapter 5](#)), photoinduced degradation has been reported in PSC with a TiO₂ ETL (Ji et al. (2020)), the migration of metallic species from the electrode to the absorber causes the corrosion of the absorber and requires diffusion barriers or new electrode materials (Arora et al. (2017)), the dopants usually employed in spiro-OMeTAD are hygroscopic and cause moisture instabilities (Kwon et al. (2019)) ... These observations justify the extensive studies made on the other constitutive layers of the perovskite solar cells (transport layers, electrodes). But instabilities also originate from extrinsic factors. The hydration of the perovskite leads to its degradation even though the precise mechanism is not completely understood yet and depends on the composition of the perovskite (FAPbI₃ converts in its δ -phase while formation of PbI₂ is observed in MAPbI₃). Additionally, the exposure to oxygen, light, thermal stresses or a combination of them induce complex degradation mechanisms which must be mitigated (He et al. (2020)). Intrinsic instabilities are mostly addressed by tailoring the cell composition (addition of passivation layers or diffusion barriers, modification of the perovskite ink), while extrinsic instabilities are mostly dealt with by devising efficient encapsulation methods (Corsini and Griffini (2020)).

The multiplication of the degradation pathways of perovskite solar cells and their interplay urge for the normalization of stability tests specific to the perovskite technology. The recent consensus on the performance assessment of PSC (Khenkin et al. (2020)) devised a series of tests (with various levels) which considerably differ from the standard tests applied to Si modules. The development of outdoor field tests would also greatly help in the prediction and comprehension of *in operando* stability of perovskite modules.

1.2.4.3 Upscale challenges

As discussed before, perovskite solar cells are a formidable technology to foster technological breakthroughs in the photovoltaic field. Most of the cells synthesized at lab scale are processed by spin coating and have an active area less than 1 cm^2 . Looking at the evolution of the performances as the active area of the cell increases, the PCE decreases and do not keep up with the high performances reached in lab-scale cells (Sang-Won Lee et al. (2020)). Due to the mechanical strain on the substrate, the large waste of perovskite ink and the low throughput of spin coating, alternative deposition methods are studied in order to define a reliable synthesis process at the industrial scale such as ink-jet printing, slot-die coating, blade coating or spray coating (D. Li et al. (2021)). A major issue of these alternative deposition processes relies in the control of the quality and of the homogeneity of the film over a large surface, towards which the major setback is the control of the crystallization of the perovskite phase. For spin coated cells, the crystallization dynamics are controlled by the antisolvent method, allowing for a rapid evaporation of the solvent at a specific moment (Saliba et al. (2018)). This kind of method is less feasible in an upscale perspective owing to the large amount of antisolvent which would be required. Other methods to control the crystallization have been explored, such as air-blading (Shi Wang et al. (2018)), flash vacuum treatment (X. Li et al. (2016)), flash infrared (IR) annealing (Sanchez et al. (2018)) or hot casting (K. Liao et al. (2020)), coupled with ink engineering. Another research area lays in the engineering and in the management of efficient module architectures to limit dead areas in the modules and reduce their series resistances (D. Li et al. (2021)).

1.2.4.4 A diversity of applications portending a promising future

The materials used in perovskite solar cells are for the most part composed of abundant materials. Owing to the variety of compositions – hence of properties – achievable for the perovskite absorber, it can be tuned in order to match specific applications. It is a promising candidate to be integrated in various tandem solar cell architectures either as a top cell for compositions with a large band gap (already reported on top of Si (Al-Ashouri et al. (2020)) or CIGS (Jošt et al. (2020))) or as a bottom cell in a perovskite/perovskite tandem architecture (R. Lin et al. (2019)) enabled by the low band gap Sn-containing perovskite. This versatility also comes handy in the frame of building-integrated PV, where the color and transparency of the perovskite can be tuned according to the requirements (Batmunkh et al. (2020)). The expedient optoelectronic properties of the perovskite and the softness of the deposition conditions allow the synthesis of thin film solar cells on light and flexible substrates (Jing Zhang et al. (2020)) which further expand the application potential

of PSC. The high defect tolerance and high quantum efficiency of perovskite solar cells also make it a promising candidate to enter the market of indoor PV, which is expected to grow with the development of the Internet of things (Mathews et al. (2019)). Finally, in regard of the recent announcements of the industrial PV actors on the release of perovskite-on-silicon tandem solar modules, sufficient progresses have already been made in the matters of upscale and stability to open the way towards mass-production.

1.3 Atomic layer deposition

Atomic layer deposition is a vapor phase deposition technique which consists in sequential, self-limiting chemical reactions at the surface of a substrate. The following chapter introduces the major characteristics and properties of the ALD process, a short chronology of its development and its current applications in the industry. Finally, the ALD reactor used for the studies presented in the manuscript is presented. For general reviews on ALD, see references Ahvenniemi et al. (2017); J. Aarik et al. (2001); George (2010); Knapas and Ritala (2013); R. W. Johnson et al. (2014).

1.3.1 Description of an ALD process

1.3.1.1 Definition of an ALD cycle

The ALD process relies on the repetition of so-called ALD cycles, during which the sample is sequentially exposed to molecular precursors. The deposition of a binary compound is usually broken down into four steps, explained below and depicted in [Figure 1.11](#) in the prototypical case of ZnO deposition with diethyl zinc (DEZ) and water (H₂O):

1. DEZ is pulsed for a duration t_1 in the reaction chamber and chemisorbs at the surface on the available hydroxyl groups. Ethane is released in the atmosphere as a byproduct, and the surface is terminated with ethyl groups.
2. The reactor chamber is purged for t_2 with an inert gas (usually N₂) to remove the unreacted gaseous DEZ precursors and the byproducts of the first chemisorption.
3. H₂O is pulsed for t_3 in the reaction chamber and chemisorbs at the surface on the available ethyl ligands, releasing ethane. The surface is terminated with hydroxyl groups.
4. The reactor chamber is purged for t_4 with an inert gas to remove the unreacted gaseous H₂O precursors and the byproducts of the second chemisorption.

The purge step is of high importance. Since the supply of the precursors is separated temporally (there should never be DEZ and H₂O simultaneously in the chamber) – with the prerequisite that there is no thermal decomposition – precursors can only react at the surface of the substrate. In the opposite case, ZnO could form in the vapor phase and then condense on the surface of the substrate,

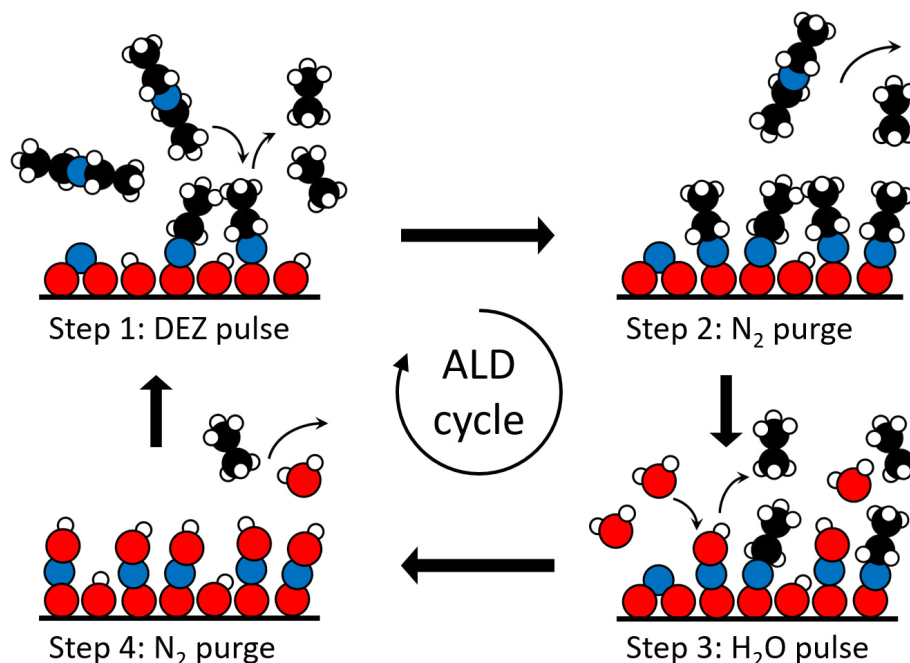
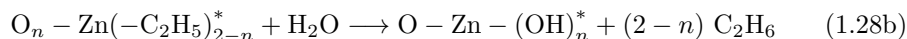
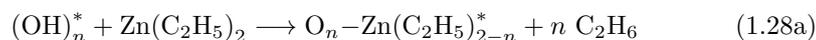


Figure 1.11: Schematic representation of the ALD cycle of the deposition of ZnO with DEZ and H₂O. Carbon: black sphere, hydrogen: white sphere, oxygen: red sphere, zinc: blue sphere. Inspired from Parsons et al. (2011).

which would limit the control of the quality of the film. Theoretically at the end of the cycle, at most a monolayer of ZnO is deposited on the surface. The substrate is back to its initial state before step 1 with a hydroxylated surface. A new ALD cycle can take place and the thickness of the film is gradually increased with each new cycle.

In its simplest form, the reaction of the precursors on the surface of the substrate can be described by two half reactions involving an exchange of n ethyl ligands:



where the species marked with an * are surface species. Note that DEZ can coordinate with the hydroxyl surface groups in different ways, hence n is not necessarily an integer. This formalism insists on the fact that the constitutive reactions occur at the surface of the sample, with a chemisorbed species and a gaseous precursor. Equation (1.28a) corresponds to the first step of the ALD process, and Equation (1.28b) to the third step.

In the rest of the manuscript the ALD sequence will be written $t_1/t_2//t_3/t_4$ (to give the duration of each step) or A/N₂//B/N₂ (to give the sequence of precursors

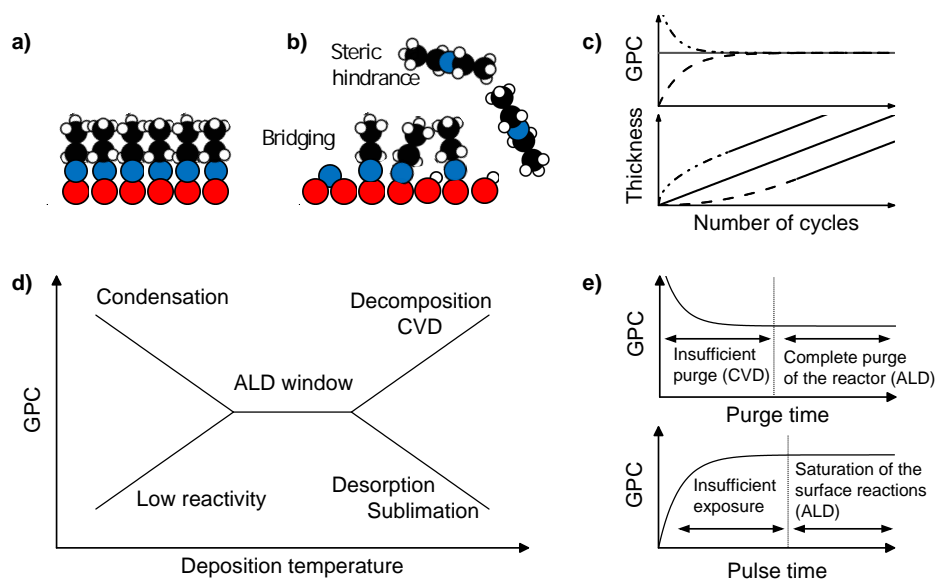


Figure 1.12: Main properties of an ALD process. a) Ideal state of the surface at the end of the step 1 (DEZ adsorption). b) More realistic state of the surface at the end of the step 1, including bridging species and steric hindrance. c) Influence of the nature of the substrate on the variation of the thickness of the ALD-film and of the growth per cycle function of the number of cycles, either promoting the growth (dotted-dashed line), hindering the growth (dashed line) or having no influence on the growth (plain line). d) Variation of the GPC function of the deposition temperature. e) Typical saturation curves for the pulse and for the purge.

A and B). Note that the double slash fictionally separates the two half reactions presented above.

1.3.1.2 Characterization of an ALD process

As pointed out in the previous section, an ALD process is defined by the sequence of the chemical reactions in vapor phase at the surface of the substrate. These surface reactions (*e.g.* Equation (1.28a) and Equation (1.28b)) are irreversible and saturated (commonly described as self-limiting). To assess the ALD regime, the process must satisfy certain properties and key-notions that are described hereafter.

Growth per cycle (GPC). The ALD process is by essence sequential on contrary to other processes such as chemical vapor deposition (CVD) or evaporation which are continuous. Hence, the common growth rate (expressed for instance in nm s^{-1}) used in the latter two processes does not apply well for ALD, since the duration of a cycle depends on the individual durations of each step which themselves can depend on various parameters (nature of the precursors, geometry of the reaction chamber, temperature ...). For ALD, the notion of growth per cycle (expressed in nm/cycle or in \AA/cycle) is preferred in order to qualify a process and compare ALD processes with each other.

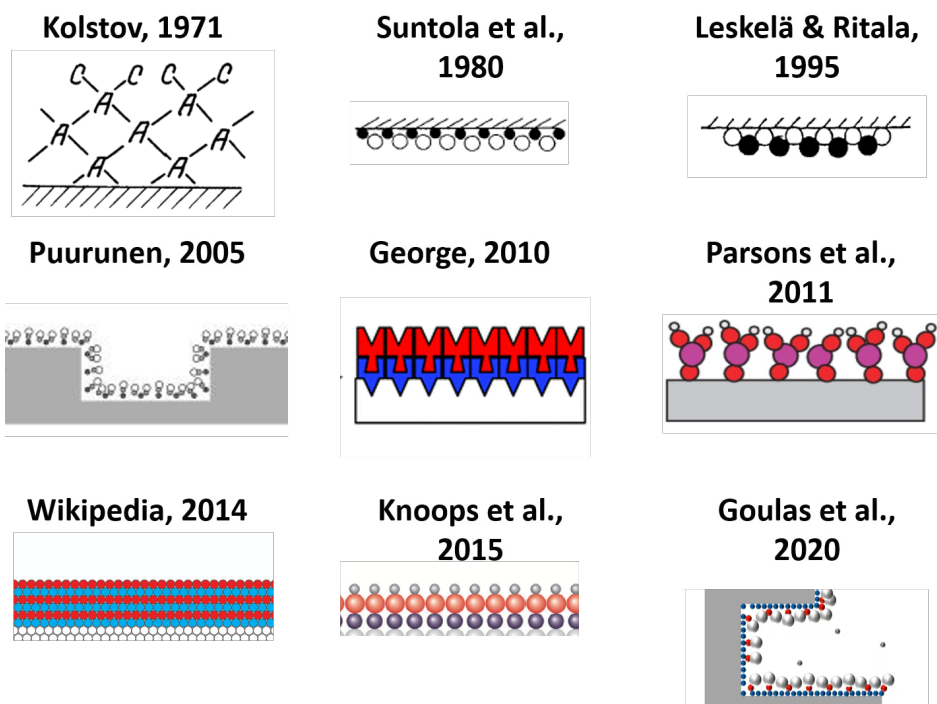


Figure 1.13: Examples of evolution of the schematic representation of the ALD process. Adapted from Openlearning (2021).

The GPC is defined as the incremental thickness of *material* deposited after one complete ALD cycle. A common misconception of ALD is to think that a complete and uniform layer of material is deposited after each cycle. In the case of ZnO, the theoretical GPC should be $GPC_{th} = (M_{ZnO} / (\rho_{ZnO} \cdot N_A))^{1/3} = 2.8 \text{ \AA/cycle}$ where M_{ZnO} is the molecular weight of ZnO, ρ_{ZnO} its density (taken for ZnO würtzite) and N_A the Avogadro's number. However, the GPC measured in the literature is commonly reported between 0.5 \AA/cycle and 2.5 \AA/cycle which is less than this GPC_{th} (Tynell and Karppinen (2014)) (some works report on higher GPCs but are not majority, Janocha and Pettenkofer (2011)). In reality, after an ALD step, a complete layer of *adsorbate* is actually deposited.

To better understand this fundamental difference, let us assume that the substrate is completely covered with $-\text{OH}$ groups. In the ideal and simplest case (if a complete monolayer of ZnO is to be deposited at the end of the ALD cycle) at the end of step 1, each Zn atom should be bound to one oxygen of the substrate and vice versa (Figure 1.12.a). A more realistic situation at the end of step 1 is depicted in Figure 1.12.b. At least two reasons can explain that there is on average less Zn chemisorbed at the surface than initially available $-\text{OH}$ groups. i) The DEZ precursor can react either with one hydroxyl group (releasing one molecule of ethane) or can bridge over two hydroxyl groups (releasing two molecules of ethane). ii) After the chemisorption, the remaining ligands cause a steric hindrance.

Because of it, the remaining precursors cannot reach available $-OH$ sites, reducing the amount of Zn adsorbed on the surface. Using bulkier precursors results in fewer deposited elements per cycle (Y. Wu et al. (2013)). These two situations are examples of reasons why the GPC deviates from its theoretical value, but other mechanisms might come into play (diffusion inside the layer for instance), and the understanding of the dynamics of the ALD surface reactions is still an active field of study. Hence over the years, the representations of ALD have evolved and considerable efforts have been devoted to finding a realistic depiction of the process. Some examples are presented in [Figure 1.13](#).

Nucleation phase and impact of the substrate. In an ideal ALD process, the initial state (before step 1) and the final state (after step 4) of the surface are the same. Hence, the GPC is supposed to be constant with respect to the number of cycles. In practice, variations of the GPC are often observed during the first couple of ALD cycles due to the effect of the substrate: it is the nucleation phase. The substrate can either i) increase the GPC (lower energy barrier towards the chemisorption, more reactive groups at the surface ...) or ii) decrease the GPC (higher energy barrier towards the chemisorption, less reactive groups at the surface ...)([Figure 1.12.c](#)). At some point, the substrate does not influence the surface reaction anymore and the ALD-material "grows on itself": it is the growth phase and the GPC is constant with the number of cycles.

ALD window. Since the completion of an ALD step relies on the saturation of the surface by the chemisorption of the precursors, the GPC (in the growth phase) should not depend on the deposition temperature, unless other mechanisms become thermodynamically favored over the chemisorption. The range of temperature where it is true is called the ALD window: within this temperature range, the properties of the film should not depend on the deposition temperature. Outside the ALD window, different scenarios can occur, represented in [Figure 1.12.d](#):

- At low temperature, the GPC increases with the temperature: the temperature is not high enough to overcome the activation energy for the chemisorption of the precursors.
- At low temperature, the GPC decreases with the temperature: the precursors condense at the surface of the substrate.
- At high temperature, the GPC increases with the temperature: the precursors undergo a thermal decomposition in the vapor phase before reacting at the surface.
- At high temperature, the GPC decreases with the temperature: the precursors desorb from the surface or the deposited material sublimates.

In practice, a slight variation of the GPC with the temperature can be observed within the ALD window due to a variation of the reactivity of the precursors or of the number of surface groups.

Saturation curves. The pulse and purge times define the ALD sequence. A schematic of the influence of these times on the GPC is given in [Figure 1.12.e](#). An increase of the GPC is generally observed with the pulse time until a plateau. If the pulse time is too short, there is not enough time for the surface reaction to saturate (accounting for the time needed for the precursor to be transported at the surface of the substrate, for the reaction to occur and for the species to diffuse/crawl at the surface until saturation). If the pulse time is too long, it unnecessarily reduces the throughput of the process and increases the amount of precursor wasted (the excess precursors will not react on the saturated surface, and will be evacuated during the purge). A decrease of the GPC is generally observed with the purge time. If the purge time is too short, the two precursors can coexist in the reaction chamber and lead to a CVD-type deposition. If the purge time is too long, it reduces the throughput of the process without additional benefit. In this work, the optimization of the programs are done using quartz crystal microbalance (QCM) measurements.

Choice of the precursors. The ALD process depends on the set of molecular precursors used for the deposition. The growth parameters and the properties of the deposited film are dictated by the precursors (H. Y. Kim et al. (2019)). The research on the chemistry of organometallic precursors for ALD is active and aims at developing new processes and materials. The reader can refer to A. L. Johnson and Parish (2018) for further details on the recent progresses.

The design of new precursors must fulfill several requirements: (i) a high volatility to enable the transport and reaction of the precursor in vapor phase, (ii) a good thermal stability to avoid decomposition during the process, (iii) a high reactivity, (iv) it should not release damaging or reactive by-products, (v) a high purity to limit the film contamination, (vi) cheap synthesis to increase the competitiveness of the ALD process.

1.3.1.3 Evolution of ALD processes

Following the development of the thermal ALD, evolutions have gradually been developed to diversify the field of applications or increase the throughput of the technique. A sketch of some techniques is proposed in [Figure 1.14](#).

- Plasma-enhanced ALD (PE-ALD). Instead of relying solely on the thermal energy to drive the surface reactions, highly reactive species (*e.g.* O_3 or radicals) created in a plasma inside the reactor are used as precursors. Because of the enhanced reactivity, it brings the possible deposition temperature further down allowing for ALD at room temperature and the use of more sensitive substrates but at the cost of conformality (H. Kim (2011)).
- Spatial ALD (S-ALD). A major drawback of the ALD as presented before is the long duration of an ALD cycle, limited by the time needed to completely saturate the surface and then completely purge the volume of the chamber for each half reaction. S-ALD consists in separating the precursors not temporarily but spatially. In practice the substrate is placed on a holder which moves between two continuous flow precursor zones separated by inert

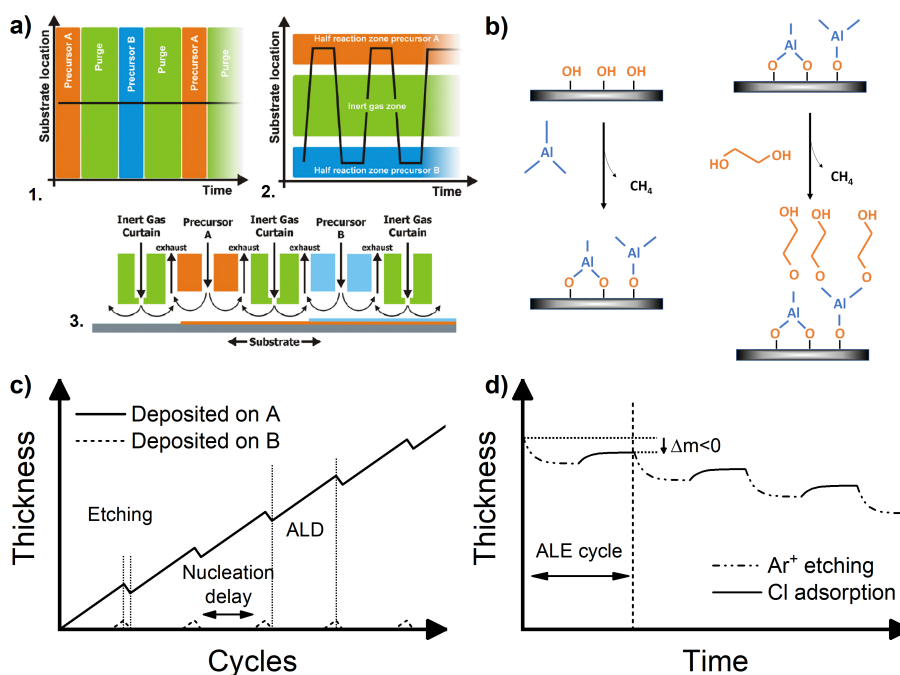


Figure 1.14: Evolution of the ALD process. a) Schematic representation of the precursor pulsed and of the position of the substrate during 1) a thermal ALD process and 2) a spatial ALD (S-ALD) process. 3) Schematic representation of a S-ALD reactor (adapted from Poodt et al. (2012)). b) Schematic representation of a molecular layer deposition cycle (adapted from George et al. (2009)). c) Evolution of the thickness on different substrates while alternating between ALD growth and etching phases (area selective ALD) and d) typical evolution of the thickness of a Si substrate etched with the Cl/ Ar^+ process.

gas windows. It especially allows for a much shorter purge step. Providing that the substrate stays long enough in each precursor region to saturate the reactions, the duration of the S-ALD process is mostly dictated by the time taken to move the substrate from one zone to another. It is a very promising way to adapt the ALD process to industries which require a high throughput as deposition rates up to 1 nm s^{-1} are achieved (Poodt et al. (2012)).

- Molecular layer deposition (MLD). Molecular layer deposition is based on principles similar to those of ALD. The difference mostly lays in the nature of the precursors. ALD focuses on the synthesis of inorganic materials: each half reaction ultimately consists in the deposition of a monoatomic element at the surface (for instance Zn during the step 1 in the example presented above). With MLD, the precursors are designed to enable the deposition of complete molecules at the surface of the substrate, forming hybrid organic-inorganic structures such as metal-organic frameworks. It poses multiple challenges, among which the design of the precursors and of the experimental conditions, due to the usually low thermal stability of the organic molecules (Meng (2017)).

- Area-selective ALD (ASALD). Area-selective ALD makes use of the sensitivity of the ALD process towards the nature of the substrate during the nucleation step. As an example, let us suppose the substrate consists of a pattern of two different materials A and B (because of the high conformality of ALD, nano-scale patterning is allowed), and a material C can be deposited by ALD. Let us also suppose that the growth of C on A has no nucleation delay, while the growth of C on B has a 100 cycles nucleation delay. After 100 ALD cycles, a certain thickness of C is deposited on the A-substrate, while only little to no C is deposited on B. If a larger thickness of C material is required, or if the difference of nucleation delay is not large enough, the sample can then be etched (using an isotropic etching process such as atomic layer etching (ALE) if existing) to completely clean material B. At this point, there is C on A, but there is no C on B. If these steps of ALD growth and etching are cycled, material C will grow exclusively on the parts of the substrates which were covered by A. This method is very promising in the nano-electronics, especially as an easier and cheaper alternative to lithography (Parsons and Clark (2020)).
- Atomic layer etching (ALE). This technique can be seen as a derivative of ALD with a negative GPC. It allows for a precise and controlled etching of a material even in complex geometries. A prototypical example consists in the etching of Si using a sequence of chloride deposition on the surface followed by an exposure to Ar^+ ions leading to a self-limited etching of the surface (Fischer et al. (2021)).

1.3.2 Strengths and limitations of the technique

The ALD is a very versatile and promising deposition process. The conjugated benefits of the self limiting reactions and of the precursors being in vapor phase allows for an unprecedented conformality and potentially nano-scale control on the thickness of the deposited film. These attractive assets allowed for the use of ALD layers in various applications, such as the synthesis of dense and pinhole-free barrier layers (Brennan et al. (2013)), the deposition on substrates with very high aspect ratio (Pore et al. (2011)) or the synthesis of nanolaminates (Meyer et al. (2009)) (Figure 1.15). The composition of the film can conveniently be tuned while keeping a high control on it by using and combining different strategies (supercycles, dehydration, steric hindrance (Mackus et al. (2018))). A large variety of materials can now be deposited by ALD comprising mostly – but not limited to – oxide or sulfide compounds (*Database of ALD processes* (2021)). Elemental, binary or multinary compounds can easily be obtained by adjusting the ALD sequences. The development of new classes of materials is however a tedious task which involves first to design the right precursors (especially aiming at a good volatility, reactivity, purity and stability) and then to optimize the process in order to ensure proper ALD conditions. Compared to other CVD or physical vapor deposition (PVD) processes, ALD can operate under milder conditions of pressure (a primary vacuum is enough) and temperatures, which is beneficial for the deposition on soft substrates. Processes in ambient atmosphere are even being developed (Zardetto et al. (2018)).

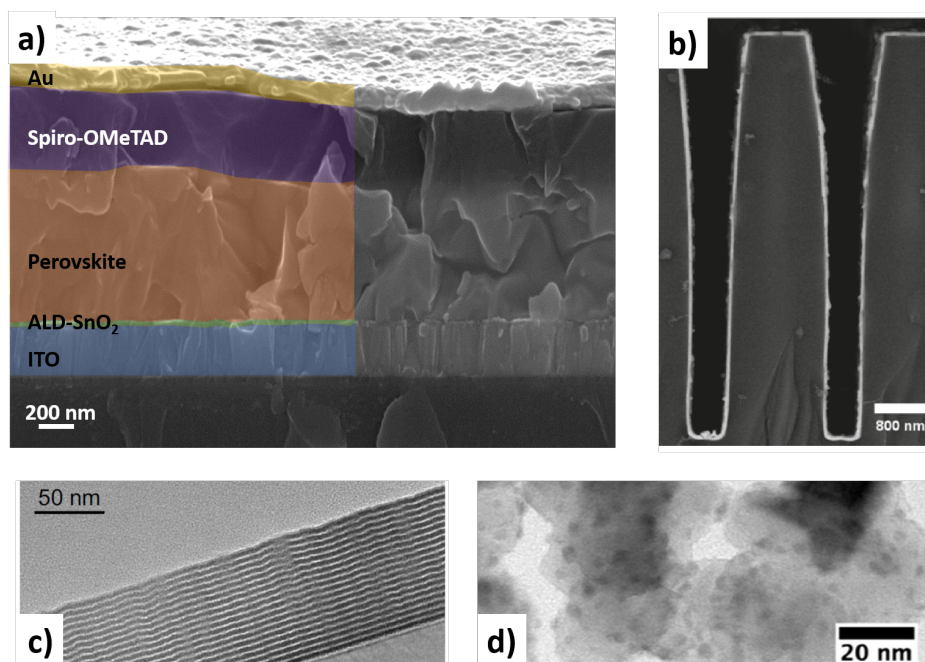


Figure 1.15: Various applications of the ALD process. a) ALD-SnO₂ layer used as electron transport layer at IPVF for perovskite solar cells. b) ALD-Sb layer deposited on a high aspect ratio tranch structure (reproduced from Pore et al. (2011)). c) ALD-Al₂O₃/ALD-ZrO₂ nanolaminates for encapsulation of OLED devices (reproduced from Meyer et al. (2009)). d) ALD-Al₂O₃ barrier layer applied for PbS quantum dots (reproduced from Brennan et al. (2013)).

A major drawback of the ALD process is the low deposition rate caused by the sequential nature of the process. Nonetheless, because of the high conformality and superior quality of the ALD-films, the deposition of very thin layers can be sufficient to synthesize a film with suitable properties, mitigating this issue (*e.g.* in the case of diffusion barriers). While ALD is already well-implanted in the microelectronics industry, other strategies such as the development of the S-ALD are investigated in order to increase the throughput of the process and make ALD more attractive as a deposition technique.

1.3.3 A brief history of ALD

1.3.3.1 First applications of the ALD

Atomic layer deposition can at least be related to two independent origins: in the course of the 1960s, a deposition method called molecular layering is developed in the Soviet Union; independently in 1974, atomic layer epitaxy is developed in Finland. Even though the latter is usually referred to as the origin of the contemporary ALD, a think tank named "virtual project on the history of ALD" has been created within the ALD community in order to clarify the chronology of the earliest years of ALD. They suggest in Ahvenniemi et al. (2017) a collection of

publications from 1965 to 1985 most relevant to this matter, which the reader can refer to in order to get insight into the history of ALD.

The development of molecular layering in the Soviet Union stems from the work of S. Koltsov and V. Aleskovsky and the "framework" hypothesis devised by V. Aleskovsky. Molecular layering became an active research field in the Soviet Union, and various binary materials were synthesized that way such as TiO₂ or SiO₂ using mostly chloride or oxychloride precursors (Malygin et al. (2015)). So-called atomic layer epitaxy (at that time) was first used for the deposition of Mg:ZnS layers for thin film electroluminescent devices by T. Suntola grown at very low pressure (1×10^{-6} torr), using elemental sources. It led to the application in 1974 of a patent for this process, which evolved in 1979 into a new patent to account for the use of compound reactants instead of elemental reactants (which brings the process one step closer to what ALD actually is nowadays) (Puurunen (2014)). It is agreed that the work of T. Suntola has vastly contributed to rise a worldwide interest in this new deposition method whose fundamental principles were already known in the Soviet Union, and to its industrialization. Based on the work developed in Finland by T. Suntola, various manufacturers offered commercial ALD-reactor from the 1990s/early 2000s (*e.g.* ASM International, Beneq Oy, Picosun Oy) allowing the research on this topic to quickly evolve.

1.3.3.2 A mature technology used in various academic and industrial fields

The development of the ALD has gone along with the boom of the micro-electronic industry and the strive towards further miniaturization (Ritala and J. Niinistö (2009)). The need for high quality materials which can be deposited on complex geometries found a solution with ALD and fostered the research efforts. With miniaturization, the typical scales of thicknesses shrank from the micrometer to the nanometer level, further promoting the use of ALD. An important application of ALD in the industry concerns the deposition of thin films of high-*k* materials for dynamic random access memory devices (DRAMs) and metal oxide semiconductor field effect transistors (MOSFET), due to the need of conformal layers on increasingly complex geometries. In 1998, Samsung announced the use of ALD in their DRAM technology. Intel uses ALD to deposit the gate electrode in MOSFET. Thin film electroluminescent devices are also an evident industrial application and caused the development of the process by T. Suntola in the first place. Other applications of ALD have been found over the past decades. ALD films are usually dense and pinhole-free which makes them suitable for device encapsulation (AlO_x films are widely used for this purpose). This applies very well for the luxury market where these thin layers are used as anti-tarnishing coatings for jewelry (*e.g.* by Lapponia Jewelry). Recently, IBM announced the creation of the smallest microchip (2 nm chip) enabled by the use of ALD. The good conformality of the layer is an undeniable asset for the coating of optics where the deposition of homogeneous layers of well-controlled thickness are key in the elaboration of interference coatings.

New applications in other industrial sectors emerge. Coatings on powders and on porous substrates with ALD-films draw a lot of interest owing to the conformal

deposition of ALD, especially for core-shell structures. The ALD can also become of interest in fields such as the aeronautics or the car industry as protection layer for components of increasing complexity. The photovoltaics field has also a lot of potential applications for ALD. It is already used in Si-based technologies as passivation layer (Delft et al. (2012)), but interesting opportunities also appear in thin film technologies, once again driven by the need of high-quality, thin layers of materials (Zardetto et al. (2017)).

It should however be noted that due to the slowness of the process and the relative complexity of the development of a recipe, ALD is usually used at an industrial scale when the materials deposited by other methods cannot match the requirements.

1.3.4 Presentation of the Beneq TFS-200 ALD reactor

1.3.4.1 General characteristics of the reactor

All the ALD materials presented in the manuscript have been deposited in a Beneq TFS-200 reactor. It is a pre-industrial reactor produced by the Finnish company Beneq Oy. used mostly for research. [Figure 1.16](#) presents a schematic of the reaction chamber. It is a cross flow reactor: the precursors and carrier/purge gases are let in through a series of openings aligned on one side of the chamber and are let out through a similar range of openings on the opposite side of the reactor to ensure a homogeneous flow across the chamber. The homogeneity of the ALD-processes is observed by comparing the thickness of a film deposited at various places in the reaction chamber during a single batch. To do so, a piece of Si/SiO_x is put next to the gas inlet of the chamber and another one next to the gas outlet. The reaction chamber is of the hot-wall type: the substrate can be heated up to 500 °C with an external cooling system (300 °C without) by resistors. It usually operates under a primary vacuum (1-2 mbar). The reaction chamber is isolated from the outside by an external chamber under a primary vacuum around 10 mbar. The reaction chamber can host a substrate up to 15.6×15.6 cm² (maximum thickness of 3 mm). The reactor can be accessorized with *in situ* characterization tools such as a QCM. In this case, a specific and larger reaction chamber is used.

Multiple precursor sources of different natures can be connected to the reactor. Up to four lines for gaseous precursors, four lines connected to bubblers for liquid sources (two of which can be heated) and four lines connected to canisters for solid sources can be used simultaneously. At the time this thesis was conducted, three liquid lines, two solid lines and no gas line were available.

1.3.4.2 Transport of precursors

A key issue of the ALD process is to transport the precursor species from their storing canister to the reaction chamber while preventing the decomposition or the condensation of the precursor. A simple way to do so is to transport the precursor by its own vapor pressure at the conditions of pressure and temperature of the canister (typically 1-2 mbar, 25 °C). In practice, this kind of transport can be achieved if the precursor is volatile enough. If the vapor pressure (P_{sat}) of

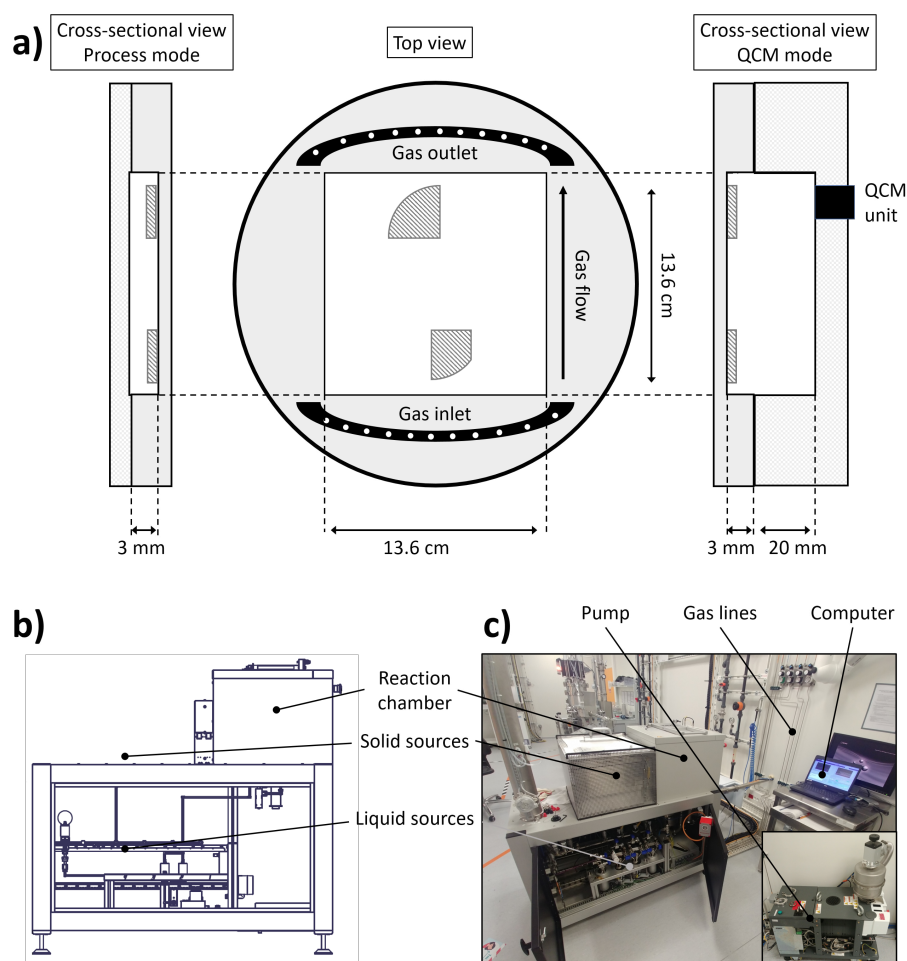


Figure 1.16: Schematic of a) the reaction chamber of the Beneq TFS-200 reactor in process and QCM configurations and b) of the whole reactor with the main components indicated. c) Photograph of the installation at IPVF. The locations of the substrates for the homogeneity studies are indicated.

the precursor is higher than the pressure inside the reaction chamber (around 1 mbar) at room temperature, the precursor can be transported without additional assistance (as is the case for DEZ, H₂O and H₂O₂ in this manuscript). If the compound is not volatile enough, the temperature of the source T_{source} can be increased in order to increase P_{sat} (as is the case for TTIP and TDMASn in this manuscript). This method can facilitate the transport of less volatile compounds, but comes with additional experimental requirements. The temperature has to be carefully controlled all the way from the source to the reactor. If at some point a "cold-point" forms (*i.e.* $T < T_{source}$), there is a risk that the precursor condenses in the pipes and forms a clog. An excessive temperature can also lead to the degradation of the precursor and must be avoided to ensure the ALD.

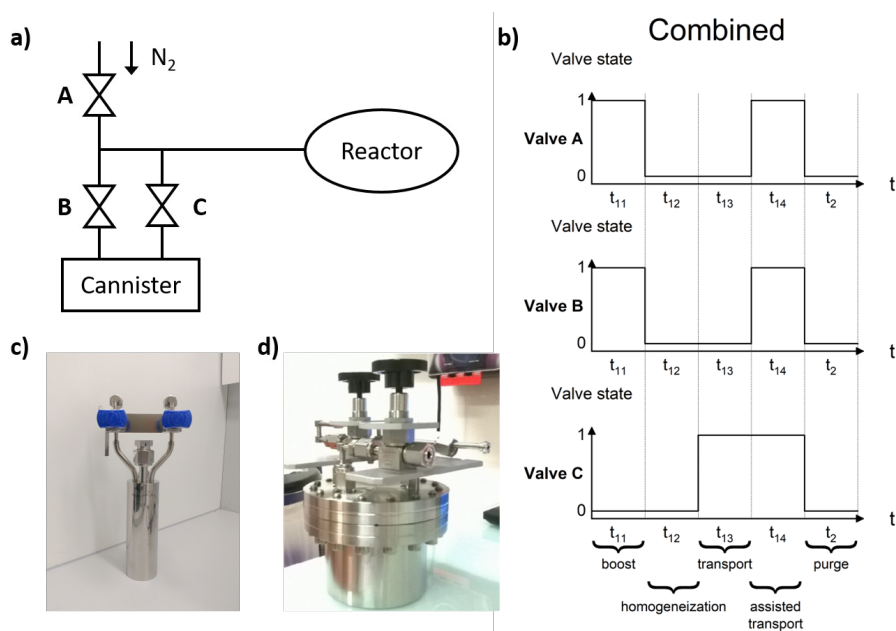


Figure 1.17: a) Schematic of the solid source system with its controllable electrovalves. b) Control diagram of the electrovalves in the "combination" mode. Photographs of a canister for c) a liquid source and d) a solid source used with the Beneq TFS-200.

The use of the "HS (hot solid) system" of the Beneq TFS-200 reactor allows for additional strategies to assist the transport of liquid or solid precursors with a low volatility, using a neutral carrier gas (N₂). A "combination mode" strategy is used to transport TTIP and TDMASn and is described below. Figure 1.17 shows a scheme of the source with its three controllable electrovalves, and the control scheme of the electrovalves. The "combination mode" can be broken down in four steps:

- During t_{11} , electrovalves A and B are simultaneously open to fill the canister with N₂.
- During t_{12} , all electrovalves are closed to allow for the homogeneization of the mixture in the canister.
- During t_{13} , electrovalve C is open to transport the precursor to the reaction chamber.
- During t_{14} , all electrovalves are open to assist the transport by N₂.

In this manuscript, the sequence for the combination mode will be written $[t_{11}/t_{12}/t_{13}/t_{14}]$, so that a complete ALD sequence with the first precursor transported with the combination mode reads $[t_{11}/t_{12}/t_{13}/t_{14}]/t_2//t_3/t_4$.

1.3.5 Conclusion

In this introduction chapter, the basic principles of the physics of solar cells have been presented. From thermodynamics considerations, the ultimate PV parameters of a PV converter and of a single junction solar cell have been derived. The latter ones serve to estimate how much the real devices differ from their optimal performances, and help in the identification of the limitations of the cell. The main properties of the hybrid organic-inorganic perovskite have been discussed. The expedient opto-electrical properties of these materials were compared with other semiconductors and their variations with the chemical composition of the perovskite have been discussed. Because of the good absorption, of the low exciton energy and the μm -scale diffusion length of the carriers, the perovskite materials are suitable to be integrated in thin film architectures. In spite of the multiple assets of the perovskite solar cells, challenges are still to be tackled (upscale, stability, further increase of the efficiency) to foster the entry of perovskite-based solar devices in the global market. Finally, the main principles of the ALD process have been presented based on the prototypical example of ZnO deposition from DEZ and H_2O . The definition of the different steps of the ALD cycles have been explained and the notion of self-limiting surface reactions has been illustrated. The change in the schematic representations of ALD across the years has also been presented and helped with apprehending the subtleties of the process, going beyond the naive "atomic layer-by-atomic layer" deposition. Emerging processes derived from the ALD process (*e.g.* S-ALD, AS-ALD and ALE) have also been introduced and underline the diversity of applications of ALD techniques. The specificities of the Beneq TFS-200 – and especially the mean of transporting precursors with a low volatility – have finally been introduced.

Chapter 2

Methods and processes¹

2.1 Development of TiO₂ by ALD²

The synthesis of titanium dioxide thin films has been developed by thermal ALD at IPVF. After a short introduction on the properties and uses of TiO₂, this section describes and compares the processes and the basic properties of TiO₂ thin films obtained with titanium tetra(isopropoxide) as Ti precursor and H₂O or H₂O₂ as oxygen precursors.

2.1.1 Introduction

2.1.1.1 General properties of TiO₂

TiO₂ is a large band gap transition metal (usually n-type) semiconductor composed of abundant elements. Titania is used in a large variety of applications as a white pigment (Pigment White 6, representing 60% of the market of the TiO₂ consumption in 2017, Ceresa (2018)) due to its high refractive index or as whitening and opacifying agent in diverse products (paints, solar cream, food, toothpaste or plastics). TiO₂ is a non-toxic and biologically inert material which makes it valuable for medical applications (B. Yang (2020)); the impact of nano-scale particles on health (*e.g.* for cosmetics or food) is however questioned and many studies are lead to unravel its potential effects. Titania is also used for its photocatalytic properties, for instance in self-cleaning glasses (S. Sun et al. (2019)). Thanks to its suitable electrical and optical properties, it has also to some extent been used in photovoltaic devices, which is discussed in [Chapter 3](#).

Titania exists in three crystalline polymorphs (anatase, rutile or brookite) but can also be synthesized in an amorphous phase. All phases are constituted of TiO₆ octahedra and differ by their organization (orientation, number of edge- or corner-sharing neighbors, distortion of the octahedra). A detailed crystallographic description of each phase can be found in X. Chen and Mao (2007) and S. Sun et

¹The other – less original – methods and processes are discussed briefly in [chapter A.1](#).

²TiO₂ has been developed at IPVF with help of D. Coutancier, CNRS Assistant Engineer. A more comprehensive study of the process developed at IPVF is reported in Coutancier et al. (2020).

al. (2019). The amorphous phase is reported to be thermodynamically metastable and can easily be turned to one of the crystalline phase after a specific treatment such as an annealing. The crystallization into one or the other phase as well as the transition from one phase to another depends on various parameters such as the process of synthesis of TiO₂, the size of the particles, the pressure and temperature conditions, etc. (X. Chen and Mao (2007); S. Sun et al. (2019); M. Song et al. (2020)). In the experimental conditions used during the process of making a PSC, the TiO₂ is usually found in its amorphous or anatase phase. The anatase phase is reported to have a good transparency in the visible region owing to its wide indirect band gap of 3.2 eV for thin films (Tang et al. (1994)). Computation performed on the dielectric functions of anatase and amorphous TiO₂ show very similar behaviors for the two materials, which implies similar optical properties. Mobilities ranging from 0.1 cm V⁻² s⁻¹ up to 10 cm V⁻² s⁻¹ at room temperature have been reported (Tang et al. (1994); Mazzolini et al. (2016)).

TiO₂ thin films and nanostructures can be synthesized by many different ways including: sol-gel method, hydro- and solvothermal methods, direct oxidation of metallic Ti, chemical or physical vapor deposition, electrodeposition, atomic layer deposition (X. Chen and Mao (2007); Niemelä et al. (2017)). The electronic and optical properties of the film can be tuned by doping with metallic (Cr, V, Fe ...) or non metallic (B, C, N, Cl ...) elements. This doping is mostly reported to affect the optical properties of the film and is especially used for photocatalytic applications, introducing new energy states close to midgap or to the band edges, in order to increase the absorption of the TiO₂ layer.

2.1.1.2 ALD deposition of TiO₂

Owing to the benefits and limitations of the ALD, and to the properties of the oxide, ALD-TiO₂ has been used extensively in biomedical (B. Yang (2020)), photocatalytic (Eswar et al. (2019)) and PV fields (Hossain et al. (2020)). Niemelä et al. (2017) detailed the large variety of precursors combinations which have been used to deposit TiO₂: for the Ti precursors, halides (*e.g.* TiCl₄), alkoxides (*e.g.* Ti(IV) tetraisopropoxide – Ti(O^{*i*}Pr)₄ – TTIP), alkylamides (*e.g.* tetrakis(dimethylamino) Ti(IV) – TDMAT), or less frequently heteroleptics; for the O precursors, water H₂O, hydrogen peroxide H₂O₂, dioxygen O₂, ozone O₃, alcohols R-OH or nitrogen oxide NO₂.

Table 2.1 presents a representative selection of properties of the ALD process and of the material for typical processes using various combinations of precursor species. GPC are globally high (GPC = 0.1-1.5 Å/cycle) and lead in most cases to TiO₂ thin films in amorphous or anatase phase. Processes relying on TiCl₄ usually occur at higher temperature owing to the better thermal stability of the Ti precursor. It leads however to the formation of chlorinated by-products (such as HCl) which are complicated to handle. Using TDMAT or TTIP usually allows for deposition at lower temperatures which is beneficial to work with temperature-sensitive substrates. ALD processes at temperatures as low as 50 °C have been reported when using TDMAT (Xie et al. (2008)). TTIP and TiCl₄ are less expensive than TDMAT (at least at lab scale) allowing for a more flexible development and use of the material.

2.1 Development of TiO₂ by ALD

Table 2.1: Selection of properties of ALD-TiO₂ processes and materials from the literature using common precursors. ⁺The values of GPC in italic font are not given in the respective references, hence are given as typical ranges of values extracted from Niemelä et al. (2017). ^{*}Prices offered by Strem chemicals, based on 25 g/250 g of ALD-grade chemicals.

Reagent 1 (Ti source)	TiCl ₄	TDMAT	TTIP	TTIP
Reagent 2 (O source)	H ₂ O	H ₂ O	H ₂ O	O ₂ plasma
Substrate	Si/SiO ₂	Si(100)	Si/SiO ₂	Si (100)
T_{ALD} (°C)	150-425	50-250	100-250	120-275
GPC (Å/cycle)⁺	<i>0.5-1.5</i>	0.6-1.4	<i>0.15-1</i>	0.4
Crystalline structure	anatase rutile	amorphous	amorphous anatase	amorphous
Reference	J. Aarik et al. (2001)	Xie et al. (2008)	J. Aarik et al. (2000)	Kil et al. (2002)
Cost of Ti precursor (€/g)[*]	5.2	23.3	0.2	0.2

As discussed previously, the properties of ALD-TiO₂ thin films can vary within a certain range and can depend on the precursors used. The films can either be grown amorphous or polycrystalline (rutile, or anatase phase), with an optical band gap reported between 3.2 eV and 3.7 eV (Shi et al. (2017)), a high refractive index from 2.2 and up to 3.0 at 632 nm (Yu et al. (2013); Kasikov et al. (2006)), a good transmission in the visible and near infrared regions, and usually display high resistivity without extrinsic doping (above $1 \times 10^3 \Omega \text{ cm}$, Tian et al. (2015)).

2.1.2 Choice, transport and reactivity of the precursors

2.1.2.1 Choice of the precursors

Owing to the large amount of studies using TTIP and to its benefits listed in the previous section, TTIP has been chosen as Ti precursor for this work. TTIP is a mildly pyrophoric chemical whose main properties are given in Table 2.2. Water and hydrogen peroxide have been used alternatively as counter-reactants to grow TiO₂ films. Due to the higher reactivity of H₂O₂ compared to H₂O (J. Aarik et al. (2000)), the parameters of the process and the properties of the final film may vary, which is examined in details in the following sections.

For all this section, the ALD reactor is set in "QCM-mode", meaning that a specific chamber designed to integrate a QCM is used for the reaction. It allows for the *in situ* characterization of the ALD process.

2.1 Development of TiO₂ by ALD

Table 2.2: Properties of the ALD precursors used at IPVF for the synthesis of SnO₂ and TiO₂.

Precursor	P _{sat} (Torr @ 40°C)	Boiling point (°C @ 0.1mm)	T _{decomp} (°C)	Price (€/g)
TTIP	10 ^{-4.3}	232	≥ 220	0.2
TDMASn	0.04	51	325	34.9
H ₂ O	55.5	-38.7	-	-
H ₂ O ₂	25 (@ 30°C)	108 (@ 760 mmHg)	-	<5 cent.

2.1.2.2 Transport conditions of the precursors (TTIP, H₂O, H₂O₂)

The first step to enable the ALD is to ensure the transport of the precursor species from their storing canister to the reaction chamber without decomposition. Due to its low vapor pressure, TTIP is transported using the combination mode described in [section 1.3.4.2](#). A suitable T_{source} for TTIP has been determined by recording the frequency variations of the quartz after the TTIP pulse for various T_{source}, averaged over multiple ALD cycles at constant deposition temperature (T_{dep} = 225 °C). Using water as counter-reactant, if the TTIP source is not heated, and up to T_{source} = 70 °C, no mass gain is observed on the QCM. However, when the temperature is further increased at 85 °C, the positive mass gain indicates that the precursor is transported adequately. Since higher source temperatures increase the risk of long term decomposition of the precursor, and in agreement with the range of source temperature usually adopted for this process in the literature (Aghaee et al. (2015); Barreca et al. (2015)), T_{source} is set at 85 °C. When hydrogen peroxide is used, the mass gain occurs at a lower temperature (60 °C), which is ascribed to the higher reactivity of H₂O₂ at low temperature. For the TTIP/H₂O₂ process, the source is hence set at 60 °C. H₂O and H₂O₂ are volatile enough to be transported at room temperature.

2.1.2.3 ALD surface reactions

The QCM allows to follow the progress of the film growth through the entire ALD cycle and to characterize the surface reactions occurring. [Figure 2.1.a](#) presents the typical shape of a QCM measurement over one ALD cycle of TiO₂ from TTIP and H₂O, deposited at T_{dep} = 175 °C, with a sequence [10/0.2/10/2]/30//5/20 TTIP/N₂//H₂O/N₂ (see [sections 1.3.1.1](#) and [1.3.4.2](#) for the signification of each step of the sequence). [Figure 2.1.b](#) presents the typical shape of a QCM measurement over one ALD cycle of TiO₂ from TTIP and H₂O₂, deposited at T_{dep} = 100 °C, with a sequence [10/0.2/10/2]/30//5/20 TTIP/N₂//H₂O₂/N₂. The QCM observations are in line with what has been reported before with similar precursors (J. Aarik et al. (2000); Rahtu and Ritala (2002)). As TTIP reacts with the surface hydroxyl

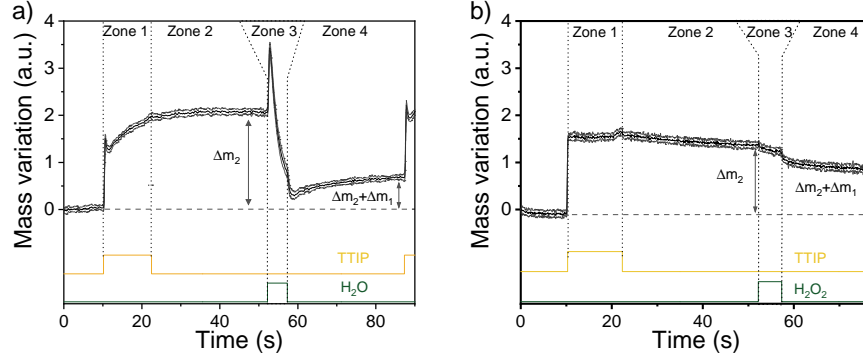
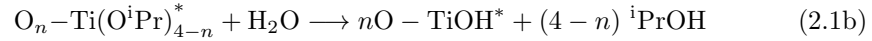
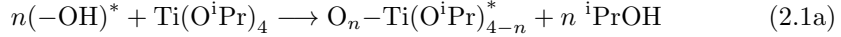


Figure 2.1: Mass variations recorded by *in situ* QCM measurements during the growth of TiO₂ from TTIP and a) H₂O; b) H₂O₂.

groups and releases isopropanol, the total mass on the QCM increases (zone 1) until stabilization due to a saturation of the available reactive sites. The reactor is purged (zone 2 – net mass gain after the Ti pulse $\Delta m_2 > 0$) and then H₂O or H₂O₂ is pulsed and reacts with the isopropoxide groups at the surface and releases isopropanol leading to a mass loss (zone 3). Finally, the reactor is purged before another ALD cycle occurs (zone 4 – net mass loss $\Delta m_1 < 0$ after the O pulse). The net mass gain is given by $\Delta m_2 + \Delta m_1 > 0$, acknowledging the effective deposition of material during the ALD cycle. The surface reactions in the ALD process with TTIP and H₂O has already been studied with QCM (Rahtu and Ritala (2002)). The reactions occur through the exchange of n ligands (n is not necessarily an integer):



The superscript * refers to surface species. From the ratio $\Delta m_1/\Delta m_2 = -0.67$, one can determine the number n of ligands released during the TTIP pulse (Aarik and Aidla (1999)). It corresponds here to $n = 3.3$, which is slightly higher than the reported values ($n = 2.2\text{-}2.5$ at $T_{dep} = 200\text{-}250$ °C, J. Aarik et al. (2000)).

From the QCM data of Figure 2.1, a larger mass gain is observed from the TTIP/H₂O₂ process than for TTIP/H₂O process. To the best of our knowledge, little has been reported on the specific mechanisms of the reaction between TTIP and H₂O₂ (J. Aarik et al. (2000)). Here, the growth mechanism can involve both acid-base and redox reactions which makes a fine interpretation of the QCM data more difficult (compared to what is presented for TTIP/H₂O).

2.1.3 Properties of the ALD process

The QCM configuration is useful to have insights on the reaction mechanisms at play during the ALD process, or screening a set of recipe during the first

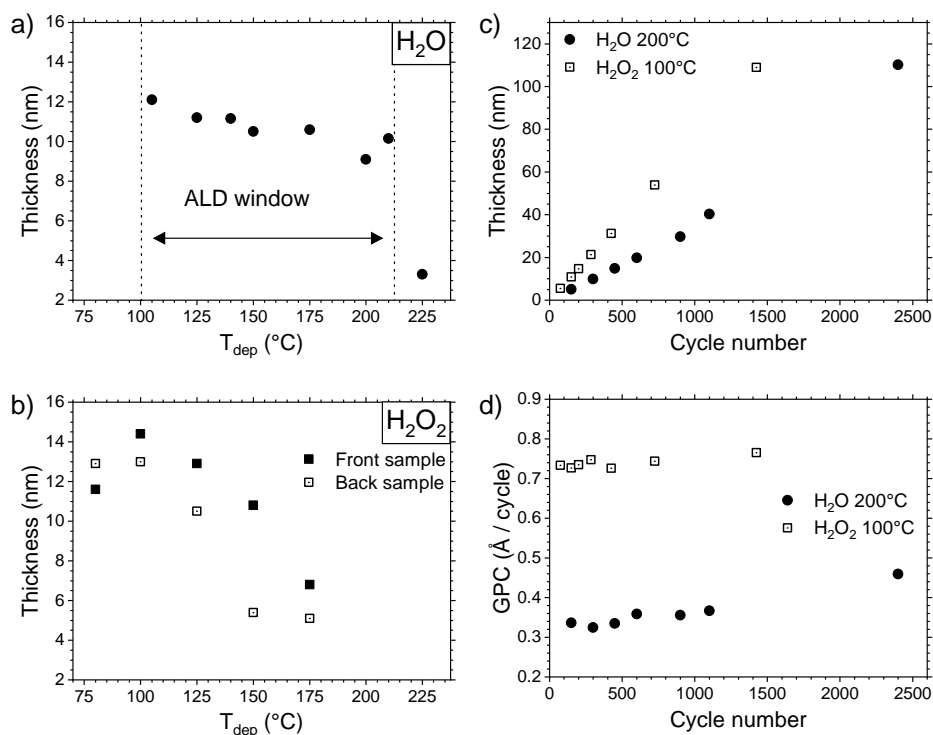


Figure 2.2: Characterization of the ALD process for TTIP/H₂O and TTIP/H₂O₂ processes. a) Variation of the thickness of ALD-TiO₂ as function of the deposition temperature for the TTIP/H₂O (n = 300 cycles). b) Variation of the thickness at the front and at the back of the reactor function of the deposition temperature for the TTIP/H₂O₂ process (n = 200 cycles). Variation of c) the thickness and d) the growth per cycle of TiO₂ as function of the cycle number for TTIP/H₂O and TTIP/H₂O₂.

development of a new material. There is however a large unoccupied volume in this chamber meaning that a large amount of precursors has to be consumed in order to ensure the correct deposition of the film. In order to reduce the consumption of precursors and to reduce the duration of the ALD cycle (less volume to fill means a lower dose of precursors is needed), another chamber is used, with a lower volume (560 cm³ vs. 73 cm³). The recipes are rectified as following [0.5/0.05/0.5/0.5]/5//2/5 (TTIP/H₂O) and [0.5/0.05/0.5/0.5]/5//1/5 (TTIP/H₂O₂) to accommodate to the new chamber.

2.1.3.1 Determination of the ALD window

Within the ALD window, all properties (typically the thickness) of the film should not be affected by the temperature of the substrate (*i.e.* the temperature of the reactor). To determine this ALD window for the TTIP/H₂O and the TTIP/H₂O₂ processes, samples of 300 cycles (TTIP/H₂O) and 200 cycles (TTIP/H₂O₂) are deposited at various deposition temperatures ranging from

100 °C to 225 °C. The thicknesses are determined by X-ray reflectivity (XRR) and are presented in [Figure 2.2.a,b](#).

For TTIP/H₂O, the thickness does not vary much between 100 °C and 210 °C around 11 nm. It drops dramatically to about 3 nm at 225 °C. It indicates that the ALD window for the TTIP/H₂O extends from 100 °C (lower temperatures are not probed because the temperature gradient between the source and the reactor has to be large enough to prevent cold points in the circuit) up to 210 °C. For TTIP/H₂O₂, the thickness varies constantly with a large drop from 140 °C going from around 15 nm to below 12 nm, down to 7 nm at 175 °C. The limits of the ALD window in this case are blurry. However, the QCM data show a typical ALD behavior (self-limiting surface reactions) at least for the lowest temperatures. A similar behavior has been observed by J. Aarik et al. (2000) and ascribed to a temperature-dependent steric hindrance.

2.1.3.2 Determination of the growth per cycle and the nucleation phase

The growth per cycle and the nucleation phase of the two processes are determined by measuring the thickness of samples deposited at 200 °C for TTIP/H₂O and 100 °C for TTIP/H₂O₂ while varying the number of ALD cycles from 75 cycles to 2400 cycles. These variations are displayed in [Figure 2.2.c](#), along with the average GPC (computed as the thickness divided by the total number of cycles – [Figure 2.2.d](#)). The GPC is determined to be around 0.35 Å/cycle for TTIP/H₂O and about twice as much for TTIP/H₂O₂ (0.75 Å/cycle). This higher value is ascribed to the higher reactivity of H₂O₂ compared to H₂O, in line with the previous QCM observations and with what is reported in the literature (Aghaee et al. (2015); J. Aarik et al. (2000)). For both processes, the thickness scales linearly with the number of cycles (as illustrated by the quasi constant GPC for all number of cycles) typical of an ALD process with Si/native SiO_x as substrate. Almost no nucleation delay is observed and – if existing – would only concerns the first tens of cycles; it depends however strongly on the nature of the substrate and the situation might be different on another substrate.

2.1.3.3 Homogeneity of the deposition

The homogeneity of the TTIP/H₂O process across the whole chamber is good and discussed more in details in [chapter 3.3](#). Regarding the TTIP/H₂O₂ process, the thickness of material deposited on a Si wafer close to the gas inlet (front of the reaction chamber) and on a Si wafer close to the gas outlet (back of the reaction chamber) are compared at various deposition temperatures, for 200 cycles ([Figure 2.2.b](#)). The homogeneity of the deposition across the chamber degrades as the temperature increases. It further justifies the choice of a low temperature for the TTIP/H₂O₂ ALD process.

2.1.4 Properties of the as-deposited ALD-TiO₂ thin films

XPS measurements have been performed on ALD-TiO₂ thin films deposited with the TTIP/H₂O process and the TTIP/H₂O₂ process on a Si wafer to determine

2.1 Development of TiO₂ by ALD

Table 2.3: Composition of the ALD-TiO₂ thin films as determined by XPS for the TTIP/H₂O and the TTIP/H₂O₂ processes.

	TTIP/H ₂ O	TTIP/H ₂ O ₂
Ti	15.9%	22.2%
O (TiO ₂)	33.7%	44.0%
O (conta/SiO _x)	12.6%	11.4%
C	12.5%	19.0%
Si	25.3%	3.4%

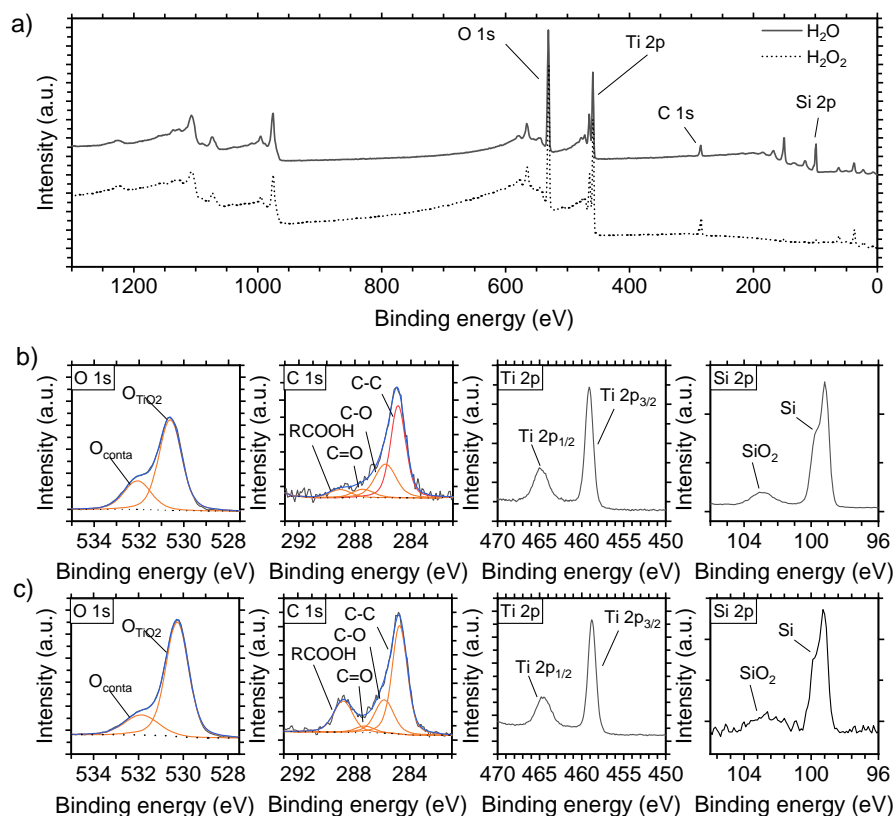


Figure 2.3: XPS survey spectra of films deposited with a) the TTIP/H₂O process and b) the TTIP/H₂O₂ process. High resolution core level spectra of O 1s, Ti 2p, C 1s and Si 2p for c) the TTIP/H₂O process and d) the TTIP/H₂O₂ process.

the composition of the as-deposited films. On the survey spectra (Figure 2.3.a), only O, Ti, C and Si contributions are observed in the case of TTIP/H₂O which demonstrates no extrinsic contamination of the film. The Si contribution originates from the substrate, due to the thinness of the film (remember the XPS depth probe is in the order of 10 nm), C mainly to surface contamination and O to the oxide phase and to a minor extent to the surface contamination as well. Note that the Si 2p content is drastically lower, in agreement with the higher thickness of the layer. High energy resolution core level spectra of Ti 2p, C 1s, O 1s and Si 2p are also acquired and presented in Figure 2.3.b (for TTIP/H₂O) and Figure 2.3.c. Ti 2p displays typical features of Ti⁴⁺: a broader Ti 2p_{1/2} contribution at binding energy (BE) = 464.7 eV separated from the sharper Ti 2p_{3/2} contribution at 459.0 eV by 5.7 eV, with a small satellite contribution at 572.0 eV. No contribution at 453.8 eV from metallic Ti is observed (X. Liang et al. (2009)). C 1s displays in both cases characteristic features of adventitious contamination. However, the contribution ascribed to R-COOH species is unusually higher in the case of TTIP/H₂O₂ compared to TTIP/H₂O. This could be due either to a higher surface contamination or to an additional contribution from precursor fragments. An in-depth analysis of the sample shows a persistent atomic fraction of C of 4% which is consistent with the inclusion of precursor fragments in the film. The elemental compositions of the surface of the films have been quantified and are presented in Table 2.3 for TTIP/H₂O and TTIP/H₂O₂. Note that from the Si 2p high energy resolution core level spectra, an oxide contribution is evidenced (the Si wafer is not etched before ALD) and the atomic ratio of SiO_x/Si is determined at 0.16 for H₂O and 0.31 for H₂O₂. The stoichiometry of the films has hence been determined as TiO_{2.12} for TTIP/H₂O and TiO_{2.00} for TTIP/H₂O₂ which correlates well with a Ti(IV) oxide.

The influence of the process parameters on the properties of the as-deposited TiO₂ are also investigated. The reference conditions of deposition are T_{source} = 85 °C, T_{dep} = 200 °C for 300 cycles following the sequence [0.5/0.05/0.5/0.5]/5//2/5 (TTIP/H₂O) and T_{source} = 60 °C, T_{dep} = 100 °C for 200 cycles following the sequence [0.5/0.05/0.5/0.5]/5//1/5 (TTIP/H₂O₂). The influence of the deposition temperature and of the film thickness have been investigated by varying T_{dep} (from 100 °C to 210 °C) and the number of cycles (from 105 cycles to 2400 cycles). The main optical and structural properties of the films are analyzed (Figure 2.4 for TTIP/H₂O and Figure 2.5 for TTIP/H₂O₂). Titania is deposited on Si wafers with native SiO_x (XRR, GI-XRD, ellipsometry) and on 1 mm-thick sodalime glass (SLG) substrates (photospectroscopy).

For deposition temperatures between 100 °C and 200 °C, the as-deposited TTIP/H₂O film is amorphous, with a good transmission above 85% in the visible and near infrared region. The optical band gap is determined to be indirect between 3.4 eV and 3.5 eV, which is in line with the properties of ALD-TiO₂ reported in the literature (Shi et al. (2017)). The refractive index (determined by ellipsometry and given here at 632 nm) is between 2.2 and 2.3, which is somewhat lower than values reported for bulk titania, but has still already been reported for ALD-TiO₂ films (Yu et al. (2013)). The lower refractive index can be related to the crystalline phase of TiO₂, where $n_{amorphous} < n_{anatase} < n_{rutile}$ as suggested by Bendavid

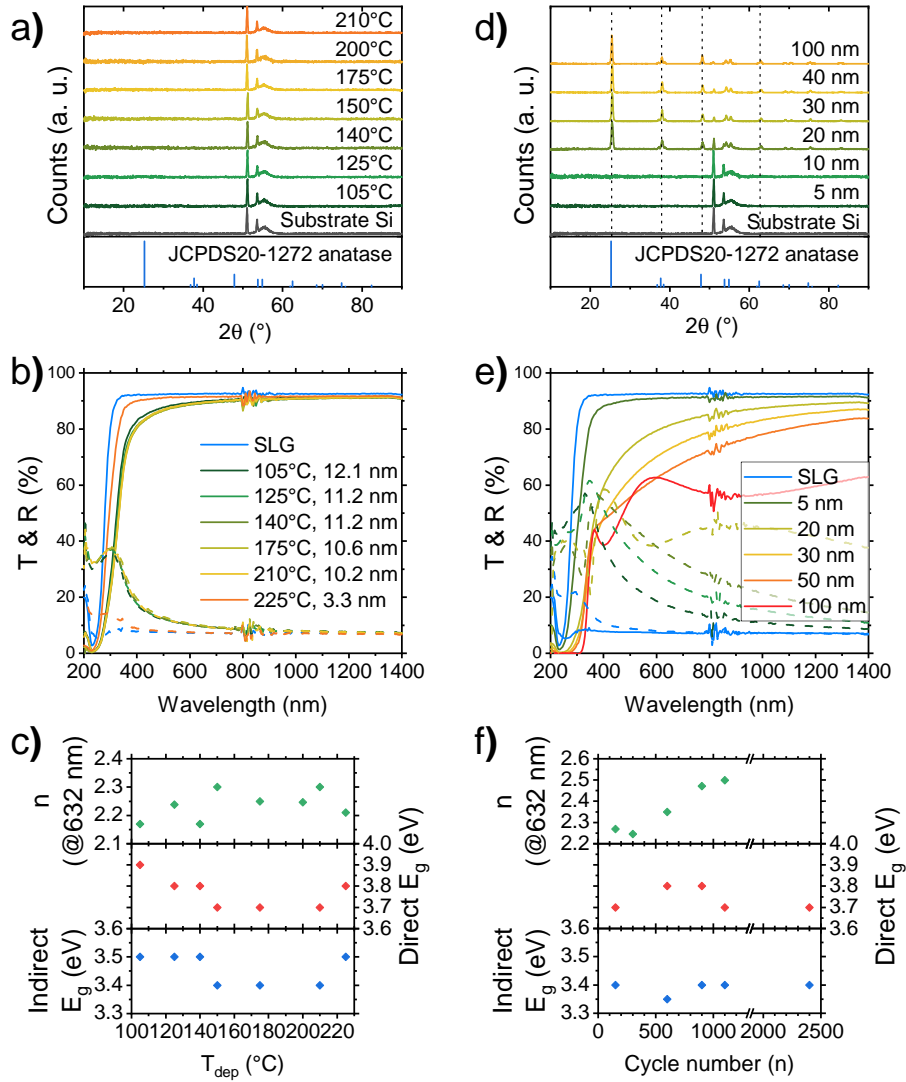


Figure 2.4: Characterization of the as-deposited ALD-TiO₂ material for TTIP/H₂O process as function of a)-c) the deposition temperature and d)-e) the cycle number. a,d) GIXRD diffractograms of the TiO₂ on a Si substrate. b,e) Transmission and reflection spectra. c,f) Optical band gap and refractive index at 632 nm.

et al. (2000). When the deposition temperature is further increased to 225 °C for TTIP/H₂O, the film keeps the same optical and structural properties, but its thickness drops dramatically (accounting for the higher transmission of the sample). This can be the sign of decomposition of the precursors, confirming that the ALD window does not extend above 210 °C, in line with the decomposition temperature

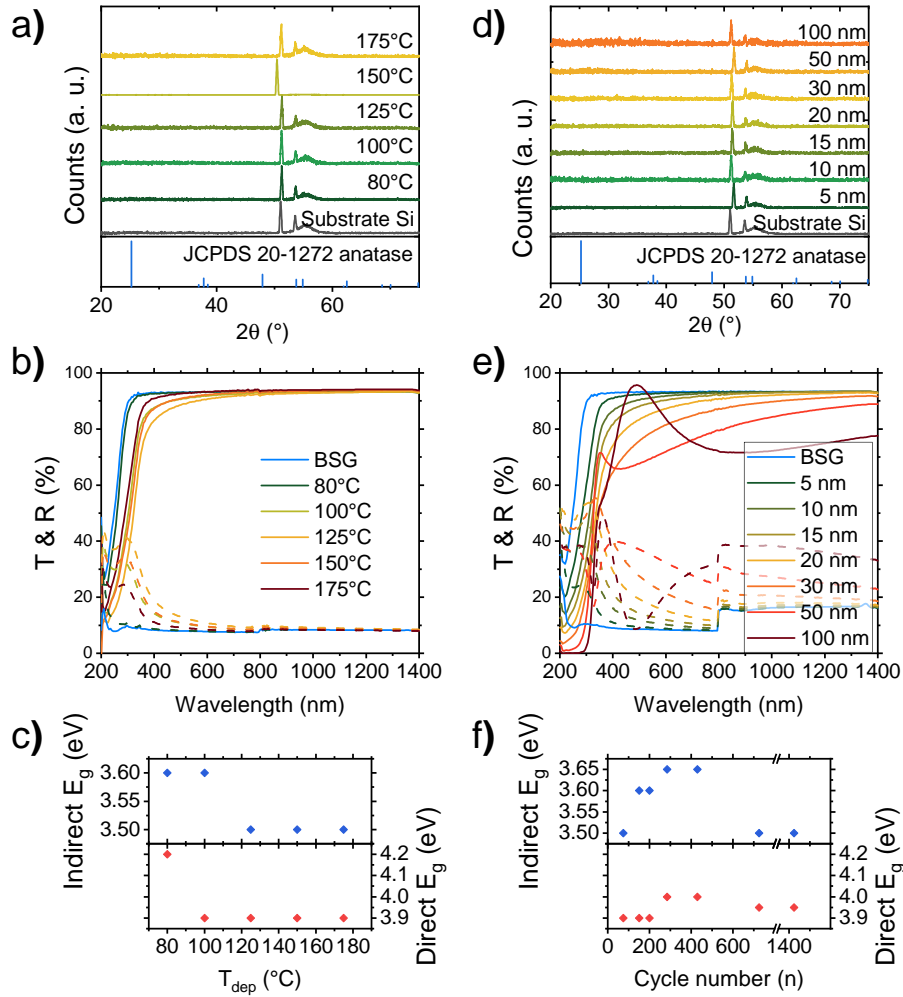


Figure 2.5: Characterization of the as-deposited ALD-TiO₂ material for TTIP/H₂O₂ process as function of a)-c) the deposition temperature and d)-e) the cycle number. a,d) GIXRD diffractograms of the TiO₂ on a Si substrate. b,e) Transmission and reflection spectra. d,f) Optical band gap and refractive index at 632 nm.

of TTIP given in [Table 2.2](#).

Regarding the variation of the film properties with the thickness, a noticeable phase transition from the amorphous phase to the anatase phase can be deduced from the GI-XRD measurements. Using complementary measurements for thicknesses between 15 nm and 20 nm, the transition occurs at a thickness between

17 nm and 18 nm. It does not affect the indirect optical band gap of the material, but an increase of the refractive index is observed concomitantly to the phase transition. The refractive index at 632 nm increases from 2.35 (600 cycles, 20 nm) up to 2.5 at higher thicknesses. This increase can be related to the phase transition (Bendavid et al. (2000)) as well as to the increase of the thickness of the film as reported by Shi et al. (2017). The increase in thickness also affects the transmission of the data due to interferences.

The properties of the TTIP/H₂O₂ films are similar to the ones described for the TTIP/H₂O films with a few exceptions: 1) increasing the thickness of the film up to 100 nm does not induce the crystallization of the layer. 2) Due to the large variation of the GPC with the temperature (as stated in [section 2.1.3.1](#)), the transmission of the sample depends on T_{dep} .

2.1.5 Conclusions on the development of ALD-TiO₂

Two ALD processes have been newly developed at IPVF using TTIP as Ti source and either H₂O or H₂O₂ as O source. A large ALD window has been determined for the TTIP/H₂O process between 100 °C and 210 °C, with a relatively low GPC of 0.35 Å/cycle. Using H₂O₂ instead allowed to reach twice as high GPC (0.7 Å/cycle at 100 °C) but no clear ALD window was found. The QCM analysis confirmed however that the deposition takes place in an ALD-regime at the chosen deposition temperatures (200 °C for TTIP/H₂O and 100 °C for TTIP/H₂O₂).

The XPS analysis of the thin films revealed that a stoichiometry close to TiO₂ is achieved for both processes, and that the TTIP/H₂O₂ process seems to yield films with a higher surface contamination. The properties of the films were found to be relatively independent from the oxygen source. The films grow amorphous, with a refractive index of 2.4 at 632 nm, a good transmission in the visible and infrared regions, and a relatively high indirect optical band gap above 3.4 eV. In the TTIP/H₂O process at 200 °C, the thin films crystallize in the anatase phase for thicknesses between 10 nm and 20 nm (a more precise threshold is discussed in [chapter 3.2](#)). The electric properties of the thin films have not been determined due to a too high resistivity of the layers. The suitability of the ALD-TiO₂ layers for applications in PSCs is discussed in [Chapter 3](#).

2.2 Development of SnO₂ by ALD³

2.2.1 Introduction

2.2.1.1 General properties of SnO₂

Tin oxide can be found with tin atoms in various oxidation states: Sn (II) oxide – SnO, stannous oxide – or Sn (IV) oxide – SnO₂, stannic oxide. SnO has a moderate range of applications, being mostly used as precursor in the synthesis of other tin-based compounds (Cocks and Zuckerman (1965); Gitlitz and Moran (2000)).

³SnO₂ has been developed at IPVF with help of D. Coutancier, CNRS Assistant Engineer and T. Vincent, IPVF Engineer.

It can also be involved in the process of fabrication of ruby-glass. SnO₂ finds a wider range of applications. It is used in ceramic glazes as whitening agent and opacifier owing to its high refractive index. In the glass industry, SnO₂ acts also commonly as seed layer to increase the adherence between glass and superstrate. Owing to its stability and its good sensitivity, SnO₂ figures as one of the promising oxides for gas sensor applications towards a variety of chemicals including ethanol, CO, NH₃ and other volatile compounds (Staerz et al. (2020); Ponzoni (2020)). Associated with graphene, SnO₂ has been used as anode in Li-ion batteries (Y. Deng et al. (2016)). When doped with F or Sb, it becomes a good transparent conductive oxide (Kykyneshi et al. (2011)). Finally it can be associated with other elements, in particular indium to obtain highly effective TCOs. Thanks to its suitable optical and electrical properties, SnO₂ is also a privileged material for photovoltaic applications, as discussed in [Chapter 4](#).

Tin oxides are non toxic materials composed of abundant elements. SnO₂ exists in various polymorphs, but is mostly found in its cassiterite form which crystallizes in the rutile phase (space group P4₂/mmm). The crystallographic organization of these polymorphs is discussed in Das and Jayaraman (2014). SnO₂ thin films can also be found in an amorphous phase which is reported to crystallize in the rutile phase for temperatures above 250 °C (Jung et al. (2017); Choi and J.-S. Park (2014)). SnO₂ is reported as being intrinsically an n-type semiconductor due to oxygen vacancies in the lattice. Cassiterite has a large direct band gap which varies from 3.6 eV for monocrystals to 4.0 eV for thin films (Jarzebski and Morton (1976b)), along with a good transparency in the visible and near infrared region and a rather high refractive index in the visible range around 1.9 (Akgul et al. (2013)). Higher electronic mobilities have been reported for SnO₂ thin films compared to TiO₂ (up to 30 cm² s⁻¹ V⁻¹ Won et al. (2020); Jarzebski and Morton (1976a)). The amorphous phase has been reported with slightly different properties compared to its crystalline counterpart, with a direct band gap ranging from 3.26 eV (Avis et al. (2019)) to more than 4.3 eV (Choi et al. (2014)). It benefits from enhanced mechanical properties which can allow for a better resilience of the layer to mechanical stresses as suggested by Xianghong Liu et al. (2015).

SnO is reported as a p-type semiconductor with a smaller band gap than SnO₂ from 2.7 eV to 3.2 eV (Guo et al. (2010); Barros et al. (2019)). It draws some interest in research because few oxides are naturally p-doped. SnO can be synthesized as an amorphous material or a crystalline one, crystallizing in a tetragonal phase (romarchite, space group P4/nmm). It shows good hole mobilities reported at room temperature around 1 cm² s⁻¹ V⁻¹ (Guo et al. (2010)).

SnO and SnO₂ can be synthesized by different means such as spray pyrolysis, hydrothermal deposition, electrochemical deposition, physical or chemical vapor deposition (Kykyneshi et al. (2011)). The electronic and optical properties of the oxides can be tuned by doping with various elements such as Ag, Y or Mg for SnO (Pham et al. (2017)); Ta, F, Sb for SnO₂ (Kykyneshi et al. (2011)).

2.2 Development of SnO₂ by ALD

Table 2.4: Selection of properties of ALD-SnO₂ processes and of as-deposited materials from the literature using common precursors. *Prices offered by Strem chemicals, based on 25 g of ALD-grade chemicals.

Reagent 1 (Sn source)	SnCl ₄	TDMAStn	TDMAStn	TDMAStn
Reagent 2 (O source)	H ₂ O	H ₂ O	O ₃	H ₂ O ₂
Substrate	glass	Si(100)	Si/SiO ₂	Si (100)
T_{ALD} (°C)	300-600	30-200	100-200	50-325
GPC (Å/cycle)	0.1-0.3	0.5-2.1	1.1	0.8-1.6
Crystalline structure	rutile	amorphous	amorphous	amorphous
Reference	Viirola and L. Niinistö (1994)	Mullings et al. (2013)	Choi and J.-S. Park (2014)	Elam et al. (2008)
Cost of Sn precursor (€/g)*	7.4	34.9	34.9	34.9

2.2.1.2 ALD deposition of SnO₂

Successful attempts at synthesizing stannous oxide by atomic layer deposition are limited, owing to the metastability of SnO and its propensity to be oxidized in SnO₂. Han et al. (2014) achieved it by using bis(1-dimethylamino-2-methyl-2-propoxy)tin and H₂O between 90 °C and 210 °C. H. Y. Kim et al. (2019) showed that using bis(N-ethoxy-2,2-dimethyl propanamido)tin and either H₂O or an O₂ plasma as oxidizing species, SnO or SnO₂ could be grown respectively. In contrast to SnO, SnO₂ (or similar stoichiometries) has been extensively studied by ALD (Nazarov et al. (2015)). The applications of ALD-SnO₂ are multiple, and ALD benefits greatly to the deposition of thin layers (tens of nm) on high aspect ratio substrates. It makes ALD-SnO₂ especially useful in the domains of batteries (Aravindan et al. (2013)), TFT (Sheng et al. (2018)), gas sensor (Das and Jayaraman (2014)) and photovoltaics (Zardetto et al. (2017)). SnO₂ can be synthesized using a large variety of precursors in thermal or plasma enhanced ALD such as halides (*e.g.* SnCl₄), alkylamides (*e.g.* tetrakis(dimethylamino)Sn(IV), TDMAStn), acetylacetonates, alkoxides for the Sn precursor; water H₂O, hydrogen peroxide H₂O₂, ozone O₃ or nitrogen oxides NO_x for the O precursor (Nazarov et al. (2015)).

Table 2.4 displays a representative selection of ALD processes and of as-deposited material properties, using various precursor combinations. Even though the precursor can be found at a very affordable price, processes using TiCl₄ usually occur at high temperature (>300 °C) and lead to the formation of as-deposited rutile films with a rather lower GPC (up to 1.0 Å/cycle). As discussed in section 4.1.1,

amorphous SnO₂ is preferred for the integration of SnO₂ in perovskite solar cells. Moreover, the surface reactions release chlorinated by-products (such as HCl) which are complicated to handle. The ALD window for TDMASn processes is reported at lower temperatures (below 300 °C due to the degradation of TDMASn at higher temperatures) typically between 50 °C and 200 °C, with a GPC above 1.0 Å/cycle which usually depends on the temperature. The as-deposited layer is reported as amorphous which suits better the perovskite solar cells application. The O precursor mostly influences the growth per cycle (and its temperature dependence) and the dose needed to saturate the surface. Choi and J.-S. Park (2014) as well as Elam et al. (2008) report a significant contamination of the film with precursor fragments for deposition temperatures below 200 °C.

As shown previously, the properties of ALD-SnO₂ thin films depend on the precursors used and can vary in a certain range. The films can either be grown amorphous or polycrystalline (rutile phase), with an optical band gap reported between 3.0 eV and 4.3 eV (Mullings et al. (2013); Choi and J.-S. Park (2014)), a refractive index between 1.6 and 2.0 at 632 nm (Elam et al. (2008); Mullings et al. (2013)), an excellent transmission in the visible and near infrared region, and a large range of resistivity (from 1×10^{-4} to $10 \Omega \text{ cm}$ Nazarov et al. (2015)).

2.2.2 Choice, transport and reactivity of the precursors

2.2.2.1 Choice of the precursors

Based on the abundant literature using TDMASn as Sn precursor to synthesize SnO₂ (especially for application in perovskite solar cells), and to its benefits listed in the previous section, TDMASn has been chosen as Sn precursor for this work. Some properties of the precursor are given in [Table 2.2](#). Water and hydrogen peroxide have been chosen alternatively as O sources to grow the tin oxide films, to have a larger tunability of the thin film synthesis conditions and properties.

For all this section, the ALD reactor is set in "QCM-mode", meaning that a specific chamber designed to integrate a QCM is used for the reaction. It allows for the *in situ* characterization of the ALD process.

2.2.2.2 Transport conditions of the precursors (TDMASn, H₂O, H₂O₂)

First the conditions required to ensure a good transport of the precursor species from the canister to the reactor without decomposition are determined. Due to the low volatility of TDMASn, the combination mode for solid sources is used for its transport (cf. [section 1.3.4.2](#) for a detailed explanation on this mode). To adjust the source temperature for TDMASn, the mass variation on the QCM is recorded over several ALD cycles. For both H₂O and H₂O₂ processes, a positive mass gain was found for $T_{source} > 60 \text{ °C}$, which is in the range of the source temperature used to transport TDMASn as reported in the literature for similar processes (Trost et al. (2015); Stefik et al. (2012)). Thus, to prevent any small thermal degradation, the source temperature is set at 60 °C.

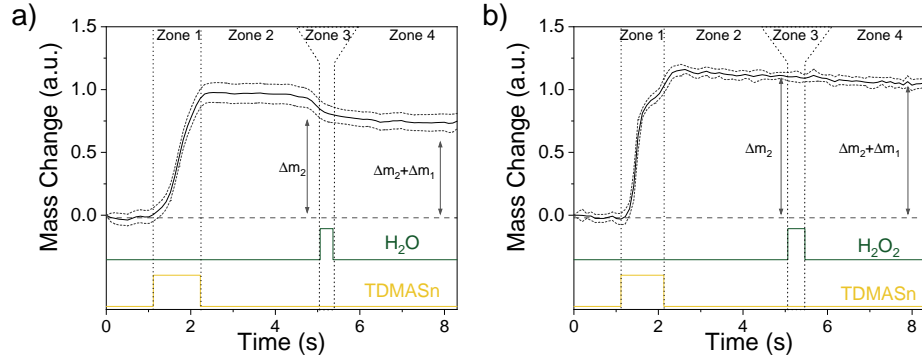
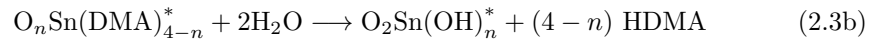


Figure 2.6: Mass variations recorded by *in situ* QCM measurements during the growth of SnO₂ from TDMASn and a) H₂O; b) H₂O₂.

2.2.2.3 ALD surface reactions

With the *in-situ* QCM measurements, the different steps of the ALD cycle can be examined. Figure 2.6 shows the typical variations of the QCM frequency (converted into mass variations) during a complete SnO₂-ALD cycle with either H₂O or H₂O₂. The variations are averaged over 10 cycles. The deposition temperature is set at $T_{dep} = 100\text{ }^{\circ}\text{C}$ with a sequence [1/0.1/0.5/0.5]/3//0.3/3 (see sections 1.3.1.1 and 1.3.4.2 for the signification of each step of the sequence). The QCM observations are in line with what has been observed with similar precursors (Mullings et al. (2013) for H₂O, Elam et al. (2008) for H₂O₂). A large increase of the mass $\Delta m_2 > 0$ is observed as TDMASn is pulsed, corresponding to the chemisorption of the heavy TDMASn precursor on the surface hydroxyl groups and the release of by-products such as dimethylamine (zone 1). The reactor is purged with N₂ (zone 2) and H₂O or H₂O₂ is pulsed leading to the hydroxylation of the surface and the release of by-products with a mass variation Δm_1 (zone 3). The reactor is purged with N₂ (zone 4) before another ALD cycle starts. The total mass gain during the cycle is given by $\Delta m = \Delta m_1 + \Delta m_2$. In Figure 2.6.a and Figure 2.6.b, the total mass gain is positive indicating an effective deposition of material on the QCM. Mechanisms of the ALD surface reactions have been suggested in the literature based on QCM and quadrupole mass spectroscopy observations (Mullings et al. (2013) for H₂O, Elam et al. (2008) for H₂O₂), and involve the exchange of ligands through acid-base reactions (H₂O process) and acid-base and redox reactions (H₂O₂ process):



The superscript * refers to surface species. From the ratio of the total mass gain and the mass gain during the TDMASn pulse $R = \Delta m / \Delta m_2$, the number n of

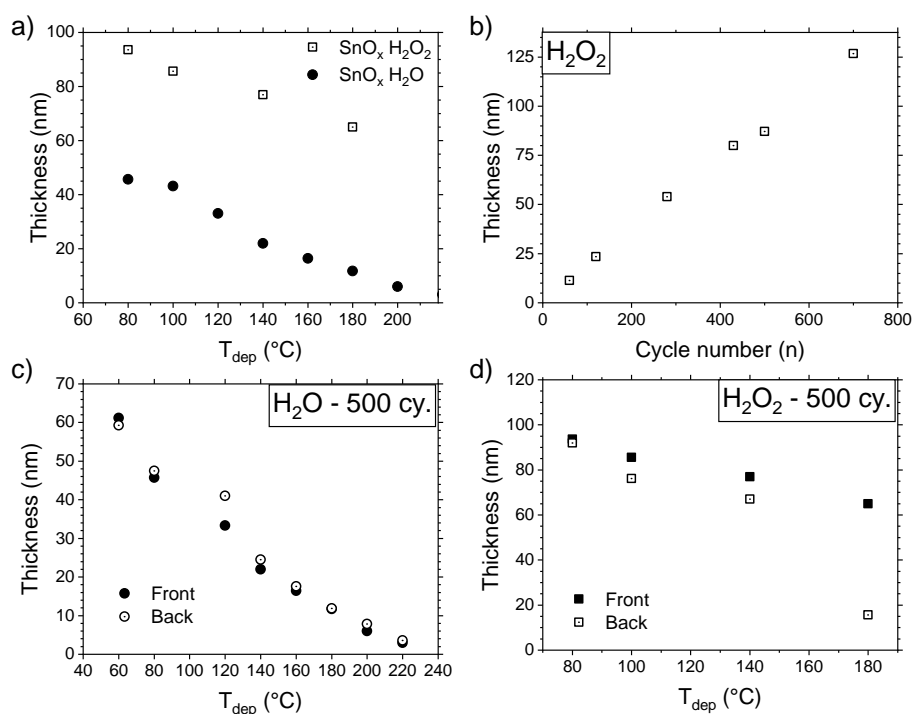


Figure 2.7: Characterization of the ALD process for TDMASn/H₂O and TDMASn/H₂O₂ processes. a) Variation of the thickness of ALD-SnO_x as function of the deposition temperature ($n = 500$ cycles) for TDMASn/H₂O and TDMASn/H₂O₂. b) Variation of the thickness of SnO_x as function of the cycle number for TDMASn/H₂O₂. Variation of the thickness at the front and at the back of the reactor function of the deposition temperature for the d) TDMASn/H₂O and e) TDMASn/H₂O₂ processes.

DMA ligands released during the first pulse can be determined as explained by Elam et al. (2008). By supposing that pure SnO₂ is deposited at each ALD cycle, $R = 0.78$ in case of H₂O, which corresponds to $n = 2.3$. For H₂O₂, $R = 0.94$ which corresponds to $n = 3.0$. These values are in line with what Elam et al. (2008) report for their process ($n = 2.5$ for H₂O and $n = 3.2$ for H₂O₂ at $T_{dep} = 150$ °C).

2.2.3 Properties of the ALD process

As explained previously in section 2.1.3, the process and material are characterized in a different reaction chamber. The ALD is modified accordingly to adapt to the new chamber from $[1/0.1/0.5/0.5]/3//0.3/3$ to $[1/0.1/0.5/0.5]/3//1/3$ (pulse time of H₂O₂ increased from 0.3 s to 1 s) for the TDMASn/H₂O₂ process. The TDMASn/H₂O sequence is not modified.

2.2.3.1 Determination of the ALD window

The influence of the deposition temperature on the film thickness has been investigated in order to determine the ALD window of the process. Figure 2.7.a

shows the variation of the thickness determined by XRR for films deposited at temperatures from $T_{dep} = 80^\circ\text{C}$ to 180°C on Si/SiO_x substrates for 500 ALD cycles. For the TDMASn/H₂O process, the thickness varies steadily from 45 nm at 80°C down to 12 nm at 180°C . For the TDMASn/H₂O₂ process, the thickness also decreases from 93 nm at 80°C down to 65 nm at 180°C . In both cases, there is no temperature range in which the thickness is independent of the deposition temperature, which is in accordance with the literature (Mullings et al. (2013) for H₂O, Elam et al. (2008) for H₂O₂). The authors ascribe this temperature dependence of the thickness to a decreasing amount of surface hydroxyl groups when increasing the temperature. Note that Choi et al. (2014) report on an ALD window between 100°C and 200°C when using TDMASn and H₂O₂, but still no ALD window when using H₂O, in a homemade reactor, without heating the TDMASn precursor.

2.2.3.2 Determination of the growth per cycle and of the nucleation phase

Figure 2.7.b shows the variation of the thickness of the film of the TDMASn/H₂O₂ process function of the number of ALD cycles varied between 60 cycles and 860 cycles for a deposition temperature of 100°C . No nucleation delay are observed on Si/SiO_x substrates within these experimental conditions. The thickness of the film scales linearly with the number of cycles which is characteristic of ALD. The GPC is relatively constant between 1.75 and 1.9 Å/cycle which is slightly higher than what is reported for similar processes (1.4 Å/cycle for Elam et al. (2008), 1.2 Å/cycle for Choi et al. (2014)). The complete study has not been performed on the TDMASn/H₂O process, but its GPC at 100°C can still be measured at 0.9 Å/cycle, for 500 cycles. It is almost twice as low as the GPC of the TDMASn/H₂O₂ process for the same thickness. This observation is also reported in the literature and ascribed to the higher reactivity of H₂O₂ compared to H₂O. Those are well in line with the QCM observations, *i.e.* the higher number of released ligands during the TDMASn pulse for H₂O₂ (section 2.2.2.3). As Elam et al. (2008) suggest, the lower amount of ligands released with H₂O results in a larger steric hindrance of the remaining DMA ligands. It limits the adsorption of TDMASn, which in turn explains the lower GPC.

2.2.3.3 Homogeneity of the deposition

For both processes, the thicknesses of the two samples function of the deposition temperature are compared in Figure 2.7.c,d. for 500 ALD cycles (see Figure 1.16 for the position of the samples). The homogeneity for the TDMASn/H₂O process is satisfactory across the scanned range of temperature. For TDMASn/H₂O₂, the homogeneity is also good, but degrades at higher temperatures.

2.2.4 Properties of the as-deposited ALD-SnO₂ thin films

The composition of a thick film of SnO₂ (TDMASn/H₂O₂ – 165 nm) has been analyzed by XPS in order to determine the composition of the film. The survey spectrum (Figure 2.8.a) evidences the contributions of O 1s, C 1s, Sn 3d and N 1s core levels. As previously, O is mainly attributed to the oxide phase formation,

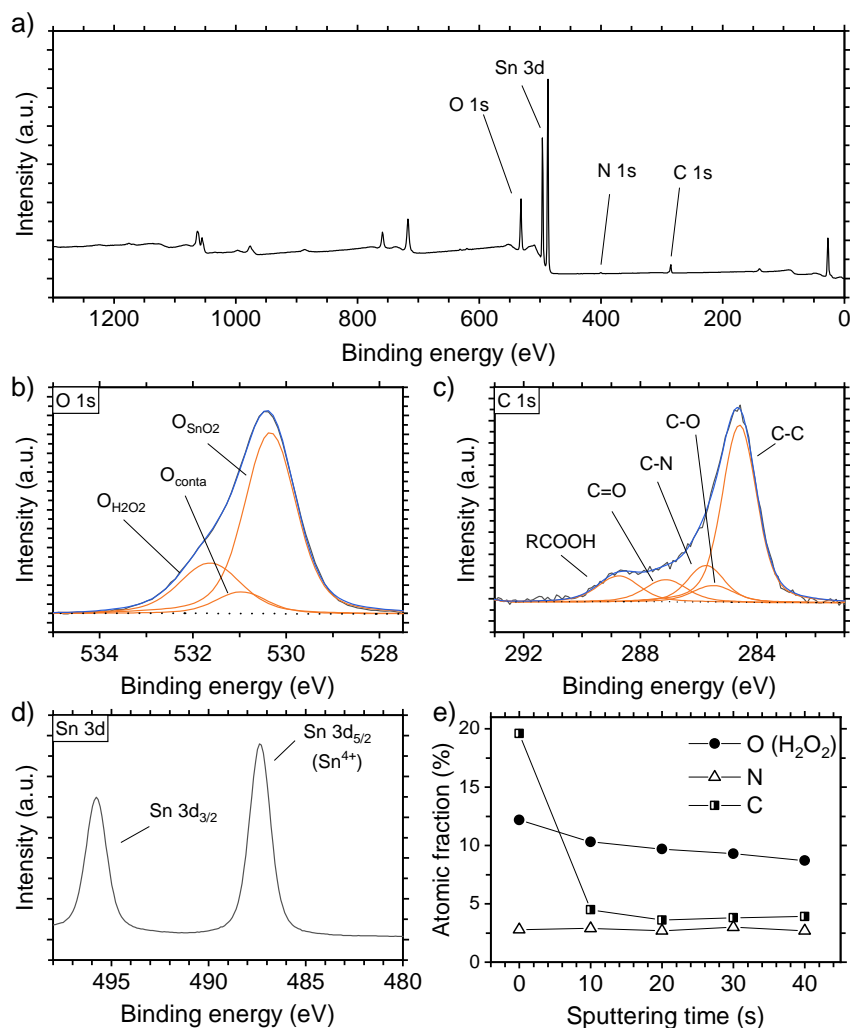


Figure 2.8: a) XPS survey spectra of films deposited with the TDMASn/H₂O₂ process. High resolution core level spectra of b) O 1s, c) C 1s and d) Sn 3d for the TDMASn/H₂O₂ process. e) Atomic concentration of N, C and O associated to the precursor contamination, as function of the sputtering time by Ar⁺.

C to surface contamination and the presence of N argues for DMA fragments remaining at the surface film. These points will be specified when considering the high energy resolution spectra of O 1s, C 1s, Sn 3d (Figure 2.8.b-d.). The Sn 3d_{5/2} contribution is centered around 486.7 eV characteristic of Sn in the oxidation state IV (Kwoka et al. (2005)). No evident contribution of Sn(II) (486.0 eV) or metallic Sn (485.2 eV) could be observed. The high energy resolution core level spectrum of O 1s requires three contributions for its reconstruction. The one centered around

530.3 eV is ascribed to SnO₂ and the one at 531.0 eV to the surface contamination. Considering the atomic balance between the O and C contributions ascribed to superficial contamination, an additional contribution at 531.6 eV is needed. This last contribution has been reported for CVD and hydrothermal synthesis of SnO₂, and was ascribed to adsorbed O₂ or to –OH groups (Kwoka et al. (2005); Jinghui Wang et al. (2017)). In this work, it can also be due to the presence of unreacted –OH fragments in the film. To investigate further the contamination of the film by the ALD precursors, in-depth determination of the composition of the film is performed with Ar⁺ bombardment at 500 eV (Figure 2.8.e). The atomic fractions of nitrogen, carbon and oxygen (related to the high energy contribution) remain at a similar level all along the profile (around 4% for C, 3% for N and 10% for O), with a specific fingerprint, indicating that these species are consistently present throughout the probed thickness. This agrees well with previous reports of ALD-SnO₂ deposited at low temperature in which the presence of unreacted precursors was evidenced (Elam et al. (2008)). The XPS analysis allows for the determination of the stoichiometry of the film given as SnO_{2.04}, which is in line with the intended SnO₂ stoichiometry.

The influence of the deposition temperature and of the number of ALD cycles on the properties of the films using both processes have been investigated. The standard deposition conditions are the following: ALD sequence [1/0.1/0.5/0.5]/3//0.3/3 for TDMASn/H₂O and [1/0.1/0.5/0.5]/3//1/3 for TDMASn/H₂O₂, $T_{dep} = 100\text{ }^{\circ}\text{C}$, $n = 500$ cycles, $T_{source} = 60\text{ }^{\circ}\text{C}$. The process parameters are varied alternatively in the range $80\text{ }^{\circ}\text{C} - 220\text{ }^{\circ}\text{C}$ for the deposition temperatures (both processes) and $60 - 860$ for the number of cycles (TDMASn/H₂O₂). By contrast to what has been observed with TiO₂ – where both processes yield similar materials – the final material depends highly on the O precursor used: if H₂O is used, the final film has properties between SnO and SnO₂ (thereafter called SnO_x); if H₂O₂ is used, the final film has properties close to SnO₂.

2.2.4.1 Properties of ALD-SnO_x (TDMASn/H₂O process)

The properties of as-deposited thin films deposited with TDMASn and H₂O function of the deposition temperature are gathered in Figure 2.9. For temperatures below $180\text{ }^{\circ}\text{C}$, the thin film is amorphous or highly disordered as stressed by the very broad and weak peak around 30° . When the temperature is further increased, diffraction patterns appear ascribed to the SnO romarchite phase (JCPDS 06-0395) at $2\theta = 18.3^{\circ}$ (001), 30.0° (101), 33.5° (110) and 37.5° (002). When deposited on borosilicate glass, the films exhibit an increasing transmission in the visible range as the deposition temperature increases. This is ascribed to the decrease of the thickness of the film for a given number of ALD cycle with increasing deposition temperature, as stressed in section 2.2.3.1. The band gaps extracted from the transmission and reflection data decrease from 3.8 eV to 3.2 eV for the direct optical transitions, and from 2.8 eV to 2.4 eV for the indirect optical transitions. These values and trends are in line with what is reported by Mullings et al. (2013) which speculate that quantum confinement effects causes these variations of the band gap. Finally, Hall effect measurements indicate that the majority carriers in the material are the holes, hence that the material is p-type ($p_0 \sim 1 \times 10^{13}\text{ cm}^{-3}$).

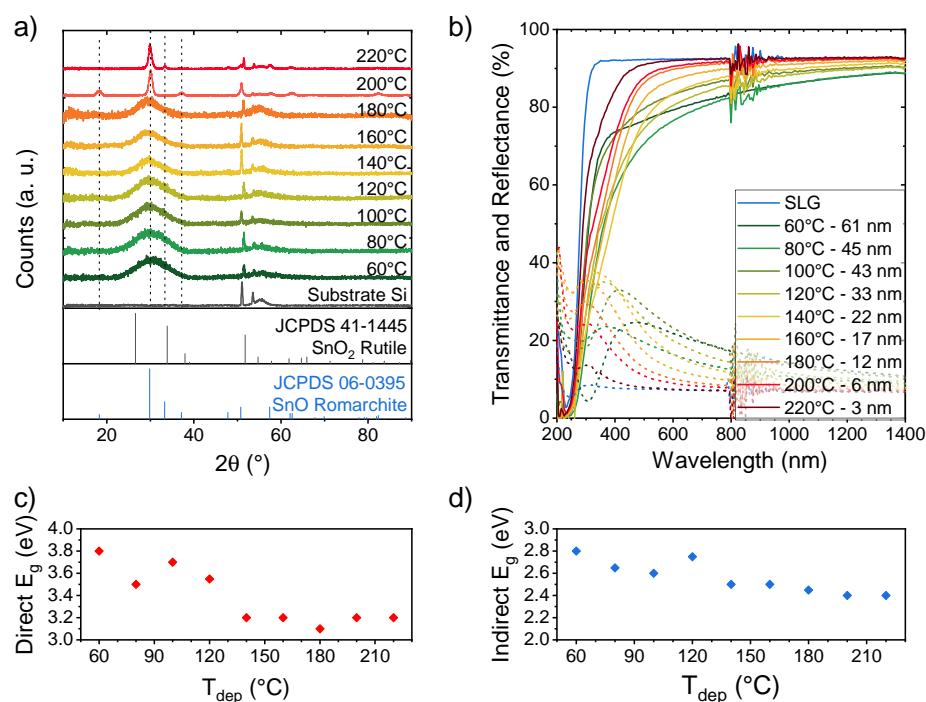


Figure 2.9: Characterization of the as-deposited ALD-SnO_x material for TDMASn/H₂O process as function of the deposition temperature. a) GIXRD diffractograms of the SnO_x on a Si substrate. b) Transmission and reflection spectra. c) Direct and d) indirect optical band gaps.

2.2.4.2 Properties of ALD-SnO₂ thin films (TDMASn/H₂O₂)

The properties of as-deposited films deposited with TDMASn and H₂O₂ function of the deposition temperature and of the number of ALD cycles are gathered in Figure 2.10. For deposition temperatures below 180 °C, the film is amorphous or highly disordered as stressed by the very broad and weak peak around 32.6°. At 180 °C, the film crystallizes with diffraction peaks appearing at $2\theta = 26.6^\circ$ (110 plane), 34.2° (101), 38.6° (200) and 52.4° (211), characteristic of the SnO₂ rutile phase (JCPDS 41-1445). The optical band gap varies with the temperature: the direct band gap decreases from 4.5 eV (at 80 °C) to 4.1 eV (at 140 °C) and increases at higher temperatures, while the indirect band gap decreases from 3.3 eV (at 80 °C) to 2.9 eV (at 140 °C) and increases at higher temperatures. These band gaps are higher than those observed in the film deposited with H₂O, which further hints towards a stoichiometry closer to SnO₂. The gap values are higher than what is usually reported for SnO₂, but similar high values of ALD-SnO₂ have been reported by Choi et al. (2014). The films show a good transparency in the visible and near infrared range (> 75% for thicknesses > 60 nm). Finally, Hall effect measurements indicate that the majority carriers in the material are the electrons, hence that the material is n-type. For thin films grown at 100 °C, the carrier density increases with the film thickness from $n_0 \sim 1 \times 10^{16} \text{ cm}^{-3}$ at 20 nm up to $n_0 \sim 1 \times 10^{18} \text{ cm}^{-3}$ for

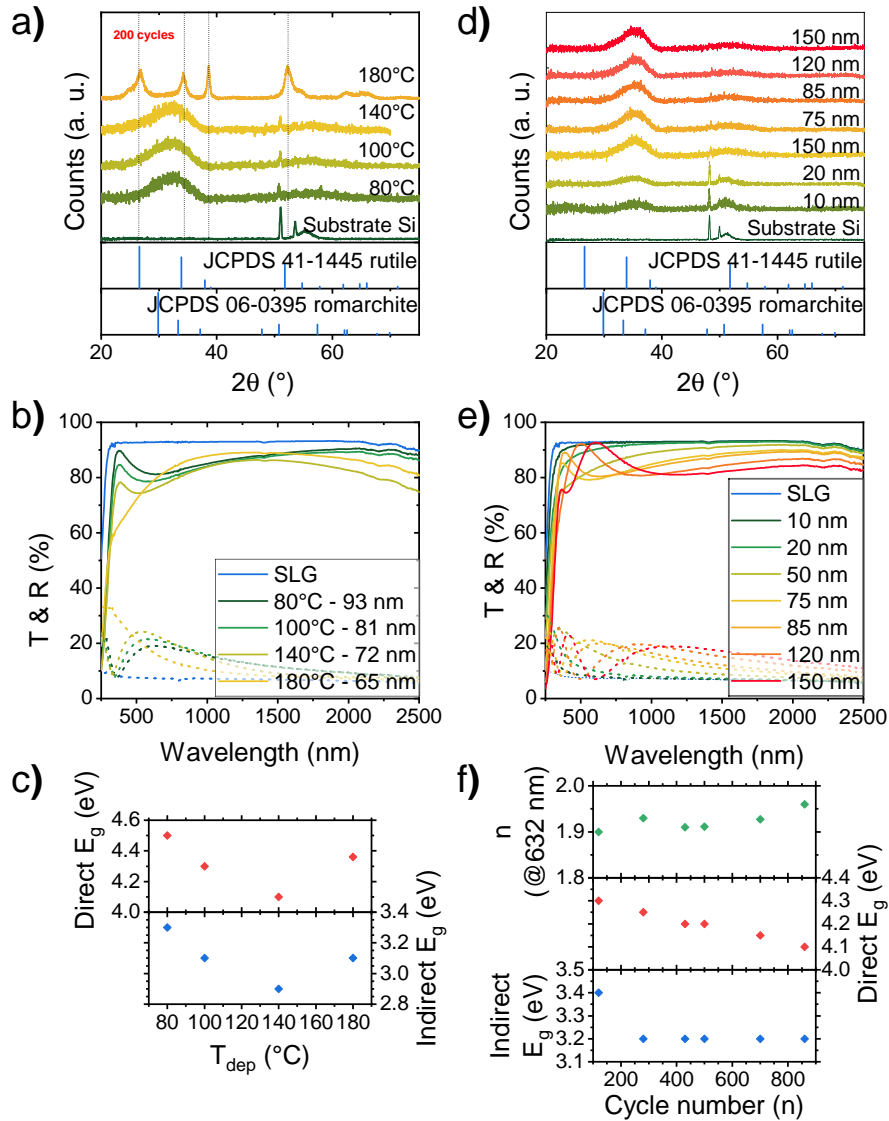


Figure 2.10: Characterization of the as-deposited ALD-SnO₂ material for TDMASn/H₂O₂ process as function of a)-c) the deposition temperature and d)-e) the cycle number. a,d) GIXRD diffractograms of the SnO₂ on a Si substrate. b,e) Transmission and reflection spectra. c,f) Optical band gaps and refractive index at 632 nm.

thicknesses above 80 nm in line with the literature (Choi et al. (2014)).

The structural properties of the film do not vary with the number of ALD cycles and the film remains amorphous. The optical band gaps decrease steadily with the thickness of the film as reported by Mullings et al. (2013), although on a smaller range (0.4 eV vs. 1.0 eV). The refractive index at 632 nm does not vary

much with the number of cycles and is measured between 1.9 and 2.0, which agrees well with values reported for SnO₂ (Elam et al. (2008); Mullings et al. (2013)). Finally, the films show a very good transparency (> 85% in the visible and near infrared range for thickness >20 nm).

2.2.5 Conclusion on the deposition of ALD-SnO₂

Two processes have been developed and characterized in order to synthesize SnO₂ thin films. Using TDMASn as Sn precursor, the deposition can occur at relatively low temperatures (100 °C) using H₂O or H₂O₂ as O precursor. In agreement with processes reported in the literature, no clear ALD window could be determined with either of the O precursors. However, the QCM analysis demonstrates that for the chosen process parameters (ALD sequence, T_{dep} = 100 °C), the saturation of the surface is achieved at each step of the ALD cycle. As expected from the higher reactivity of H₂O₂ and from the higher number of DMA ligands released during the TDMASn pulse, the GPC of the H₂O₂ is almost twice as high as the one observed with H₂O (1.75 Å/cycle vs. 0.9 Å/cycle at 100 °C), which is a bit higher than what is reported in the literature.

The study of the properties of the as-deposited films reveals that the choice of the precursor affects greatly the nature of the film. When grown with H₂O, the film is p-doped, with a narrower optical band gap, and starts crystallizing into the romarchite phase. These characteristics are not suitable for the application in perovskite solar cells as intended in this work. On the contrary, thin films grown with H₂O₂ are n-type materials which have a larger band gap (E_g^{dir} = 4.1-4.5 eV, E_g^{indir} = 2.9-3.3 eV) and a refractive index (n = 1.9) matching those of SnO₂. When deposited at higher temperatures (> 180 °C for 500 ALD-cycles), it starts to crystallize into the rutile phase. XPS analysis confirm that Sn is in its +IV oxidation state, with a stoichiometry close to SnO₂. Contamination from the ALD-precursors in the bulk of the film is evidenced (which has already been reported for low-temperature ALD of SnO₂).

2.3 Photoluminescence imaging

2.3.1 Motivations

Optical spectroscopy techniques based on the study of a luminescence signal are widely used to probe a variety of properties of semiconducting materials, not only in material science, but also in other fields such as biology (Monteiro (2020)). The specimen can either be pumped with an electric bias (electroluminescence Jahn et al. (2018)), a light bias (photoluminescence Kirchartz et al. (2020)) or both. For photovoltaic devices, photoluminescence (PL) is a useful technique to probe the recombination and transport properties of carriers in a non-destructive manner and is used as a quality check in the silicon PV industry (Trupke et al. (2012)). In perovskite solar cells, PL has been used in a large variety of conditions, including temperature- (Wright et al. (2016)), fluence- (Caprioglio et al. (2019)), voltage- (Dreessen et al. (2020)) or composition-dependent studies (Slotcavage et al. (2016)).

The measurements can be spectrally, temporally or spatially resolved, and can be applied at the microscopic or macroscopic scale. It also allows for *in-situ* or *ex-situ* measurements. Temperature-dependent measurements have been used to follow the phase transition of the perovskite or identify the position of defect states within its gap (Gerhard et al. (2019)). Voltage-dependent studies of full devices or of specific architectures give indications on the complex interactions between the absorber and the extraction layers (Stolterfoht et al. (2019)) as well as observations of ions migration (Bercegol et al. (2020)). Varying the fluence allows for the evaluation of the efficiency potential of a device without being limited by transport resistances (Caprioglio et al. (2019); Stolterfoht et al. (2020)). PL measurements provide a direct observation of the phase stability and of the composition heterogeneities of the perovskite film when varying the film composition (Bercegol, Ramos, Rebai, Guillemot, Puel, et al. (2018)). Recent reviews and papers describe the progresses made in the understanding of steady-state and transient photoluminescence studies, which the reader can refer to (Kirchartz et al. (2020); Krückemeier et al. (2021)).

Combined spectrally-resolved and time-resolved PL measurements have been a formidable tool to unravel and study new transport mechanisms such as photon recycling (Pazos-Outon et al. (2016)) or photon-assisted transport (Bercegol et al. (2019)). Steady state photoluminescence has been performed on a large variety of samples and architectures. In architectures combining charge transport layers and an absorber, SSPL is often used to assess the quality of extraction layers. The results must however be carefully examined in order to distinguish competitive phenomena such as extraction and non-radiative recombination. Contradictory results can be found in the literature on such interpretations. On the one hand, the quench of the PL signal of an absorber deposited on top of an extracting layer is often related to an enhanced charge separation and a better extraction of the carrier of interest (*e.g.* electrons for an ETL) (Azmi, Hadmojo, et al. (2018)), close to the PL observations made in DSSCs (Snaith et al. (2009)). But contrary to DSSCs, carriers can diffuse in the perovskite absorber, which strongly influences the rates and lifetimes that can be measured with PL techniques. Thorough PL studies on various architectures (absorber, absorber/ETL, HTL/absorber/ETL) suggest on the contrary that – for half cells in open circuit condition – the aim should be to limit the PL signal drop observed between a simple absorber and an absorber on a charge transport layer, which reveals an increase of non-radiative recombinations (Wolff et al. (2019)). In the latter studies, the contribution of each additional layer to the variation of the PL intensity (and consequently of the QFLS) is described which constitutes a solid justification of the latter interpretation of the SSPL signal on complex architectures.

Hyperspectral imaging of a PL signal refers to the acquisition of a PL spectrum for each pixel of an image. Contrary to other techniques such as confocal mapping where the spectra are taken one at a time at various locations of the specimen, the hyperspectral imager combines two dimensions in one snapshot. For instance, snapshots of the entire region of interest are taken at different wavelengths. With the superposition of these snapshots, the spectra can be reconstructed at each spatial location. This technique benefits among other things from a faster acquisition time and a larger region of interest. Hyperspectral imaging systems are still not

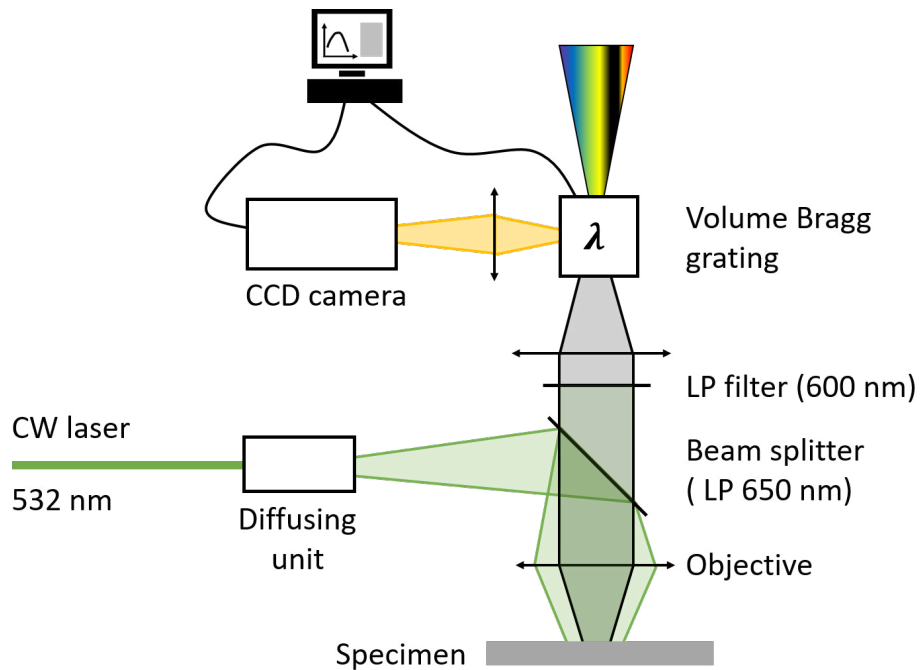


Figure 2.11: Schematic of the hyperspectral imager setup in wide-field illumination. The volume Bragg grating selects a narrow spectral range of the image (orange in the scheme). The computer controls the volume Bragg grating and monitors the acquisition of the data by the CCD camera. LP stands for long pass. Adapted from Bercegol (2020).

very common in the photovoltaic field but have proved useful to observe spatial variations of intrinsic properties of PV materials (El-Hajje et al. (2016); Bercegol et al. (2019); Cacovich et al. (2020); Ory et al. (2020)). Combined with a local illumination, it allows to discuss diffusion properties of the carriers in absorbers. In a wide-field illumination configuration, artifacts due to lateral diffusion of carriers can be prevented.

2.3.2 Absolute SSPL on a hyperspectral imager: experimental setup and calibration procedure

Steady state photoluminescence spectra are acquired on a home-made setup based on a commercial laser excitation, a volume Bragg grating and a CCD camera. The hyperspectral imager is able to output a 3D data set containing the PL spectrum at each point of a 2D image. The following section aims at describing the components of the experimental setup and the calibration procedure to obtain the PL spectra in absolute units ($\text{ph s}^{-1} \text{m}^{-2} \text{nm}^{-1} \text{sr}^{-1}$). Finally, the fitting procedure with the generalized Planck law is presented.

2.3.2.1 Description of the experimental set-up

The experimental setup used to acquire steady state photoluminescence is schematically represented in Figure 2.11. It is composed of two main optical branches: the illumination branch and the collection branch. The illumination branch is composed of a coherent light source (continuous wave laser Coherent Genesis CX STM at 532 nm), guided to the illumination optics by a multimodal optical fiber. The excitation laser is spread using a diffusion filter to obtain a homogeneous wide field-illumination focused on the specimen. The absorption of the radiation causes the emission of a photoluminescence signal from the sample into the collection branch. A fraction of the excitation signal is also reflected at the air/specimen interface back into the collection branch. It is filtered out by a long-pass dichroic mirror (cut-off wavelength 650 nm) and a second long pass filter (cut-off wavelength 600 nm), so that only the luminescence signal is analyzed. A volume Bragg grating developed by Photon Etc. allows for the spectral decomposition of the photoluminescence signal focused on the CCD camera. The grating has a 2 nm spectral resolution. Exposing the camera to the photoluminescence for an exposure time t_{exp} for each position of the grating (hence for each selected wavelength $\lambda_1 \dots \lambda_n$) yields a 3D data set $I_{raw}(x, y, \lambda)$. The spectral decomposition of the volume Bragg grating causes a combination of the spectral and of one of the spatial components, which has to be rectified in order to get a 3D $I_{rect}(x, y, \lambda)$ data set (or "cube") with physical meaning. This rectification is performed by the acquisition software. In summary, a spectrally-resolved image is acquired with a minimal spectral resolution of 2 nm and a typical spatial resolution of 1 μm (determined by the numerical aperture of the objective), in a time span of approximately $n t_{exp}$.

2.3.2.2 Absolute calibration of the data

After the acquisition, the 3D data gives a number of counts, per pixel area, per wavelength band-width of the grating $\delta\lambda$. A series of calibrations are required in order to extract PL photon flux spectra in absolute units (in $\text{ph m}^{-2} \text{s}^{-1} \text{nm}^{-1} \text{sr}^{-1}$). The thorough calibration procedure is devised in A. Delamarre's thesis (Delamarre (2013)) and its main steps are described in the following.

Dark image subtraction. For every considered data set, two cubes are acquired: a first one in the illuminated condition (I) and a second one in "dark" condition (I_d) with similar experimental parameters (especially same t_{exp}). In the dark condition, the excitation radiation is cut just before entering the objective, hence no direct illumination enters the collection branch. The aim of this acquisition is to record the parasitic signal due to the camera read noise, to its dark current noise and to an eventual parasitic illumination in the collection branch. The dark signal is subtracted from I , and the corrected signal is converted in counts per second $(I - I_d)/t_{exp}$. In the following sections, this corrected quantity is directly considered.

Correction of the transmission. The collection branch of the setup is composed of various optical components which may filter the radiation passing through. The spectral sensibility of the CCD detector also varies with the wavelength. In

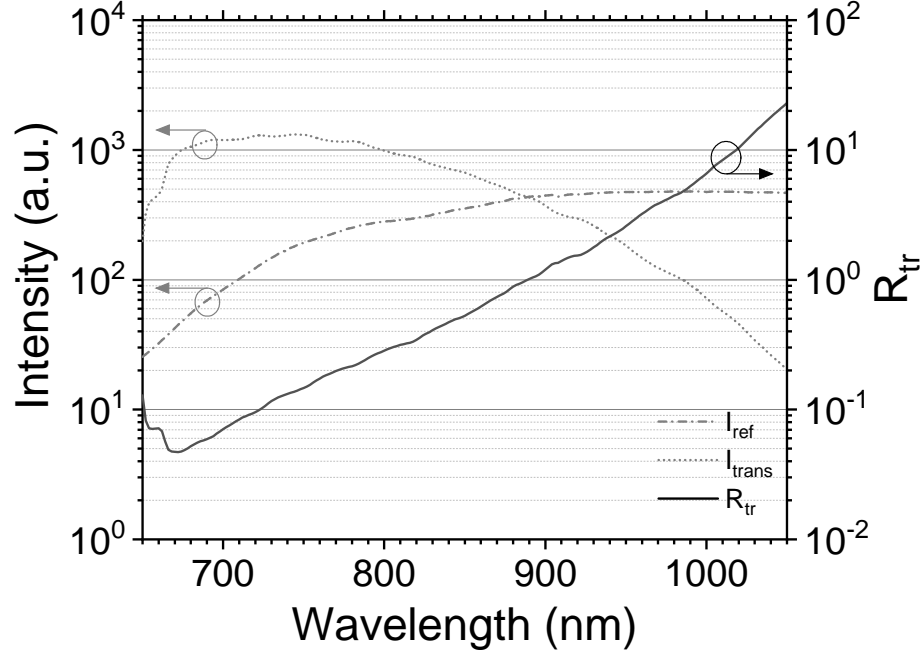


Figure 2.12: Transmission of the collection branch. The reference calibrated lamp spectrum (dotted-dashed line), the image collected by the CCD camera (dotted line) and the factor R_{trans} (full line) are presented. I_{trans} is averaged over the whole captor and its dark signal is subtracted.

order to reconstruct the initial spectrum which enters the collection branch, a transmission calibration is performed. A cube of a homogeneous light source of known spectrum (Spectral Products) is acquired (I_{ref}). The light is guided into an integrating sphere with a small aperture which is imaged by the hyperspectral setup. The emission is lambertian and spatially homogeneous. The comparison between the acquired spectrum I_{trans} and the reference spectrum allows for the determination of the correcting ratio R_{trans} defined for each wavelength as:

$$I_{ref}(x, y, \lambda) = R_{tr}(x, y, \lambda) \cdot I_{trans}(x, y, \lambda) \quad (2.4)$$

A typical spectrum of R_{trans} is presented in Figure 2.12 for the usual band width analyzed for perovskite solar cells.

Conversion to photon flux. In order to relate the counts per second on the CCD detector with the emitted photon flux, a laser of known power P_{las} is imaged in a narrow bandwidth $\lambda_0 - \Delta\lambda \dots \lambda_0 + \Delta\lambda$ around its emission wavelength (cube I_{las}). The laser is coupled in an optical fiber. The complete collection of the signal is ensured by selecting a fiber with a smaller numerical aperture (NA) than the objective and by focusing in a way that the whole fiber output is imaged. The number of emitted photons and the number of counts on the camera are linked by

the following relation:

$$R_{ctp} = \frac{n_{photons}}{n_{counts}} = \frac{n_{photons}}{\int_{\lambda} \iint_{x,y} R_{tr} I_{las} d\lambda dx dy} \quad (2.5)$$

Spatial calibration. The CCD camera integrates the PL signal over the area of each pixel. In order to convert the cube into a flux per surface unit, the size of a pixel has to be estimated. It varies depending on the objective used for the acquisition. The size of a pixel S_{px} is determined by imaging the 1951 USAF resolution target. The output cube is divided by S_{px} to be expressed in m^{-2} .

Solid angle normalization. A Lambertian emission of the photoluminescence of the sample is assumed. Only a fraction of it is collected by the objective, depending on its numerical aperture NA . The collection solid angle is given by $\Omega_{coll} = \pi NA^2$. The output cube is divided by Ω_{coll} to be expressed in sr^{-1} .

Final form of the calibrated data By combining the different steps mentioned above, the PL cube can be converted to absolute physical units as follows:

$$I_{abs}(x, y, \lambda) = \frac{I_{rect}(x, y, \lambda) - I_{rect,d}(x, y, \lambda)}{t_{exp}} \cdot R_{tr}(x, y, \lambda) \cdot R_{ctn} \cdot \frac{1}{\delta\lambda} \cdot \frac{1}{S_{px}} \cdot \frac{1}{\Omega_{coll}} \quad (2.6)$$

The quantity I_{abs} is expressed in $ph\ s^{-1}\ m^{-2}\ nm^{-1}\ sr^{-1}$ or alternatively in $ph\ s^{-1}\ m^{-2}\ eV^{-1}\ sr^{-1}$ (multiplying Equation (2.6) by hc/qE^2) and can be fitted with the generalized Planck law (Equation (2.7)) to extract local optoelectronic parameters of the absorber.

2.3.2.3 Absorption model

As presented in section 1.1.3.1, the photoluminescence spectrum of a semiconductor can be modelled by the generalized Planck law:

$$\Phi_{em}(E, T, \Delta\mu) = \frac{2}{h^3 c^2} \frac{E^2 a(E)}{\exp\left(\frac{E - \Delta\mu}{k_B T} - 1\right)} \quad (2.7)$$

In order to correctly fit PL data, a model must be decided for the absorptivity of the absorber. Not taking into account the multiple reflections at the front and back interfaces of the absorber, the absorptivity can be expressed as

$$a(E) = 1 - \exp[(f_V - f_C)\alpha(E)d] \quad (2.8)$$

where f_V and f_C are the occupation factors of the valence band and of the conduction band respectively, which depend on $\Delta\mu$; α is the absorption coefficient and d is the thickness of the sample. This is true under the assumption that the QFLS is constant across the absorber (which is made in the rest of the dissertation). The variation of QFLS could be taken into account by considering successive slabs of material characterized by a constant QFLS, which considerably complicates the fitting procedure. Now, the model comes down to using a proper model for the

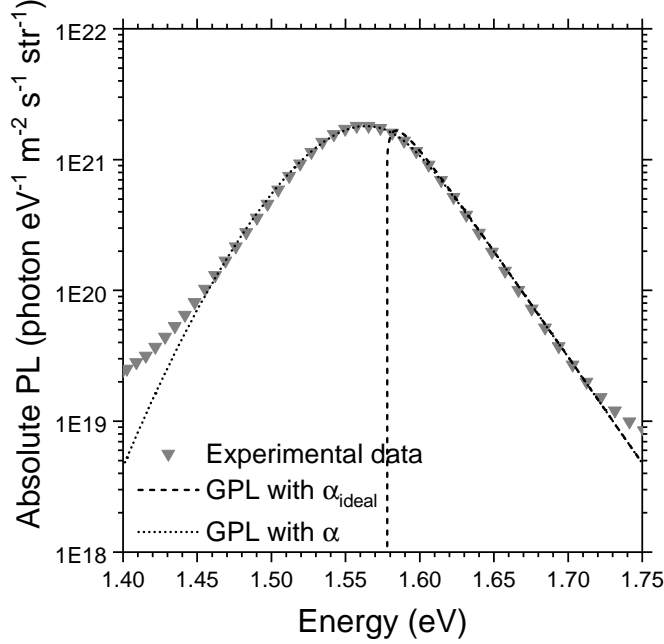


Figure 2.13: Influence of the shape of the absorption coefficient on the PL emission. Experimental data of perovskite deposited on a TiO_2 bilayer is fitted with the generalized Planck law (GPL), with either an absorption spectrum derived from the quadratic DOS model (dashed line) or from the general absorption model derived by Katahara and Hillhouse (2014) (dotted line). The fit parameters are $E_g = 1.583$ eV, $\Delta\mu = 1.226$ eV, $\alpha_0 d = 14$, $\gamma = 36$ meV, $\theta = 1.50$, $T = 300$ K.

absorption coefficient. The simplest form of α can be derived assuming a quadratic DOS near the edge of the conduction and of the valence band which leads to a square-root dependence of the absorption on the photon energy $\alpha_{id}(E) = \alpha_0 \sqrt{E - E_g}$. Figure 2.13 shows a simulated PL spectrum with this absorption coefficient along with a typical PL spectrum measured on a perovskite absorber. It is quite clear that the quadratic DOS is too naive a model to fit the real PL spectrum, as it cannot account for the PL emission at low energies. Other absorption models have been developed to take into account more contributions in the absorption, especially sub band gap states (Urbach tail model – Urbach (1953), Thomas-Fermi approach – Kane (1963), inclusion of the Franz-Keldysh effect – Fox (2001)). Katahara and Hillhouse (2014) derived a general form for the absorption coefficient which encompasses all of the previous cases. It consists in the convolution of the ideal absorption presented earlier (α_{id}) and a contribution of a given distribution of sub-band gap states:

$$\alpha(E) = \alpha_0 \frac{1}{\gamma 2\Gamma(1 + \frac{1}{\theta})} \int_{-\infty}^{+\infty} \exp\left(-\left|\frac{u}{\gamma}\right|^\theta\right) \sqrt{E - E_1 - u} du \quad (2.9)$$

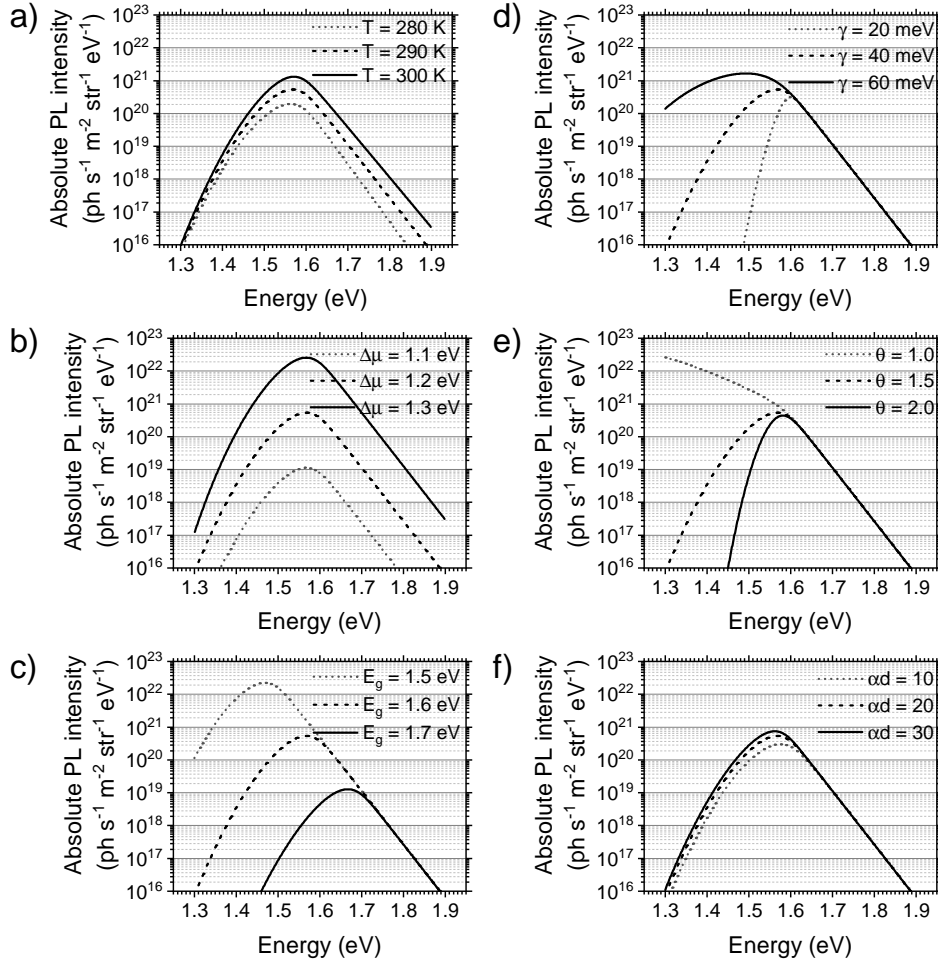


Figure 2.14: Influence of the fitting parameters a) T , b) $\Delta\mu$, c) E_g , d) γ , e) θ and f) $\alpha_0 d$ on the PL spectrum. The standard parameters are $E_g = 1.6$ eV, $\Delta\mu = 1.2$ eV, $\alpha_0 d = 20$, $\gamma = 40$ meV, $\theta = 1.50$, $T = 300$ K.

where Γ is the Euler gamma function, γ is an energy broadening parameter, θ describes the decay of the tail states and E_1 is a characteristic energy. In the case of the Urbach tail model, $\gamma = E_U$, $\theta = 1$ and $E_1 = E_g$. As shown in [Figure 2.13](#), using this kind of model allows for a better fit of the PL signal.

Considering the absorption model presented in [Equation \(2.9\)](#), PL signals can be fitted using six parameters: the temperature T , the QFLS $\Delta\mu$, the dimensionless product $\alpha_0 d$ and the three parameters γ , θ and E_g . To get an insight of the influence of each parameter on the spectral shape of the PL emission, PL spectra have been simulated varying the parameters one at a time over a representative

range. Figure 2.14.a shows the influence of the temperature. The simulation is performed under low injection so that $E_g - \Delta\mu > 6k_B T$ hence f_V and f_C are constant. In this case, the temperature only affects the slope of the high-energy part of the spectrum, according to the expression of the PL in the Boltzmann approximation (Equation (1.10)). The variation of $\Delta\mu$ essentially increases the intensity without modifying the spectral shape (Figure 2.14.b). It gives incidentally an easy method to estimate the variation of QFLS of a sample under various light intensities, since the ratio of the integrated PL signals scales as $\exp(\Delta(\Delta\mu)/k_B T)$, which can be calculated even for non calibrated data. The PL signal at lower energy is mainly dominated by the absorption properties of the absorber; hence the four remaining parameters describing the absorption of the material drive the shape of the low energy part (Figure 2.14.c-f). Varying the band gap mostly affects the position of the maximum PL peak: the lower the band gap, the more the maximum is red-shifted. It concurrently increases the maximum PL because the ratio $\Delta\mu/E_g$ increases. Similarly to the Urbach energy in the Urbach tail model, the parameter γ indicates the quality of the material in term of sub-band gap states. For a given θ , a lower γ value translates in sharper absorption onset. The influence of $\alpha_0 d$ and θ are less easy to interpret and are further discussed in the paper of Katahara and Willhouse (Katahara and Hillhouse (2014)).

This model is implemented in a numerical model which estimates the material properties by fitting the experimental data.

2.4 Conclusion

In this chapter, the development of two materials by ALD has been presented. Two processes have been examined for TiO_2 and for SnO_x , with various combinations A/B of molecular precursors (A = TTIP, TDMASn; B = H_2O , H_2O_2). The ALD processes have been characterized with QCM measurements and XRR. Only the TTIP/ H_2O had a clear ALD window extending from 100 °C to 210 °C with a GPC of 0.35 Å/cycle. The other three processes have a temperature-dependent GPC, similar to what has already been reported in the literature. For the chosen deposition temperatures, the GPC were determined at 0.7 Å/cycle (TTIP/ H_2O_2 , 100 °C), 0.9 Å/cycle (TDMASn/ H_2O , 100 °C) and 1.75-1.9 Å/cycle (TDMASn/ H_2O_2 , 100 °C).

The material properties of the ALD- TiO_2 thin films are relatively insensitive to the oxygen source. The stoichiometries of the film determined by XPS agreed with the target TiO_2 composition. The films are amorphous with a high indirect band gap (3.4 - 3.6 eV), a high refractive index around 2.4 at 632 nm, a good transmission in the visible range and a high resistivity. For large numbers of cycles in the TTIP/ H_2O process, the films started to crystallize into the anatase phase. Conversely the material properties of ALD- SnO_x thin films varied a lot depending on the choice of the O source. With H_2O , the film is amorphous and crystallizes in the SnO romarchite phase at high deposition temperatures (> 200 °C). Optoelectrical characterizations revealed that the thin films have a relatively low band gap (2.6 eV), a medium transmission in the visible range and are weakly p-doped ($1 \times 10^{13} \text{ cm}^{-3}$). The characterization of thin films grown from TDMASn/ H_2O_2 indicated that the

film were amorphous at low deposition temperatures but crystallize into the SnO₂ rutile phase at higher deposition temperatures (> 180 °C). The films have a large optical band gap (indirect: 3 eV; direct: 4.2 eV), an excellent transmission in the visible and near-IR region, a relatively high refractive index of 1.9 at 632 nm, but are moderately n-doped for low thicknesses ($n_0 \sim 1 \times 10^{16} \text{ cm}^{-3}$). XPS analysis of the TDMA_{Sn}/H₂O₂ thin films showed an in-depth contamination of the ALD precursors (spurs of N, C and O), but the overall stoichiometry of the film matched that of SnO₂. In summary, three processes were found suitable to be applied in perovskite solar cells (TTIP/H₂O - 200 °C, TTIP/H₂O₂ - 100 °C and TDMA_{Sn}/H₂O₂ 100 °C) and are further discussed in [Chapters 3](#) and [4](#).

This chapter also discussed the characterization of the absorber's steady-state photoluminescence by hyperspectral imaging. The use of this technique for solar cells is quite original and was developed at IPVF during a previous thesis. It allows for the determination of optoelectrical properties of the absorber ($\Delta\mu$, T , E_g , absorption properties) with a spatial resolution down to 1 μm and a spectral resolution of 2 nm with the benefit of short acquisition times compared to confocal mapping. The absorption model used to fit the generalized Planck law has also been presented and shown to be able to describe a large variety of PL profiles. Coupled with the expressions derived in [chapter 1.1](#), it allows to characterize the quality of the absorber compared to its radiative limit.

Chapter 3

Optimization and integration of ALD-TiO₂ in perovskite solar cells

3.1 Motivations

3.1.1 Previous uses of TiO₂ in perovskite solar cells

As mentioned in [section 2.1.1](#), titanium dioxide is an n-type, wide band gap semiconductor with a high refractive index. Among others, TiO₂ has been widely used in various PV technologies. Owing to its suitable optical properties (good transmission and high refractive index) and to its low fabrication cost, it has been applied as anti reflective coating in Si solar cells (X. Sun et al. (2019)) and in III-V solar cells (Saint-André et al. (2021)). ALD-TiO₂ has also been reported as passivation layer and electron selective contact at the back surface of n-type Si solar cells where efficiencies higher than 21% have been achieved (X. Yang et al. (2016)). Attempts to use TiO₂ as selective contacts in CIGS technologies as a replacement to the i-ZnO layer have also been reported (Löckinger et al. (2018)).

3.1.1.1 From the DSSCs to the PSCs

The most common application of TiO₂ in solar cells concerned the fields of organic PV and DSSCs (Bai et al. (2014)). TiO₂ presents several benefits for its integration in DSSCs as electron selective layer and as scaffold for the sensitizer. Thick mesoporous TiO₂ structures are relatively simple to synthesize, and offer a large specific area which increases the light absorption by these cells. The anchoring of the sensitizers is also favored by the large use of carboxylic groups in the dye which readily condensate on the metal oxide surface. Finally, titanium oxide presents a good chemical stability, which is essential for DSSCs because of the use of corrosive liquid electrolyte.

When Kojima et al. (2009) first used a hybrid organic-inorganic halide perovskite

as sensitizer, the substrate was hence naturally TiO_2 . Since then and even after the PSC and DSSC technologies forked, TiO_2 has always been part of the most efficient PSC devices produced at lab scale (M. M. Lee et al. (2012); W. S. Yang et al. (2017); J. Jeong et al. (2021)). The standard architecture used with TiO_2 consists in a bilayer of a dense and compact anatase TiO_2 (acting as hole blocking layer) and a mesoporous anatase TiO_2 layer. Interestingly, the mesoporous layer is essential to ensure good performances of the cells, and only little works report on efficient planar architectures with TiO_2 . This is usually ascribed to the need of a large interface area between the perovskite and TiO_2 to mitigate its poor extraction abilities – even though the matter is still not settled – and to a better control over the crystallization of the perovskite. Incidentally, it has been reported that the use of TiO_2 as ETL in monolithic perovskite on silicon tandem solar cells allows for a low resistance contact between the ETL and the p-type silicon (Shen et al. (2018)).

However, the use of TiO_2 raises several issues. In order to obtain high quality anatase films by the usual deposition process, TiO_2 has to be sintered at high temperatures ($> 450^\circ\text{C}$). Moreover, the need of a mesoporous scaffold complicates the synthesis of complete devices. Finally, the photocatalytic activity of TiO_2 (Sang-Won Lee et al. (2016)) tends to decrease the stability of the perovskite (eventhough this issue can be mitigated to a certain extent by working on the composition of the perovskite ink, J. Jeong et al. (2021)).

3.1.1.2 What about ALD- TiO_2 ?

The use of ALD- TiO_2 as electron transport layer has been explored multiple times in the literature (Raiford et al. (2020)). The process usually involves the use of TDMAT and H_2O as Ti and O sources (Shen et al. (2018)). The use of an ALD process allows for the deposition of TiO_2 in n-i-p configuration but also in p-i-n configuration, thanks to low deposition temperatures (ranging from 60°C to 250°C). However, in the case of p-i-n architectures, a PCBM interlayer is usually used to prevent the degradation of the perovskite layer by the ALD precursors (Lv et al. (2018)). Compact TiO_2 layers of thicknesses between less than 1 nm up to 30 nm have been reported in mesoporous architectures with PCE higher than 18% (Jiahuan Zhang et al. (2018)). When integrated in planar n-i-p structures, ALD- TiO_2 is usually capped by another ETL material (SnO_2 , PCBM ...) to ensure high efficiencies (D. Chen et al. (2019)). Yongzhen Wu et al. (2014) compared the performances of compact TiO_2 deposited by ALD, sol-gel and spray pyrolysis in mesoporous architectures. The highest performances were achieved with ALD and have been ascribed to the better quality of the film (in terms of defects density and coverage). Only few works reported on the use of ALD- TiO_2 based on TTIP/ H_2O precursors, which is developed in this chapter.

3.1.2 Potential benefits of ALD versus spray pyrolysis (SP) deposition of TiO_2 for perovskite solar cells

TiO_2 can be synthesized by various ways. In this section, a presentation of the traditional spray-pyrolysis method is provided, which is then compared with the

deposition by ALD. The limitations of TiO_2 deposited by spray pyrolysis are also discussed.

3.1.2.1 Deposition of TiO_2 by spray pyrolysis

In mesoscopic perovskite PV devices, the compact layer of TiO_2 is often deposited by spray pyrolysis ever since the first working devices were presented by Kojima et al. (2009). The process used in the lab is inspired by the one proposed by Kavan and Grätzel (1995) and adapted from the DSSC technology.

Several substrates are usually placed on a hot plate under ambient atmosphere, occupying an area of approximately 120 cm^2 . A solution of titanium(IV) diisopropoxide bis(acetylacetonate) (TAA, see [section A.1.1](#) for further details) is sprayed and atomized into droplets through a nozzle, using O_2 as carrier gas. The substrates are heated at 450°C . The compact TiO_2 film is formed by the evaporation of the solution droplets and by the pyrolytic reaction of the remaining species at the surface of the substrate, and is stabilized in the anatase phase.

The film thickness depends mostly on the number of passes of the nozzle over the substrate. The deposition parameters for perovskite solar cells have already been optimized for IPVF lab's conditions.

3.1.2.2 Limitations of the SP- TiO_2 and assets of ALD- TiO_2

The use of spray pyrolysis for the synthesis of the TiO_2 compact layer allows for the fabrication of efficient solar cells. Based on observations made at IPVF, limiting factors of this method have been identified in the scope of producing reproducible and efficient cells:

- **Solution preparation.** TAA is a hygroscopic chemical. Hydration of the solution leads to the formation of a film of lesser quality. Hence, this makes the storage and manipulation of the chemical, and the preparation of the solution more demanding, and prone to errors.
- **Homogeneity.** The spray pyrolysis process developed at IPVF has been shown to be homogeneous on the scale of a single substrate (approximately 4 cm^2). It has however been observed that large variations in the thickness of the film can occur over the whole deposited surface (see [chapter 3.3](#)), which can hamper the upscale of the process.
- **Variability of the process.** Spray pyrolysis coating can be done either automatically (the relative motion of the substrate and the nozzle, and the spray parameters are remotely controlled) or manually (an operator uses the nozzle to perform the deposition). In either case, the quality of the film will be largely determined by the size of the droplets and the homogeneity of the sprayed aerosol over the substrate, which is sensitive to the dynamic of the air between the substrate and the nozzle and to the conditions of the surrounding (moisture, temperature, dust ...). In the case of manual spray pyrolysis – as is the case at IPVF – the quality of the film will also depend on the specific gestures used by the operator.

- **High deposition temperature.** The spray pyrolysis process requires high temperatures to yield compact anatase films ($> 450\text{ }^\circ\text{C}$). It limits the choice of substrate (*e.g.* ITO or most flexible substrate cannot withstand these temperatures) which reduces the spectrum of possible applications of PSCs.

Some issues raised about the manual spray pyrolysis process could be solved using an automatic spray-coater. Here, ALD was chosen to synthesize the compact layer of TiO_2 , which comes with additional benefits:

- **Precursors stability.** Once connected to the ALD reactor, the precursors used for the ALD reaction (TTIP, H_2O) can be stored during several weeks without noticing a degradation in the quality of the film.
- **Homogeneity.** An ALD process is governed by self-limiting surface reactions in vapor phase. This characteristic allows for a good homogeneity of the deposited film over the whole substrate (up to 230 cm^2) even for very thin layers (see [chapter 3.3](#)).
- **Reproducibility.** The reproducibility of the deposition is also a consequence of the ALD process. It should in theory only be affected by the quality of the precursors used.
- **Control over the thickness.** Past the nucleation step – which depends on the substrate – the thickness of an ALD layer scales with the number of ALD cycles. This gives a fine control over the thickness of the film.
- **Coverage and density of the film.** The self-limiting reactions in vapor phase of an ALD process also ensure the synthesis of very conformal layers even on substrates with a high aspect ratio (Pore et al. (2011)), and the formation of very dense films. In a mesoscopic architecture, the c- TiO_2 layer aims at preventing a direct contact between the TCO and the absorber. With ALD, this can be achieved even with very thin c- TiO_2 layers, which can potentially limit unnecessary optical and resistive losses in this layer.
- **Low deposition temperatures.** As shown in [chapter 2.1](#), anatase TiO_2 films can be deposited at lower temperatures ($200\text{ }^\circ\text{C}$) without annealing, which opens up to more diverse applications and limits the thermal budget of the process.

However, ALD also comes with limitations and difficulties, among which the substrate-dependent growth of the layer (need for optimization of the process for each substrate), a long development process of new materials (to ensure the ALD regime and characterize the effective growth of the material), the possible contamination of the film by precursor fragments, and the low growth per cycle (which limits the thickness which can reasonably be deposited).

The following section will focus on the development of perovskite solar cells with ALD- TiO_2 , and compare their properties (homogeneity, performances ...) with perovskite solar cells based on spray pyrolysis.

3.2 Influence of post-annealing treatments on ALD-TiO₂ thin films properties

As presented in [chapter 2.1](#), ALD-TiO₂ thin films are deposited at 200 °C. In a mesoscopic architecture, the c-TiO₂ layer is associated with a mesoporous layer of TiO₂ whose synthesis requires an annealing step at temperatures up to 500 °C. The ALD layers will hence be annealed at 500 °C, which can influence their properties.

Hence, the critical properties of the film were investigated after 1 h annealing in air at 300 °C, 400 °C, and 500 °C. The ageing of the ALD-TiO₂ thin films has also been examined by comparing fresh ALD thin films and thin films aged for 4 months in ambient lab atmosphere. No dramatic modifications of their properties have been observed (as described below). The ALD thin films can hence be stored before use, which is compliant with a baseline utilization of the thin films.

3.2.1 Structural changes

3.2.1.1 Determination of the thickness variation of the ALD-TiO₂ thin films

XRR analysis of the different films is applied in order to detect a variation of the thickness, the roughness or the density of the materials. [Table 3.1](#) gathers the results of the fits shown in [Figure 3.1.a](#).

The method is highly sensitive towards the determination of the thickness. The absolute change in the thickness of the annealed samples compared to the fresh references ranges from 0.1 nm (TiO₂-20nm-300°C) to 0.7 nm (TiO₂-20nm-500°C), supported by the increase of the angular period of the Kiessig fringes. [Figure 3.1.b](#) shows the relative difference in thickness of the TiO₂ layer after annealing $\frac{e_{annealed} - e_{fresh}}{e_{fresh}}$ for TiO₂-15nm and TiO₂-20nm. It reveals that in both cases, the thickness of the film decreases as the annealing temperature increases, down to 96% of the initial thickness at 500 °C. Upon annealing, the material can undergo a slight densification which causes this shrinkage. Similar effects of the annealing temperature on the density of TiO₂ have been mentioned in the literature for both films deposited by sol-gel (Bakri et al. (2017); Bockmeyer and Löbmann (2006)) and by ALD (Hsu et al. (2020); Karwal et al. (2018)).

The densification of the film with the XRR measurement could not be confirmed. The shape of the signal near the critical angle can be affected by artifacts due to a mismatch between the projected height of the X-ray beam on the sample and the length of the sample. This parameter is not considered in the fitting procedure, hence a large uncertainty on the fitted densities. The order of magnitude is however once again in the range of that of anatase TiO₂ (Jin et al. (2015)).

3.2.1.2 Investigation of the crystalline phase of the annealed ALD-TiO₂ thin films

The structural changes of the ALD-TiO₂ upon air-ageing and annealing have been investigated by GI-XRD acquired with an incident angle $\Omega = 0.4^\circ$. [Figure 3.2](#)

3.2 Influence of post-annealing treatments on ALD-TiO₂ thin films properties

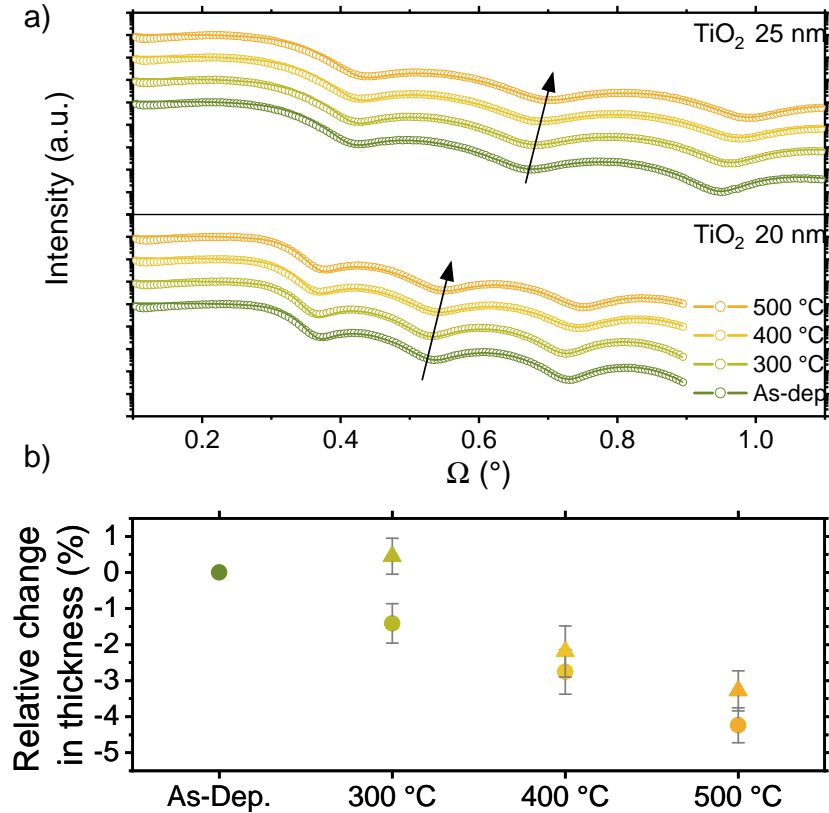


Figure 3.1: XRR analysis of annealed TiO₂ thin films function of the annealing temperature. a) Reflectograms of 15 nm-thick (top) and 20 nm-thick (bottom) ALD-TiO₂ samples on Si annealed at various temperatures. The data are normalized and shifted for clarity. A Parratt-fit (full lines) is applied to the data points (open circles). The arrows highlight the increase of the angular period of the Kiessig fringes. b) Relative variation of the thickness of the annealed samples. The reference thickness is that of the as-deposited film.

presents the diffraction spectra of 15 nm- (Figure 3.2.a) and 20 nm-thick ALD-TiO₂ thin films (Figure 3.2.b), air-aged and annealed at 300 °C, 400 °C and 500 °C in air, deposited on Si-(100) substrates. The reference pattern of TiO₂ anatase (reference JCPDS04-0477) is added for phase identification. The Si substrate contributes to the diffraction signal between $2\theta = 50^\circ$ and $2\theta = 60^\circ$ as seen on the diffractogram of the amorphous TiO₂-15nm-AsDep. The intensity of the sharp and broad features at $2\theta = 53.50^\circ$ and $2\theta = 55^\circ$ respectively can vary in intensity depending on the in-plane orientation of the substrate with respect to the X-ray beam.

As stated in section 2.1.4, only the thicker films (≥ 20 nm) are crystallized in the anatase phase as deposited. After annealing, all the layers crystallize into the anatase phase, as demonstrated by the appearance of diffraction peaks at $2\theta = 25.45^\circ$ (101), $2\theta = 37.17^\circ$ (103), $2\theta = 38.00^\circ$ (004), $2\theta = 38.78^\circ$ (112), $2\theta = 48.21^\circ$ (200), $2\theta = 53.97^\circ$ (105), $2\theta = 55.25^\circ$ (211), and $2\theta = 62.82^\circ$ (204). The planes

3.2 Influence of post-annealing treatments on ALD-TiO₂ thin films properties

Table 3.1: Fitted parameters of the XRR data of ALD-TiO₂ of 15 and 20 nm on Si substrate annealed at various temperatures. The structure of the samples is modeled with three layers: Si (substrate)/SiO₂ (native oxide)/TiO₂. The density of the substrate is fixed at 2.2 g cm⁻³, its roughness at 0.1 nm, and its thickness is infinite.

Sample	Layer	Thickness (nm)	Roughness (nm)	Density (g cm ⁻³)
15 nm as dep.	TiO ₂	14.87 ± 0.03	0.64 ± 0.02	4.54 ± 0.04
	SiO ₂	3.1 ± 0.6		2.80 ± 0.07
	Si		1.6 ± 0.7	
15 nm 300°C	TiO ₂	14.66 ± 0.05	0.31 ± 0.04	4.48 ± 0.05
	SiO ₂	3.3 ± 0.4		2.51 ± 0.06
	Si		0.7 ± 0.1	
15 nm 400°C	TiO ₂	14.46 ± 0.06	0.18 ± 0.10	4.56 ± 0.06
	SiO ₂	3.1 ± 0.5		2.64 ± 0.08
	Si		1.1 ± 0.6	
15 nm 500°C	TiO ₂	14.24 ± 0.04	0.34 ± 0.03	4.75 ± 0.05
	SiO ₂	3.2 ± 0.7		2.85 ± 0.08
	Si		1.6 ± 0.6	
20 nm as dep.	TiO ₂	20.11 ± 0.05	0.76 ± 0.03	4.42 ± 0.03
	SiO ₂	3.7 ± 0.7		2.71 ± 0.06
	Si		2.0 ± 0.6	
20 nm 300°C	TiO ₂	20.20 ± 0.05	0.51 ± 0.04	4.31 ± 0.03
	SiO ₂	4.1 ± 0.6		2.49 ± 0.05
	Si		1.2 ± 0.7	
20 nm 400°C	TiO ₂	19.67 ± 0.09	0.10 ± 0.01	4.25 ± 0.05
	SiO ₂	4.1 ± 0.9		2.59 ± 0.08
	Si		1.5 ± 1.0	
20 nm 500°C	TiO ₂	19.45 ± 0.06	0.42 ± 0.40	4.42 ± 0.03
	SiO ₂	3.7 ± 0.7		2.75 ± 0.06
	Si		2.0 ± 0.5	

diffracting at higher angles are not considered for the analysis as their intensities are very low. Similarly, the (213) plane diffracting at $2\theta = 61.9^\circ$ was not intense enough to be consistently analyzed.

The diffractograms have been fitted using pseudo-Voigt functions to access the broadening of the anatase diffraction peaks. The broad contribution from the substrate overlaps with the (105) and (211) diffraction planes of the anatase phase, and was modeled by a pseudo-Voigt function with a large full width at half

3.2 Influence of post-annealing treatments on ALD-TiO₂ thin films properties

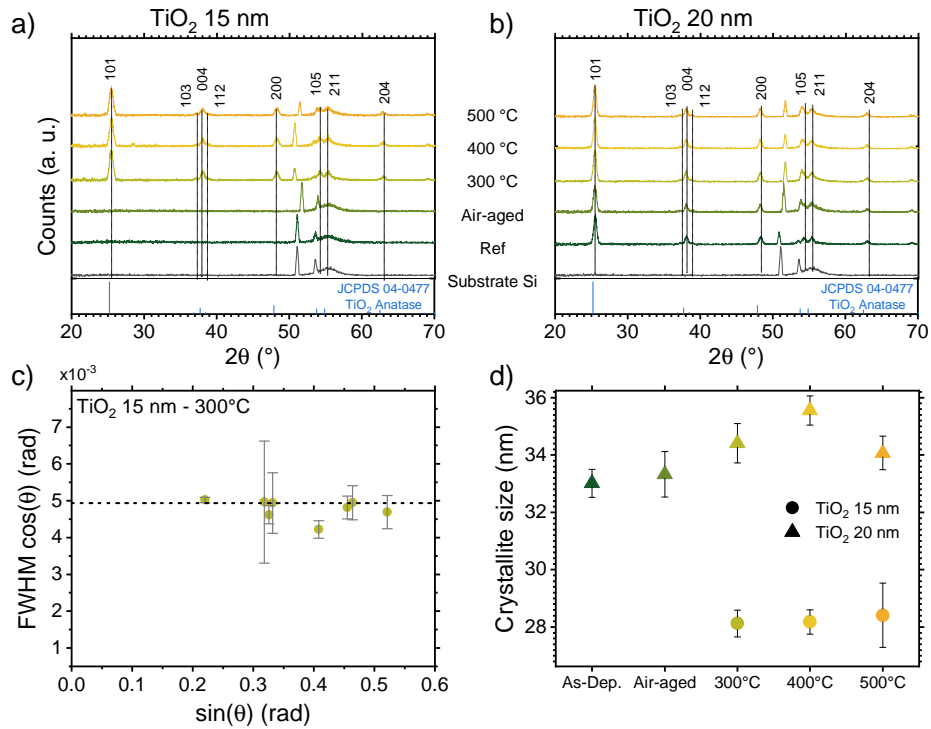


Figure 3.2: GI-XRD analysis of ALD-TiO₂ thin films function of the annealing temperature. Diffractograms of a) 15 nm-thick and b) 20 nm-thick ALD-TiO₂ samples on Si annealed at various temperatures. The reference pattern of the anatase phase is used for the indexing. c) Williamson-Hall plot of TiO₂-15nm-300°C taking the FWHM as broadening parameter with a linear fit (dashed line). d) Variations of the crystallite size as determined by the Williamson Hall method.

maximum – FWHM (from 2° to 4°). The broadening of XRD peaks is usually ascribed to three causes: 1) the finite size of the crystallites, 2) residual microstrains in the material and 3) instrumental broadening, mostly due to the divergence of the beam. The instrumental broadening being much smaller than the typical broadening of the samples, only causes 1) and 2) are considered. These factors were examined on the fitted data with the Williamson-Hall plot method (Williamson and W. Hall (1953)), which allows to distinguish between the two contributions under the assumption that their effects are not correlated. This technique is originally used for powder materials; however, it can fairly be extended to polycrystalline thin films assuming randomly distributed orientations. Comparing the relative intensities of the peaks with the anatase reference reveals that the crystallized TiO₂ films do not present a preferential orientation, which justify the use of this method.

A typical Williamson-Hall plot of the crystallized samples is presented in Figure 3.2.c. The uncertainty on the FWHM values caused by the fitting procedure are taken into account to correctly weigh the various points in the Williamson-Hall plot and factor in the linear fit the fact that some peaks are better-defined than

3.2 Influence of post-annealing treatments on ALD-TiO₂ thin films properties

others. A first observation is that all points are located at similar ordinates. In a Williamson-Hall plot, the slope of the linear fit is related to the strain broadening, while the intercept is related to the size-broadening. For these samples, the slope is negligible and is set to 0 while staying within the margin of error due to the XRD peak fitting, showing that strain broadening is not prevailing in these films.

Reducing the Williamson-Hall relation to the size-broadening component, the data are fitted with a constant value reflecting the size-broadening, which is related to the average crystallite size by the Debye-Scherrer relation:

$$B \cos(\theta) = \frac{K \cdot \lambda_{Cu, K\alpha 1}}{L} \quad (3.1)$$

where B is the broadening factor (here the FWHM in rad), K is a shape factor accounting for the average geometry of the crystallite taken as 0.9 (for spherical crystallites, Mote et al. (2012)), L is the average size of the crystallites and $\lambda_{Cu, K\alpha 1} = 1.5406 \text{ \AA}$ is the wavelength of the $K_{\alpha 1}$ emission of Cu. The resulting crystallite sizes are presented in Figure 3.2.d.

For the TiO₂-15nm, the crystallites are $28.1 \pm 0.5 \text{ nm}$ large, and the slight variation of their size with the annealing temperature falls within the margin of error of the fit. The average size of the crystallite is larger than the thickness of the film, which shows the limitation of the method and of the spherical model of crystallites. Because of the numerous assumptions made here, the sizes extracted here should not be interpreted as absolute values, but rather relatively with each other. For the TiO₂-20nm-AsDep, the crystallite size was estimated to be $33.3 \pm 0.8 \text{ nm}$, increasing slightly upon annealing up to $35.6 \pm 0.5 \text{ nm}$ at 400 °C. It is striking that the crystallite size increases largely as the thickness of the film increases. Similar variations have already been reported on ALD-TiO₂ films grown with TiCl₄ and H₂O (Chiappim et al. (2016)), where both the film thickness and the process temperature influence the crystallization of the final film, which was related to the chemical composition of the film.

In summary, the XRD analysis of the samples revealed that after annealing, layers are crystallized in the anatase phase. A relative independence of the crystallinity of the films with respect to the annealing temperature has been demonstrated for temperatures between 300 °C and 500 °C. The crystallinity is however slightly enhanced as the ALD film gets thicker.

3.2.2 Optical properties of the ALD-TiO₂ thin films

Figure 3.3 displays the variations of the optical properties of the films before and after air-ageing and annealing. Photospectroscopy data are shown in Figure 3.3.a. The transmission and the reflectance data are acquired for thin films deposited on 2 nm-thick borosilicate glass (BSG). The TiO₂ film is exposed first to the light beam. The values of the apparent optical indirect band gap are extracted via a Tauc plot analysis. Since the substrate has a high and steady transmission near the absorption edge of TiO₂ (above 350 nm), the absorption is calculated from the transmission and reflectance data of the stack thin film/substrate. The thicknesses are extracted from the XRR analysis (cf. Table 3.1).

3.2 Influence of post-annealing treatments on ALD-TiO₂ thin films properties

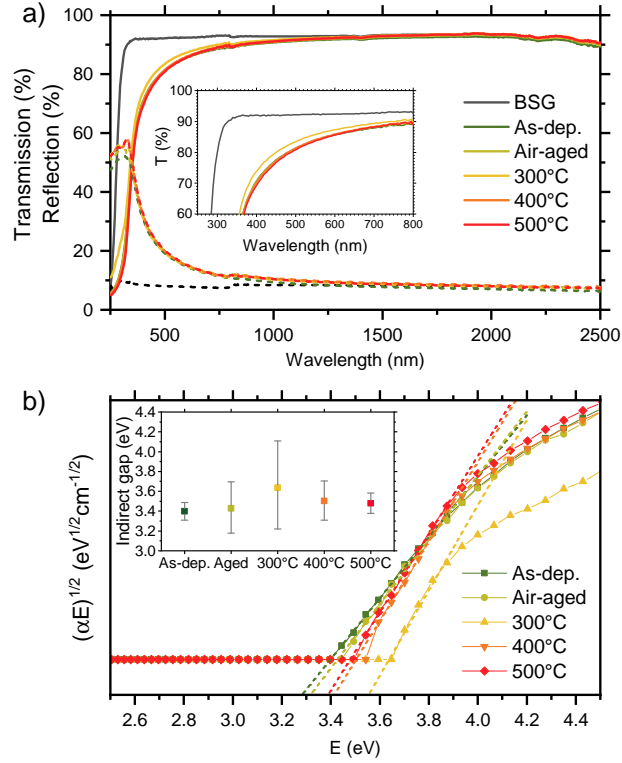


Figure 3.3: Optical properties of 15 nm-thick ALD-TiO₂ thin films function of the annealing temperature. a) Transmission (full lines) and reflectance (dashed lines) data of TiO₂/BSG specimen. The inset shows a magnification of the transmission at short wavelengths. b) Tauc-plot derived from the spectroscopic data for the determination of an indirect band gap. The fits of the linear part of the plot are shown in dashed lines. The inset gives the extracted indirect band gaps function of the annealing temperature.

The transmission and the reflectance of the TiO₂ layer do not vary much upon air ageing and annealing over the whole range of wavelengths, especially in the range of interest for perovskite solar cells (below 800 nm for single junction cells, below 1100 nm for Si/perovskite tandem applications). There is particularly no optical degradation of the layer after four months of air-ageing (sample "Air-aged"). The film annealed at 300 °C stands out, with a transmission 2% to 3% higher than the other samples, even at very low wavelengths (below the usual absorption onset of TiO₂). This feature is probably due to an experimental artifact rather than to an intrinsic property of the TiO₂ annealed at 300 °C (*e.g.* part of the incident light of the spectrophotometer might have missed the sample).

The inset of Figure 3.3.b presents the variation of the indirect band gap energy with the annealing temperature, as extracted from the linearization of the Tauc plot near the absorption edge. The large uncertainties on the band gap originates from the constant wavelength step of the spectrophotometer (set at 5 nm) which translates into large and increasing energy steps at short wavelengths ($\Delta E = hc \cdot \frac{\Delta \lambda}{\lambda^2}$,

3.2 Influence of post-annealing treatments on ALD-TiO₂ thin films properties

$\Delta E = 50 \text{ meV}$ at $E = 3.4 \text{ eV}$), hence reducing the number of points of interest in the linear region. The observed variations stay in the margin of error of the measure and the indirect band gap is determined to be $3.4 \pm 0.3 \text{ eV}$, which is in line with the values observed in the literature for anatase TiO₂ (Shi et al. (2017)).

3.2.3 Characterization of the blocking ability of the ALD-TiO₂ thin films

To assess the suitability of the annealed layers to act as proper ETLs (*i.e.* promoting electrons transport while blocking the holes), samples have been mounted for electrochemical characterization. Various thicknesses of TiO₂ have been deposited on FTO to perform cyclic voltamperometry on them.

The I(V) curves are presented in Figure 3.4.a, where the voltage is set relatively to the saturated calomel electrode (SCE). Experimental details can be found in section A.1.2. The curve for bare FTO shows the typical double "duck-shape" of a conductive working electrode as described in section A.2.1. When the electrode is coated with the different layers of fresh ALD-TiO₂ or SP-TiO₂, the oxidation is inhibited which confirms the n-doped nature of TiO₂ and the hole blocking ability of the layer. Moreover, a shift of the cathodic peak towards more negative potentials is observed as the thickness of the titania layer increases: -1.27 Vvs SCE for TiO₂-15nm, -1.05 Vvs SCE for TiO₂-10nm, and -0.84 Vvs SCE for TiO₂-5nm, while the cathodic peak of SP-TiO₂ is at -0.79 Vvs SCE . There is also a crossover of the reverse and forward scans in the reduction region. The inset in Figure 3.4.a is a magnification of the cyclic voltammetry in the oxidation region in log scale, stressing an increase of the leakage current as the thickness of the ALD-TiO₂ layer decreases. When several cycles in potential are applied, the shape of the I-V in the cathodic region changes (Figure 3.4.b). For ALD-TiO₂, the cathodic peak shifts back to lower potentials stabilizing at -0.63 Vvs SCE , similar to that of SP-TiO₂ stabilizing at -0.51 Vvs SCE , while the crossover of the backward and forward scan reduces. The effect is much less dramatic for SP-TiO₂. The stability of the electrolyte has been checked by acquiring voltammetry with an FTO electrode before and after this cycling, and the voltammograms superimpose which evidences no degradation of the electrolyte. Hence, the modification of the curve's shape for ALD-TiO₂ during the cycling is ascribed to a modification of the working electrode, and most probably of the TiO₂ surface.

As it has been stressed before, the properties of an ALD-grown layer can vary with the deposited thickness, and it is also true regarding their surface properties. The shift in the cathodic peak position for fresh ALD films indicates that the surfaces of the as-deposited films are not similar. However, after the annealing at 500°C the cathodic peaks of TiO₂-15nm-500°C and TiO₂-10nm-500°C are both located at -0.74 Vvs SCE , and the large crossover has disappeared (Figure 3.4.c). This indicates that the thermal treatment evens out the surface of the different samples. The anodic leakage current has increased as compared to the fresh samples. It can be another manifestation of the shrinkage of the layer due to the annealing, as evidenced by the X-ray data. The case of TiO₂-5nm-500°C is even more striking, as in this case, the anodic current is not blocked anymore, and the voltammogram

3.2 Influence of post-annealing treatments on ALD-TiO₂ thin films properties

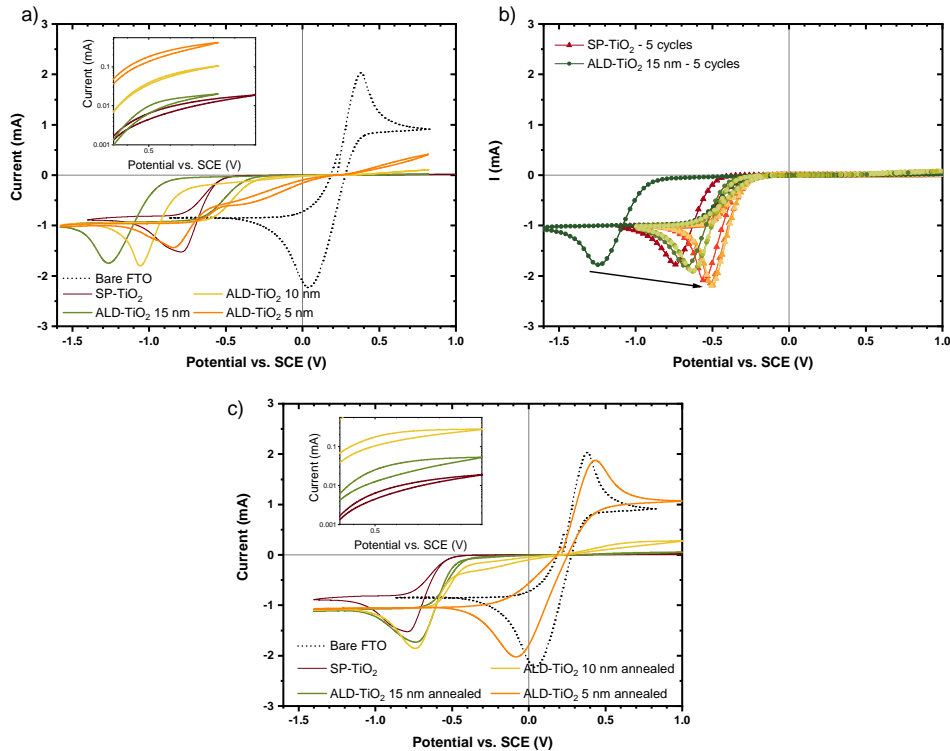


Figure 3.4: a) Cyclic voltammetry of as-deposited ALD-TiO₂ films of thicknesses of 5 nm to 20 nm on an FTO electrode. The voltamograms of the bare FTO electrode and of SP-TiO₂ coated FTO are added for comparison. The inset shows the $I > 0$ region in log scale to evaluate the leakage current. b) Voltamograms over 5 cycles for SP-TiO₂ and ALD-TiO₂ (15 nm-thick). As the number of cycles increases, the data are colored in lighter colors. c) Cyclic voltammetry of ALD-TiO₂ films of thicknesses of 5 nm to 20 nm annealed at 500 °C on an FTO electrode.

looks like the one of bare FTO. In this case, the layer does not block holes anymore. Either the layer has become thin enough to allow for tunneling of holes through the TiO₂ layer, or pinholes are formed upon annealing as described by Karwal et al. (2018).

3.2.4 Conclusions on the effect of the annealing on ALD-TiO₂

In this section the changes of the optical properties and of the structure of the ALD-TiO₂ layers of different thicknesses (from 5 nm to 20 nm) after ageing and annealing at various temperatures up to 500 °C were discussed. Hence, the properties of the layers in conditions close to their use in a baseline integration process (after potential storage and after annealing) have been discussed. The transmission and reflection spectra, as well as the determined indirect band gap (3.4 ± 0.3 eV) of the oxide do not vary upon annealing or air-ageing. This has been

3.3 Comparison of the homogeneity of the TiO₂ thin films deposited by ALD and by SP

extensively discussed for the TiO₂-15nm samples, but similar conclusions have been drawn for other thicknesses. The GIXRD and cyclic voltammetry show that the annealing tends to even out several properties of the films. For low thicknesses (≤ 15 nm), the as-deposited films are amorphous, but all films crystallize in the anatase form after annealing at $T \geq 300$ °C (lower temperatures have not been explored). Similarly, the position of the cathodic peaks suggests that the nature of the surfaces is comparable after annealing. The analysis of the X-ray reflectograms indicates in all cases a shrinkage of the layers upon annealing which has also been reported in the literature for titania films deposited by various methods at similar temperatures. This densification can be explained by the reorganization of the material at the microscopic scale allowed by the thermal energy brought by the annealing (relaxation of stresses, increased mobility of dislocations or crystalline defects ...). In the case of very thin layers of titania (5 nm), the densification could induce the formation of pinholes in the layer, hence compromising its hole-blocking nature. However no change in the crystallinity (*i.e.* crystallite size) of the layers after annealing was noticed. In short, the ALD-TiO₂ films annealed have similar properties as the SP-TiO₂, with some variations observed with the thickness of the titania (cf [section 3.4.2](#)).

3.3 Comparison of the homogeneity of the TiO₂ thin films deposited by ALD and by SP

One of the most interesting feature of ALD is the good homogeneity and conformality which can be achieved on large areas and textured substrates. In this section, the homogeneity of the TiO₂ layers deposited by SP vs. ALD at the scale of a batch of perovskite solar cells (usually 16 cells of dimension 2×2 cm²) are compared. In the case of spray pyrolysis, the cells are positioned in four rows with strips of silicon on top to cover part of the FTO as displayed in [Figure 3.5.a.ii](#). This protection is required to properly contact the FTO and extract photogenerated electrons without suffering from additional resistive losses. Four FTO substrates were added at the four corners of the layout in order to assess the x-wise and y-wise homogeneities of the deposition. For the ALD, a large FTO substrate of dimension 13×15 cm² is used in order to prevent parasitic deposition of TiO₂ on the back of the substrate due to the infiltration of gaseous precursors on the side of the substrate (an example of such parasitic deposition on small-sized samples is shown in [Figure 3.5.b](#)). The samples are cut from the substrate at the desired size after the deposition of TiO₂. To protect part of the FTO from the deposition of TiO₂, a mask with marker pen ink is used. It has been verified beforehand that it does not affect in a sensible way the chemistry happening during the ALD reaction.

A difference can be observed by visual inspection. For ALD-TiO₂, the deposition looks homogeneous as long as the cleaning of the substrate is thorough enough, because of the substrate-dependent nature of ALD. For SP-TiO₂, the deposition looks homogeneous y-wise, but seems to grow thicker along the x-axis. Looking carefully at the substrates, one can also spot local inhomogeneities probably due to an inhomogeneity in the droplets size ([Figure 3.5.b](#)).

3.3 Comparison of the homogeneity of the TiO₂ thin films deposited by ALD and by SP

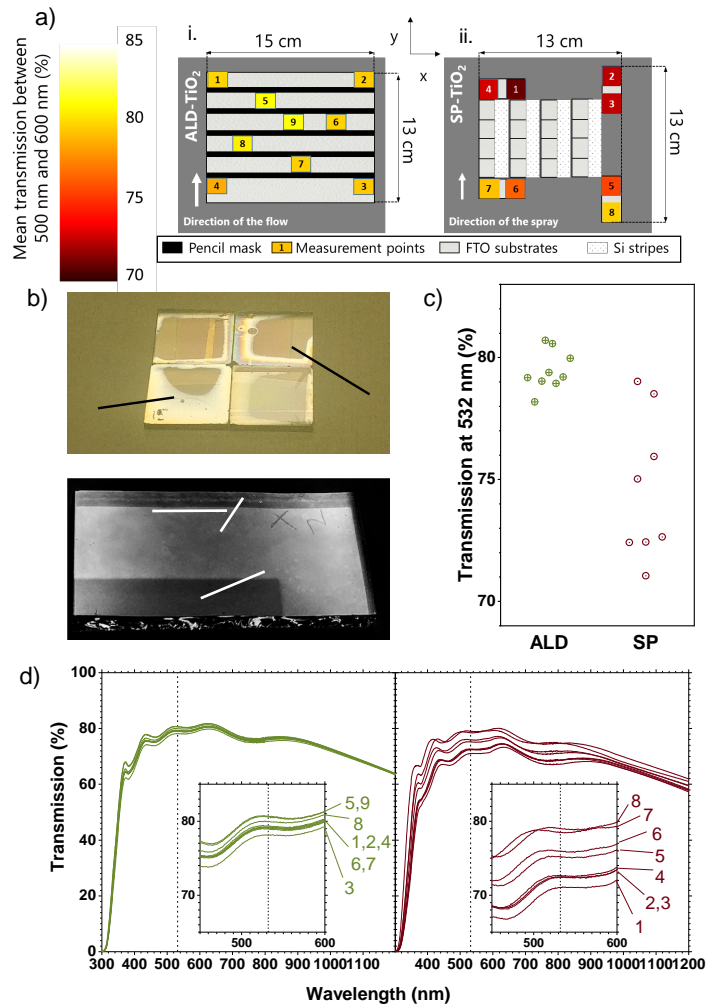


Figure 3.5: a) Sketch of the lay out of the samples for the ALD (left) and SP deposition (right) of TiO₂. The location where transmission data are acquired are colored according to the mean transmission between 500 nm and 600 nm. b) Back of a 2×2 cm² glass sample after deposition of TiO₂ by ALD (top). The arrows point towards parasitic deposition of TiO₂. Sample after deposition of SP-TiO₂ (bottom). The white arrows point at visible inhomogeneities in the layer. The picture has been edited to reveal these inhomogeneities. c) Transmission of ALD- and SP-TiO₂ at 532 nm at various locations. d) Transmission data of ALD-TiO₂ (left) and SP-TiO₂ (right). The insets couple the transmission data and their location on sketch a).

In order to have a more quantitative assessment of the homogeneity of the films, UV-vis spectroscopy on a glass/FTO/TiO₂ stack was performed. The resulting spectra are stacked in Figure 3.5.d for ALD-TiO₂ and for SP-TiO₂, and the positions where the spectra are acquired are reported on the Figure 3.5.a.i and Figure 3.5.a.ii. A variation in transmission is closely related to a variation of the

3.4 Integration of ALD-TiO₂ layers as compact ETL in perovskite solar cells

thickness of the constitutive elements of the stack. For $E > E_g$, thicker films absorb more radiation, and so the transmission decreases. For $E < E_g$, a change in titania thickness changes the interference patterns within the layer, hence its reflection and its transmission. The ALD-TiO₂ thin film has a rather uniform transmission across the whole substrate ($13 \times 15 \text{ cm}^2$), while the SP-TiO₂ samples present larger variations – as high as 9% absolute difference in the visible range. The insets in Figure 3.5.d show a magnification of the transmission data around a local maximum of transmission just above 500 nm. In the case of ALD-TiO₂, the position of the interference pattern does not change across the substrate. It indicates that there are no significant change in thickness of TiO₂. For SP-TiO₂, the reduction in transmission across the substrates is accompanied by a shift of the interference pattern towards higher wavelengths explained by the variation of TiO₂ thickness.

The transmissions are averaged between 500 nm and 600 nm and the locations of the measurements are colored accordingly in Figure 3.5.a.i and Figure 3.5.a.ii. The transmission at 532 nm for all locations is plotted in Figure 3.5.c to assess the dispersion of the measurements. For the ALD, the homogeneity of the layer is confirmed. For the spray deposition, the thickness of the layers increases along the y-axis while it varies less along the x-axis. This difference most likely originates from the spraying gesture which is performed along the y-axis (nozzle pointed towards the ascending y) favoring the deposition of more material when y increases.

3.4 Integration of ALD-TiO₂ layers as compact ETL in perovskite solar cells

In this section, the layers which were characterized in chapters 2.1 and 3.2 are integrated into different architectures of perovskite photovoltaic devices. The focus is first set on the properties of the perovskite layer grown on the c-TiO₂/mp-TiO₂ bilayer. The proper integration of the ALD-TiO₂ layer in complete devices is then discussed. The thickness of the ALD-TiO₂ thin film is varied, and the performances of the optimized process are compared with those of baseline cells (based on SP-TiO₂). An attempt to synthesize devices with the planar n-i-p architecture with TiO₂ is also introduced. Unless stated otherwise, the samples with perovskite grown on a substrate with TiO₂ deposited by spray pyrolysis will be named SP-TiO₂ and the samples with perovskite grown on a substrate with XX nm of TiO₂ deposited by ALD will be named ALD(XX)-TiO₂.

3.4.1 Properties of the perovskite deposited on a c-TiO₂/mp-TiO₂ bilayer

Since the perovskite grows mostly on the mesoporous scaffold, the nature of the compact layer is not expected to influence the structure nor the morphology of the perovskite. To ascertain it, a triple cation perovskite (composition $\text{Cs}_{0.05}(\text{MA}_{0.17}\text{FA}_{0.83})_{0.95}\text{Pb}(\text{I}_{0.83}\text{Br}_{0.17})_3$) is deposited on SP-TiO₂/mp-TiO₂ or ALD(15)-TiO₂/mp-TiO₂ and is inspected by the mean of scanning electron microscopy (SEM) and XRD.

3.4 Integration of ALD-TiO₂ layers as compact ETL in perovskite solar cells

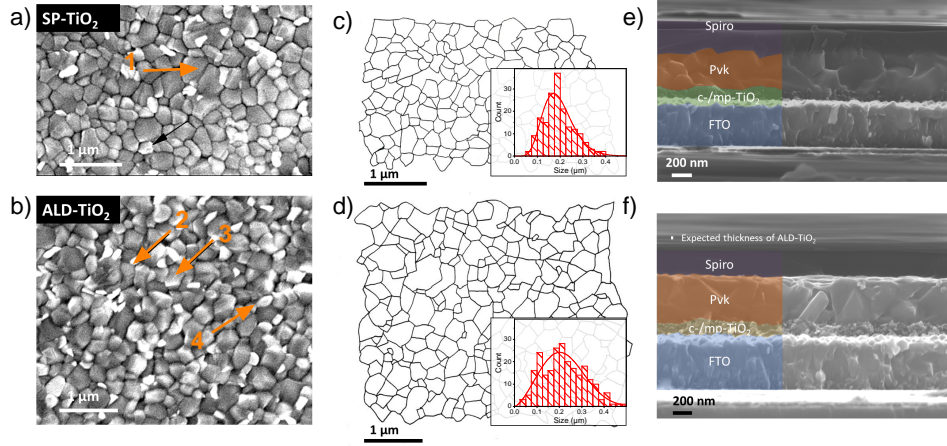


Figure 3.6: Morphology of the perovskite on SP-TiO₂ (a,c,e) and ALD TiO₂ (b,d,f). a,b) Top surface SEM micrographs of the perovskite (magnification 25k). c,d) Contours of the grain boundaries for statistical analysis. The associated grain size distributions are given in the insets, fitted with a Weibull distribution. e,f) Cross sectional images with identification of the constitutive layers.

Figure 3.6 presents the BSE top surface images of half cells (glass/FTO/c-TiO₂/mp-TiO₂/perovskite) based on ALD(15)-TiO₂ and SP-TiO₂. The micrographs reveal that the perovskite forms quite similarly on both bilayers. Some unreacted lead iodide is present at the surface of the film as stressed by the difference of chemical contrast between the small bright grains at the foreground (associated to the heavy PbI₂) and the larger and darker grains at the background (associated to the perovskite). This is in accordance with the stoichiometry of the solution in which 10% molar excess of PbI₂ is added. A moderate amount of PbI₂ is not harmful for the proper working of complete devices and several studies claim that it can actually participate in the passivation of grain boundaries (Q. Chen et al. (2014)). The images are treated as detailed in section A.2.2 in order to extract the distribution of the grains' size (more than 180 grains are analyzed for each image). They are shown in Figure 3.6.c and Figure 3.6.d with the associated histograms in insets. For SP-TiO₂, the grain sizes span from 66 nm to 394 nm, with a mean size estimated at 194 ± 68 nm. For ALD(15)-TiO₂, the grain sizes span from 31 nm to 498 nm, with a mean size estimated at 219 ± 93 nm. These results should be considered carefully for several reasons detailed in section A.2.2.

The structural properties of the perovskite deposited on the two different substrates are probed with XRD. Figure 3.7 presents the diffractograms of two full cells (glass/FTO/c-TiO₂/mp-TiO₂/perovskite/spiro-OMeTAD/Au) grown with SP-TiO₂ and ALD(15)-TiO₂. Four phases are visible and labeled: 1) the FTO substrate (cassiterite, space group $P4_2/mnm$), diffracting at $2\theta = 26.44^\circ$ (110) and 37.73° (200), 2) the gold layer (face-centered cubic, space group $Fm-3m$), diffracting at $2\theta = 38.14^\circ$ (111) and 44.36° (200), 3) lead iodide (hexagonal, space group $P-3m1$), diffracting at $2\theta = 12.62^\circ$ (001), and 4) the perovskite layer crystallizing in

3.4 Integration of ALD-TiO₂ layers as compact ETL in perovskite solar cells

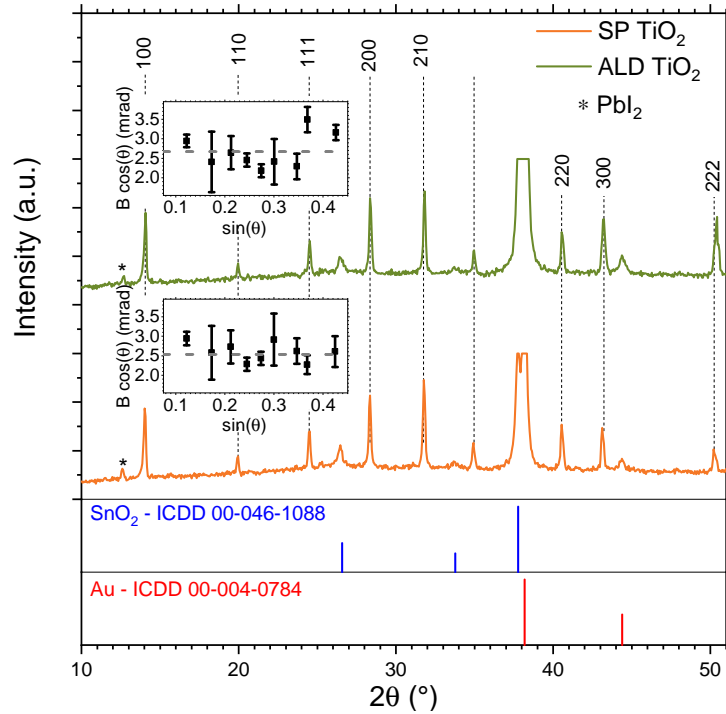


Figure 3.7: Diffractograms of perovskite on SP- and ALD-TiO₂ in Bragg Brentano configuration. The references of SnO₂ (FTO) and Au are added. The diffraction planes of the perovskite phase are indexed according to the cubic phase. The insets are the Williamson Hall plots of the respective architecture with the linear fit (dashed line).

its cubic phase (space group $Pm-3m$), with diffraction peaks at $2\theta = 14.04^\circ$ (100), 19.96° (110), 24.52° (111), 28.34° (200), 31.77° (210), 34.91° (211), 40.53° (220), 43.09° (300) and 50.19° (222) (Xia et al. (2015)). The diffraction peak of Au (111) has been cut off in order to enhance the smaller signal coming from the perovskite layer. The relative intensities of the perovskite peaks are similar in both samples, which indicates that the preferential orientation of the polycrystalline film is similar. The contribution of the PbI₂ peak to the overall signal is low which suggests a good conversion of the precursors into the photoactive α -phase of the perovskite. The diffractograms are fitted and the Williamson-Hall plots related to the two samples are presented in Figure 3.7. As in section 3.2.1.2, the contribution of strain to the peak broadening is negligible so the data were fitted with Equation (3.1). The distributions of the data on the Williamson-Hall plot are comparable for the two samples, yielding close mean crystallite sizes (52.9 ± 1.9 nm for SP-TiO₂ and 51.9 ± 2.8 nm for ALD(15)-TiO₂).

The XRD and SEM analysis of the samples confirm that the perovskite grows similarly whether the compact layer of titania is deposited by spray pyrolysis or ALD. As it can be seen on the cross sections (Figure 3.6.e and Figure 3.6.f), the compact layer is completely covered by the mesoporous titania, which the

perovskite grows on, further explaining the relative independence of the perovskite properties on the nature of the compact layer.

3.4.2 Optimization of the thickness of the ALD-TiO₂ compact layer

As stated in [chapter 3.2](#), most of the properties of the compact layer are quite similar after annealing, except for their blocking ability which decreases as the thickness increases. For a 5 nm-thick layer of TiO₂, the compact layer loses completely its blocking ability after annealing. Consequently, the influence of the titania thickness on the final performances of the cells has been probed with compact ALD-TiO₂ layers of thicknesses ranging from 11 nm to 21 nm. In the same way as what was demonstrated in [section 3.4.1](#), the perovskite is not affected by the thickness of the compact layer deposited by ALD. The cells were completed as described in [section A.1.1](#) with spiro-OMeTAD (doped with Li-TFSI, FK209 and ^tBp) as HTL and a gold electrode. The cells have been characterized by J–V measurements under an AM1.5G sun simulator whose illumination is calibrated at 1 sun. The dependence of the PV parameters (V_{OC} , J_{SC} , FF and PCE) on the parameters of the J–V acquisition (primarily the rate and the direction of the voltage scan) has already been extensively discussed in the literature (Unger et al. (2014); Khenkin et al. (2020)). In particular, Unger *et al.* showed that for high (5 s) and low (1 ms) delay times between two consecutive voltage steps (*i.e.* low and high scan rates respectively), the cells showed almost no hysteresis as compared to a medium delay time (100 ms) but the J–V characteristics are nevertheless not the same – higher PV parameters were generally found for higher scan rates. The authors ascribe these different behaviors to transient phenomena in the cell (*i.e.* impedance effects). As the scan rate decreases, the cell is closer to quasi-steady-state conditions for each measurement of the current density. For this reason, the cells are measured at relatively low scan rate (20 mV s⁻¹). In order to have reliable measurements of the sheer performance and stability of a perovskite solar cell, a consensus on an appropriate protocol was discussed during the 11th International Summit on Organic and Hybrid Photovoltaics Stability and has been published in 2020 by researchers of the field from more than 50 labs (Khenkin et al. (2020)). Among other topics, the importance to study the stabilized output power of the cell is stressed as a robust estimation of its performance. As such, maximum power point tracking (MPPT) study for at least 180 s under illumination are included in the present study.

The evolution of the PV parameters for the different thicknesses are summarized in [Figure 3.8](#). In order to maximize the amount of samples of each condition, the study has been lead in two separate batches: thicknesses smaller than 15 nm (batch 1) and thicknesses larger than 15 nm (batch 2). Due to the variability of the process of making complete devices, the comparison between batches is not always straightforward. Hence, the 15 nm-thick titania – which appears in both batches – is used as reference. In [Figure 3.8](#), the PV parameters have been normalized with respect to the average parameter of the 15 nm-thick samples in the respective scan direction (*e.g.* $PCE_{11nm}^{norm} = PCE_{11nm} / PCE_{15nm}^{batch1}$ and $PCE_{21nm}^{norm} = PCE_{21nm} / PCE_{15nm}^{batch2}$). This normalization method gives a clearer

3.4 Integration of ALD-TiO₂ layers as compact ETL in perovskite solar cells

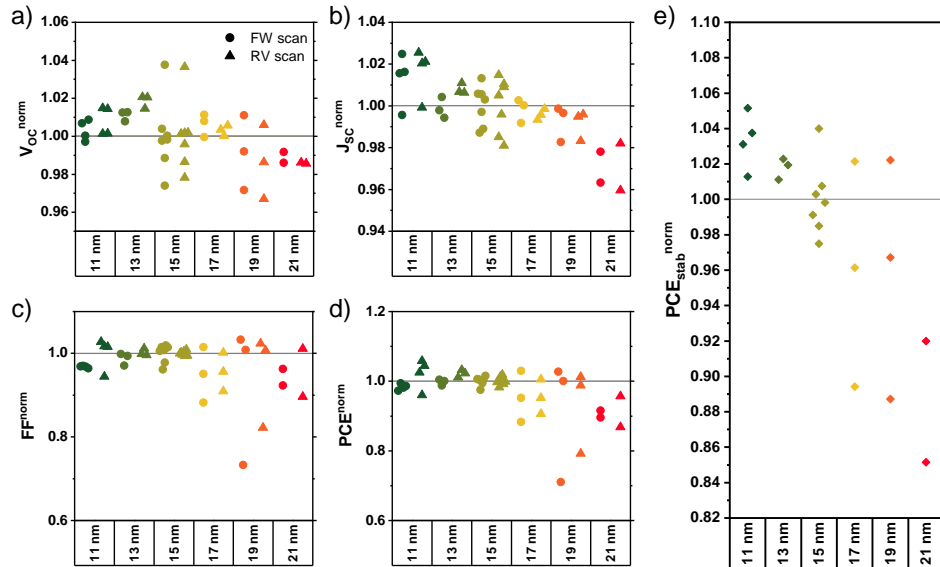


Figure 3.8: Normalized PV parameters function of the thickness of the ALD-TiO₂ layer acquired at 20 mV s^{-1} . a) V_{OC} , b) J_{SC} , c) FF and d) PCE are normalized with respect to the mean value of the 15 nm-thick sample for the given scan direction. e) Mean normalized stabilized PCE between 3 min to 5 min of illumination. The stack is glass/FTO/ALD-TiO₂/mp-TiO₂/perovskite/spiro-OMeTAD/Au.

view on the general trends, but completely flattens out the hysteresis phenomenon commonly observed for mesoscopic structures between the forward and reverse scan directions.

The measured PV parameters for each condition are given in Table 3.2, with the normalized value in parenthesis.

A first observation concerns the difficulty in having reproducible batches. Even if the reproducibility of the synthesis of the compact layer of titania is improved through the mean of ALD, it would not be enough to settle the issue of the variability of the performance of full cells. It also requires a strict control over the quality and the ageing of the chemicals (especially regarding the perovskite and HTL solutions), a rigorous regulation of the lab environment (temperature and moisture level), a good reproducibility of operator-dependent tasks (spin coating, final etching of the cells), which was not realistically achievable on large time scales in the lab. This point is reflected by the large difference in absolute performance between batch 1 ($PCE \sim 17\%$ in reverse scan) and batch 2 ($PCE \sim 14\%$ in reverse scan). In extreme circumstances – as is the case of batch 2 due to a mediocre control of the lab’s atmosphere – even the intra-batch reproducibility can be compromised. Still, as demonstrated in chapter 3.2, the deposition of the compact layer of titania is reproducible enough to be able to compare qualitatively batches deposited at different times.

In spite of the poor interbatch reproducibility, some tendencies were observed

3.4 Integration of ALD-TiO₂ layers as compact ETL in perovskite solar cells

Table 3.2: Average PV parameters of cells based on ALD-TiO₂ compact layer as a function of the TiO₂ thickness. Results are given for two batches. The quantities are given in forward (roman style) and backward (*italic style*) scans, for a scan speed of 20 mV s⁻¹. The relative variations are given in parenthesis, with respect to the mean parameters measured for the 15 nm cells of each batch.

	V_{OC} (mV)	J_{SC} (mA cm ⁻²)	FF (%)	PCE (%)
11 nm	1056 ± 5 (+0.38%)	21.8 ± 0.2 (+0.93%)	68.5 ± 0.1 (-3.3%)	15.8 ± 0.1 (-1.8%)
	<i>1052 ± 7</i> (+0.77%)	<i>21.7 ± 0.2</i> (+1.88%)	<i>77.5 ± 2.6</i> (+0%)	<i>17.9 ± 0.7</i> (+2.9%)
13 nm	1064 ± 2 (+1.14%)	21.5 ± 0.1 (-0.46%)	69.9 ± 0.9 (-1.3%)	16.0 ± 0.1 (-0.6%)
	<i>1063 ± 3</i> (+1.82%)	<i>21.6 ± 0.1</i> (+1.4%)	<i>77.6 ± 0.5</i> (+0.1%)	<i>17.9 ± 0.2</i> (+2.3%)
15nm	1052 ± 2	21.6 ± 0.2	70.8 ± 1.6	16.1 ± 0.2
	<i>1044 ± 2</i>	<i>21.3 ± 0.2</i>	<i>77.5 ± 0.4</i>	<i>17.5 ± 0.1</i>
15 nm	1032 ± 28	18.9 ± 0.1	62.9 ± 1.0	12.2 ± 0.1
	<i>1040 ± 27</i>	<i>18.7 ± 0.3</i>	<i>76.4 ± 0.4</i>	<i>14.9 ± 0.2</i>
17 nm	1031 ± 10 (-0.09%)	19.0 ± 0.2 (+0.53%)	61.4 ± 1.7 (-2.4%)	12.0 ± 0.4 (-1.6%)
	<i>1037 ± 9</i> (-0.29%)	<i>18.8 ± 0.3</i> (+0.53%)	<i>75.1 ± 1.5</i> (-1.7%)	<i>14.7 ± 0.4</i> (-1.3%)
19 nm	1023 ± 17 (-0.87%)	18.7 ± 0.1 (-1.06%)	58.1 ± 8.6 (-7.6%)	11.1 ± 1.7 (-9.0%)
	<i>1026 ± 17</i> (-1.35%)	<i>18.5 ± 0.1</i> (-1.07%)	<i>72.7 ± 7.0</i> (-4.8%)	<i>13.8 ± 1.5</i> (-6.9%)
21 nm	1020 ± 3 (-1.16%)	18.3 ± 0.1 (-3.17%)	59.3 ± 1.2 (-5.7%)	11.1 ± 0.1 (-9.0%)
	<i>1025 ± 1</i> (-1.44%)	<i>18.1 ± 0.2</i> (-3.21%)	<i>72.9 ± 4.4</i> (-4.6%)	<i>13.6 ± 0.7</i> (-8.7%)

in the variation of the PV parameters depending on the thickness of titania used, best seen on the normalized parameters.

- V_{OC} . The V_{OC} varies slightly with the thickness of titania ($\pm 1.44\%$ variation at most with respect to the reference 15 nm-thick TiO₂). It has a slight

3.4 Integration of ALD-TiO₂ layers as compact ETL in perovskite solar cells

tendency to decrease with increasing thickness. It is lower than what is reported in the literature for titania mesoscopic structures (J. Jeong et al. (2021)) and to the radiative limit derived in [section 1.1.4.2](#), indicating that there are still optimizations to be performed on the quality of the absorber and on its interfaces.

- **J_{SC}**. The influence of the thickness on the J_{SC} is more pronounced. As shown in [section 2.1.4](#), the thickness of the film influences strongly the transmission of the front window. Even for changes of thickness as low as 2 nm, the transmission of the glass/FTO/ETL layer is reduced. The spectra of such stacks are presented in [Figure 3.9](#), for thicknesses of 11 nm, 13 nm, and 15 nm. A reduced transmission of this stack implies that fewer photons can be absorbed by the perovskite, hence a reduction in the photocurrent. If the strong assumption is made that the transmission can be assimilated to the EQE of the cell up to the wavelength corresponding to the band gap of the perovskite (*i.e.* considering no parasitic reflection on the ETL/absorber interface, step-function absorbance and internal quantum efficiency $IQE = 1$), a rough estimate of the photocurrent deficit due to this lesser transmission can be derived:

$$\begin{aligned}\Delta J_{1/2}^{ph} &= J_{thickness\ 1}^{ph} - J_{thickness\ 2}^{ph} \\ J_{thickness\ i}^{ph} &= q \int_0^{\infty} EQE_i(\lambda) \phi_{AM1.5G} d\lambda \\ &\approx q \int_0^{\lambda_{gap}} T_i(\lambda) \phi_{AM1.5G} d\lambda\end{aligned}\quad (3.2)$$

where q is the elementary charge, T is the transmission and $\phi_{AM1.5G}$ is the incoming photon flux corresponding to an illumination at 1 sun with the AM1.5G solar spectrum. It yields $\Delta J_{11\ nm/15\ nm}^{ph} = 0.50\ \text{mA cm}^{-2}$ and $\Delta J_{13\ nm/15\ nm}^{ph} = 0.52\ \text{mA cm}^{-2}$. The absolute value derived this way are smaller than the one measured with the J–V characterization, which can be explained by the strong hypothesis (especially $EQE(\lambda) = T(\lambda)$), and the fact that the light coupling at the titania/perovskite interface in the full device is different than the titania/air coupling in the stack used for transmission. Nonetheless, similar order of magnitudes and trends in the variation of J_{SC} with the thickness of titania were found.

- **FF**. The fill factor is the most affected parameter with variations as large as 7.6% between the 15 nm and the 19 nm cells. From these data, the fill factor seems to reach a maximum at 15 nm. For lower thicknesses, the inferior blocking ability of the titania after annealing increases the leakage current, while at larger thicknesses, the series resistance of the titania layer degrades the fill factor.
- **PCE**. All things considered, the output power of the cells during J–V measurements does not vary much for thicknesses of titania up to 17 nm, but starts decreasing for thicker films. Regarding the stabilized power output, thinner layers of titania tend to yield better results.

3.4 Integration of ALD-TiO₂ layers as compact ETL in perovskite solar cells

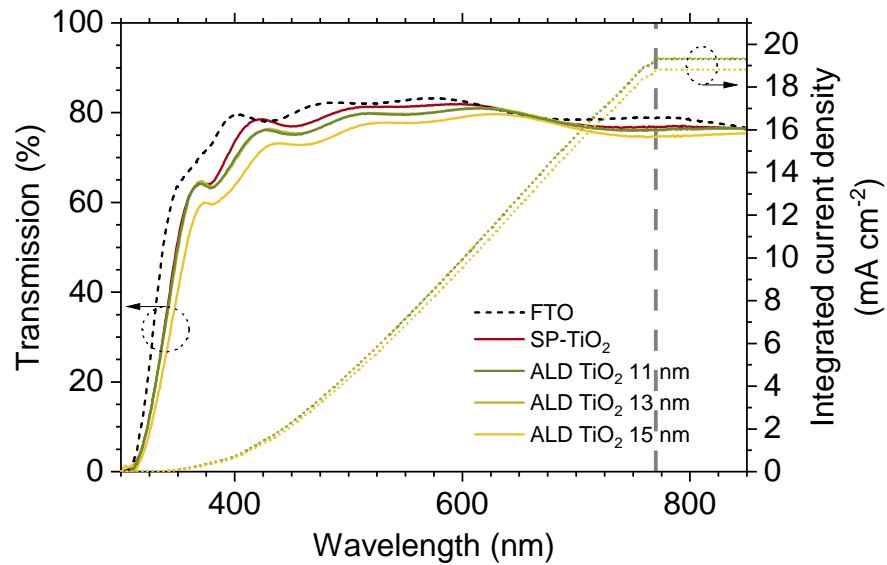


Figure 3.9: Transmission of ALD-TiO₂ films of 11, 13 and 15 nm deposited on FTO. The transmission of the FTO substrate and of SP-TiO₂ are given as comparison. The cumulative current density is calculated assuming that the IQE equals the transmission up to 770 nm (dashed line).

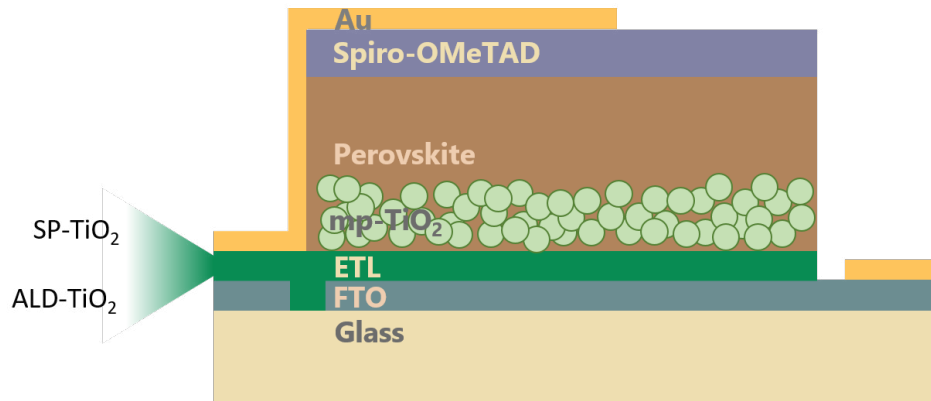


Figure 3.10: Sketch of the cell architecture considered for the comparison of SP- and ALD-TiO₂.

In summary, this screening test proves a relative insensibility of the performance of the final cell towards the thickness of the ALD-TiO₂ layer, as long as it stays below 17 nm. For the future discussions, the thickness is set at 15 nm.

3.4 Integration of ALD-TiO₂ layers as compact ETL in perovskite solar cells

Table 3.3: Photovoltaic parameters of the best performing cells made on ALD-TiO₂ and SP-TiO₂ substrates in mesoporous architecture. The quantities are given for forward scan (roman style) and reverse scan (*italic style*) at 20 mV s⁻¹.

	V_{OC} (mV)	J_{SC} (mA cm ⁻²)	FF (%)	PCE (%)
ALD-TiO ₂	1101	23.0	74.3	18.8
	<i>1104</i>	<i>23.0</i>	<i>77.6</i>	<i>19.7</i>
SP-TiO ₂	1079	23.3	73.5	18.5
	<i>1082</i>	<i>23.3</i>	<i>76.7</i>	<i>19.3</i>

3.4.3 PV performances of cells based on the two deposition methods

The thickness of the ALD titania layer being optimized, the performances of full devices built on ALD-TiO₂ with respect to the ones built on SP-TiO₂ are compared (cf Figure 3.10). In this regard and in order to have an idea of the variability of the two processes, the PV parameters of cells synthesized in various batches (batch 1 to batch 5) are gathered in Figure 3.11. As seen in batches n°3 and n°5, the dataset can be polluted by outliers that can originate from various causes including a mishandling of these specific samples during the deposition process or a bad electrical contact during the J-V measurement. Due to the rather small amount of data point in each dataset, the presence of an outlier can easily drift the mean and the standard deviation of the dataset away from sensible and meaningful values. The median value and the median absolute deviation (MAD) were chosen over the usual mean and standard deviation to determine an estimate of the dispersion of the datasets. This metric has been reported as more robust when the dataset includes outliers (Leys et al. (2013)), the median value of a dataset being much less sensitive to outliers than its mean. The MAD of a dataset $(X_i)_{i \in I}$ is defined as

$$MAD(X) = \text{median}_j \left(|X_j - \tilde{X}| \right) \quad (3.3)$$

where \tilde{X} is the median value of X . The values for the median and MAD of each PV parameter are consigned in Table A.2. The down side of this method is that is it quite sensitive to clusters of values. For instance the MAD(PCE) of batch 1 – spray – forward scan is low (0.25%), due to the three data points clustered around 12%, but it does not seem to reflect the true dispersion of the dataset. These questioning values appear mostly for SP-cells because of the even lower amount of samples for each condition within a batch due to practical limitations, and the statistical results should hence be considered carefully. The PV parameter for the champion cell of each condition (found both in batch 2) are given in table 3.3.

All batches gather a collection of ALD-based cells and SP-based cells. The conditions of synthesis (preparation of the cells, deposition of the mesoporous titania, of the perovskite, of the HTL and of the Au electrode, atmospheric conditions in the lab) and of characterization were similar within a batch, with the obvious

3.4 Integration of ALD-TiO₂ layers as compact ETL in perovskite solar cells

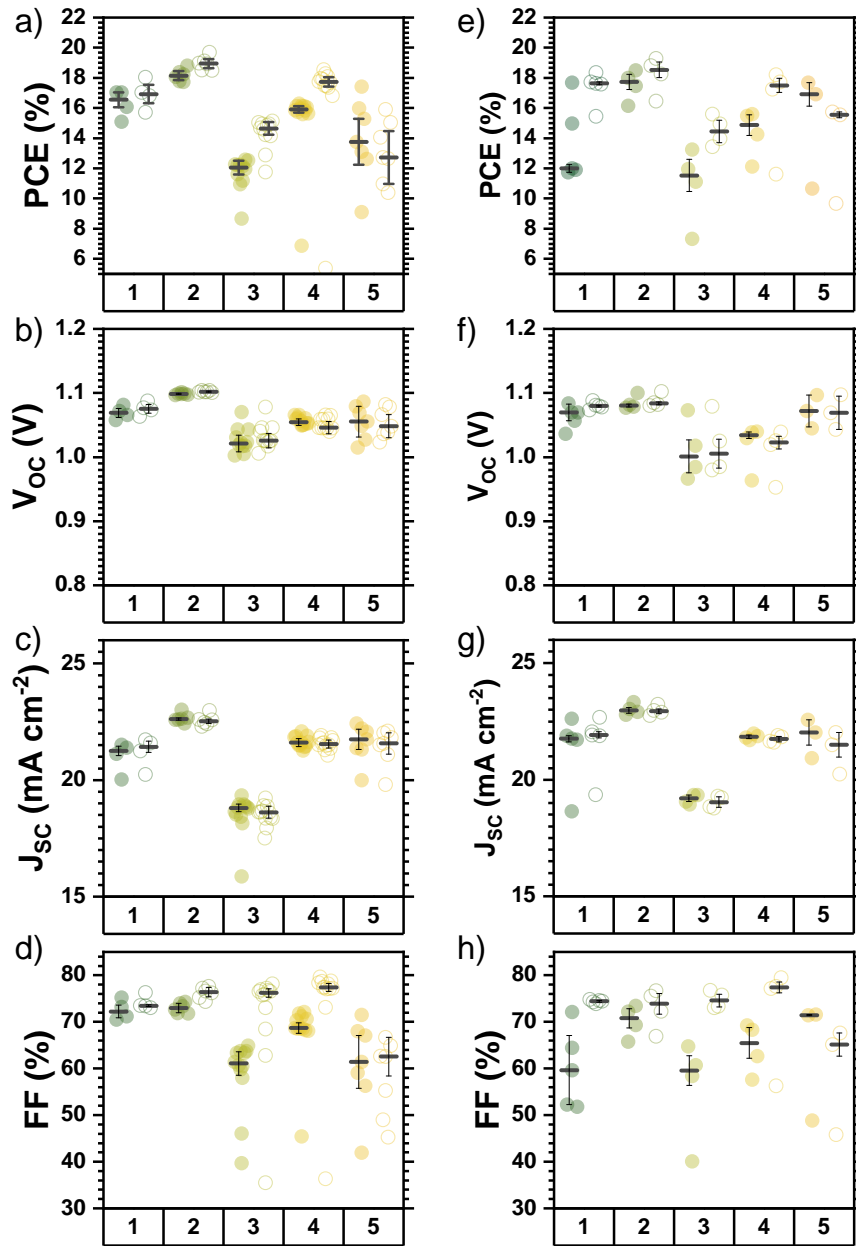


Figure 3.11: PV parameters of 5 batches comparing cells deposited on ALD-TiO₂ (a-d) and SP-TiO₂ (e-h). a,e) PCE, b,f) V_{OC} , c,g) J_{SC} and d,h) FF are displayed for forward (full circles) and reverse (open circles) scan directions. The median and MAD of each dataset are given in black.

exception of the deposition of c-TiO₂. The time window during which these different

3.4 Integration of ALD-TiO₂ layers as compact ETL in perovskite solar cells

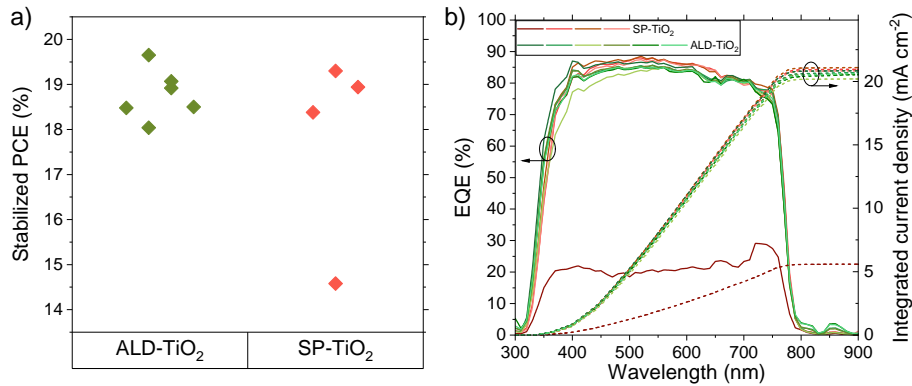


Figure 3.12: a) MPPT and b) EQE of the best batch comparing cells using SP- and ALD-TiO₂. the tracking was performed between 3 min and 5 min of continuous illumination at 1 sun (AM1.5G spectrum). The integrated current density are derived from the EQE measurements.

batches were deposited spans over a year in which the atmospheric conditions in the lab varied. This can account for the large variability of the parameters observed in between the batches (PCE < 15% for batch n°3 whereas PCE > 18% for batch n°2). Within a single batch, the PCE of SP-cells and ALD-cells are quite similar. However, breaking down the contribution of the V_{OC} , J_{SC} and FF, specific trends appear depending on the nature of the compact layer of TiO₂. The short circuit current density is lower for ALD-TiO₂ by 0.2 to 0.5 mA cm⁻², which will be discussed later in this section. The V_{OC} of ALD-based cells is usually slightly higher than that of SP-based cells, but this trend cannot be consistently assessed and can be due to an intra-batch variability. These questions are addressed in sections 3.4.4 and 3.4.5. The largest difference between the conditions concerns the fill factor and the resulting hysteresis of the cells. A reduction of the hysteresis of variable magnitude depending on the batch considered in ALD-based cells is observed, which is correlated with more consistent values of the forward and reverse fill factors. The origin of this feature is still unknown.

Figure 3.12 focuses on the best performing batch (batch n°2). The stabilized output power for the two architectures are given in Figure 3.12.a. The values are given as the mean of the output power of a cell between 3 min and 5 min of MPPT under 1 sun illumination. As suggested by the PCE extracted from the J-V curves, the ALD-based cells perform equally good compared to the SP-based cells, with a good reproducibility. The spectral quantum responses of the cells were also compared. The EQE and the resulting integrated current of the different cells are displayed in Figure 3.12.b. The values of the integrated J_{SC} differ from the J-V J_{SC} by 1 mA cm⁻². Such mismatches have already been reported in perovskite devices, although in the case of the best performing cells, the EQE measurements match the J-V measurements (J. Jeong et al. (2021)). This feature can be due to calibration issues or to intrinsic causes in the material, such as micro shunts or barriers for the photo current (Scheer and Schock (2011)). Nevertheless, it corroborates the trends observed in the J-V measurements, in that the integrated

3.4 Integration of ALD-TiO₂ layers as compact ETL in perovskite solar cells

J_{SC} of SP-based cells is higher than that of ALD-based cells. The loss in J_{SC} is spread across the whole absorption range. As is visible in [Figure 3.9](#), ALD-TiO₂ substrates have a lower transmission in the absorption range of the perovskite compared to SP-TiO₂ substrates, which can account for this lower current density. A last observation on the EQE spectra is that the EQE plateaus at 87%, whereas best performing devices are reported to have EQE higher than 95% (J. Jeong et al. (2021)), resulting in lower J_{SC} of the cells. Some current can be gained by optimizing the light management in the devices by increasing the transmission of the substrate (use of thinner glass, working on the TCO, adding an anti-reflective coating), but that was not part of the work presented here.

In summary, this section shows that compact titania synthesised by ALD can be successfully implemented in working devices, which display similar performances as the reference based on compact titania deposited by spray pyrolysis. In spite of having similar performances, the two architectures differ, the SP-based cells having usually a higher J_{SC} but the ALD-based cells having a higher FF, and an increased reproducibility within a batch.

3.4.4 Photoluminescence imaging of half cells

In order to get an idea of the quality of the ETL/perovskite interface without being influenced by the HTL, steady state photoluminescence spectra of half cells were acquired. The results are presented in [Figure 3.13.a](#). The spectra were acquired between 4.4 and 4.8 sun. Going towards lower illumination levels requires longer acquisitions to obtain a reasonable signal-to-noise ratio which could alter the analysis of the spectrum (Cacovich et al. (2020)). The obtained spectra were fitted with the generalized Planck law ([Equation \(1.9\)](#)) with the absorption model described in [section 2.3.2.3](#), with relative reconstruction errors lower than 3%. The results of the fit are presented in [chapter A.3](#). The three samples can be fitted with a similar QFLS of 1.220 ± 0.001 eV as displayed in [Figure 3.13.b](#). However, the fitted band gap of the perovskite on either of the ETL (SP-TiO₂ and ALD-TiO₂) is higher by 20 mV than the one of the perovskite on glass. This is supported by the slight red-shift of the PL spectra on ETL. This results in a larger V_{OC} deficit ($\Delta\mu - qV_{OC}$) in the case of perovskite deposited on an ETL, in line with additional non-radiative recombination pathways. From the V_{OC} deficit, the PLQY of each absorber can be estimated: PLQY = 0.041% for the perovskite film on glass, and PLQY = 0.022% for the perovskite on either ETL. These medium values of PLQY indicate that there is still improvements to be made in the quality of the absorber, given that PLQY up to 5% have been reported for perovskite – even though it is highly dependent on the chemical composition of the perovskite (Caprioglio et al. (2019); Zhifa Liu et al. (2019)). The lower values of the PLQY for the films deposited on the ETLs confirm the presence of additional non-radiative recombination pathways, and their similar values indicate that they have the same magnitude of defects. In the end, SSPL measurements support the observation from the J–V measurements that the V_{OC} is not consistently dependent on the nature of the compact layer in the mesoporous architecture.

3.4 Integration of ALD-TiO₂ layers as compact ETL in perovskite solar cells

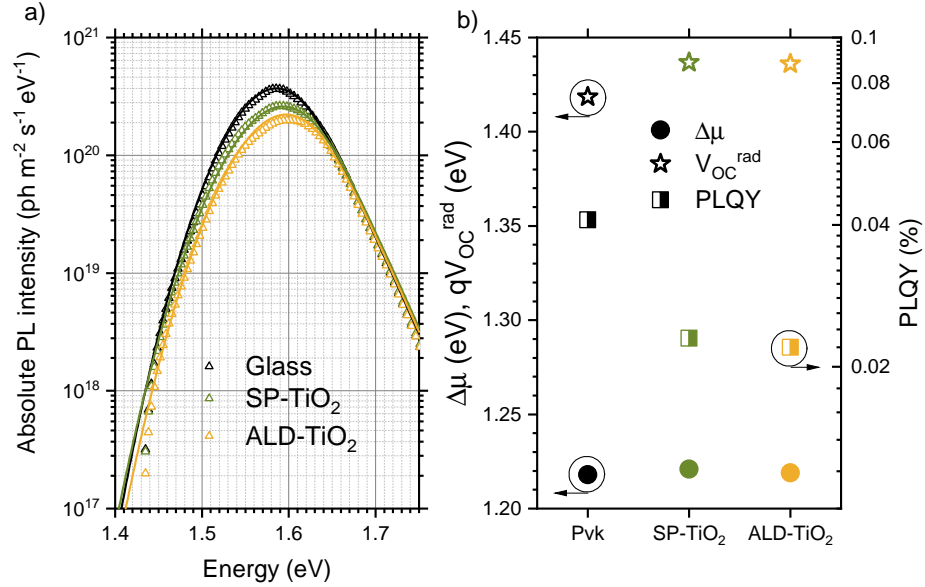


Figure 3.13: a) Absolute steady state photoluminescence spectra of half cells composed of perovskite on glass (glass), perovskite on glass/SP-TiO₂/mp-TiO₂ (SP-TiO₂) and perovskite on glass/ALD-TiO₂/mp-TiO₂ (ALD-TiO₂) under 4.4-4.8 sun excitation. The experimental results (empty triangles) are fitted with the generalized Planck law (full lines). b) The photoluminescence quantum yield (PLQY) and the quasi Fermi level splitting ($\Delta\mu$) for each substrate as extracted from the integrated PL. The radiative limit for the V_{OC} at the corresponding illumination is also included.

3.4.5 Integration into planar devices

Cells based on ALD-TiO₂ show similar performances than cells based on SP-TiO₂, but still differ in their PV parameters. However, the mesoscopic architecture makes it harder to isolate the origin of the differences. Hence, an attempt to produce planar cells with TiO₂ as ETL was made. The fabrication was the same as the one described in [section A.1.1](#) up to after the deposition of the c-TiO₂ layer. The ALD substrates underwent an annealing step similar to the one used for the deposition of mp-TiO₂. Finally, all the substrates (annealed ALD-TiO₂ and SP-TiO₂) were exposed to UV-O₃ for 15 min before introduction in the glovebox for the deposition of the perovskite. The rest of the process was similar to the usual procedure.

As seen on the SEM images of [Figure 3.14.a-c](#), the top surfaces of the perovskite deposited on either substrate are similar, which suggests that the growth of the perovskite is not sensitive to the deposition process of the TiO₂. However, once integrated in full devices, the behaviors are completely different. [Figure 3.14.d](#) shows the J-V curves of the best working devices for each condition. First of all, the efficiency of the cells is much lower than what can be obtained with a

mesoscopic architecture. This is due to a concurrent drop of all PV parameters. This result is in agreement with the literature, where the compact titania is exclusively used in conjunction to a mesoporous scaffold in order to achieve high efficiency devices. The low mobility of TiO_2 is often reported as the cause because of which TiO_2 planar structures are not a viable option. High efficiency cells in planar architecture are usually achieved with other oxides such as SnO_2 , organic materials or a superposition of both (Al-Ashouri et al. (2019); Liyan Yang et al. (2018)).

Our low-efficiency cells allow nonetheless for a discussion on the differences between the nature of the ETL. The cell based on SP- TiO_2 has a PCE of 8.7%, with $V_{OC} = 1005$ mV, $J_{SC} = 12.2$ mA cm^{-2} and FF = 70.6%, while the ALD-based cell only performed at 1.1% with $V_{OC} = 786$ mV, $J_{SC} = 4.1$ mA cm^{-2} and FF = 34%. The very low short circuit current density is similar to what has already been reported in the literature for planar devices based on ALD titania deposited with TDMAT and H_2O_2 and MAPbI_3 as absorber (Correa Baena et al. (2015)). The authors suggest that this can arise from a barrier to the charge collection due to an energetic mismatch between the titania and the perovskite. However for the cells considered here, the very low V_{OC} indicates a high contribution of non radiative recombinations which in turn reduces the current density. The V_{OC} of planar ALD- TiO_2 cells is much lower than that of SP- TiO_2 cells which argues in favor of a more defective interface

Our attempt to process planar structures based on TiO_2 was unsuccessful but still provided qualitative insights on the TiO_2 /perovskite interface. Based on these observations, the higher fill factor observed in the mesoscopic case does not originate from a better quality of the perovskite/*c*- TiO_2 interface, but rather from the dynamics occurring between the compact and the mesoporous titania.

3.5 Conclusion

In this chapter, the use of titania ALD deposited with TTIP and H_2O as blocking layer in perovskite solar cells has been discussed. The modification of ALD- TiO_2 upon annealing at various temperatures up to 500 °C has been investigated. The properties of the material at 500 °C were especially important to characterize, because during the synthesis of the mesoporous layer, the compact layer undergoes an annealing at this temperature. Right after its synthesis, the properties of ALD- TiO_2 are different depending on the thickness of the layer. Thinner layers (< 17 nm) do not crystallize during the synthesis, while thicker layers crystallize in the anatase phase, similar to the SP- TiO_2 . The transmission of ALD- TiO_2 layers is not affected by the annealing but their structure is: all films crystallize in the anatase phase regardless of their thickness. No conclusion could be drawn on a sensible effect of the annealing on the size of the domain of coherence of the anatase phase but a shrinkage of the layers of 4% of their initial thickness was observed at 500 °C. For the thinner layers, this shrinkage may lead to the creation of pinholes in the compact layer. This behavior has been evidence with cyclic voltamperometry, where the thinnest layers (5 nm) lose their blocking ability in oxidation. For thicknesses above 10 nm, a slight increase of the leakage current was observed but the oxidation reaction was still delayed, confirming the integrity

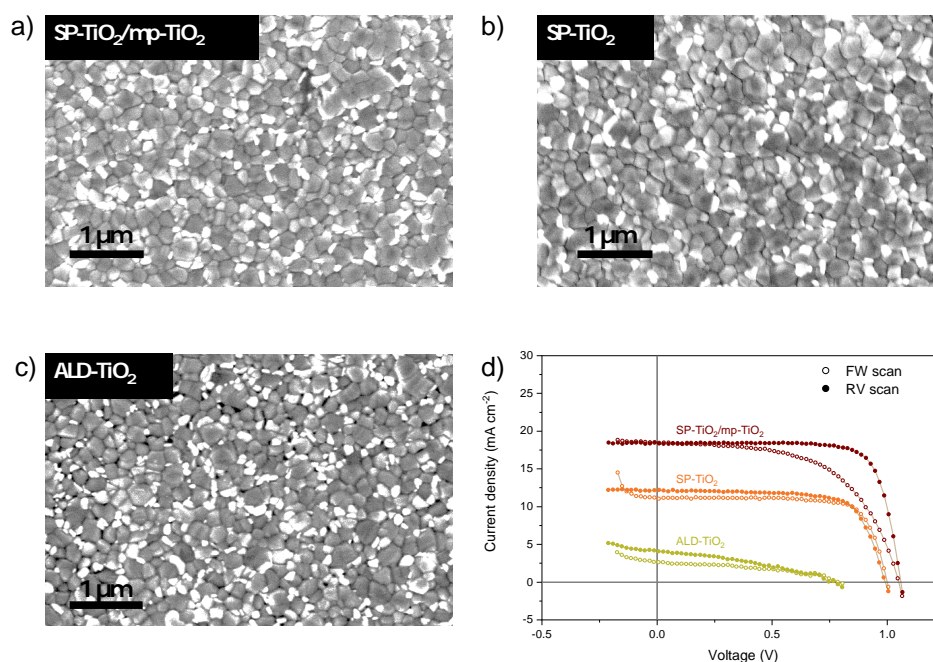


Figure 3.14: Integration of c-TiO₂ in planar devices. SEM top images of the perovskite deposited on top of a) SP-TiO₂/mp-TiO₂ bilayer, b) SP-TiO₂ compact layer and c) ALD-TiO₂ compact layer (magnification 25k). d) J-V curves of the best cell for each condition at 20 mV s⁻¹.

of the layer after annealing. In summary, the c-TiO₂ layer deposited by ALD has similar properties compared to the usual sprayed TiO₂. The ALD-TiO₂ also proved to be much more homogeneous over large substrates than the manually sprayed TiO₂, which is a common mean of depositing TiO₂ for perovskite applications. It has the benefit on small scale cells to narrow down the causes of variability in a batch and to allow for more controlled studies on the other constitutive layers of the cell, and on large cells to ensure the homogeneity of the blocking layer, which is of high importance.

Since the presence of pinholes would lead to shunt pathways in a complete device, only layers of ALD-TiO₂ thicker than 10 nm were integrated in perovskite solar cells. In mesoscopic architectures, the role of the compact layer is mostly to prevent the transport of holes toward the negative electrode. The growth of the perovskite is mostly influenced by the mesoporous scaffold, which explains why the properties of the perovskite layer are very similar on SP-TiO₂/mp-TiO₂ or on ALD-TiO₂/mp-TiO₂. The morphology of the perovskite is actually similar even if grown directly on the compact layers. All the similarities found so far between the ALD-TiO₂ and the SP-TiO₂ also reflect in the performance of full cells, where similar stabilized efficiencies up to 19.65% for ALD-TiO₂ and 19.30% for SP-TiO₂ are achieved. The breakdown of the PV parameters indicates however that the

cells do not operate exactly similarly; the SP-TiO₂ cells usually display a higher short circuit current density, while the ALD-TiO₂ have an enhanced reproducibility and fill factor.

Since the quality of the perovskite/*c*-TiO₂ is not better (in terms of defects), the increase in fill factor could be due to different dynamics between the mesoporous and compact layers, but the origin of these differences are still to be further investigated. The ALD-TiO₂ layer is very resistive, which can lead to preventable losses. With ALD, it is possible to tune the chemistry of the deposited layer by adding doping species or making nanolaminate layers of different materials. These approaches could be used in order to increase the electron conductivity of the compact TiO₂. Finally, the deposition of TiO₂ by ALD can ease the upscale of perovskite cells towards mini-modules. The differences between the SP-TiO₂ and ALD-TiO₂ could be further emphasized at larger scales.

Chapter 4

Optimization and integration of ALD-SnO₂ in perovskite solar cells

4.1 Motivation

As reported in [chapter 2.2](#), tin (IV) oxide is a wide band gap, transparent, n-type semiconductor, which usually exhibits a superior conductivity than TiO₂. SnO₂ has been used in PV technologies, albeit in fewer occasions than TiO₂. Before being used in perovskite solar cells, SnO₂ has mostly been investigated as a TCO when doped or alloyed with other elements (*e.g.* F or In) or in DSSCs and organic solar cells (OSCs, [Pari et al. \(2013\)](#)).

4.1.1 SnO₂ in PSC: an efficient oxide in planar structures

From only a few studies published in 2015 up to several hundreds in 2019 ([K. Deng et al. \(2020\)](#)), the interest in SnO₂ as ETL of a PV device has rapidly risen within the perovskite community. The reason behind it lies in the shortcomings identified with the use of TiO₂. SnO₂ can be deposited with a variety of low temperature processes ($T < 180\text{ }^{\circ}\text{C}$, [Jiang et al. \(2016\)](#); [Ke, G. Fang, et al. \(2015\)](#); [C. Wang et al. \(2016\)](#)) which makes it compatible with a larger range of substrates than TiO₂. Its higher optical band gap (given around 4.0 eV for rutile and amorphous SnO₂, and around 3.2 eV for anatase TiO₂) makes it less reactive to UV radiations, limiting the photodegradation of the perovskite. Finally, its electron extraction properties are often considered superior to those of TiO₂ because of its higher electron mobility combined to a lower energy position of the conduction band minimum ([Correa Baena et al. \(2015\)](#)).

In the framework of perovskite solar cells, SnO₂ has been synthesized by various means such as: chemical bath deposition ([Anaraki et al. \(2016\)](#)), sol gel methods ([Ke, G. Fang, et al. \(2015\)](#)), deposition from a commercial colloid suspension ([Jiang et al. \(2016\)](#)) or ALD ([Correa Baena et al. \(2015\)](#)). The deposition and annealing

temperatures of SnO₂ often play a major role in the final efficiency of the PV device. The annealing of SnO₂ at moderate temperatures goes along with an increase of the performances, usually ascribed to a reduction of the defect concentration and an increase of the conductivity of the film. Yet, Ke, Zhao, et al. (2015) showed that low annealing temperatures (typically under 200 °C) preserve a good coverage of the substrate, while higher annealing temperatures cause the agglomeration of SnO₂ and reveal the underlying FTO, negating its hole-blocking capacity. Hence a balance must be found between the improvement of the quality of the SnO₂ film and the preservation of its hole-blocking ability (Jung et al. (2017)).

One of the main benefits of the use of SnO₂ as ETL is its ability to enable high efficiencies in planar architectures, significantly easing the fabrication process of perovskite solar cells. PCE above 21% are reached for planar devices based only on SnO₂ for the ETL (Jiang et al. (2017)). Even higher performances have been achieved by a careful optimization of the HTL/perovskite interface yielding cells with a PCE of 23.5% (Jiang et al. (2019)). The stability of the cell was also remarkable with no noticeable performance loss after 40 h under 1 sun illumination at maximum power point. Finally, the use of low temperature processes allows for the deposition of SnO₂ in p-i-n configurations on top of the absorber layer. Such a process was implemented in the most efficient monolithic perovskite on silicon tandem solar cell so far, reaching > 29% efficiency (Al-Ashouri et al. (2020)). This latter study uses ALD for the deposition of SnO₂ on top of a PCBM layer.

4.1.2 ALD-SnO₂ in PSC

Various ALD processes have been reported for the integration of ALD-SnO₂ layers in perovskite solar cells (Zardetto et al. (2017); Raiford et al. (2020)). The chosen Sn precursor is systematically TDMASn, while the O source varies (H₂O, O₂ plasma or O₃). The deposition temperature are usually very low (< 120 °C), suitable for a variety of n-i-p and p-i-n architectures. A comparative study of ALD-SnO₂ and ALD-TiO₂ (15 nm) has been proposed by Correa Baena et al. (2015) on planar n-i-p structures. A large discrepancy in the efficiency was observed: planar ALD-TiO₂ cells had a much lower J_{SC} (around 5 mA cm⁻²), while the ALD-SnO₂ cells displayed a J_{SC} of 21 mA cm⁻² and a PCE over 18%. S. Jeong et al. (2019) showed similar performances with a 12 nm-thick ALD-SnO₂ layer annealed at 180 °C after deposition. Higher annealing temperatures resulted in a loss of V_{OC} and FF due once again to a poorer hole-blocking ability. Both studies used O₃ as O source. As mentioned before, one of the major asset of ALD-SnO₂ is the low process temperatures. Several studies have examined the possibility to grow it directly on top of the perovskite layer. Hultqvist et al. (2021) discussed the degradation mechanisms induced by the exposure of the perovskite surface to the ALD precursors. These precursors have been shown to damage the surface of the absorber which leads to very poor PV performances. In contrast, devices including a PCBM interlayer had efficiencies comparable to that of their reference p-i-n cell. The use of an organic interlayer is thus essential to reach high efficiencies in p-i-n architectures, as demonstrated by Al-Ashouri et al. (2019) (> 18%).

4.2 Influence of post-annealing treatments on ALD-SnO₂ thin films properties

As mentioned in [chapter 2.2](#), tin oxide thin films in various stoichiometries were obtained by tuning the oxidizing reactant. The use of H₂O results in a lower incorporation of O in the thin films which are not suitable to be integrated (and thus not integrated) in perovskite solar cells. Tin oxide thin films obtained from TDMASn/H₂O₂ result in the formation of tin (IV) oxide and were selected. Contrary to what has been discussed for TiO₂ ([section 3.1.2.2](#)), there are no thermal post-deposition constraints on the SnO₂ film during its integration in PSCs. However, annealing the SnO₂ film may still prove beneficial in that it can change its properties (bulk and surface). With respect to its integration in PSCs as ETL (in an n-i-p configuration), the annealing of SnO₂ at 180 °C has often been reported beneficial for the cell, whether it is needed for a proper formation of the film (chemical bath deposition – CBD or sol-gel deposition) or simply used as a post-treatment step (S. Jeong et al. (2019); Y. Lee et al. (2018)). Besides, while as-deposited ALD-SnO₂ thin films grow amorphous ([section 2.2.4.2](#)), a crystallization into the rutile phase is commonly reported to occur between 200 °C and 300 °C. Hence, the effect of air-annealing at three different temperatures (180 °C, 300 °C and 500 °C) on ALD-SnO₂ was investigated. The annealing procedure is detailed in [section A.1.1](#). Unless stated otherwise, all films presented in this section are deposited at 100 °C. Two thicknesses have been studied: 15 nm which is a thickness commonly used for perovskite solar cells applications, and 80 nm to increase the signal and access more bulk-like properties of the film.

4.2.1 Structural properties

4.2.1.1 Determination of the thickness variation of the annealed ALD-SnO₂ thin films

The thickness of the films is investigated by XRR ([Figure 4.1](#)). The reflectograms are acquired for angles up to 1.1° (open circles) and are fitted using a Parratt model (full lines, same methodology as the one described in [chapter 3.2](#)). The fitted parameters are given in [Table 4.1](#). In the case of SnO₂ annealed at 180 °C and at 300 °C, the period of the Kiessig fringes increases slightly indicating a thinning of the film while the critical angle stays around similar values (when compared to the as-deposited sample). In the case of SnO₂ annealed at 500 °C however, the increase in the angular period of the Kiessig fringes is much more dramatic and goes along with a noticeable shift of the critical angle towards higher angles – suggesting an increase in the density of the material. The analysis of the fitted values of the thickness and of the density of the SnO₂ layers confirm these observations. The thickness of the film drops from 16.2 nm as-deposited to 12.4 nm (-24% relative change) after annealing at 500 °C, which correlates well with a variation of the film's density in the opposite direction from 6.4 g cm⁻³ for the as-deposited film to 7.7 g cm⁻³ (+20% relative change) for the film annealed at 500 °C. Interestingly, the variations of thickness and density can also be brought together with the change of crystallinity of the film observed by XRD. This is particularly supported by the

4.2 Influence of post-annealing treatments on ALD-SnO₂ thin films properties

Table 4.1: Fitted parameters of the XRR data of ALD-SnO₂ of 15 nm on Si substrate annealed at various temperatures. The stack is modeled with three layers Si/SiO₂/SnO₂. The thickness of Si is infinite, its density is set at 2.2 g cm⁻³. The uncertainties are given so that the fitting error does not increase by more than 10%.

Sample	Layer	Thickness (nm)	Roughness (nm)	Density (g cm ⁻³)
15 nm ref	SnO ₂	16.21 ± 0.03	0.55 ± 0.15	6.39 ± 0.10
	SiO ₂	2.1 ± 0.5	0.24 ± 0.10	2.9 ± 0.1
	Si		1.4 ± 0.5	
15 nm 180°C	SnO ₂	15.86 ± 0.05	0	6.35 ± 0.05
	SiO ₂	2.5 ± 0.7	0.1 ± 0.7	2.9 ± 0.1
	Si		1.5 ± 0.5	
15 nm 300°C	SnO ₂	15.48 ± 0.10	0	6.19 ± 0.10
	SiO ₂	3.0 ± 0.5	0	2.7 ± 0.1
	Si		0	
15 nm 500°C	SnO ₂	12.35 ± 0.03	1.12 ± 0.01	7.70 ± 0.07
	SiO ₂	4.8 ± 0.2	1.11 ± 0.05	2.6 ± 0.1
	Si		0.8 ± 0.2	

fact that the largest variations of thickness and density occur for temperatures between 300 °C and 500 °C where the material transitions from an amorphous phase to a crystalline (rutile) phase. The values of density found for the amorphous and crystalline phases are quite high compared to what can be found in the literature (Heo et al. (2010)). As Heo et al. (2010) suggest, it can originate from the fact that ALD-materials are usually more dense compared to materials synthesized by other deposition techniques. However, a probable overestimation of the density during the fitting procedure of the diffractograms at low angles cannot be disregarded.

4.2.1.2 Investigation of the crystalline phase of the ALD-SnO₂ films after annealing.

Figure 4.2 shows the diffractograms of 15 nm and 80 nm-thick SnO₂ films deposited on an ITO substrate (Figure 4.2.a and Figure 4.2.b respectively) and on a Si substrate (Figure 4.2.c and Figure 4.2.d respectively), along with reference patterns of rutile SnO₂ (JCPDS 41-1445) and cubic In₂O₃ (JCPDS 06-0416, accounting for the ITO substrate). All films were deposited during the same ALD run.

In all cases, the substrate itself contributes to the signal. For the 15 nm-thick samples, the diffraction peaks of SnO₂ are not visible after annealing at temperatures up to 300 °C on both substrates. At 500 °C however, diffraction peaks at $2\theta = 26.78^\circ$ (110), 34.21° (101), 38.38° (200), 52.36° (211), 62.50° (310) and 65.9° (112) appear, characteristic of the rutile phase of SnO₂. Hence, the film

4.2 Influence of post-annealing treatments on ALD-SnO₂ thin films properties

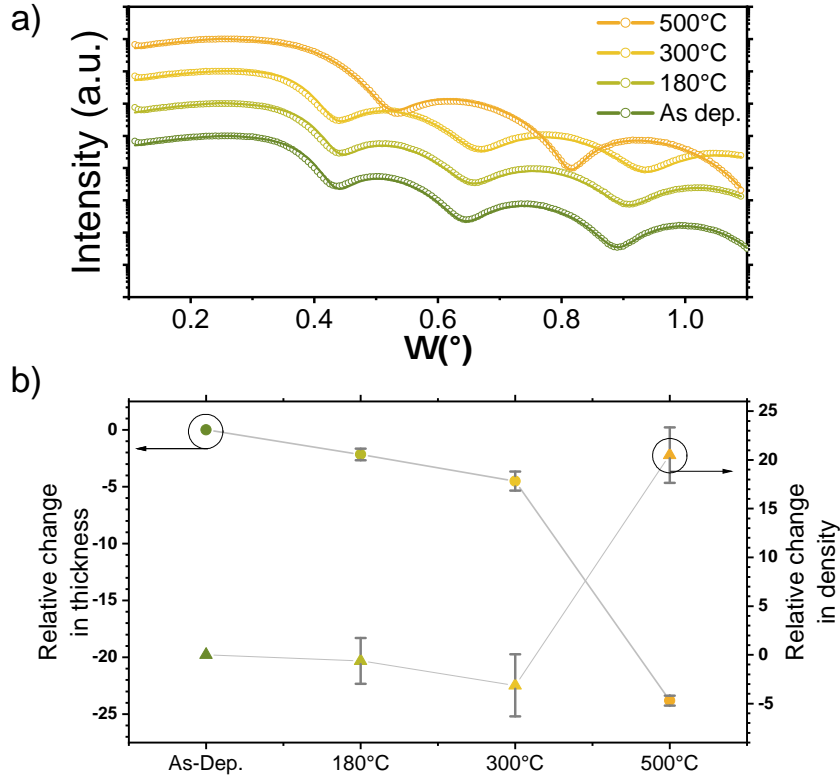


Figure 4.1: XRR analysis of ALD-SnO₂ films function of annealing temperature (as-deposited, 180 °C, 300 °C and 500 °C). a) Reflectograms of 15 nm-thick ALD-SnO₂ samples on Si annealed at various temperatures. The data are normalized and shifted for clarity. A Parratt-fit (full lines) is applied to the data points (open circles). b) Relative variation of the thickness (full circles) and density (full triangles) of the annealed samples. The reference thickness and density are those of the as-deposited film. Connecting lines are only here as guide lines.

crystalline after annealing at 500 °C, in agreement with the literature. One can also notice that the FWHM of the SnO₂ peaks are large (over 2° for most peaks), which indicates a high disorder in the structure of the film.

The 80 nm-thick sample exhibits additional features. While the material is also amorphous as-deposited and crystallized at 500 °C on both substrates, the situation changes for an annealing temperature of 300 °C. On the Si substrate, the film is still amorphous, while when grown on ITO the characteristic diffraction pattern of the rutile phase starts to appear, though with very broad and relatively low-intensity features (compared to the ITO substrate).

It points at conjugated effects of the thickness of deposited material and of the substrate on which the ALD layer is grown. The effect of the thickness (no crystallization for 15 nm on ITO vs. crystallization for 80 nm on ITO) can be compared to what has been observed for the c-TiO₂ layers in [chapter 3.2](#), and

4.2 Influence of post-annealing treatments on ALD-SnO₂ thin films properties

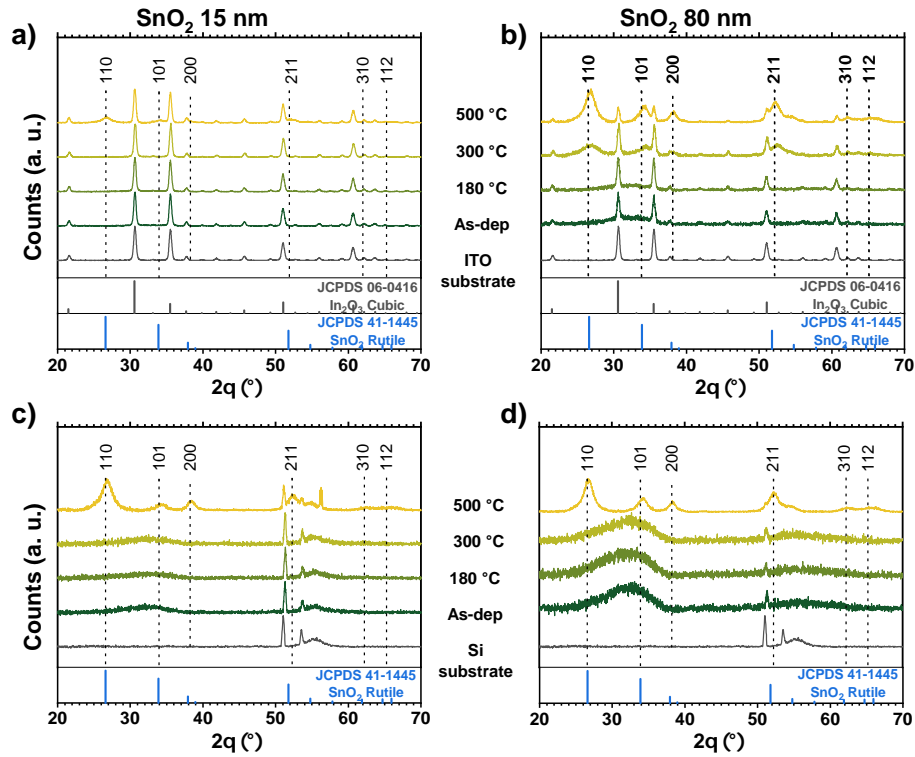


Figure 4.2: GI-XRD analysis of ALD-SnO₂ thin films function of the annealing temperature (as-deposited, 180 °C, 300 °C and 500 °C). Diffractograms of a) 15 nm and b) 80 nm ALD-SnO₂ deposited on ITO substrates, and of c) 15 nm and b) 80 nm ALD-SnO₂ deposited on Si substrates. The reference patterns of the cubic phase of In₂O₃ (JCPDS 06-0416) and of the rutile phase of SnO₂ (JCPDS 41-1445) are provided.

reported in the literature, where the crystallinity of oxides deposited by ALD increases with the deposited thickness (Shi et al. (2017)). It could also be related to a too low signal from the 15 nm-thick sample, which would fall below the detection range (even at 500 °C, the signal is much lower for 15 nm than for 80 nm). As for the effect of the substrate (no crystallization for 80 nm on the Si substrate vs. crystallization for 80 nm on the ITO substrate), it promotes or delays the crystallization of the ALD layer (Weinreich et al. (2013)). As discussed in [chapter 4.3](#), the use of SnO₂ for PSC devices is limited to low thicknesses (typically 20 nm), so this specific feature should not influence the rest of the study. It however underlines the fact that properties of ALD layers depend on the nature of the substrate.

4.2.2 Optical properties of the ALD-SnO₂ thin films

[Figure 4.3](#) displays the variations of the optical properties of the films before and after annealing. Photospectroscopy data are shown in [Figure 4.3.a](#). The

4.2 Influence of post-annealing treatments on ALD-SnO₂ thin films properties

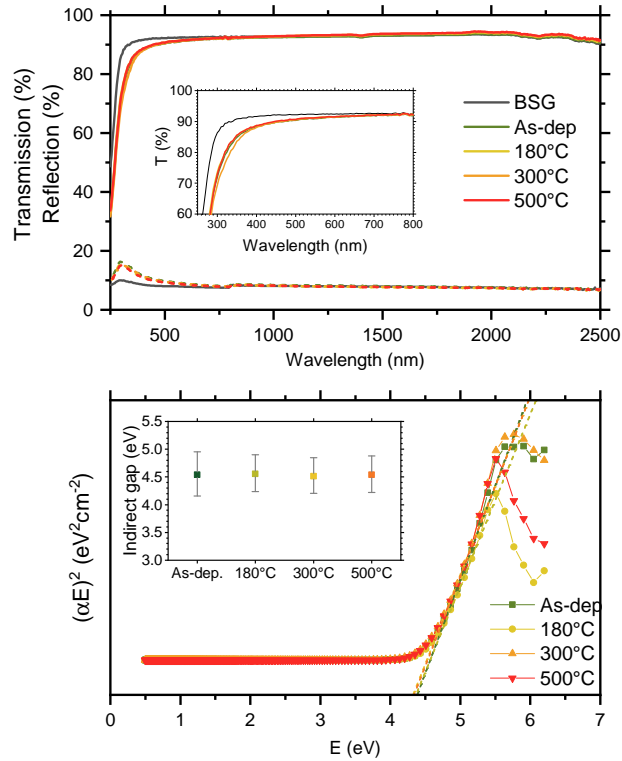


Figure 4.3: Optical properties of 15 nm-thick ALD-SnO₂ thin films function of the annealing temperature. a) Transmission (full lines) and reflectance (dashed lines) data of SnO₂/BSG specimen. The inset shows a magnification of the transmission at short wavelengths. b) Tauc-plot derived from the spectroscopic data for the determination of a direct band gap. The fit of the linear parts of the plot are shown in dashed lines. The inset gives the extracted direct band gaps function of the annealing temperature.

transmission and the reflectance data are acquired for thin films deposited on 2 nm-thick borosilicate glass (BSG). The light impinges the specimen on the glass side. The values of the optical direct band gaps are extracted via a Tauc plot analysis. Since the substrate has a relatively high and steady transmission near the absorption edge of SnO₂ (above 350 nm), the absorption is calculated from the transmission and reflectance data of the stack thin film/substrate, although an additional error on the derived values cannot be excluded. The thicknesses are extracted from ellipsometry measurements.

The transmission and the reflectance of the SnO₂ layers are excellent (> 85% in the visible-IR range, including 8% loss due to the glass substrate) and do not vary much upon annealing over the whole range of wavelengths, especially in the range of interest for perovskite solar cells (below 800 nm for single cells, below 1100 nm for Si/perovskite tandem applications). The inset of Figure 4.3.b presents the variations of the direct band gap energy with the annealing temperature, as extracted from the linearization of the Tauc plot near the absorption edge. Similarly

4.2 Influence of post-annealing treatments on ALD-SnO₂ thin films properties

to what has been discussed in [section 3.2.2](#), the large uncertainties on the band gap originates from the constant wavelength step of the spectrophotometer. There are no obvious variation of the direct band gap, determined at 4.5 ± 0.4 eV, which is in line with the values observed in the literature for SnO₂ (Mullings et al. (2013)).

4.2.3 Characterization of the blocking abilities of the ALD-SnO₂ thin films

The blocking ability of tin oxide deposited on a conductive electrode is investigated by cyclic voltametry. The I-V characteristics for two voltage sweeps ($V \in [-0.7V; 1.0V]$, all potentials vs. SCE) are presented in [Figure 4.4](#) for various thicknesses of as-deposited ALD-SnO₂ on an FTO electrode (10 nm, 15 nm and 20 nm), and air-annealed 15 nm ALD-SnO₂ (180 °C, 300 °C and 500 °C) deposited on an ITO electrode. For all samples, the n-type nature of the oxide and its good hole-blocking ability are confirmed by the effective inhibition of the oxidation reaction at the working electrode at positive potentials (vs. V_{OC}) and the promotion of the reduction at the working electrode at negative potentials (vs. V_{OC}). Interestingly, for all samples the two scans superimpose quite well hinting for a good stability of the surface properties during the experiment. Contrary to what was observed for TiO₂ layers ([chapter 3.2](#)), the thickness of SnO₂ does not have a large influence on the position of the cathodic peak which is located at -0.40 V vs. SCE, with values comparable as what can be found in the literature for other deposition techniques (Ko et al. (2017)). This would mean that the surface state of the samples is relatively independent of the thickness of the film. It is quite in line with the conclusions of [section 2.2.5](#) where the properties of SnO₂ are determined to be stable with respect to the thickness of the film (except for optical ones). As the thickness of the oxide increases, the anodic current decreases which is similar to what is observed for TiO₂ layers (cf [chapter 3.2](#)).

The annealing changes the shape of the voltamograms. The curves can be grouped in two sets: on the one hand the as-deposited sample and the sample annealed at 180 °C which have a cathodic peak at $V = -0.4$ V vs. SCE, and on the other hand the samples annealed at 300 °C and 500 °C whose cathodic peaks are shifted towards higher potentials ($V = -0.2$ V vs. SCE). The changes could originate from a thermal degradation of the TCO properties of the ITO electrode (degradation reported from 250 °C depending on the quality of the ITO substrate), but similar voltamograms are obtained for SnO₂ deposited on a much more stable FTO electrode. Thus, the shift of the peak is related to a change in the SnO₂ layer and matches the structural changes observed by the XRD measurements ([section 4.2.1.2](#)). Finally, the anodic current also increases as the annealing temperature increases, which can be related to the shrinkage of the layer observed with XRR.

4.2.4 Conclusions on the annealing study

In this section, tin oxide layers deposited by ALD after annealing at various temperatures going from 180 °C (a temperature usually found in the literature when integrated in solar cells) to 500 °C (a temperature at which the layer is reported to

4.2 Influence of post-annealing treatments on ALD-SnO₂ thin films properties

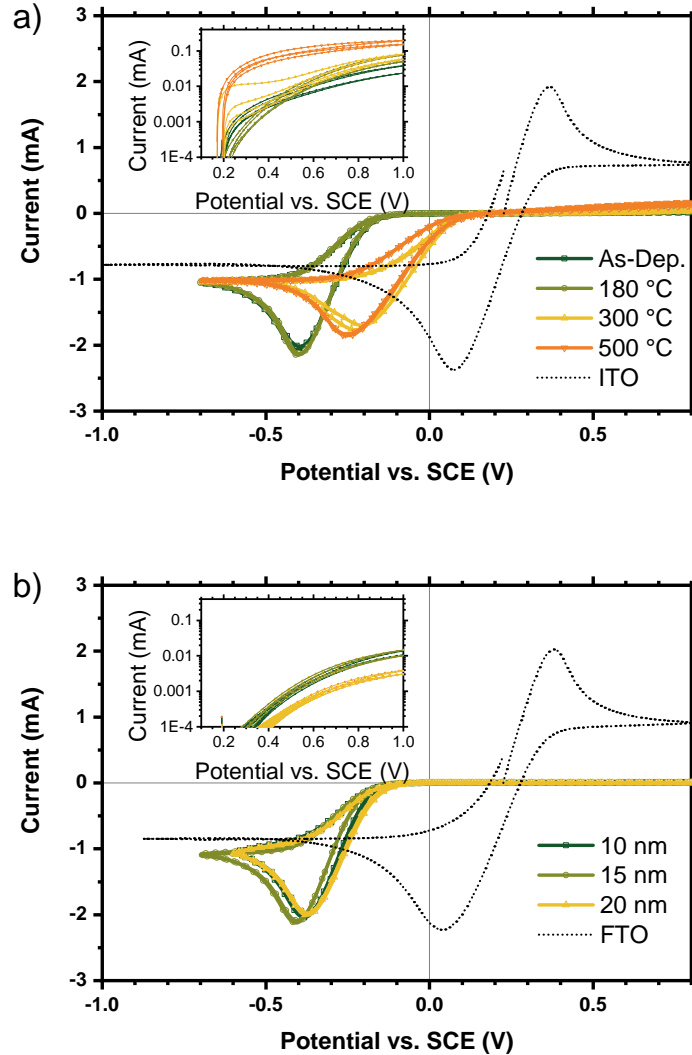


Figure 4.4: a) Voltamograms over two cycles of 15 nm-thick ALD-SnO₂ films annealed at various temperatures (as-deposited, 180 °C, 300 °C and 500 °C) on an ITO electrode. The voltamogram of the bare ITO electrode is added for comparison. b) Voltamograms over 2 cycles of as-deposited ALD-SnO₂ of thickness 10 nm, 15 nm and 20 nm deposited on an FTO electrode. The voltamogram of the bare FTO electrode is added for comparison. The insets (figures a and b) show the $I > 0$ region in log scale to evaluate the leakage current. The cycles start at open circuit condition with increasing voltage.

be crystalline) on different substrates (including target substrates for PSC) were characterized. For all conditions, the SnO₂ thin films have a wide optical band gap associated to a high transmission in the visible range, compatible with its use as front selective contact. They exhibit a good thermal stability and the essential hole

4.3 Integration of ALD-SnO₂ layers in planar perovskite solar cells

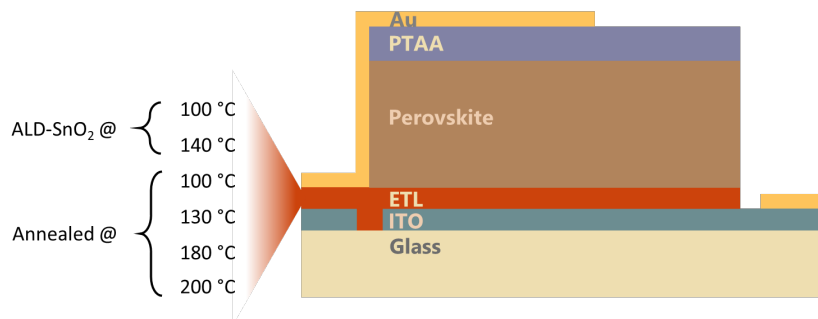


Figure 4.5: Sketch of the cell architecture for the study on the effect of the annealing and deposition temperatures of SnO₂ in full devices.

blocking layer ability of ALD-SnO₂ is preserved upon annealing. The structure of the annealed layer differ slightly: the ones annealed at low temperatures remain amorphous while the ones annealed at high temperatures start to crystallize in the rutile phase. This crystallization goes along with a reduction of the thickness of the film and a modification of the surface electronic properties. As stated in [chapter 4.1](#), amorphous SnO₂ ETLs are usually preferred when integrated in perovskite solar cells so only ALD layers annealed at low temperatures (< 200 °C) are selected for integration.

4.3 Integration of ALD-SnO₂ layers in planar perovskite solar cells

This section focuses on the integration of ALD-tin oxide layers developed and characterized in [chapters 2.2](#) and [4.2](#) in planar perovskite solar cells. The influence of the deposition temperature and of the thermal post-treatment on the performance of the devices is assessed ([section 4.3.1](#)). As suggested by the literature, an attempt to improve the cell performances by adding a layer of PCBM is described. The wettability of the perovskite solution on the PCBM is quite poor so various ways of increasing its wettability in order to obtain homogeneous perovskite layers on larger substrates were compared ([section 4.3.2.3](#)). Finally, the thickness of SnO₂ is varied and its impact on the final cells is discussed ([section 4.3.3](#)). The same masking procedure as the one developed for TiO₂ ([chapter 3.3](#)) was used here.

4.3.1 Influence of the deposition temperature and of the annealing temperature

SnO₂ is deposited on a 13×15 cm² sheet of masked glass/ITO in which 42 substrates of size 19×19 mm² are cut to make small cells. The samples are cleaned with acetone and IPA (5 min each in ultrasonic bath) to remove all traces of marker

4.3 Integration of ALD-SnO₂ layers in planar perovskite solar cells

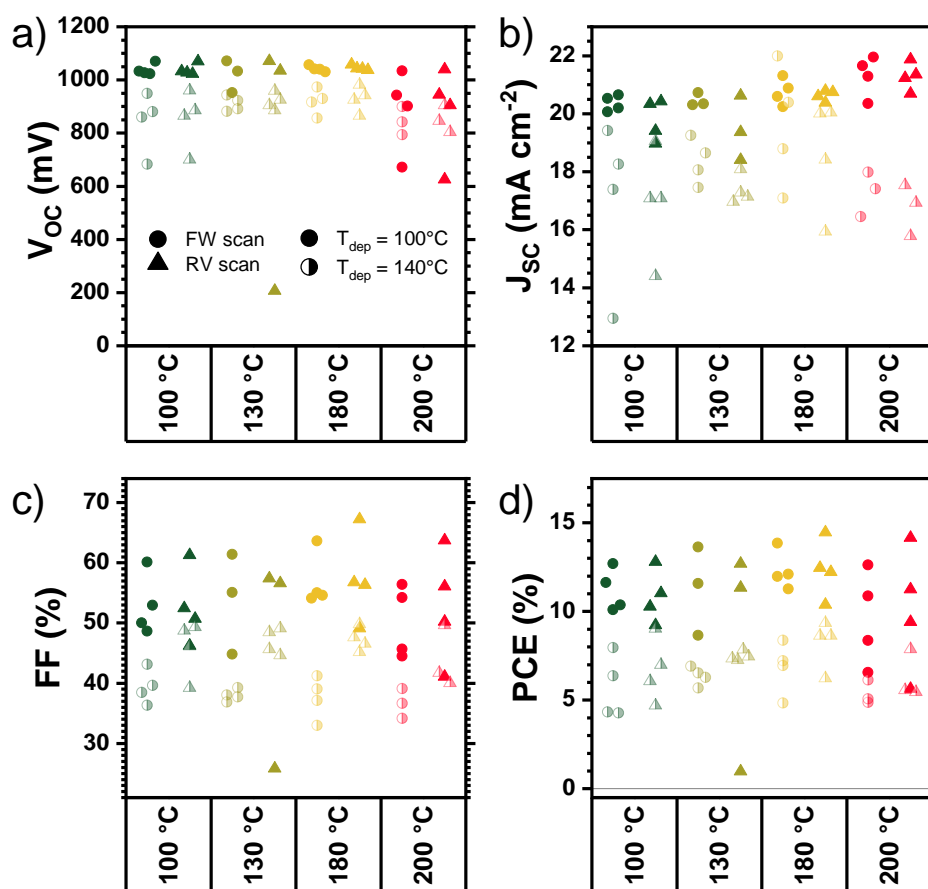


Figure 4.6: PV parameters function of the thickness of the ALD-SnO₂ layer acquired at 20 mV s⁻¹ under 1 sun simulated illumination (a) V_{OC} , b) J_{SC} , c) FF and d) PCE. Circles are the parameters measured in forward scan, triangles those measured in backward scan. The full symbols correspond to ALD-SnO₂ deposited at 100 °C and half-full symbols to ALD-SnO₂ deposited at 140 °C. The data given for an annealing temperature of 100 °C (resp. of 130 °C) correspond to the as-deposited condition for SnO₂ deposited at 100 °C (resp. at 140 °C).

pen ink, and the samples are then annealed for 1 h in the Nabertherm muffle furnace. Before introduction in the glove box, the samples are treated with UV-O₃ for 15 min. The same perovskite as presented before is deposited shortly after in the glovebox. The HTL consists in poly(triaryl amine) (PTAA), dissolved at 10 mg mL⁻¹ in toluene. PTAA is doped with Li-TFSI and ^tBp (2.5 μL and 3.75 μL for 1 mL of PTAA respectively). The deposition conditions are the same as the one described for the Spiro-OMeTAD in [section A.1.1](#). Finally a 100 nm-thick gold layer is deposited on top of the stack by metallic evaporation as back electrode to complete the cell, for a total active area of 9 mm². A schematic of the final architecture is provided in [Figure 4.5](#).

In order to mitigate the inter-batch variability, all the annealing conditions

4.3 Integration of ALD-SnO₂ layers in planar perovskite solar cells

are tested in each batch of 16 cells. To mitigate the intra-batch variability, the conditions are alternated during all the synthesis (*e.g.* deposition of one cell with condition A, then one with condition B, then back to condition A ...). The performances of cells with SnO₂ deposited at 100 °C and annealed at 130 °C, 180 °C and 200 °C or as-deposited are compared in Figure 4.6. The J–V characteristics are acquired under 1 sun illumination at a scan rate of 20 mV s⁻¹. Table 4.2 sums up the PV parameters of the cells. The PCE of the cells increases slightly upon annealing from 11.20% for the as-deposited SnO₂ up to 12.30% for SnO₂ annealed at 180 °C (FW scan). It then decreases to 9.6% for SnO₂ annealed at 200 °C. The efficiencies are quite low compared to what can be found in the literature (Correa Baena et al. (2015); Anaraki et al. (2016); C. Wang et al. (2016)). For annealing temperatures up to 180 °C, the V_{OC} is not varying much with mean values around 1040 mV. The increase of the PCE of the cells essentially originates from a slight increase in FF (from 53% to 57%). The larger loss of performance observed when the SnO₂ layer is annealed at 200 °C is mostly due to a dramatic loss of V_{OC} (V_{OC} = 890 mV) and of FF (FF = 50%), which are only slightly counterbalanced by a gain in J_{SC} (J_{SC} = 21.3 mA cm⁻²). Similar behaviors have been reported by S. Jeong et al. (2019) after annealing ALD-SnO₂ films at 180 °C and 300 °C, with a loss of PCE mostly due to a loss of FF and V_{OC} along with an increase in the variability of the PCE at 300 °C. The authors ascribed this loss of performance at high annealing temperatures to a decrease of the hole blocking ability of the film as it transitions from an amorphous to a crystalline phase. The same observation has been made by Y. Lee et al. (2018) for solution-processed SnO₂.

The influence of the deposition temperature of the SnO₂ layer has also been investigated and the PV parameters of cells synthesized in similar conditions on SnO₂ grown at 140 °C are presented in Figure 4.6 by half-full symbols. The performances are lower than for the cells deposited at 100 °C, with a maximal PCE just above 9%. There is a global loss in all PV parameters but also quite interestingly a larger variability within the batch. Wang et al. also experienced these variations (especially for the FF and the V_{OC}) when varying the deposition temperature of their PE-ALD SnO₂ from 50 °C to 100 °C (increase) and from 100 °C to 200 °C (decrease). The increase in performances between 50 °C and 100 °C was explained by a higher reactivity of the precursors during the ALD depositions at higher temperatures, while the decrease at higher temperatures was once again ascribed to the crystallization of SnO₂. Here, it can also be related to a poorer homogeneity of the deposition of SnO₂ at 140 °C (section 2.2.3.3). As this inhomogeneity reveals an issue about the ALD process at this temperature (*e.g.* decomposition of the precursor or inadequate duration of the ALD steps), the quality of the oxide layer can be affected.

The outcome of this parametric study on the deposition and annealing temperatures is that best-performing cells are obtained with SnO₂ grown at reasonably low temperature (100 °C) and annealed at 180 °C, which is in agreement with the findings previously reported for this kind of material. With this simple optimization, cell efficiencies up to 14.4% (reverse direction) were reached. This value is however still quite far from the state of the art. Looking at each PV parameter,

4.3 Integration of ALD-SnO₂ layers in planar perovskite solar cells

Table 4.2: Average PV parameters of cells based on ALD-SnO₂ compact layer function of the annealing temperature, where SnO₂ deposited at 100 °C (top) and at 140 °C (bottom) are separated by the median line. The quantities are given in forward (roman style) and backward (*italic style*) scans, for a scan speed of 20 mV s⁻¹.

	V_{OC} (mV)	J_{SC} (mA cm ⁻²)	FF (%)	PCE (%)
As-dep	1038 ± 22	20.4 ± 0.3	52.9 ± 5.1	11.20 ± 1.21
	<i>1039 ± 21</i>	<i>19.8 ± 0.7</i>	<i>52.7 ± 6.3</i>	<i>10.84 ± 1.51</i>
130 °C	1018 ± 61	20.5 ± 0.2	53.8 ± 8.4	11.29 ± 2.50
	<i>1053 ± 26</i>	<i>20.0 ± 0.9</i>	<i>57.0 ± 0.6</i>	<i>12.03 ± 0.95</i>
300 °C	1042 ± 11	20.8 ± 0.5	56.8 ± 4.6	12.30 ± 1.09
	<i>1045 ± 9</i>	<i>20.6 ± 0.2</i>	<i>57.3 ± 7.5</i>	<i>12.38 ± 1.67</i>
500 °C	887 ± 154	21.3 ± 0.7	50.2 ± 6.0	9.61 ± 2.68
	<i>879 ± 178</i>	<i>21.3 ± 0.5</i>	<i>52.8 ± 9.6</i>	<i>10.12 ± 3.57</i>
100 °C	844 ± 113	17.0 ± 2.8	39.4 ± 2.8	5.74 ± 1.77
	<i>853 ± 110</i>	<i>16.9 ± 1.9</i>	<i>45.6 ± 4.6</i>	<i>6.70 ± 1.82</i>
As-dep	910 ± 28	18.4 ± 0.8	38.0 ± 1.0	6.36 ± 0.52
	<i>919 ± 32</i>	<i>17.4 ± 0.5</i>	<i>47.0 ± 2.2</i>	<i>7.49 ± 0.26</i>
300 °C	920 ± 48	19.6 ± 2.1	37.6 ± 3.5	6.85 ± 1.48
	<i>929 ± 49</i>	<i>18.6 ± 1.9</i>	<i>47.3 ± 1.9</i>	<i>8.22 ± 1.37</i>
500 °C	846 ± 53	17.3 ± 0.8	36.7 ± 2.5	5.37 ± 0.68
	<i>852 ± 51</i>	<i>16.8 ± 0.9</i>	<i>43.8 ± 5.1</i>	<i>6.30 ± 1.37</i>

it seems that there is still potential to gain in V_{OC} (the radiative limit derived in section 1.1.4.2 gives a theoretical V_{OC} of 1.32 V for an absorber with a gap of 1.6 eV, V_{OC} above 1.1 V are realistically achievable provided a good spatial homogeneity of the materials (U. Rau et al. (2004)) and in J_{SC} . However, the largest area of improvement is related to the FF which is about 60% in these cells, while it can usually get over 75%.

4.3 Integration of ALD-SnO₂ layers in planar perovskite solar cells

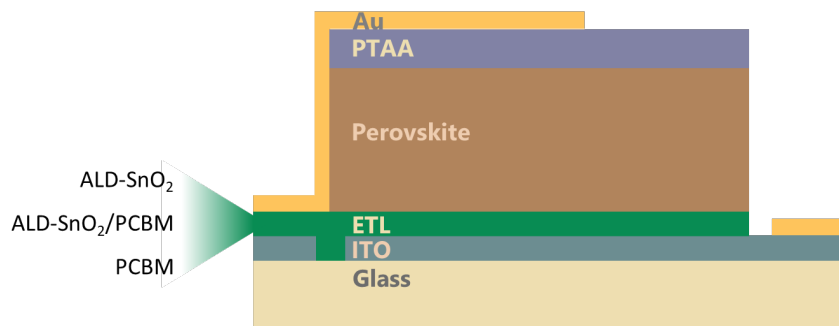


Figure 4.7: Sketch of the cell architecture for the study on the effect of the addition of PCBM on SnO₂ in full devices.

4.3.2 Passivation with PCBM

Based on this observation an interlayer between the perovskite and the oxide was added in order to enhance the carrier collection and improve the quality of the ETL/absorber interface. Fullerene derivatives have been an attractive way of modulating the properties of this interface on various oxides including TiO₂ and SnO₂ (Kumari et al. (2018)). The widely used Phenyl-C₆₀-butyric acid methyl ester (PCBM) – acknowledged for its passivating properties (Zhong et al. (2020)) – has been chosen.

4.3.2.1 Basic properties and deposition process

PCBM is an organic n-type semiconductor which is widely used in organic PV (Berger and M. Kim (2018)) or OFET (Nam et al. (2012)). Its lowest unoccupied molecular orbital (LUMO) has been reported at 3.8 eV and its highest occupied molecular orbital (HOMO) at 5.8 eV with respect to the vacuum level from UV photoemission spectroscopy and inverse photoelectron spectroscopy (Guan et al. (2010)). It has hence a smaller band gap than the metal oxides which are discussed in this manuscript (2.0 eV). In the scope of perovskite solar cells, PCBM has been used either blended with the perovskite ink or as an interlayer acting as ETL on n-i-p and p-i-n architectures (Xu et al. (2015); J. Jeong et al. (2021)). The studies made on PCBM agree on the fact that the layer simultaneously improves the charge extraction, helps towards the passivation of the defects and limits the iodide migration (Junke Wang et al. (2019)). The deposition process used in this study follows one which is widely used in the literature and is done in the controlled atmosphere of a glovebox. PCBM is dissolved in chlorobenzene at 5 mg mL⁻¹ shortly before the deposition. For convenience, a stock solution with a PCBM concentration of 25 mg mL⁻¹ could be used up to 1 month after dissolution without reducing the quality of the final cell if the stock solution is diluted down to 5 mg mL⁻¹ just before the deposition. The SnO₂ samples are introduced in the glovebox after 15 min of UV-O₃ treatment. Once in the glovebox, the deposition of

4.3 Integration of ALD-SnO₂ layers in planar perovskite solar cells

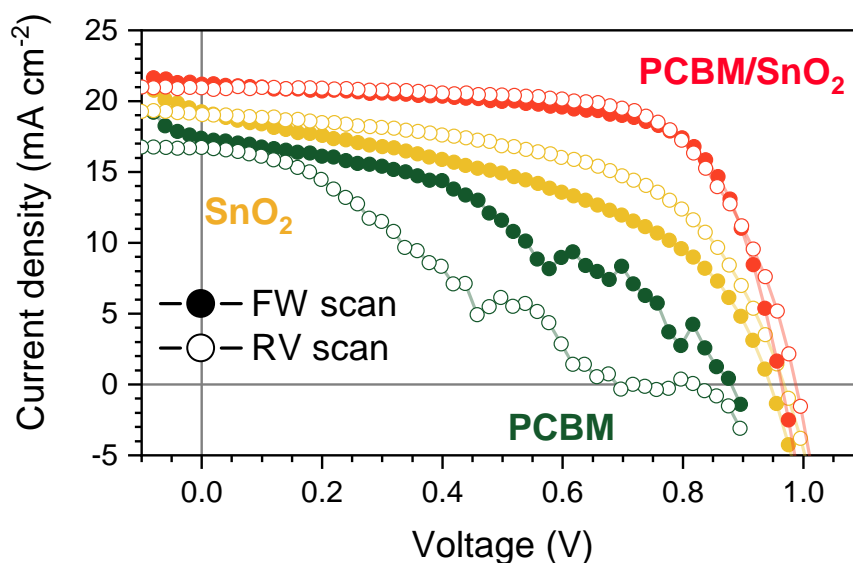


Figure 4.8: IV curves of cells deposited on SnO₂, SnO₂/PCBM and PCBM under 1 sun simulated illumination at 20 mV s⁻¹.

PCBM is performed right after. 35 μ L of solution are spun dynamically on 2×2 cm² samples at 2000 rpm for 30 s. After deposition, the samples are annealed for 10 min at 100 °C. After this step, the deposition of the perovskite solution proceeds as described in [section A.1.1](#).

4.3.2.2 Impact on the PV performances

Full cells using SnO₂ (reference), SnO₂/PCBM (bilayer) or simply PCBM as ETL have been investigated. The 15 nm-thick SnO₂ is deposited at 100 °C and annealed at 180 °C. The final architecture of the cells is given in [Figure 4.7](#). The top part of the stack (perovskite, HTL and electrode) is deposited as described in [section A.1.1](#). The PV parameters have been measured from J–V characterization under 1 sun illumination and are presented in [Figure 4.8](#), and the PV parameters are reported in [Table 4.3](#). The reference cell has a lower efficiency than the one described before which shows once again the difficulty to ensure interbatch reproducibility. Because of this variability, cells synthesized in the same batch were compared, ensuring that the deposition conditions are as similar as possible for the different samples. The reference cell has a PCE of 10.38% with a $V_{OC} = 968$ mV, a $J_{SC} = 19.0$ mA cm⁻² and a FF = 56.3% (RV scan). When the PCBM layer is added, the PCE increases to 14.05%, with a $V_{OC} = 987$ mV, a $J_{SC} = 20.9$ mA cm² and a FF = 68.0%. It is striking that all PV parameters increase with the addition of PCBM. However, the PCBM layer alone is not enough to ensure good performances of the cell, as shown by the cell based only on PCBM. Its PCE drops down to 5.97%, with a $V_{OC} = 881$ mV, a $J_{SC} = 17.4$ mA cm⁻² and a FF = 39%. These parameters are worse than those of the reference.

4.3 Integration of ALD-SnO₂ layers in planar perovskite solar cells

Table 4.3: PV parameters of the best performing cells deposited on SnO₂, SnO₂/PCBM and PCBM. The quantities are given in forward (roman style) and backward (*italic style*) scans, for a scan speed of 20 mV s⁻¹.

	V _{OC} (mV)	J _{SC} (mA cm ⁻²)	FF (%)	PCE (%)
SnO₂	937	19.2	46.3	8.34
	<i>976</i>	<i>19.0</i>	<i>55.9</i>	<i>10.38</i>
SnO₂/PCBM	964	21.2	68.2	13.94
	<i>987</i>	<i>20.9</i>	<i>68.0</i>	<i>14.05</i>
PCBM	876	17.4	39.2	5.97
	<i>697</i>	<i>16.6</i>	<i>29.8</i>	<i>3.45</i>

The PCBM-only sample works very poorly. This can be ascribed to a poor hole blocking ability of the PCBM which is related to its smaller band gap (2.0 eV compared to 4.2 eV for the ALD-SnO₂, compared with the band gap of the perovskite of 1.60-1.65 eV see [section 3.4.4](#)). In the literature, PCBM is usually associated with another wide-band gap, n-type material in order to make an honorable ETL (for instance an oxide; Al-Ashouri et al. (2019)). This sample confirms that the bilayer is required in order to have proper devices. The comparison of the reference with the bilayer shows that the PCBM has a large influence on the V_{OC} and the FF. The higher V_{OC} suggests that the quality of the interface between the ETL and the perovskite absorber has improved. PCBM was reported to passivate grain boundaries near the ETL interface. By comparing the cells obtained on TiO₂ with a layer of PCBM or of a polymerized form of PCBM, Zhong et al. (2020) showed that the diffusion of PCBM inside the perovskite layer was of great importance in order to have an effective passivation. A proposed mechanism relies on the passivation of lead interstitial sites by the fullerene derivative. A poor fill factor can either be the consequence of a large series and/or shunt resistance in the cell, or be a consequence of the violation of the shifting approximation, *i.e.* of the fact that the carrier collection is dependent on the forward voltage. To identify the cause of the lower fill factor of SnO₂-based cells, dark J-V measurements presented in [Figure 4.9](#) were performed on the best cells for each condition. According to [section 1.1.5](#), if the shifting approximation is valid, the J-V curve under illumination can be obtained by translating the dark J-V curve along the J axis by J_{ph} (in practice J_{SC}). As it is clearly seen on the measurements, the sample on SnO₂ under illumination deviates from the shifting approximation, while the sample deposited on the bilayer deviates only at higher voltages. This demonstrates that the cause of the bad fill factor is not due to large series or shunt resistances, which would have been visible on the dark J-V curve. It would have been surprising if the PCBM layer had an impact on R_s and R_{sh}, given that the oxide layer is already completely covering the ITO (as demonstrated by the electrochemical characterization in [chapter 4.2](#)). According

4.3 Integration of ALD-SnO₂ layers in planar perovskite solar cells

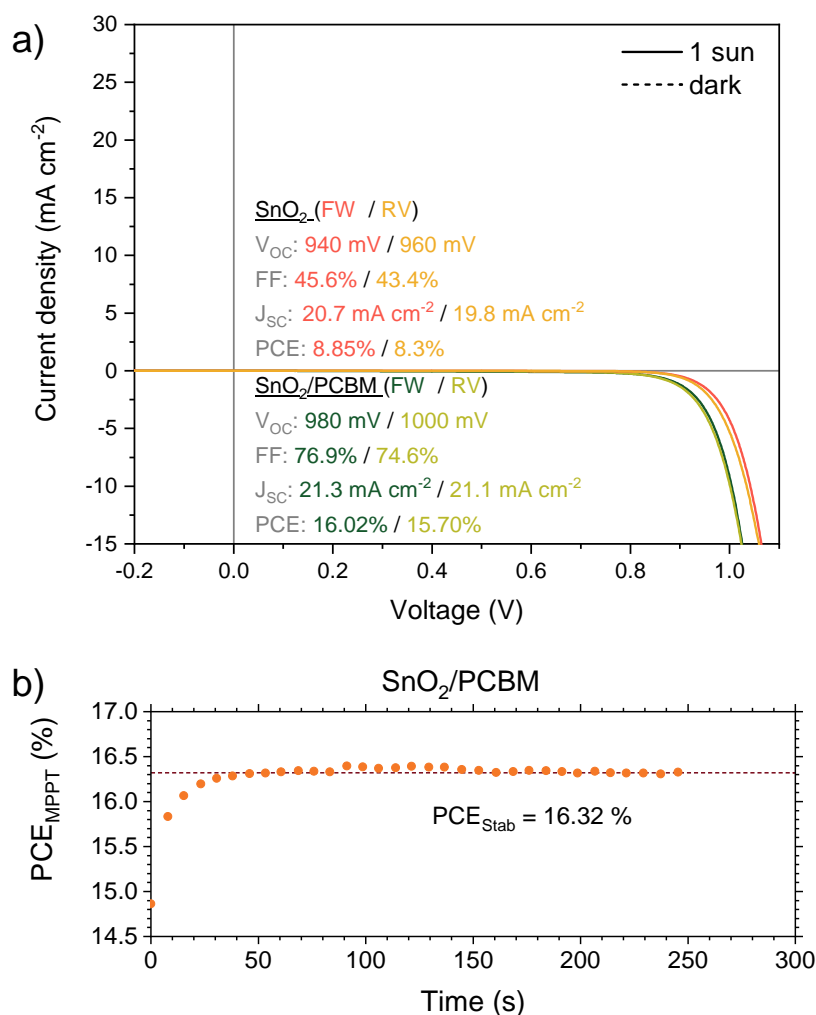


Figure 4.9: a) J-V curves of full devices deposited on SnO₂ (red) and on SnO₂/PCBM (green) under 1 sun simulated illumination (full lines) and in the dark (dashed lines). The measurements are taken in forward (dark colors) and reverse (light colors) scans. b) MPP tracking of the cell based on SnO₂/PCBM under 1 sun simulated illumination.

to Scheer and Schock (2011), the deviation from the shifting approximation can be ascribed to various causes such as interface recombinations which increase when the internal electric field decreases (*i.e.* when the forward bias increases) or the existence of a photo-current barrier whose effect gets stronger when the internal electric field decreases. Both effects are involved in this case: the increase of V_{OC} hints for a passivation of the interface, while addition of PCBM can modify the energetic barriers to the extraction of the electrons.

4.3 Integration of ALD-SnO₂ layers in planar perovskite solar cells

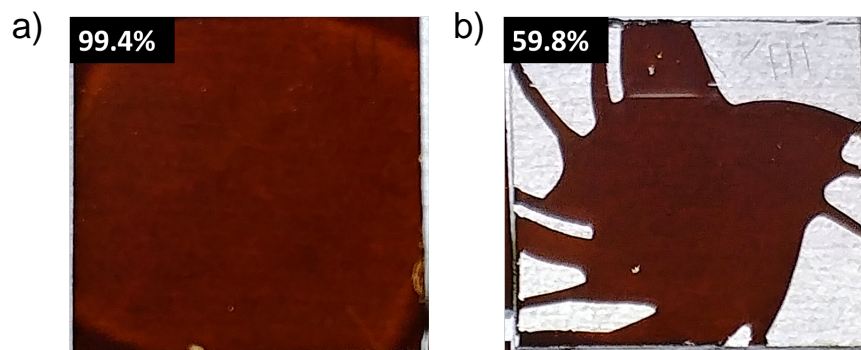


Figure 4.10: Evidence of the wettability issue of the perovskite ink on PCBM, on $2 \times 2 \text{ cm}^2$ substrates. a) Perovskite deposited on UV-O₃ treated ALD-SnO₂. b) Perovskite deposited on ADL-SnO₂/PCBM. The values indicated correspond to the mean fraction of the substrate covered with perovskite after a standard deposition, averaged over 6 samples.

4.3.2.3 Wettability issues

The addition of the PCBM layer allows for a large increase of the fill factor of the planar solar cells based on ALD-SnO₂. However, PCBM is a hydrophobic material, which is problematic to obtain a covering layer of perovskite on top of it. Several studies also report on a direct correlation between the wettability of the perovskite solution and the hysteresis of the planar structure (J. Liu et al. (2020)). Strategies have been proposed to circumvent this issue: blending the PCBM solution with another chemical (polyethylene glycol, Wei et al. (2016), PMMA, Peng et al. (2017)) or addition of a modified fullerene derivative to increase the wettability of polar solvents (Zhou et al. (2017)). A simple visual inspection of the cells presented in the previous section is enough to assess that the wettability of the perovskite ink is indeed very poor (Figure 4.10). On average, the perovskite solution covers 99.4% of the substrate when deposited on UV-O₃-treated substrate versus only 59.8% of the substrate when deposited on the PCBM layer. In order to mitigate this effect, a series of simple modifications of the PCBM layer were devised and the fractions of the substrates covered with perovskite were compared. All samples consist at least of a 15 nm-thick SnO₂ layer deposited on ITO at 100 °C and annealed for 1 h at 180 °C, treated with UV-O₃ (15 min) right before introduction in the glovebox.. The experimental protocol for the preparation of each layer is summarized in Table 4.4

Another strategy can consist in doing a UV-O₃ treatment similar to the one used for the SnO₂ layer to activate the surface and enhance its wettability. This would however require a study of the stability of PCBM under UV-O₃ exposure (such studies have been carried out by Belay et al. (2012)) and modify the whole process to either deposit the PCBM out of the glovebox, or to take the samples out of the glovebox in between the PCBM and the perovskite deposition.

Figure 4.11 shows the different samples after the deposition of the perovskite layer, along with the coverage of the substrate. Taking into account uncomplete

4.3 Integration of ALD-SnO₂ layers in planar perovskite solar cells

Table 4.4: Experimental protocol of each sample for the wettability study of perovskite on PCBM. * The additional layer is dissolved in chlorobenzene and is deposited by spin coating (35 μ L, for 30 s at 5000 rpm). ¹ 35 μ L of DMF are spread on the substrate just before launching the perovskite deposition. ² 35 μ L of DMF are spun on the substrate with the same program as the perovskite. A second program for the perovskite is launched shortly after.

Name	Additional layer: solution*	Perovskite: temperature of the substrate	Perovskite: modification of the process
SnO ₂	–	T _{amb}	–
PCBM ₅ hot	PCBM 5 mg/mL	100°C	–
PCBM ₅ cold	PCBM 5 mg/mL	T _{amb}	–
PCBM ₁ hot	PCBM 1 mg/mL	100°C	–
PCBM ₁ cold	PCBM 1 mg/mL	T _{amb}	–
DMF-stat	PCBM 5 mg/mL	T _{amb}	35 μ L of DMF static ¹
DMF-dyn	PCBM 5 mg/mL	T _{amb}	35 μ L of DMF dynamic ²
PCBM ₅ /PMMA	PCBM 5 mg/mL PMMA 0.1 mg/mL	T _{amb}	–
PMMA	PMMA 0.1 mg/mL	T _{amb}	–
PCBM ₅ :PMMA X:1	PCBM 5 mg/mL: PMMA 5 mg/mL X:1 (v:v)	T _{amb}	–

coverage due to manipulation issue or misfortune during the deposition process, the film was considered sufficiently covering when more than 95% of the surface is covered. The samples deposited on a hot surface do not show an increased wettability compared to their cold counterparts. Different coloration of the perovskite layer is also observed which indicates an unsatisfactory crystallization of the layer. The temperature of the surface modifies the rate at which the solvent may evaporate during the deposition. In the one step deposition as it is done for these samples, the moment at which the antisolvent is dispensed is critical for a good control of the nucleation and growth of the perovskite layer. Since the perovskite deposition process was kept the same for cold and hot samples, the timing of the antisolvent is probably off in the case of hot PCBM. This lack of control over the growth of the perovskite layer is also evidenced on the SEM images (Figure 4.12.a and Figure 4.12.e), where inhomogeneities appear. Within these meta-features, the perovskite grains seem merged together with large pinholes in between.

4.3 Integration of ALD-SnO₂ layers in planar perovskite solar cells

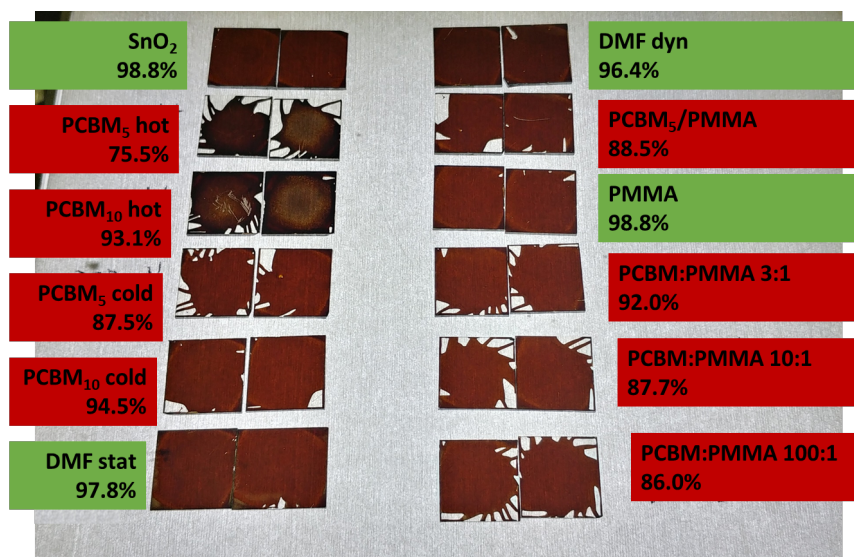


Figure 4.11: Wettability of the perovskite ink on the substrates described in section 4.3.2.3. The values indicated are the fraction of the substrate covered by the perovskite averaged over the two samples. A green box indicate a satisfactory coverage (>95%), a red one a deficient coverage (<95%).

Interestingly, in this batch of experiment, the coverage of the PCBM₅ was of 87.5% which is much higher than the one measured for the batch studied in the previous section (59.8%). This large difference can indicate that the process is not completely reproducible on a cold untreated layer of PCBM. From the other samples the following parameters seem to have a large influence on the covering of the perovskite layer: 1) a lower concentration of PCBM leads to a more covering layer, 2) the pre-wetting step with DMF leads to a complete covering of the substrate irrespective of the static or dynamic method, 3) the addition of PMMA increases the covering of the perovskite layer. Samples with a blend of PCBM and PMMA exhibit a wrinkle-like morphology as demonstrated by the SEM images (Figure 4.12c,d). Such morphologies are usually associated with constrained growth of the perovskite layer (Bush et al. (2018)). Finally, the samples considered as fully-covering are SnO₂, DMF-stat, DMF-dyn and PMMA. The SEM and confocal images reveal a similar morphology of the perovskite film, with small and compact grains of perovskite without pinholes for SnO₂, DMF-stat and DMF-dyn, but a wrinkle-like morphology for PMMA (Figure 4.12b,f,g,h). Finally, the DMF-stat condition was selected to enable a complete coverage of the PCBM layer, due to its simplicity of use. Since most of the solvent is ejected from the substrate during the first seconds of rotation (before the perovskite ink is deposited), the effect of the DMF prewetting on the perovskite could be a slight dilution of the solution. The promising DMF-stat condition has been integrated in a complete solar cell

4.3 Integration of ALD-SnO₂ layers in planar perovskite solar cells

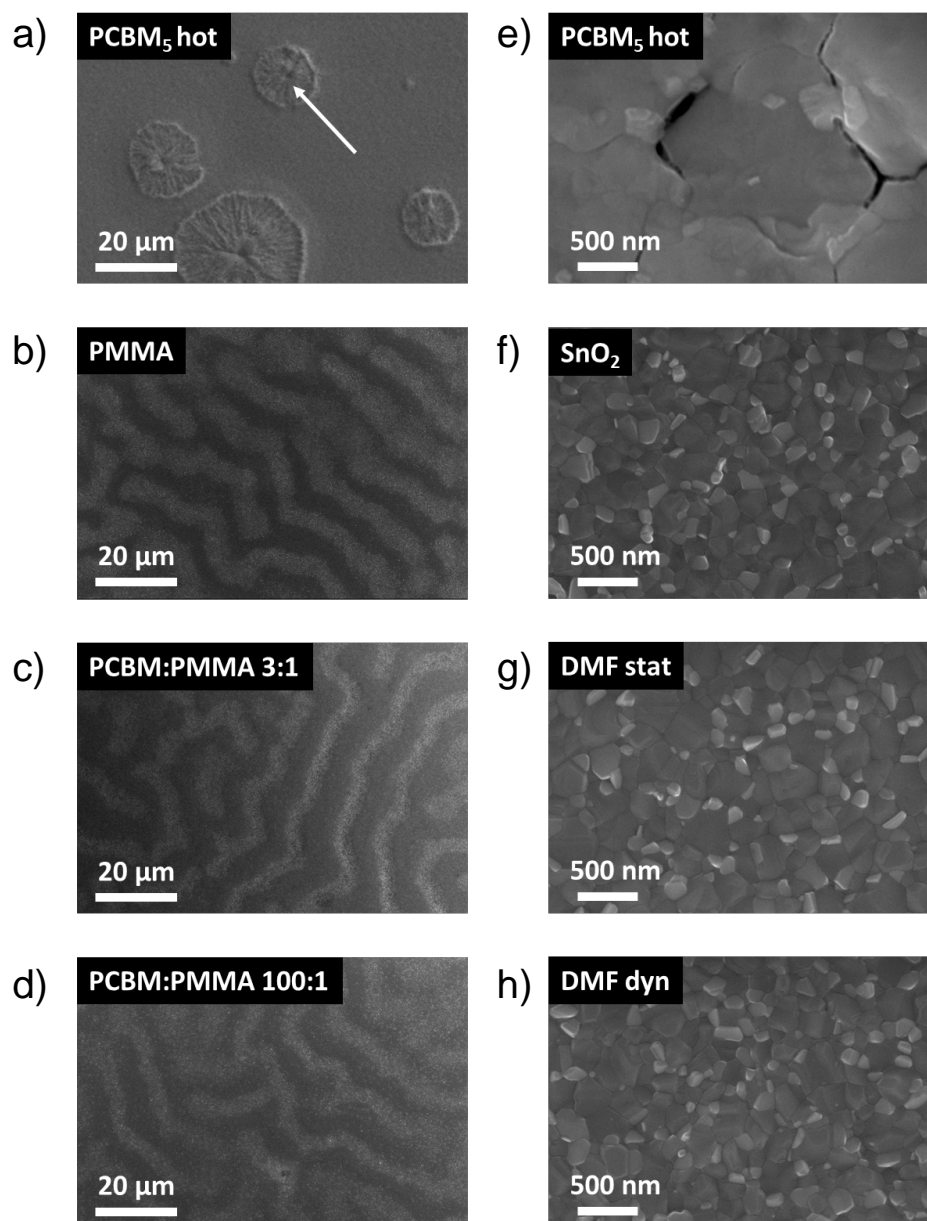


Figure 4.12: SEM micrographs of perovskite deposited on various substrates described in [section 4.3.2.3](#). Micrographs a)-d) are acquired at a x1k magnification, micrographs e)-h) are acquired at a x50k magnification. Micrograph e) is a magnification of the area indicated by the white arrow in micrograph a).

([Figure 4.13](#)). The results suggest that the pre-wetting step does not impact the performances of the cell while solving the wettability issue of the perovskite.

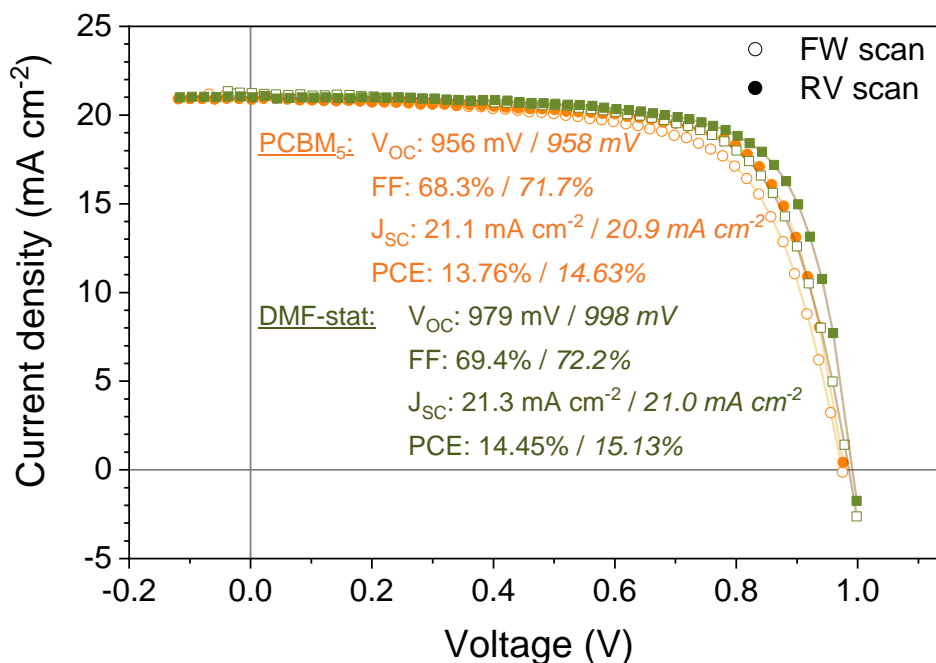


Figure 4.13: IV curves of cells deposited on PCBM₅ (circles) and DMF-stat (squares) under 1 sun simulated illumination at 20 mV s⁻¹.

However, this validation has only been performed on a limited amount of samples and should be extended to more samples to assess trustfully its validity.

4.3.3 Thickness study

To complete the study of the SnO₂ layer, cells deposited on different thicknesses of SnO₂ are synthesized. The stack consists in ITO-coated glass/SnO₂/PCBM/perovskite/PTAA/Au. The PCBM is deposited according to the PCBM₅-cold recipe discussed previously. The final architecture of the cells is given in Figure 4.14. SnO₂ is deposited at 100 °C and annealed at 180 °C for 1 h. Thicknesses of 10 nm (SnO₂-10), 15 nm (SnO₂-15) and 20 nm (SnO₂-20) are investigated using four cells for each condition (one device was not working for SnO₂-15) The resulting PV parameters are given in Figure 4.15.

SnO₂-10 and SnO₂-15 outperform SnO₂-20 by a large margin – if the outlier for SnO₂-15 is excluded – reaching efficiencies between 13% and 15% vs. less than 7%. A larger variability in the results is found for SnO₂-20. A similar observation goes for the stabilized output PCE. Taking into account the best performing cells for each condition (summarized in Table 4.5), trends can be extracted for each individual PV parameter. The cells show similar hysteresis, so only the reverse values are discussed. The small variations of J_{SC} are comparable to what has been

4.3 Integration of ALD-SnO₂ layers in planar perovskite solar cells

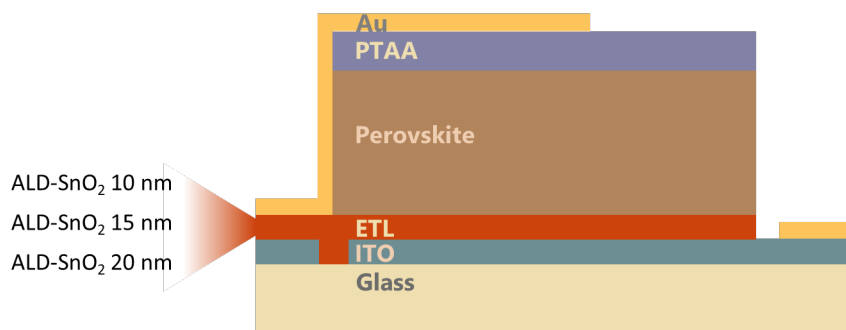


Figure 4.14: Sketch of the cell architecture for the study on the effect of the thickness of ALD-SnO₂ in full devices.

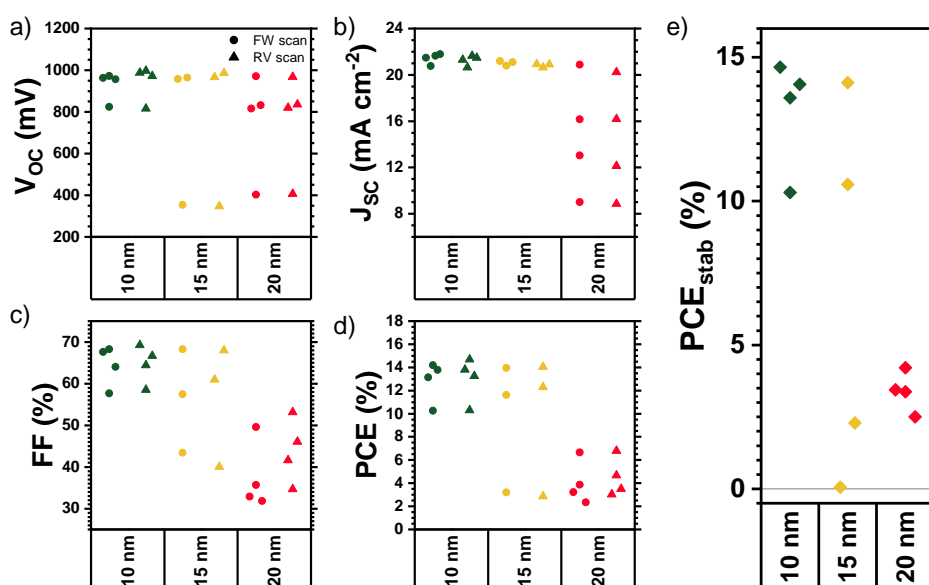


Figure 4.15: PV parameters function of the thickness of the ALD-SnO₂ layer acquired at 20 mV s⁻¹ under 1 sun simulated illumination (a) V_{OC}, b) J_{SC}, c) FF and d) PCE). f) Mean stabilized PCE between 3 min to 5 min of illumination.

discussed in [section 3.4.2](#): the thicker the SnO₂ film, the lower the J_{SC}, ranging from 21.5 mA cm⁻² for SnO₂-10 to 20.2 mA cm⁻² for SnO₂-20. These variations can be explained by a variation of the transmission of the glass/ITO/SnO₂(/PCBM) stack which decreases as the thickness of SnO₂ increases (as explained in the case of ALD-TiO₂ in [section 3.4.2](#)). The V_{OC} is quite stable over the range of thickness studied, the differences observed being within the range of variability of SnO₂-10 (988 mV for SnO₂-10, 987 mV for SnO₂-15 and 968 mV for SnO₂-20). However,

Table 4.5: PV parameters of the best cells based on ALD-SnO₂/PCBM bilayer, function of the thickness of SnO₂. The quantities are given in forward (roman style) and backward (*italic style*) scans, for a scan speed of 20 mV s⁻¹.

	V _{OC} (mV)	J _{SC} (mA cm ⁻²)	FF (%)	PCE (%)
10 nm	963	21.8	67.6	14.18
	<i>988</i>	<i>21.5</i>	<i>69.2</i>	<i>14.68</i>
15 nm	964	21.2	68.2	13.94
	<i>987</i>	<i>20.9</i>	<i>68.0</i>	<i>14.05</i>
20 nm	971	20.9	32.9	6.66
	<i>968</i>	<i>20.2</i>	<i>34.7</i>	<i>6.79</i>

the large difference in efficiency mostly comes from the reduced FF of SnO₂-20 (36.7%) compared to that of SnO₂-10 and SnO₂-15 (69.2% and 68% respectively). Since there is a buffer layer of PCBM between the perovskite and the SnO₂, the defect density at the perovskite/ETL interface is assumed similar. Hence, this change is rather ascribed to an increase of the series resistance when the thickness of SnO₂ is increased, which is in line with the relatively high resistivity of the layers (cf. section 2.2.4.2). This short study shows that in order to get higher efficiency devices, thinner layers of SnO₂ should be preferred. It can also be interesting to investigate even thinner layers of oxide. At some point, the hole blocking ability of the layer is expected to degrade and the cell would endure degradation of its V_{OC} and FF, due to either tunneling of the holes or creation of pinholes in the ALD layer.

4.4 Conclusion

In this chapter, the feasibility of an n-i-p planar cell using the tin oxide developed with H₂O₂ and TDMASn has been demonstrated (cf. section 4.3.2).

A focus has been made on the effect of an annealing step on the properties of the SnO₂ film examined with various tools (photospectroscopy, GI-XRD, XRR and cyclic voltametry). The study encompasses temperatures of 180 °C, 300 °C and 500 °C and the annealing is performed in air. The annealing step is not imposed by the process unlike what was discussed for ALD-TiO₂ (cf. chapter 3.2), hence the aim was to understand how it affects the material in order to narrow down the scan window of annealing temperatures for the full cell integration. Films annealed at 180 °C have properties which are similar to the as-deposited films, *i.e.* an amorphous material with a high transmission in the visible range, a high band gap and a good hole-blocking ability. When the film is annealed on ITO at 300 °C or more, the properties of the film change drastically, transitioning from

the amorphous phase to a crystalline phase. This phase transition goes along with a large shrinkage of the layer (-20% of the original thickness). This most likely also affects the electronic state of the material, as demonstrated by the shift of the cathodic peak in the electro-chemical characterization.

The effectiveness of ALD-SnO₂ in perovskite solar cells has already been reported by various research teams, and ALD-SnO₂ is actually part of the best tandem architectures so far. Hence, the suitability of ALD-SnO₂ developed at IPVF to act as the ETL in a perovskite solar cell was examined. It is worth mentioning that such material is usually deposited with O₃ as oxidizing agent (Correa Baena et al. (2015); C. Wang et al. (2016); Anaraki et al. (2016)), while H₂O₂ is used in this study. First the consequences of the deposition temperature on the PV parameters of the cell were determined. The samples showed a higher variability when grown at a higher temperature (140 °C vs 100 °C) which was ascribed to the higher inhomogeneity of the ALD deposition at these temperatures (cf section 4.3.1). Moreover, the deposition at lower temperatures has the benefit of occurring in softer conditions, allowing for the use of more sensitive substrates (such as a perovskite layer in case of an inverted p-i-n architecture). The literature agrees on the fact that amorphous SnO₂ is more suitable for PV applications than crystallized SnO₂. In agreement with this, the influence of annealing temperatures up to 200 °C on the quality of planar n-i-p solar cells was studied. Up to 180 °C, the performances of the cells increase slightly, especially due to a minor increase in J_{SC} and FF, with best efficiencies reaching 14.4%. These variations were ascribed to surface-related changes of the SnO₂ layer (desorption of remains of precursor fragments and of carbonaceous pollutants), even though a careful chemical analysis (*e.g.* XPS) of the surface could bring more insights in this matter. When the temperature further increases, the performance of the cell decreases drastically mostly due to a loss in V_{OC} which is ascribed to the start of the phase transition of SnO₂ towards the rutile phase.

Compared to SnO₂ deposited with O₃, a dramatic loss of FF in the cells was noticed. The addition of a layer of PCBM between the oxide and the absorber is beneficial to this regard, increasing effectively the FF from around 50% to more than 65% (76.9% in the best cell). This increase is ascribed to two reasons: a reduction of the interfacial defect density at the interface with the perovskite (as supported by other studies Zhong et al. (2020)) and a change in the band alignment at this interface. However, the PCBM being a hydrophobic material, the wettability of the perovskite precursor solution on it is very poor during the spin coating step, which induces the formation of a partially covering film. Even though evident formation of pinholes in the film could not be observed, only part of the substrate is covered with the perovskite film (between 50% and 70%) which is in any case not ideal from an upscale perspective. Several strategies have been tested in order to cure this issue, and the positive effect of a prewetting step of the substrate with DMF has been demonstrated, which increases the coverage of the perovskite up to adequate values all the while preserving the morphology of the perovskite layer and the performance of the final cell. Finally, a relative independence of the performance of the cell has been observed when the thickness of SnO₂ is varied up to 15 nm. For thicker layers of SnO₂, a pronounced loss of FF leads to much

poorer devices, which was ascribed to an increase of the series resistance.

These different analysis prove the suitability of the ALD-SnO₂ layer as ETL. There is still a lot of room for improvement, as it is underlined by the efficiencies lower than what can be found in the literature. Several axes of progress and development of this layer are proposed: 1) tune the electronic properties of the SnO₂. This can be achieved during the ALD process either by doping the material (for instance with niobium; Anaraki et al. (2018)) or by growing a nanolaminate with another oxide (for instance ZnO; Bush et al. (2017)). 2) Taking advantage of the good hole blocking ability of ALD-SnO₂ to test various passivation layers between the ETL and the perovskite which might not be as blocking as ALD-SnO₂ (C₆₀, SnO₂ deposited by wet chemistry). 3) Use the conformality of the ALD deposition to alleviate the issue of the homogeneity of the ETL on textured Si for monolithic tandem solar cells applications. 4) Investigate p-i-n architectures with inorganic HTL and ETL owing to the soft conditions of ALD deposition.

Chapter 5

Modification of ALD-ZnO with phosphonic acid derivatives ¹

5.1 Motivation

5.1.1 The versatility of ZnO

Zinc oxide (ZnO) is an extensively studied and versatile n-type semiconductor, with a wide range of applications due to its expedient optoelectronic properties. It is a wide band gap material (~ 3.3 eV), with a large bulk carrier mobility (from tens of $\text{cm}^2 \text{V}^{-1} \text{s}^{-1}$ (Saha et al. (2020)) up to $200 \text{ cm}^2 \text{V}^{-1} \text{s}^{-1}$ at 300 K for high-quality thin films (Tsukazaki et al. (2005))), and it can be doped with a variety of elements (Al, Ti, Ga, B, F, N, ...) (Ellmer et al. (2008)). ZnO is thus suitable for integration in UV-light emitting devices (LED), thin film transistors, detection of chemicals (Jagadish and Pearton (2006)) or solar cells, where it is used in many technologies such as copper indium gallium selenide (CIGS) (Tsin et al. (2015)), organic (Lange et al. (2015)) or perovskite solar cells (Hadouchi et al. (2016); P. Zhang et al. (2017)). Furthermore, it is a well-known transparent conductive oxide composed of abundant and non-toxic elements which can be synthesized by various thin-film deposition methods into different shapes and morphologies (nanostructures, thin films, single crystals ...) (Jagadish and Pearton (2006); Özgür et al. (2005)).

5.1.2 Issues with the integration of ZnO in perovskite solar cells

For perovskite solar cells the improvement of devices performances, and particularly their stability, is closely linked to the chemical passivation of the interfaces (He et al. (2020)). ZnO/halide perovskite interfaces are generally prone to suffer

¹The study reported in this chapter has been subject to publication (Fournier et al. (2021)).

from a strong thermal instability (J. Yang et al. (2015)), which can be mitigated by the introduction of molecular interlayers (Schulz et al. (2019)). Dkhissi et al. (2016) have suggested a degradation pathway which involves the decomposition of MAI into methylamine and HI, and reaction of HI with ZnO to form zinc-iodide species and water. Water does in turn further catalyze the decomposition of MAI, which leads to a rapid decomposition of the perovskite, as observed by XRD. A second degradation pathway could arise from the reaction between ZnO and ammonium (coming from the methylammonium). It has been shown that ZnO surface can be etched by the weak acid, leading to the formation of ammonia and zinc salt (Juarez-Perez et al. (2019); J.-K. Kim and J.-M. Lee (2017)).

Different strategies have been employed to reach good efficiencies in n-i-p configurations (*i.e.* the absorber is deposited on top of the electron transport layer): modifying the surface with self-assembled monolayers (Azmi, Hadmojo, et al. (2018); An et al. (2017)), chlorinated compounds (D. Zhang et al. (2019)), WO₃ (Tsarev and Troshin (2020)), ethanedithiol (Azmi, C.-L. Lee, et al. (2018)), MgO/ethanolamine (Cao et al. (2018)), or ZnS (R. Chen et al. (2019)), Al doping (Tseng et al. (2016)), reducing the perovskite annealing temperature (J. Song et al. (2017)), or changing the perovskite absorber composition (Schutt et al. (2019)).

5.2 Properties of the ALD-ZnO

Atomic layer deposition (ALD) can be used for the deposition of conformal and dense ZnO layers, and previous reviews have reported its application in perovskite solar cells (Zardetto et al. (2017); Brinkmann et al. (2020); H. H. Park (2021a)). The applications of ALD-ZnO mostly concern p-i-n configurations where the oxide is deposited on top of the perovskite; the use of ALD-ZnO as ETL in n-i-p structure is however relatively rare (X. Dong et al. (2014)).

5.2.1 Properties of the ALD-ZnO process

The ZnO layers are deposited using diethylzinc ($\text{Zn}(\text{C}_2\text{H}_5)_2$, DEZ) and water (H_2O) as precursors at deposition temperature 160 °C, as described by Le Tulzo et al. (2019).

The preparation of the samples is detailed in [section 5.3.2](#). Main properties of the ALD-ZnO process are described in [Figure 5.1.a](#). The deposition temperature was within the ALD window identified from 160 °C up to more than 220 °C (the upper boundary was not determined). The GPC was determined by XRR to be around 1.8 Å per cycle, in line with the literature (Tynell and Karpinen (2014); Z. Gao and Banerjee (2019)).

The process is optimized for the deposition on silicon wafers, and was transposed as such on FTO substrates.

5.2.2 Properties of the ALD-ZnO thin films

The basic properties of the oxide have previously been characterized by several means, summarized in [Figure 5.1](#) (Le Tulzo (2018)).

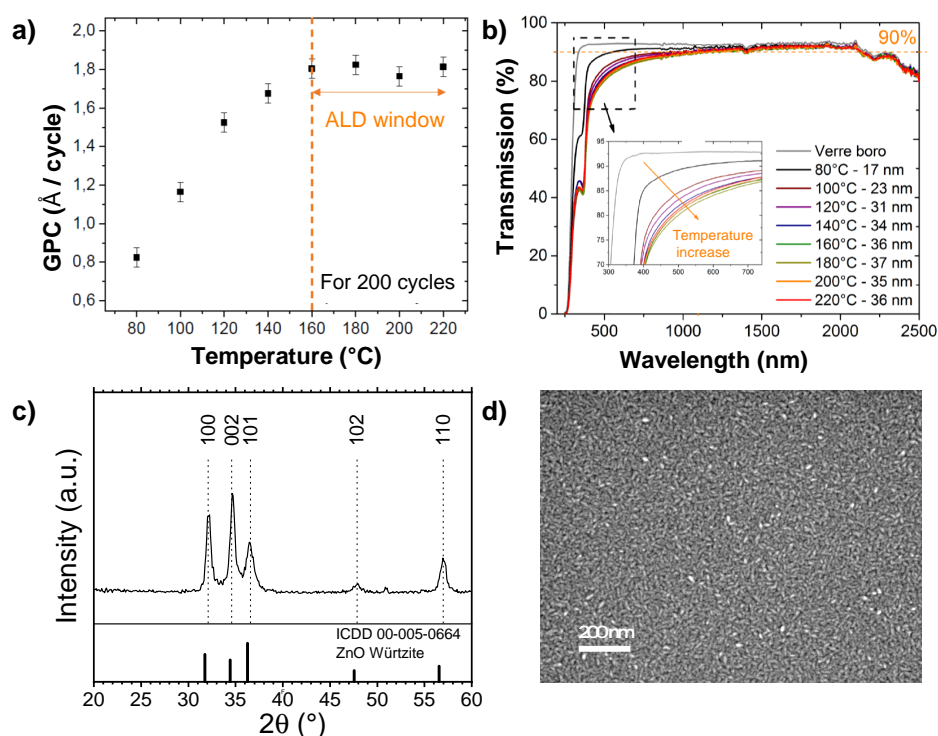


Figure 5.1: Main properties of ALD-ZnO process and thin film. a) Influence of the temperature on the growth per cycle of the DEZ/H₂O recipe. Adapted from Le Tulzo (2018). b) Variation of the transmission of a borosilicate glass/ALD-ZnO (200 cycles) stack at various temperatures. The inset is a magnification of the 300 - 750 nm region. Adapted from Le Tulzo (2018). c) Diffractogram of 50 nm ALD-ZnO on Si grown at 160°, compared with the ICDD reference of the würtzite phase. d) SEM top image of 50 nm ALD-ZnO on Si grown at 160°C, evidencing the oblong grains of the film.

The crystalline structure of the oxide after deposition has been determined by GI-XRD. According to the reference pattern ICDD 00-005-0664, it crystallizes in the würtzite phase (space group $P63mc$), which is the most stable at ambient temperature. SEM images reveal that the films are composed of a multitude of small oblong grains which cover the substrate in a homogeneous manner.

The film displays a good transparency in the visible-IR range (above 75% up to 90% for $\lambda > 400$ nm in 36 nm-thick films). Combined with a relatively high optical band gap of 3.24 ± 0.05 eV, ALD-ZnO is suitable for a use as ETL in perovskite solar cells in n-i-p configuration.

The resistivity of the films has been measured with a 4-probe apparatus. It is highly dependent on the thickness of the film: the thicker the film, the lower the resistivity, which can be related to a variation of the nature of the film with the thickness caused by the ALD process (*e.g.* large influence of the substrate for very thin films). The resistivity increases from $6 \times 10^{-2} \Omega \text{ cm}$ up to $8.36 \Omega \text{ cm}$ when the thickness decreases from 128 nm to 36 nm. Since even thinner films are

5.3 Modification of the ZnO surface with phosphonic acid derivatives (organophosphonates)

used (15 nm), a high resistivity of the film is expected. Measuring precisely the transverse resistivity of very thin films is however complicated with usual methods, and it was not determined in this study.

The properties of the ZnO film are overall in line with the literature (Tynell and Karppinen (2014); Z. Gao and Banerjee (2019)).

5.3 Modification of the ZnO surface with phosphonic acid derivatives (organophosphonates)

Surface functionalization through molecular grafting of zinc oxide has been extensively studied in the literature, whether on ZnO nanostructures (Sandmann et al. (2015); Quiñones et al. (2017); C. Sun et al. (2014)) or films (Lange et al. (2014); Hotchkiss et al. (2011)). A large variety of grafted molecules of different chemical functionalities and molecular weights can be designed depending on the purpose of the grafting, from large fullerene-derivatives (Lacher et al. (2011)) to smaller molecules with only a few carbon atoms (Gawalt et al. (2001)). This section will present the strategy which has been adopted in order to mitigate the decomposition reaction between a ZnO ETL and a hybrid perovskite absorber.

5.3.1 Rationale behind the design of the molecules

The modification of a layer with self-assembled monolayers (or SAM-like layers) allows for a large variety of effects depending on the nature of the chosen molecules. The latter usually consist in three main parts, namely the head group, the spacer and the tail group². By changing the chemical nature of these groups, one can tailor the properties of the grafted layer to its specific needs. This section will present the rationale behind the design of each part and the final design of the molecules of interest.

5.3.1.1 Head group

The head group (or anchoring group) is meant to ensure a proper grafting of the molecule on the surface of the substrate through chemical interactions (covalent or ionic bonding). The choice of the chemical group will influence the strength of the bond between the molecular layer and the substrate. A compromise has to be found. On the one hand stronger bonds result in more stable layer. On the other hand the self-assembly on the substrate is a dynamic process and having less energetic bonds allows for an increased mobility of the adsorbed molecules on the surface promoting a higher density of the film.

The grafting of n-alkanethiol on gold is for example a well-controlled process allowing for the deposition of dense and ordered 2D layers, which makes the thiol-gold interaction prototypical. Such specimen have been widely studied in the literature in order to understand the mechanisms behind self-assembly, but have also found practical applications (Vericat et al. (2010)). Self-assembly is also possible on

²Opposite definition for the head and tail groups can be sometimes encountered.

5.3 Modification of the ZnO surface with phosphonic acid derivatives (organophosphonates)

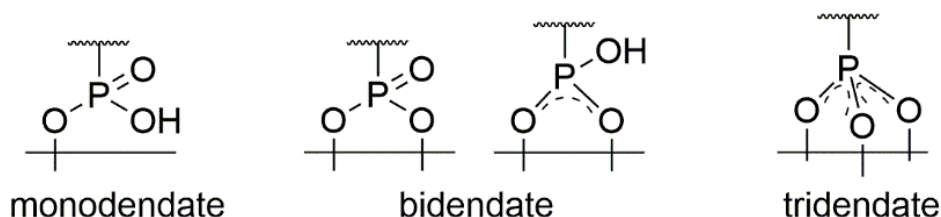


Figure 5.2: Schematic representation of the different binding modes of a phosphonic acid derivative onto a metal oxide layer.

metal-oxide (SiO_x – Onclin et al. (2005), TiO_2 – W. Gao et al. (1996), SnO_2 – Hill et al. (2019), ZnO – Lange et al. (2015), ITO – Al-Ashouri et al. (2019) ...), mostly studied in the case of the self-assembly of organosilanes on silicon oxide. The bond between the head group and the oxide results from a condensation reaction (Feichtenschlager et al. (2011); Hair and Tripp (1995)). However, organosilanes are prone to homocondensation and require a strict control over the chemical environment during the grafting reaction especially in terms of water-content due to the hydrolysis of the organic chain and the formation of silanol groups.

Other head-groups are employed on metal oxides such as carboxylic or phosphonic acids or thiols. The use of carboxylic groups results in only weakly grafted layers (Smecca et al. (2013)). The relative strength of the bond of thiol and phosphonic acids with ZnO has been investigated by Perkins (2009) by comparing the grafted layers obtained with 1-hexanethiol and 1-hexanephosphonic acid on similar substrates. The author claims that phosphonic acid is a better anchoring group than thiol, showing especially better thermal stability. The stability of alkylphosphonic SAMs on TiO_2 towards UV radiation and ambient atmosphere has also been investigated, revealing that the anchoring group is strongly bonded to the oxide (Mani et al. (2008)). Phosphonic acids are thus a key anchoring group on several oxides (also including ZrO_2 , W. Gao et al. (1996) or Al_2O_3 , Lushtinetz et al. (2007)) and have, as such, been subject of dedicated studies to determine the chemical mechanism of the grafting (Paniagua et al. (2016)). The grafting process involves an acid-base condensation between one (or more) hydroxyl groups of the metal oxide surface and the phosphonic acid, which leads to different binding configurations referred to as mono-, bi- or tridentate depending on the number of $-\text{OH}$ groups involved (Figure 5.2). In summary, organophosphonates are reported to be good candidates to modify metal oxides (McDermott et al. (2007)).

5.3.1.2 Spacer

In the simplest cases, the spacer is a linear aliphatic chain ($-\text{CH}_2-$) $_n$, but it can also have a more complex chemistry, including ramifications, cycles or conjugated systems. The nature of the spacer is of high importance in the formation and in the assembly of the SAM (Ulman and Scaringe (1992)). The stability of the 2D molecular layer is mostly determined by the weak interactions between the molecules constituting the film (Ulman (1996)).

5.3 Modification of the ZnO surface with phosphonic acid derivatives (organophosphonates)

In the case of alkyl chains, van der Waals interactions control the organization of the molecule on the surface (Ulman et al. (1989)): smaller chains (counted as number of methylene units) tend to form liquid-like, disordered layers, whereas longer chains can form organized films with a defined orientation of the molecules due to the increased interaction between the longer chains (Fukuda et al. (2009)). The threshold length of the chain is dependent on the chemistry at stake, including the substrate, the nature of the head group ... As an example, Buckholtz and Gawalt (2012) report a threshold length between 26 and 28 units for alkyl-carboxylic films deposited on Ti-6Al-4V. However, molecules which include non conjugated systems (such as alkyl chains) are usually isolating (cf. Table 5.1) so one would prefer shorter chains to obtain a thinner layer.

If the spacer includes aryl groups, the organization of the layer can further be driven by interactions of the aromatic rings (commonly named π - π interactions). K.-C. Liao et al. (2010) observed the influence of the nature of the spacer on the performances of field effect transistors, emphasizing the importance of a careful design of the SAMs.

One can also expect the choice of the spacer to influence the electronic properties of the film (Ashkenasy et al. (2002)). Thanks to the delocalization of π -electrons, conjugated systems allow for an enhanced carrier mobility, as opposed to non-conjugated ones. Smits et al. (2008) took advantage of this feature to design SAM's composed of an aliphatic spacer and a semiconducting core for SAM field effect transistors applications. The non-conjugated aliphatic spacer was used as a dielectric, while a conjugated polythiophene served as semiconducting media allowing for an integrated organic FET.

5.3.1.3 Tail group

The tail group defines the functionality of the final film. By acting on the chemistry of the terminal group, a large variety of effects can be obtained: changing the wettability or the optoelectronic properties of the film (Lange et al. (2014); Jayalakshmi et al. (2013)), being used as a catalyst for further reactions (Wallwork et al. (2001); Y. Liao et al. (2015)) or even passivating defects at the interface with adjacent layers (Lili Yang et al. (2015)).

5.3.1.4 Selected molecules

In light of the previous observations, three different molecules were investigated: 2-aminoethylphosphonic acid (2-AEPA), 4-aminobenzylphosphonic acid (4-ABzPA) and 4-fluorobenzylphosphonic acid (4-FBzPA). Some features of these molecules are summarized in Table 5.1. All molecules have a phosphonic acid head group because of the strong interaction it can have with metal oxides. Linear non-conjugated (2-AEPA) and aromatic conjugated (4-ABzPA and 4-FBzPA) systems are compared as well as different chemical functional groups. According to the literature (Wolff et al. (2020)), the use of Lewis bases (such as $-\text{NH}_2$) or of halides (such as $-\text{F}$) participates in the passivation of undercoordinated Pb at the surface of the perovskite layer. The tail groups were chosen accordingly.

5.3 Modification of the ZnO surface with phosphonic acid derivatives (organophosphonates)

Table 5.1: Basic properties of 2-AEPA, 4-ABzPA and 4-FBzPA. The separation between HOMO and LUMO was extracted from DFT calculation of a single isolated molecule (DFT calculations performed at IPVF by P. Baranek).

Molecules	2-AEPA	4-ABzPA	4-FBzPA
Head	phosphonic acid	phosphonic acid	phosphonic acid
Spacer	linear aliphatic	aromatic	aromatic
Tail	amine	amine	fluorine
Molar weight (g·mol ⁻¹)	125.06	187.13	190.11
LUMO - HOMO (eV)	7.0	5.69	6.62

The amine termination can also be used to initiate further reactions at the surface of the modified substrate, while the fluorine function rather aims at making the surface more hydrophobic. In the case of 4-ABzPA and 4-FBzPA, the change in the functional group can also greatly influence the energetics of the surface due to the change in dipole moment of the molecule, as achieved in OSCs (Lange et al. (2014); Lange et al. (2015)). 4-ABzPA has also been used to initiate the polymerization of polyaniline films on ITO substrates (Wenzhi Zhang et al. (2016)) or as a linker between a metal oxide scaffold and CdSe quantum dots for photocathodes (Norris and Cossairt (2015)) while 2-AEPA has mostly been reported as reaction auxiliary. Due to its high molecular dipole moment, 4-FBzPA can easily modify the work function of ITO substrates in organic LEDs (Sharma et al. (2009)). The chemical nature of the bond created during the grafting process on ZnO has been specifically assessed by density functional theory (DFT) calculations (Wood et al. (2012)), which describes a tridentate binding mode.

5.3.2 Description of the grafting process

Various deposition methods have been reported for the deposition of SAMs on top of oxides, including solution-based depositions of which a short description is given here:

- **DIPPING:** the sample is laid still in a solution containing the desired molecule for a certain amount of time.
- **LANGMUIR-BLODGETT FILMS:** A requisite for this kind of deposition to occur is that the desired molecules form a monolayer at a liquid-gas interface. This can easily be achieved with amphiphilic molecules, forming a monolayer at the water/air interface. The substrate is then passed through the liquid-gas interface, and a monolayer forms on the substrate for each pass (Keszthelyi et al. (2006)).

5.3 Modification of the ZnO surface with phosphonic acid derivatives (organophosphonates)

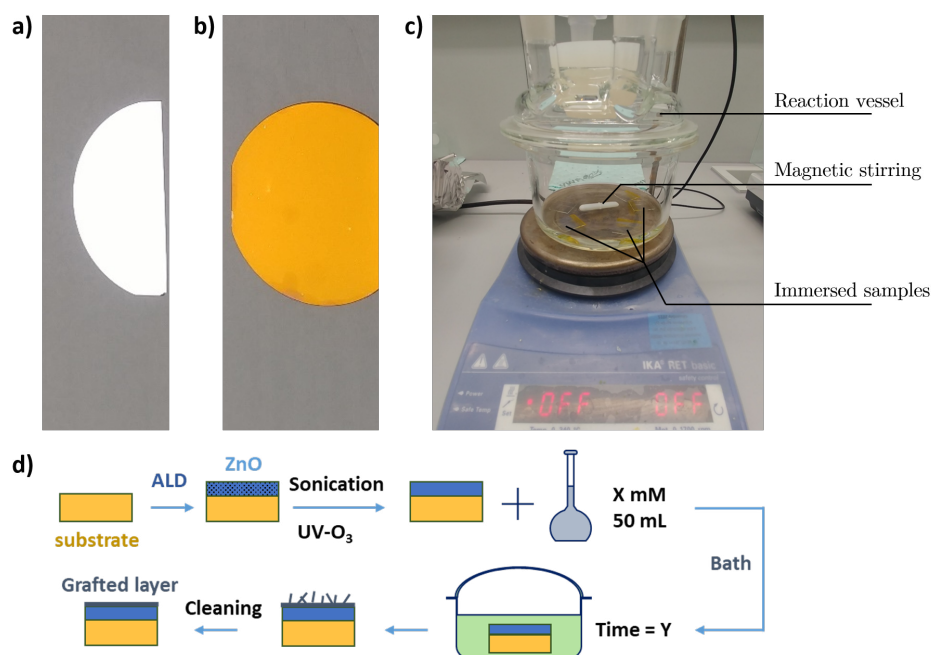


Figure 5.3: Grafting process as used in this work. a) Si substrates before deposition of the ZnO layer. b) Si substrate after deposition of 50 nm-thick ALD-ZnO at 160°C with its characteristic copper-like reflection. c) Set-up used for the grafting process. d) Cartoon of the process flow, extending from the substrate preparation to the grafting and cleaning of the samples by UV-O₃.

- **TETHERING BY AGGREGATION AND GROWTH (T-BAG):** this can be seen as a combination of the aforementioned methods. The substrate is immersed in a solution containing the molecules and held right under the liquid-gas interface. The solvent is allowed to evaporate leaving physisorbed species at the surface of the sample. The conversion to a chemisorbed layer is usually obtained by annealing of the film (Hanson et al. (2003)).
- **SPIN-COATING:** the solution containing the molecules is spun on the substrate. A second step is usually performed with the sole solvent to wash off the excess of deposited material (Zhu et al. (2019)).

In this study, the dipping method was chosen because of the relative simplicity of the process compared to T-BAG or Langmuir-Blodgett films methods, while still allowing to have a control on the grafting dynamic by varying the immersion time. The following paragraphs detail the method used in this study to perform the deposition of the different molecules. A summary of the process is cartooned in [Figure 5.3](#).

5.3.2.1 Substrates and solution

Substrates preparation. Two types of substrates are used depending on the pursued goal. To study the grafting mechanism of the molecule on ZnO, n-type

5.4 Characterization of the grafted layer

(100) Cz single side-polished silicon wafers with native oxide top layer (Neyco) are used. Si-substrates are ultrasonicated in RBS® detergent solution (2 vol%) for 5 minutes, rinsed with deionized water and dried under a flow of N₂. To study the ZnO/perovskite interface, 3 mm-thick FTO glass (Solems) is etched with zinc powder and HCl (0.1 M). These substrates are then ultrasonicated in RBS® detergent solution (2 vol%) for 30 minutes at 60 °C, rinsed with deionized water, then further ultrasonicated in acetone and propan-2-ol, and finally dried under a N₂ flow.

Deposition of ZnO by ALD. The substrates are transferred into the ALD reactor. 50 nm of ZnO are deposited for grafting analysis, while 10 nm only is deposited for cell integration. A complete description of the ZnO deposition process is proposed in [section A.1.1](#).

5.3.2.2 Surface modification of ZnO

Fresh ZnO-covered substrates are ultrasonicated in acetone and propan-2-ol for 10 min each. They are then cleaned with a UV-O₃ treatment for 15 min, and directly transferred in the reaction vessel.

Preparation of the solutions. 2-aminoethylphosphonic acid (2-AEPA), 4-aminobenzylphosphonic acid (4-ABzPA) or 4-fluorobenzylphosphonic acid (4-FBzPA) is dissolved in ethanol:H₂O 19:1 (50 mL) at 1 mM. For contact angle measurements, 4-FBzPA is dissolved in pure IPA. Control solutions consist in 50 mL of the sole solvents (ethanol:H₂O 19:1 or IPA).

Deposition of the molecules on ZnO. After activation by UV-O₃, the samples were immersed and let in the solution under magnetic stirring, at room temperature for a certain amount of time varying from 1 min to 24 h ([Figure 5.3.c](#)).

Post-treatment of the grafted film. After deposition, the samples were thoroughly sonicated for 5 min in IPA and dried under a flow of nitrogen, in order to remove the excess of deposited material. It has been reported that an annealing step could be beneficial for a good organization of organophosphonate-based SAMs (Hotchkiss et al. (2011)). After preliminary tests, no significant influence of such an annealing step could be reckoned in this work.

5.4 Characterization of the grafted layer

The modification of a 50 nm-thick ZnO layer deposited by ALD with 2-AEPA, 4-ABzPA and 4-FBzPA was characterized. Surface-sensitive techniques were used to analyze the surface of ZnO substrates immersed in different solutions of phosphonic acid derivatives – thereafter mentioned as “ZnO-X” (with X = AEPA, ABzPA or FBzPA) – and control ZnO substrates immersed in the sole solvent – thereafter mentioned as “ZnO-ref”. The use of ALD implies that the roughness of the ZnO layer will follow that of the underlying substrate (Knoops et al. (2015)); hence Si

5.4 Characterization of the grafted layer

Table 5.2: Composition and deposition conditions of the samples modified by phosphonic acid derivatives.

Name	Substrate	Immersion time	Concent.	Superstrate
ZnO-ref	Si/ZnO	1 min - 24 h	–	–
ZnO-AEPA	Si/ZnO	1 min - 24 h	1 mM	–
ZnO-ABzPA	Si/ZnO	1 min - 24 h	1 mM	–
ZnO-FBzPA	Si/ZnO	1 min - 24 h	1 mM	–
Ref-pvk	FTO/ZnO	–	–	Triple cation
AEPA-pvk	FTO/ZnO	10 min	1 mM	Triple cation
FBzPA-pvk	FTO/ZnO	10 min	1 mM	Triple cation

substrates have been chosen in order to provide a flat surface more suitable for AR-XPS and FTIR analysis. The structures of the different samples used in the study are presented in [Table 5.2](#).

5.4.1 Assessment of the presence of the molecules on the surface

5.4.1.1 Modification of the wettability.

Contact angle measurements have been performed in order to assess a change in the nature of the ZnO surface, through a modification of its wettability, induced by the presence of grafted molecules. [Figure 5.4](#) presents the static contact angle between deionized water and the samples immersed for 10 min, for substrates modified in 1 mM solution containing the different molecules (2-AEPA, 4-ABzPA or 4-FBzPA) and for the reference ones. The static contact angle measured for ZnO-ref is $77.9 \pm 1.4^\circ$. This angle varies upon modifying the surface. ZnO-FBzPA tends to have a more hydrophobic surface ($84.8 \pm 0.7^\circ$) in agreement with a fluorine termination, while amine-based samples (ZnO-AEPA and ZnO-ABzPA) yield more hydrophilic surfaces ($23.5 \pm 1.6^\circ$ and $<4.0^\circ$ respectively).

The change of static contact angle and of wettability of a surface is associated with a change of the energetics of the surface. This change can be induced by several factors such as an evolution of the surface morphology (for the same material, the wettability of a rough surface is less than that of a smooth one, M. Lee et al. (2011)) or a change in surface chemical composition (N. Li et al. (2016); Hu et al. (2013)).

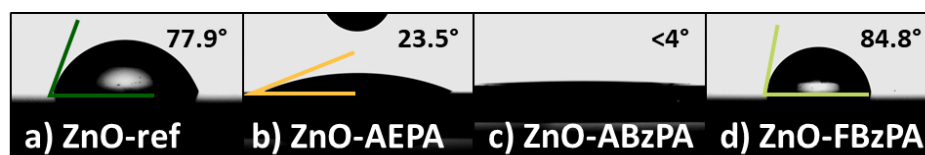


Figure 5.4: Static contact angles of deionized water on a) ZnO-ref, b) ZnO-AEPA, c) ZnO-ABzPA and d) ZnO-FBzPA, after 10 min immersion. The values are given as an average over different samples.

The change in hydrophilicity observed on the different samples is probably due to both effects, as supported by the observations presented in the next paragraph.

5.4.1.2 Evolution of the ZnO thin films in the different solutions

The integrity of the ZnO film after different durations of immersion ranging from 10 min to 24 h in either 2-AEPA containing solution or a reference solution was probed by SEM, XPS, and GI-XRD. The results are summarized in [Figure 5.5.c](#)). After 10 min of immersion, the diffractogram shows strong diffraction peaks from the (100), (002) and (101) orientations at $2\theta=32.07^\circ$, 34.64° and 36.47° respectively for both ZnO-AEPA and ZnO-ref, which is characteristic of ZnO crystallized in the würtzite phase (reference pattern ICDD 00-005-0664, similar to the diffractogram of as-deposited ZnO in [Figure 5.1.c](#)). After 24 h ZnO-AEPA exhibits the same features while there are no more diffraction peaks visible for ZnO-ref. This can either be a sign of amorphization of the layer or of etching of ZnO.

SEM micrographs give further insights on the surface morphologies of ZnO on Si after 10 min, and after 2 h of immersion in 2-AEPA or reference solutions at a similar magnification ([Figure 5.5.e-g](#)). As mentioned in [chapter 5.2](#), fresh ZnO has a rice-shaped morphology with a multitude of small oblong grains. These features are mostly preserved for ZnO-AEPA during the grafting process. In the case of ZnO-ref, a change in the morphology appears after 10 min of immersion (which was not detected with the GI-XRD). The grains start to merge and the layer seems to become porous. The SEM images are acquired with back scattered electrons (BSE) which is sensitive to the chemical environment: heavier elements scatter electrons back more strongly and thus appear brighter. As the immersion time increases, the dark area (ascribed to the light Si substrate) occupy a larger share of the image than the bright one (ascribed to the heavier Zn), indicating that ZnO is etched away during the immersion. XPS surveys support these observations: the Zn 2p signal (1046 eV and 1023 eV) decreases dramatically while the signal of Si 2p (100 eV) appears after 24 h of immersion. In the meantime photopeaks appear at 403 eV and 135 eV and are ascribed to N 1s and P 2p core levels.

These evidences show that the degradation of the ZnO thin film in contact with the solvent is mitigated when the phosphonic acid molecules are added to the solution and that the chemical environment of the ZnO-AEPA surface contains N and P, which is the first step towards proving that a protective layer is grafted on top of the ZnO film. Still, contact angle measurements and XPS surveys alone are

5.4 Characterization of the grafted layer

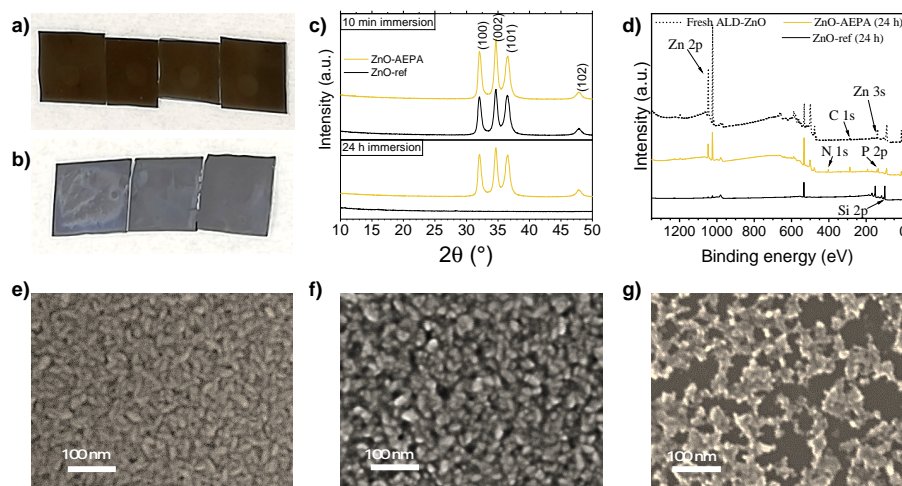


Figure 5.5: Evidences of the degradation of ref-ZnO in the solvent, and of the modification of the surface by 2-AEPA. Visual inspection of Si/ZnO (50 nm substrates after 24 h immersion in a) AEPA-containing solution and b) the sole solvent. ZnO-ref lost the copper-like reflection indicating a change in the ZnO layer. c) Diffractograms of ZnO-ref and ZnO-AEPA after 10 min and 24 h immersion. Planes corresponding to the wurtzite structure of ZnO are indicated. d) XPS survey of ZnO after ALD process, ZnO-AEPA (24 h) and ZnO-ref (24 h). The photopeaks of interest are indicated. SEM top images of e) ZnO-AEPA (2 h), f) ZnO-ref (10 min) and g) ZnO-ref (2 h).

not enough to confirm the effective coating of ZnO by the various molecules nor the way the molecules cover the surface.

5.4.2 Characterization of the chemical environment of the surface

5.4.2.1 High resolution XPS spectra

XPS has been used to confirm the molecular grafting on ZnO substrate and analyze the evolution of the chemical environment of the surfaces during the process (10 nm depth probed). The survey spectra of the three modified samples clearly evidence the presence of molecules at the surface with the detection of P (at 135 eV) and N (at 401 eV for 2-AEPA and 4-ABzPA) or F (at 688 eV for 4-FBzPA) elements. Zn, O and C elements are also visible and are attributed to the substrate, the adventitious carbon contamination, and the head and spacer groups of the molecules. The corresponding high energy resolution spectra of the main core levels Zn 2p_{3/2}, O 1s, C 1s, P 2p, F 1s and N 1s are presented in Figure 5.6 to accurately assess chemical environments.

ZnO-ref. ZnO-ref is considered first to determine the initial spectral signature of the substrate. Zn 2p_{3/2} peak is decomposed using two contributions at BE of 1022.3 eV (Zn_a) and 1023.2 eV (Zn_b) as already reported for bulk ZnO (Ali et

5.4 Characterization of the grafted layer

Table 5.3: Binding energy (eV) positions of the different contributions used to fit the core level spectra (XPS analyses). The error bar is ± 0.1 eV.

		ZnO- ref	ZnO- AEPA	ZnO- ABzPA	ZnO- FBzPA	4-FBzPA (powder)
Zn 2p _{3/2}	Zn _a	1022.3	1022.3	1022.3	1022.3	
	Zn _b	1023.2	1023.2	1023.2	1023.2	
	Zn _g		1023.3	1023.3	1023.3	
P 2p _{3/2}			134.2	133.7	133.7	134.3
N 1s	-NH ₂		400.9	400.3		
	-NH ₃ ⁺		402.5	401.9		
F 1s					687.7	687.4
O 1s	O _a	531.1	531.1	531.1	531.1	
	O _b	532.3	532.2	532.2	532.3	
	O _c	532.8	532.9	532.9	532.9	
	O _{conta}	533.1	533.6	533.0	533.2	534.1
	O _g		532.2	532.1	532.1	

al. (2015); Z. Gao and Banerjee (2019)). The O 1s peak requires four contributions, the one at 531.1 eV being assigned to Zn-O bulk network (O_a/Zn_a), the others at 532.3 eV and 532.8 eV to Zn-O surface networks (O_b and O_c/Zn_b) due to adsorbed O or water and presence of (oxy)-hydroxide species and the last at 533.1 eV to O involved in the carbonaceous contamination (O_{conta}) (Lacher et al. (2011); Rongwei Zhang et al. (2009)).

For the reference sample, the contributions for C 1s originate from contamination due either to accidental contamination during the handling of the samples, or to fragments of the Zn ALD precursor trapped in the film. It allows to set the parameters of these contributions for the following measurements and thus to distinguish the additional carbon contributions coming from the grafting from the ones coming from the contamination.

Effect of the grafting on the quantification of the signal. For all modified samples, these features observed for ZnO-ref are still present. However, a

5.4 Characterization of the grafted layer

variation of the relative signal of each contribution caused by the grafting was observed (*e.g.* Zn_a/Zn_b is not the same for all samples). As expected, the ZnO lattice (O_a/Zn_a) is still detected (the grafted layer is thinner than the depth probed). O_b , O_c and Zn_b surface contributions do not totally cancel which can indicate an incomplete surface coverage. Their intensities vary because the molecular grafting filters the photoelectron emitted beneath. The effect of this filter on the measurements depends on the nature of the molecules, their intimate organization during grafting and the coverage rate. The screening effect must differ with the kinetic energy of the photoelectrons, *i.e.* attenuation is not the same for all the photopeaks considered, as it has been reported for C contamination (Béchu et al. (2019)). Consequently, the surface contribution intensities are exacerbated (not filtered), and the quantification is not straightforward (the determination of the attenuation coefficient would be required).

Grafted molecules. The appearance of a contribution associated to the new surface environment after grafting Zn_g (1023.3 eV) is concomitant with an increase of O_g contribution (532.1 eV). This trend is more pronounced on the ZnO-AEPA sample presenting the highest molecular grafting rate ($Zn/P = 1.1$ vs 38.2 and 11.0 for ZnO-ABzPA and ZnO-FBzPA respectively). Specific contributions associated to the molecules (2-AEPA, 4-ABzPA, 4-FBzPA) are identified on the O and C spectra. Note that on the C spectra, the π - π satellite attesting for the aromatic cycle presence is not evidenced as it overlaps with the C_{conta} contribution. A unique environment is considered for P in the phosphonic group (one spin-orbit doublet). This is the same for N 1s where two contributions are required for the fitting of the N peak. They are assigned to NH_2 and NH_3^+ environments (Paniagua et al. (2016)). BE values are reported in Table 5.3.

Discussion on P 2p photopeak. It has been proposed in several studies that phosphonic acids chemisorb on zinc oxide via the deprotonation of the acid and formation of one or several Zn–O–P bonds (Figure 5.2, Smecca et al. (2013)) and the more bonds involved in the grafting, the stronger the interaction between the oxide and the molecule. Paniagua et al. (2008) reported non-resolved P 2p peaks around 133.4 eV for various phosphonic acids grafted on top of ITO, which was ascribed to phosphorus in PO_3^{2-} environment.

In the present work, the P $2p_{3/2}$ contribution is positioned at 134.2 eV for ZnO-AEPA and 133.7 eV for ZnO-ABzPA and ZnO-FBzPA, which is indicative of different protonated forms of the phosphonic acid group on the surface of modified ZnO. The comparison of this peak position with that measured on the initial 4-FBzPA powder at 134.3 eV (Figure 5.7) evidences a shift towards lower energies for ZnO-ABzPA and ZnO-FBzPA.

Keszthelyi et al. (2006) suggest that such a shift indicates a higher deprotonated state of the grafted molecule. It is associated with a chemical interaction with the transition metal. On the contrary, for ZnO-AEPA, the P 2p position does not vary much compared to that of the powder, which is in accordance with a deposition of a thicker multi-layer, as supported by AR-XPS data (see section 5.4.3). This is

5.4 Characterization of the grafted layer

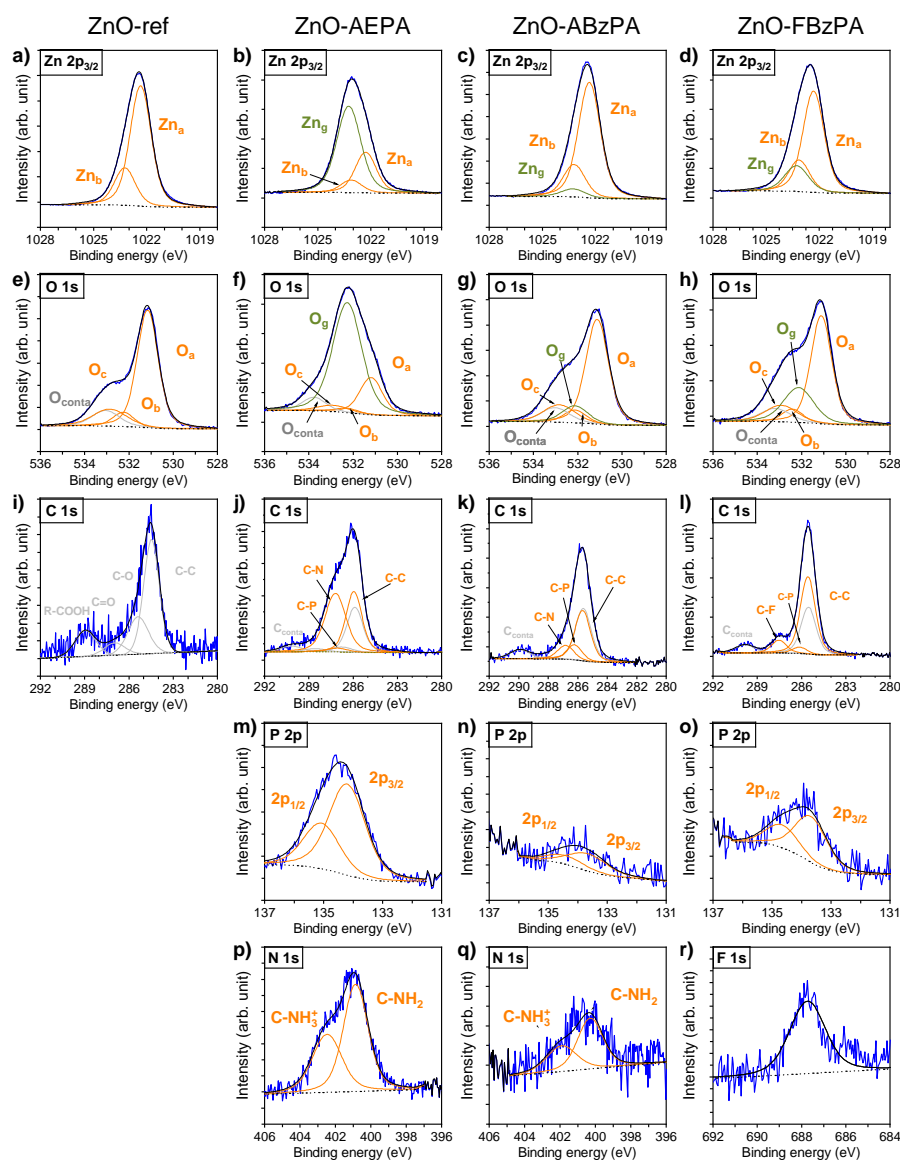


Figure 5.6: Summary of XPS measurements on reference ZnO (first column) and modified ZnO with 1 mM 2-AEPA (second column), 4-ABzPA (third column) and 4-FBzPA (fourth column). High resolution core level spectra of a)-d) Zn $2p_{3/2}$, e)-h) O 1s, i)-l) C 1s, m)-o) P 2p, p), q) N 1s and r) F 1s. For all spectra, experimental data are in plain blue, fitted data in plain dark and background in dotted black.

thus indicative of different grafting processes between the linear and the aromatic molecules.

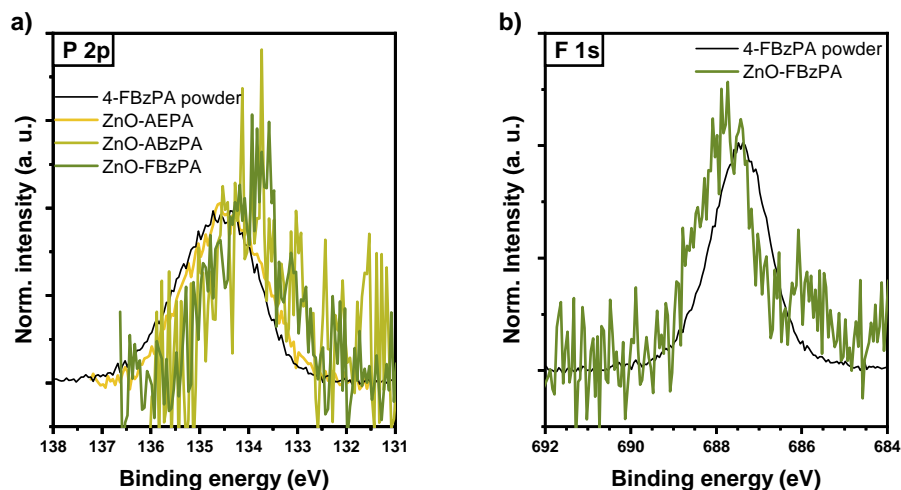


Figure 5.7: Normalized HR XPS spectra of a) P 2p photopeaks for 4-FBzPA powder, ZnO-AEPA, ZnO-ABzPA and ZnO-FBzPA and b) F 1s photopeaks for 4-FBzPA powder and ZnO-FBzPA.

Discussion on N 1s photopeak. Two contributions for N 1s were observed, which are commonly ascribed to amine (NH_2 around 400.0 eV) and ammonium groups (NH_3^+ around 401.5 eV). In the case of *n*-(6-aminoethyl)amino-propyltrimethoxysilane grafted on TiO_2 , Kassir et al. (2013) ascribed these contributions to physisorbed and chemisorbed species respectively, the physisorption involving a weak bonding between the protonated amine and a negatively charged surface state of the oxide. These two contributions systematically appear in the samples. However, in light of the analysis of the P 2p line, they might originate from different phenomena.

In ZnO-AEPA, the formation of a multilayer can explain the appearance of both protonation states, with the protonated amines being involved in an ion pairing interaction with the deprotonated phosphonic acid. In the case of ZnO-ABzPA, the P 2p signature indicates at least a partial grafting of the molecules on ZnO, and yet two contributions are found for N 1s. The ammonium groups could in this case arise from chemical bonding between the amine and the substrate (Hersh et al. (1995)).

5.4.2.2 ATR-FTIR measurements

The structure of the modified layer was also analyzed using ATR-FTIR, which gives information on the nature of the involved chemical bonds.

For that purpose, the Si substrate is shaped as a multiple-internal-reflection element in order to increase the signal-to-noise ratio from the thin grafted layer deposited on it (Figure 5.8.a). For each molecule, a reference spectrum was acquired

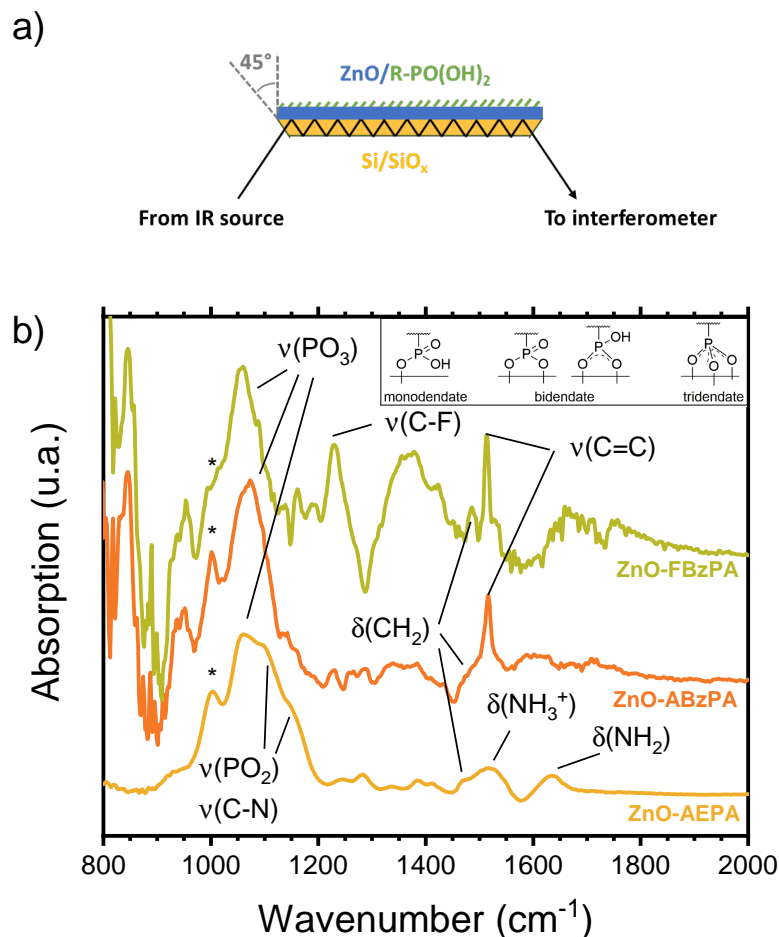


Figure 5.8: a) Sketch of the experimental set-up used for the ATR-FTIR measurement using a Si prism to enhance the signal/noise ratio. b) ATR-FTIR spectra of ZnO-AEPA, ZnO-ABzPA and ZnO-FBzPA. The Si-ZnO substrates were taken as reference. The * sign indicates the expected position of the contribution of unbounded P-O(H) moieties. The inset is a reminder of the various bonding modes of phosphonic acid derivatives on the oxide. Note that absorption of ZnO-AEPA is multiplied by 0.1.

on a Si/ZnO substrate which was subsequently modified with the desired molecule. The sample was then mounted back at the same spatial location on the sample holder, so that the resulting absorbance spectrum is characteristic of the changes induced by the grafting process

Figure 5.8 presents the ATR-FTIR spectrum of the modified layers in the fingerprint region (below 2000 cm^{-1}). The relevant identified peak positions are listed in Table 5.4. A large amount of parasitic signal is observed for ZnO-FBzPA and ZnO-ABzPA which is ascribed to the low thickness of the grafted layer and the background subtraction.

5.4 Characterization of the grafted layer

Table 5.4: Positions of the vibration modes extracted from the different FTIR spectra of ZnO-AEPA, ZnO-ABzPA and ZnO-FBzPA.

Vibration mode	ZnO-AEPA (cm ⁻¹)	ZnO-ABzPA (cm ⁻¹)	ZnO-FBzPA (cm ⁻¹)
P-O modes	950–1200	950–1200	950–1200
$\nu(\text{C-F})$			1230 (aromatic)
$\delta(\text{CH}_2)$	1468	1468	1485
$\nu(\text{C=C})$		1515 (disubs. benzyl)	1515 (disubs. benzyl)
$\delta(\text{NH}_3^+)$	1520		
$\delta(\text{NH}_2)$	1630		

Identification of each molecule. For all the molecules, the bands related to phosphonic species in the 950-1200 cm⁻¹ range (Longo et al. (2013)) attest the presence of the molecules at the surface of the oxide, and their grafting since the spectra from the surface molecule significantly differ from that of the free molecules (see [chapter A.3](#)). For ZnO-AEPA samples, the presence of amine functional groups can be associated with the two broad absorption bands at 1630 cm⁻¹ and 1520 cm⁻¹. The former is ascribed to the NH₂ in-plane bending modes of primary amines, the latter to the unresolved symmetric and asymmetric bending modes of protonated amines (Knöfel et al. (2009)). The latter peak has a shoulder at 1468 cm⁻¹ ascribed to the methylene bending mode, which can also be found on ZnO-FBzPA. The two aromatic molecules (ZnO-ABzPA and ZnO-FBzPA) feature an intense peak at 1515 cm⁻¹ characteristic of a substituent-sensitive aromatic-ring mode in di-substituted benzyl (Lin-Vien et al. (1991a)). Another sharp intense peak in ZnO-FBzPA at 1230 cm⁻¹ can be attributed to an aryl-F stretching mode (Lin-Vien et al. (1991a)).

Discussion on the grafting modes of the molecules. The mono-, bi- or tridentate nature of the bond between the phosphonic acids and ZnO should appear in the region of the P–O and P=O stretching modes. Neither of the molecule presents a contribution from P=O stretching modes (in the 1200-1250 cm⁻¹ range – the contribution at 1230 cm⁻¹ in ZnO-FBzPA being already ascribed to $\nu(\text{C-F})$). The presence of such a contribution would have implied the presence of mono- or bidentate phosphonic acid moieties. Moreover, the contribution at 1050 cm⁻¹ (in the typical range of asymmetric (P–O) vibrations of PO₃ moieties, Lin-Vien et al. (1991c)) strongly suggest a tridentate grafting on the surface.

The contribution of symmetric (P–O) vibrations of PO₂ species could also

contribute to this spectral range. However for ZnO-FBzPA and ZnO-ABzPA, no corresponding contribution of asymmetric (P–O) vibrations of PO₂ species is observed above 1100 cm⁻¹, discarding the bidentate hypothesis (Quiñones et al. (2014)). Note that the vibrational bands at 1050 cm⁻¹ is somewhat broader for ZnO-ABzPA as compared to ZnO-FBzPA. This feature could be due to a structural disorder within the grafted layer, in agreement with XPS data. ZnO-FBzPA is also characterized by the weakness of the contribution at 1000 cm⁻¹, clearly observed for ZnO-ABzPA and ZnO-AEPA; this contribution is often associated with unbound P–O(H) contributions.

For ZnO-AEPA, two additional contributions are observed at higher energy (1100 and 1150 cm⁻¹). These contributions are tentatively assigned to symmetric (P–O) vibrations of PO₂ and C–N stretching vibrations (Lin-Vien et al. (1991b)), or admixtures of these modes. They are strong indications that on ZnO-AEPA, bidentate bonding of phosphonic groups coexist with tridentate bonding.

The presence of bidentate bonding can be paralleled with the existence of a zwitterionic form suggested by the observation of a bending vibration band at 1520 cm⁻¹. As a whole, tridentate bonding can be found for all molecules, at least as the major bonding configuration. This is in line with previous reports stating that phosphonic acids tend to form tridentate bonds with ZnO (Hotchkiss et al. (2011)), and reported DFT calculations on ZnO-FBzPA that showed that tridentate configuration is more stable than the bidentate one (Wood et al. (2012)).

5.4.3 Organization of the molecules on the surface

5.4.3.1 In-depth profiling by AR-XPS measurements.

The organization of the molecules within the layer have been investigated using AR-XPS. This technique consists in acquiring the XPS signal of a specimen with different incident angles. At low angles, the signal coming from species constituting the surface of the specimen will be enhanced due to a longer effective path of the excitation through these layers. Analysing the evolution of the area ratios of the considered elements with the incidence angle can thus provide an information on the average vertical distribution of each element.

Figure 5.9.a presents a sketch of the expected result from the AR-XPS measurements, in the hypothesis that all layers form as upright, organized monolayers. In this configuration, P, Zn and O – which constitute the substrate and the head group – would be localized the deepest in the sample at the interface between ZnO and the molecule layer. On the contrary, the signature elements of the tail groups – N and F – would be localized close to the surface³. C signal would originate from somewhere in between, mostly from the spacer.

Figure 5.9.b shows the actual experimental results of the AR-XPS analysis. The relative positions of the elements Zn, O, C, P, N and F are presented in the relative depth plot. In any case, the constitutive elements of the substrate (Zn and O) are located deeper, as expected. Zn and O are close to each other for ZnO-ABzPA

³Note that the "surface" refers to the top of the molecule layer in contrast to the "interface", between ZnO and the molecule layer.

5.4 Characterization of the grafted layer

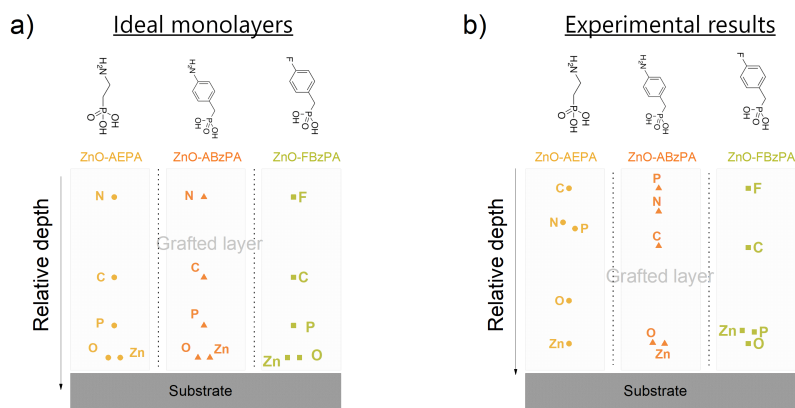


Figure 5.9: Relative depth profiles of the elements of the grafted layers. a) Sketch of the theoretical profile in the hypothesis of self assembled monolayers on top of ZnO. b) Experimental profiles as extracted from AR-XPS measurements.

and ZnO-FBzPA, while Zn is located deeper in ZnO-AEPA. For ZnO-FBzPA, the relative order of the other elements agrees well with the expectations (from the substrate to the surface P–C–F). Regarding ZnO-AEPA and ZnO-ABzPA however, P, C and N are localized close to each other and there is no correlation between the experimental results and the expected arrangement of the elements in a SAM.

5.4.3.2 Discussion

From the XPS, FTIR and AR-XPS observations, different organizations of the molecules on the ZnO substrate are proposed. These organizations are presented in [Figure 5.10](#), and the evidences supporting each layout are gathered below.

4-FBzPA: ordered monolayer. 4-FBzPA forms an ordered monolayer on the ZnO substrate. The grafting occurs through the phosphonate group and the new surface is functionalized with fluorine.

- The FTIR and XPS signals confirm the condensation of phosphonate moieties with tridentate bonding as majority.
- A higher contact angle of the modified surface with water in line with a fluorination of the surface.
- The shift in binding energy of the F 1s photopeak is low (0.2 eV) when comparing the signals from the powder of 4-FBzPA and from ZnO-FBzPA. This hints for a quasi-unperturbed chemical environment of the F in the grafted configuration.

5.4 Characterization of the grafted layer

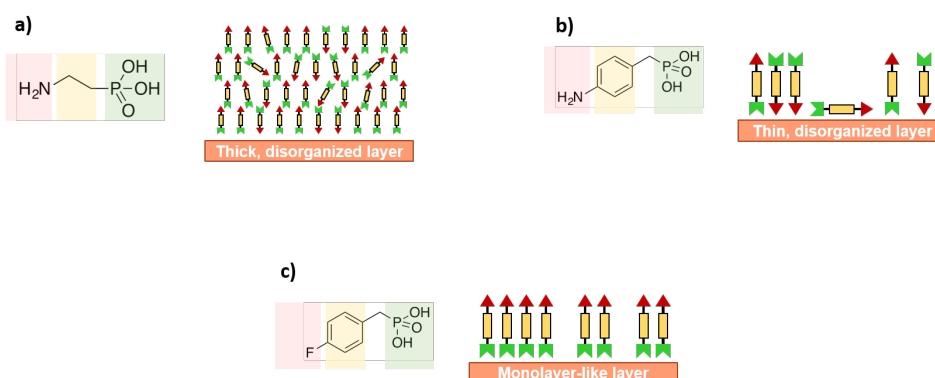


Figure 5.10: Proposed organization of the different molecules on top of ZnO, as deduced from the experimental evidences. a) 2-AEPA forms a thick multilayer, b) 4-ABzPA forms a thin disordered layer, and c) 4-FBzPA forms an organized thin layer.

- AR-XPS data reveal that the elements in the film follow the expected order of a monolayer grafted by the phosphonate group and with the fluorine pointing outwards.

4-ABzPA: thin, disordered layer. 4-ABzPA forms a disordered layer on the ZnO substrate. The disorganization is suspected to arise from a competition in the adsorption between the phosphonate and amine groups.

- The FTIR and XPS signals confirm the condensation of phosphonate moieties with tridentate bonding as majority.
- N 1s line requires two contributions to be correctly fitted. This suggests two chemical environments for nitrogen, which are ascribed to free amine groups (grafted by the $-\text{PO}(\text{OH})_2$ moiety) and to amine coordinated with undercoordinated Zn.
- The comparable intensities of the FTIR and P 2p XPS signals for ZnO-ABzPA and ZnO-FBzPA suggest that a small amount of molecules are present on the surface indicating a thin layer of 4-ABzPA.
- AR-XPS data show mixed signals from P and N localized approximately at the same depth, once again in line with a mixed-grafting process.
- The O signal is close to the Zn signal in the AR-XPS results. This also suggests that a rather thin layer of molecules is deposited (cf. next paragraph on this matter).

2-AEPA: thick, disordered multilayer. 2-AEPA forms a disordered and thick multilayer. The alkyl chain is suspected to be too short to ensure a proper organization of the molecules, as it was reported that shorter alkyl chains lead to disorganized liquid-like layers (Fukuda et al. (2009)). Moreover, the ionic

5.4 Characterization of the grafted layer

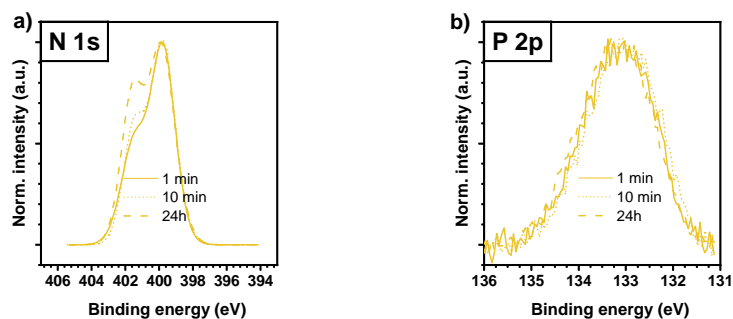


Figure 5.11: Evolution of a) N 1s and b) P 2p photopeaks for samples immersed in a solution of 2-AEPA for 1 min, 10 min, and 24 h.

interactions between the phosphonate and amine groups of the molecule can secure the stability of the multilayer.

- The FTIR and XPS signals confirm the condensation of phosphonate moieties with tridentate bonding as majority.
- The high wavenumber tail of the phosphonate moieties in IR data reveals that a second form of the phosphonate group coexists. This contribution can be ascribed to the phosphonate moieties involved in the intermolecular ionic bonds or bidentate bonds.
- Similarly, the XPS N 1s signal unravels to coexistence of two chemical environments for nitrogen, namely in protonated ($-\text{NH}_3^+$) and deprotonated ($-\text{NH}_2$) states. The former would thus be involved in the intermolecular ionic bonds.
- Looking at the evolution of the N 1s signal with immersion time (Figure 5.11), the ratio between the signal of the contribution at high energy (related to the protonated amine) and at low energy increases as the immersion time increases, accompanied with a slight shift of P 2p towards higher energies. This can be related to the formation of the multilayer which grows thicker at longer immersion times.
- Despite similar experimental set ups, both FTIR and XPS signals are much higher for 2-AEPA than for 4-ABzPA or 4-FBzPA, suggesting that a higher amount of molecules are present at the surface of the oxide. This is well in line with the multilayer hypothesis.
- AR-XPS data show mixed signals from P and N localized approximately at the same depth showing no real order in the layer.
- Additionally, the Zn signal is relatively deeper than the O signal – compared to the other samples. If the molecules were forming a monolayer, its thickness should be less than 1 nm (assuming a mean bond length of 1.5 Å). Omitting the depth-related signal attenuation and considering a probed depth of

5.5 Influence of the grafting on the properties of the absorber and on the complete solar cells

~ 10 nm, most of the O signal would come from the ZnO lattice. O and Zn would hence be localized at a similar depth. In the case of a multilayer however, the mean depth of O would be located closer to the probed surface than Zn as the thickness of the multilayer increases because for a thickness of x nm, 1) Zn signal only comes from the deepest $10-x$ nm, 2) lattice O contributes only from the deepest $10-x$ nm, 3) grafted O comes from the other x nm. Hence, Zn and O are expected to be farther apart as the thickness of the multilayer grows.

5.5 Influence of the grafting on the properties of the absorber and on the complete solar cells

Modifying the chemical state of a surface can lead to significant changes in the interfacial chemistry. It is thus of high interest to investigate the effects of the modification of ZnO by 2-AEPA and 4-FBzPA on the interface between ZnO substrate and hybrid perovskite. The grafting of 4-ABzPA was also considered but lead to non-working devices. A design that corresponds to a conventional n-i-p perovskite solar cell structure was chosen (as described in 1.2.3). Hence the substrate consists in commercial FTO-coated glass, covered with 15 nm of ZnO deposited by ALD. The substrates are modified with 1 mM 2-AEPA or 4-FBzPA for 10 min in EtOH:H₂O (19:1), and a triple cation perovskite (solution composition Cs_{0.05}(FA_{0.83}MA_{0.17})_{0.95}Pb(I_{0.83}Br_{0.17})₃) is deposited on top. The sample with perovskite deposited on ZnO-AEPA (resp. ZnO-FBzPA and ZnO-ref) is referred to as AEPA-pvk (resp. FBzPA-pvk and Ref-pvk, cf. Table 5.2).

5.5.1 Effect of ZnO modification on the perovskite thin film

5.5.1.1 Variation of the morphology and structure of the perovskite film

Morphology of the films. The morphology of the perovskite films was analyzed by SEM. Figure 5.12 presents BSE micrographs of the perovskite layer surface of Ref pvk, FBzPA-pvk and AEPA-pvk at different magnifications. Cross sections of AEPA-pvk and Ref-pvk are also displayed.

As it has been stated in section 5.4.1, BSE micrographs also reveal chemical changes of the surface, with the heavier elements appearing brighter. In the case of perovskite surface, one can distinguish dark perovskite grains and white needle-like lead iodide particles. This lead iodide can originate from a decomposition of the underlying perovskite layer. It is however usual to detect a small amount of it even in well-formed perovskite films because the initial precursor solution contains a 10% PbI₂ excess. A small amount of lead iodide has indeed been shown to help passivate the grain boundaries of the absorber (Q. Chen et al. (2014)).

On the surface images, the morphology of the perovskite appears highly dependent on the modification of ZnO by the molecules. The perovskite of AEPA-pvk forms similarly to what has been reported in efficient cells with small clusters of PbI₂ (Saliba et al. (2018)). On the other hand, the perovskite films of Ref-pvk and

5.5 Influence of the grafting on the properties of the absorber and on the complete solar cells

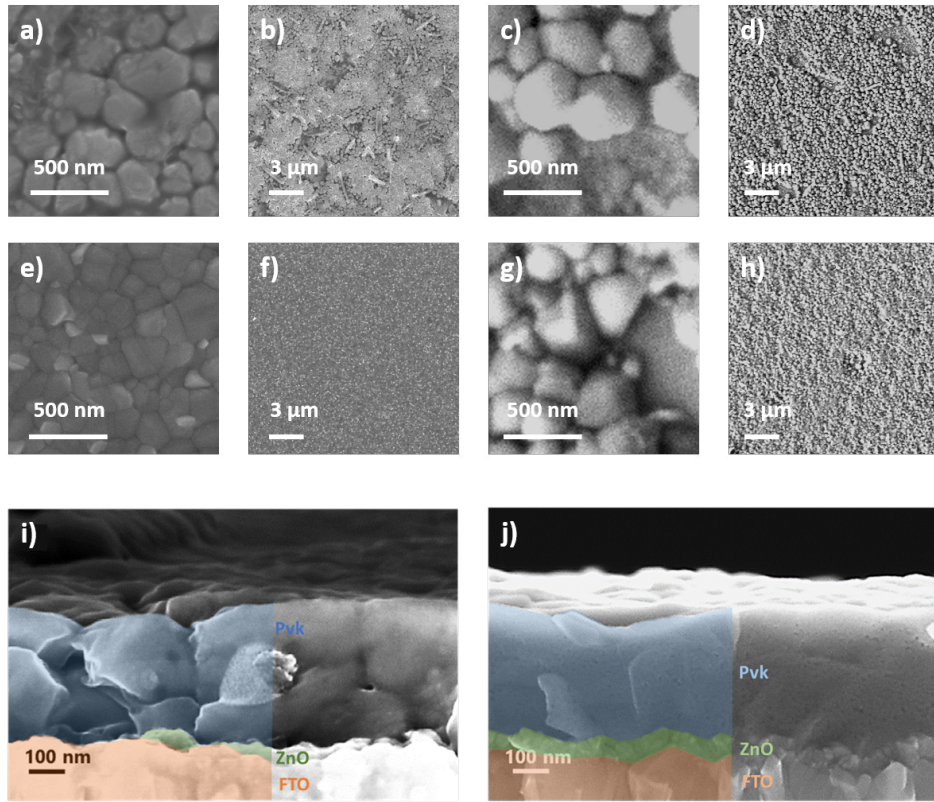


Figure 5.12: SEM micrographs (BSE) of a)-d) Ref-pvk, of e)-f) AEPA-pvk and of g)-h) FBzPA-pvk. b), d), f), h) Low magnification surface micrographs. a), c), e), g) High magnification surface micrographs. i, j) Cross-sectional images (BSE) of ref-pvk and AEPA-pvk. The perovskite surface in the case of Ref-pvk and FBzPA-pvk appear inhomogeneous and damaged.

FBzPA-pvk show a degraded crystallization with a high amount of PbI_2 , or do not completely cover the substrate, which evidences a deteriorated film formation.

On cross-sectional images, a pronounced formation of cavities between the grains can be observed for Ref-pvk compared to AEPA-pvk. Furthermore, a continuous ZnO layer is clearly visible in the AEPA-pvk cross section (Figure 5.12.j)). This is hardly the case in Ref-pvk (Figure 5.12.i)), suggesting a degradation of the ZnO layer due to the perovskite deposition in the case of Ref-pvk.

Structural properties. These very different morphological features between Ref-pvk and AEPA-pvk have been further explored with a structural characterization carried out by XRD. The corresponding diffractograms are shown in Figure 5.13.b) along with the indexation of the phases present in the specimen.

In both cases, the film crystallizes into the photo-active perovskite phase as confirmed by the high intensity diffraction peaks at $2\theta = 14^\circ$, 19.9° and 24.4° , characteristic of the $\text{Cs}_{0.05}(\text{FA}_{0.83}\text{MA}_{0.17})_{0.95}\text{Pb}(\text{I}_{0.83}\text{Br}_{0.17})_3$ perovskite crystal

5.5 Influence of the grafting on the properties of the absorber and on the complete solar cells

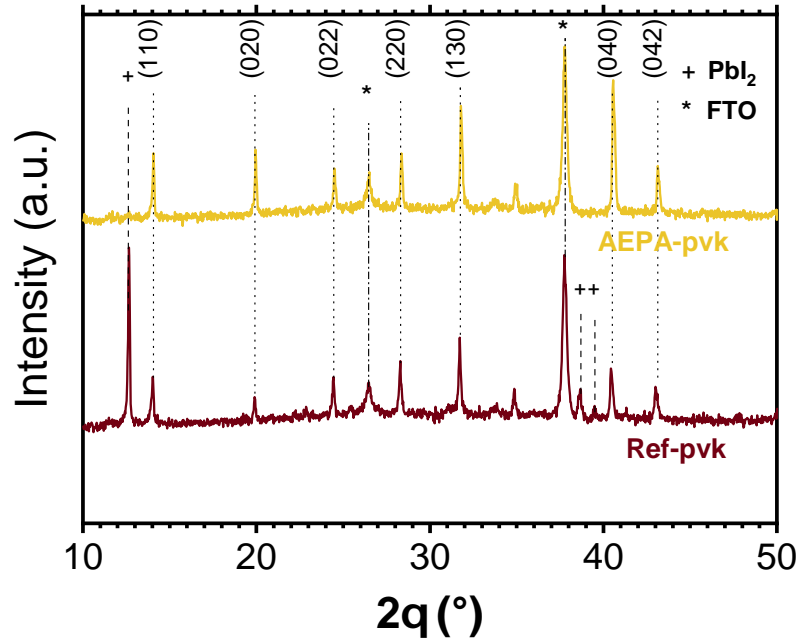


Figure 5.13: Diffractograms of AEPA-pvk and Ref-pvk on glass/FTO substrates. The diffraction planes of the cubic phase of the perovskite are identified, along with the contributions of the FTO substrate and of PbI_2 .

structure (Saliba et al. (2016)). In Ref-pvk additional peaks appear at $2\theta = 12.6^\circ$, 38.7° and 39.5° . These peaks are characteristic of lead iodide which originates from the degradation of the perovskite. The presence of lead iodide has also been confirmed by UV-Vis transmission spectroscopy as a sharp edge rises around 500 nm for Ref-pvk (Ferreira da Silva et al. (1996), [chapter A.3](#)).

GI-XRD was used to get an in-depth information, varying the depth probed by varying the incidence angle of the X-rays ([Figure 5.14.a](#)) and comparing the diffractograms of Ref-pvk and AEPA-pvk with a grazing incidence angle going from $\Omega = 0.2^\circ$ to 1.6° by step of 0.2° . The measurements have been performed right after the deposition of the perovskite to reduce atmospheric degradation ([Figure 5.14.b,c](#)). The angular window has been set between $2\theta = 12^\circ$ and $2\theta = 15^\circ$, so that the evolution of the main peaks of interest (PbI_2 , $2\theta = 12.7^\circ$, and perovskite (110) plane, $2\theta = 14.1^\circ$) is recorded within a short period of time (30 min) and thus limit the impact of degradation during the measurements performed in ambient atmosphere.

As for AEPA-pvk, the pvk-peak is observed for $\Omega = 0.2^\circ$, and its intensity increases up to $\Omega = 1.0^\circ$, and then progressively decreases for larger angles. This is ascribed to the variations of the diffracting volume of the perovskite film which first increases with Ω , up to the point where the penetration length is about the thickness of the film. The diffracting volume of perovskite then decreases as Ω

5.5 Influence of the grafting on the properties of the absorber and on the complete solar cells

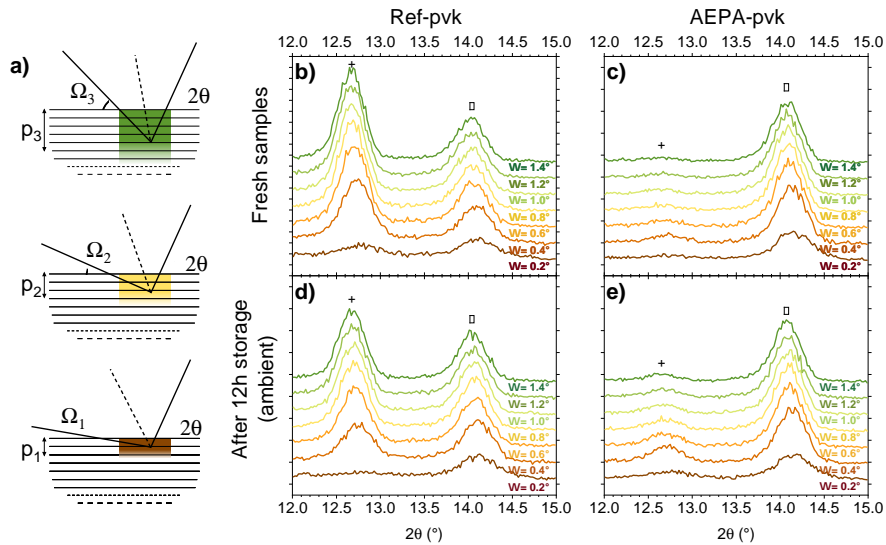


Figure 5.14: a) Sketch showing the influence of the change in Ω on the depth p probed during the measurement (shaded area). In this example, $\Omega_1 < \Omega_2 < \Omega_3$ so $p_1 < p_2 < p_3$. The penetration length of the incoming rays is the same in all three situations. GI-XRD diffractograms with varying grazing incidence angles from $\Omega = 0.2^\circ$ to 1.4° of b) fresh Ref-pvk, c) fresh AEPA-pvk, d) stored Ref-pvk and e) stored AEPA-pvk. The samples were stored on a shelf in ambient atmosphere and exposed to light. The region of interest focuses on the main PbI_2 peak (+ around 12.7°) and the main perovskite peak (\square around 14.0°). The y scale is the same for all four diffractograms.

further increases. Note that at very low angles (around 0.2°), a signal loss can originate from X-ray reflection on the sample. The PbI_2 peak is very weak at any incidence angle, consistent with the XRD observations.

Regarding Ref-pvk, the pvk peak follows the same trend as for AEPA-pvk. This is contrasted by the remarkable evolution of the PbI_2 peak: its intensity increases up to $\Omega = 1.2^\circ$, indicating that PbI_2 is located across the layer, down to the ZnO/perovskite interface.

The same samples were then investigated after storage for 12 h in ambient air and light with the results shown in Figure 5.14.d,e). There are no obvious changes for the Ref-pvk sample with the pvk peak and PbI_2 peak reaching their maximum at $\Omega = 1.0^\circ$ and $\Omega = 1.2^\circ$ respectively. Regarding AEPA-pvk, a weak PbI_2 peak appears and reaches its maximum value at $\Omega = 0.4^\circ$.

5.5.1.2 Observations on PbI_2 formation

The poor chemical stability of the ZnO/perovskite interface has been widely reported and identified as one of the main reason for the lower performance of ZnO as electron extraction layer in perovskite solar cells in comparison to TiO_2 (J. Yang et al. (2015)). Acid base reactions between MA molecules and ZnO occur during the annealing of the perovskite, leading to its detrimental degradation into PbI_2 .

5.5 Influence of the grafting on the properties of the absorber and on the complete solar cells

Accordingly in this study, the presence of pure PbI_2 in Ref-pvk has been evidenced by XRD and UV-vis spectroscopy. This degradation mechanism can also be the cause of cavity formation in the perovskite layer and the inferior morphology of the surface observed in SEM for Ref-pvk.

Similar morphologies of MA containing perovskite have already been reported by Schutt et al. (2019), and the replacement of MA by a mixture of FA and Cs led to improved morphologies. The change in the grains' compactness in the layers can be related to the degradation mechanism of the interface between MA and ZnO suggested by Dkhissi et al. (2016), or to the etching of ZnO by ammonium species (Juarez-Perez et al. (2019); J.-K. Kim and J.-M. Lee (2017)). On the other hand, none of these degradation-related features are observed in AEPA-pvk, which shows that the grafted layer of 2-AEPA chemically protects the interface between perovskite and ZnO.

This assertion is further confirmed by the GI-XRD study of the samples. Two degradation mechanisms are evidenced. First, a fast degradation occurring during the synthesis when ZnO/perovskite are annealed above 80°C as reported before (J. Yang et al. (2015)). This is characterized by a strong PbI_2 signal that increases with increasing scanning depth, hinting that the lead iodide spreads across the whole film. This feature is only seen for Ref-pvk. Second, a slower degradation process that is caused by ageing in atmospheric conditions. It has already been widely reported that moisture and oxygen are key extrinsic parameters of the perovskite degradation (Bisquert and Juarez-Perez (2019)).

Here, this degradation is revealed by the apparition of the lead iodide peak for AEPA-pvk after storage, which did not exhibit any lead iodide phase observable in the XRD experiment right after the synthesis. Note that lead iodide peak reaches its maximum at quite low incidence angles, indicating the formation of lead iodide stemming rather from the air/perovskite interface than from the perovskite/ZnO interface at the back of the cell. The modification layer thus acts as a physical barrier between ZnO and perovskite, hence preventing the different reactants of the degradation mechanism from reacting with each other.

5.5.2 Integration in complete PV devices

Complete solar devices were prepared and characterized optoelectrically (architectures presented in Figure 5.15). The J-V parameters of the cells are presented in Table 5.5, with the corresponding J-V characteristics displayed in Figure 5.16. Even if the efficiencies remain quite low, the PV parameters show interesting trends. Both Ref-pvk and FBzPA-pvk have a similar V_{OC} (720 mV and 749 mV respectively) but the modified sample shows a higher J_{sc} (9.5 mA cm^{-2} vs. 13.5 mA cm^{-2} , reverse scan). The two samples also exhibit a pronounced hysteresis between forward and reverse scans. On the other hand, the AEPA-pvk sample has a much higher V_{OC} of 1004 mV but a dramatically low J_{sc} of 3.2 mA cm^{-2} , however with a lesser hysteresis. Overall, the best performing cell is the FBzPA-pvk with a PCE of 4.1% (reverse), stabilized at 2.4%. This shows a sensible increase as compared to the Ref-pvk which has a PCE of 2.2% (reverse) stabilized at 1.2%, comparable with efficiencies shown by X. Dong et al. (2014).

5.5 Influence of the grafting on the properties of the absorber and on the complete solar cells

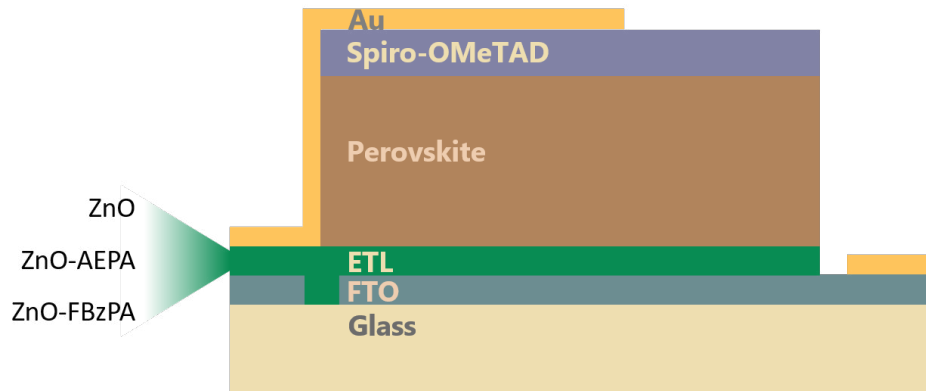


Figure 5.15: Sketch of the cell architectures considered for the study on ZnO modification.

Table 5.5: Photovoltaic parameters of the best performing cells made on Ref-pvk, AEPA-pvk and FBzPA-pvk substrates. The quantities are given for a reverse scan at 20 mV s^{-1} .

	V_{OC} (mV)	J_{SC} (mA cm^{-2})	FF (%)	PCE (%)
Ref-pvk	720	9.5	32.4	2.2
AEPA-pvk	1004	3.2	54.6	1.7
FBzPA-pvk	759	13.5	40.1	4.1

The results of the J–V analysis of the samples further support the previous conclusions of the study. AEPA-pvk exhibits a V_{OC} above 1 V, which is in the expected range. A variation in open circuit voltage can be related to a change in the quality of the interfaces between the absorber and the extraction layers (Aydin et al. (2019)). It has been shown previously on different oxide ETLs that the use of Lewis-bases (*e.g.* amine groups) or halogens can cure defects of the oxide as well as of the perovskite (undercoordinated iodide and lead specifically Shallcross et al. (2019); F. Wang et al. (2018)). Since 2-AEPA is forming a complete multilayer on the surface of ZnO, the interface between the absorber and the n-type extracting stack is indeed passivated allowing for a less defective interface, hence less non-radiative recombinations and a higher open circuit voltage. On the other hand, the short-circuit current density is very low, in spite of a good morphology and a superior absorption of the perovskite layer. Ab initio simulations show that the difference between the HOMO and the LUMO of 2-AEPA is about 7.0 eV (cf Table 5.1). The insulator-like behavior of the multilayer may be the reason impeding the extraction of the photogenerated carriers.

Regarding FBzPA-pvk, the J–V measurements combined with the SEM observations shed light on the covering of the grafted layer. The morphology resembles that of Ref-pvk, only with a smaller density of degraded spots. This suggests

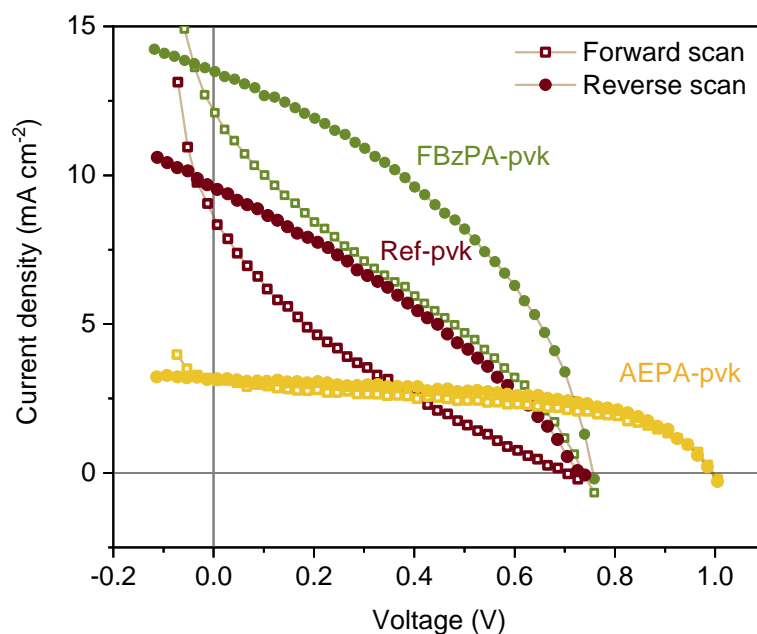


Figure 5.16: J-V characteristic of complete photovoltaic devices made on Ref-pvk, AEPA-pvk and FBzPA-pvk substrates under AM1.5G 1 sun simulated illumination.

that the molecular layer does not completely cover ZnO, leaving places where the acid-base reaction can happen and degrade the perovskite. This translates on the J-V characteristics by a low V_{OC} similar to that of Ref-pvk, probably caused by defect states related to this degradation process. The current density is however higher for the modified sample, in line with the fact that more photoactive material is preserved and can participate in the generation of photocarriers.

5.6 Conclusion

Functionalization of ZnO thin films with phosphonic acid derivatives can be an easy way to tune the properties of the film by modifying the architecture of the grafted molecule. In this chapter, the effective grafting of an ALD ZnO layer with three different molecules having different spacers and functionalizing groups has been demonstrated.

The grafted layers have been characterized by different surface characterization techniques (contact angle, XPS, FTIR). The results suggested that amine-terminated molecules tend to form hydrophilic multilayers, probably due to chemical interactions between the phosphonic and amine groups. On the other hand, fluorine-terminated molecules rather form a better-organized layer with an effective

hydrophobic F termination of the surface, which underlines the importance of the functional groups for the grafting process.

The 2-AEPA and 4-FBzPA molecules were then integrated in a ZnO/halide perovskite interface, in order to probe their chemical passivation abilities. The perovskite grows in more densely packed films on top of AEPA-modified ZnO compared to bare ZnO. Furthermore, the large contribution of the PbI_2 phase, which is known as an indicator of perovskite degradation leading to low performance in perovskite solar cells, was only observed when it is grown on bare-ZnO. This demonstrates the effective passivation of the interface by the grafted molecule as a powerful method to prevent acid-base reaction between MA and ZnO and hence inhibit the degradation of the perovskite. 4-FBzPA shows however more mitigated improvements concerning the passivation of the interface, which was principally ascribed to a non-complete coverage of the ZnO substrate.

Even though the grafting of molecules showed promising results, the integration in full devices lead to low efficiencies. It was difficult to balance a good passivation of the layer and an adequate charge extraction in full devices. Still the effects of the molecules and their assembly structure have been further reinforced by the J-V measurements.

The developed process is simple, allows for the formation of passivation layers in a reasonable time, uses non-toxic chemicals and solvents, in ambient atmosphere, aiming for a high throughput. There is plenty of room for optimization of the process, working on solvent engineering, or exploring in details post-deposition treatments to enhance the quality of the layer (annealing, washing in alkaline solutions ...). The examined molecules can exist in various forms depending on the pH of the solution. It can also be worth exploring the influence of this parameter on the nature of layer, which can help promoting or inhibiting competitive reactions.

These simple modifications can open up the way for exploring exciting opportunities where ALD-ZnO could not easily be used beforehand due to a lack of chemical passivation, by using more elaborate interfacial molecules.

General conclusion and perspectives

The aim of this dissertation was to develop and characterize inorganic electron transport layers for perovskite solar cells applications. Two materials – SnO_2 and TiO_2 – have been developed by ALD at IPVF and integrated in various architectures of perovskite solar cells (mesoporous or planar architectures). The effect of a modification of the interface between ZnO and perovskite by small organic molecules has also been studied. The major findings related to these topics are summarized in the following sections.

C.1 Development of ALD materials

The development of TiO_2 and SnO_2 by ALD using various combinations of precursors has been presented. These materials were not known at IPVF and have required a careful optimization of the deposition process to yield recipes. For each material, one precursor for the metal species (tetrakis(dimethylamino)Sn – TDMA^{Sn} , Ti tetra(isopropoxide) – TTIP) and two precursors for oxygen (H_2O and H_2O_2) have been investigated. Due to the low volatility of the organometallic precursors, the transport of these precursors from the canisters to the reaction chamber has been optimized by combining a heating of the canister and a gas-assisted transport of the precursors (using N_2).

The ALD process has been identified as such by QCM studies for all combinations of precursors with the recognition of the self-limiting surface reactions. For TiO_2 , an ALD window with H_2O is found between 100°C and 210°C , while no obvious ALD window could be determined with H_2O_2 . For SnO_2 , there was no ALD window in either case, but the thickness variation with the deposition temperature of the H_2O process was higher than that of the H_2O_2 process.

The characterization of the films deposited with TTIP revealed in both cases the formation of a TiO_2 film whose stoichiometry has been confirmed by XPS measurements. A sensible difference lies in the shape of the C 1s high resolution spectrum, which can indicate a different contamination of the film (either surface contamination or contamination by fragments of ALD precursors). When grown from H_2O_2 , the as-deposited film is an amorphous wide band gap (3.6 eV) material with a good transparency in the visible range. When grown from H_2O , the as-

deposited film has similar properties but transitions from the amorphous to the anatase phase at a specific thickness (18 nm at 200 °C). In regard of the process and material characterizations, the deposition temperature of TTIP/H₂O was set at 200 °C (GPC = 0.35 Å/cycle), while that of the TTIP/H₂O₂ process was set at 100 °C (GPC = 0.7 Å/cycle).

The characterization of the film deposited with TDMASn showed large differences depending on the O source. Using H₂O yields a weakly doped p-type material with a narrow optical band gap (2.6 eV), relatively resistive and with structural properties close to those of the SnO romarchite phase, not suitable for the intended application as charge transport layer. Using H₂O₂ results in an n-type material, with a larger optical band gap (4.2 eV) granting an excellent transmission in the visible range, and with structural properties close to those of the SnO₂ rutile phase. The latter film has been investigated with XPS, which reveals a contamination of the film by DMA ligands and -OH groups, and confirms the SnO₂ stoichiometry of the film. In regard of the process and material characterizations, the deposition temperature has been set at 100 °C for the TDMASn/H₂O₂ process (GPC = 1.8 Å/cycle).

C.2 Integration of ALD-TiO₂

The integration of ALD-TiO₂ as a substitute to the traditional compact layer of TiO₂ deposited by spray pyrolysis in a mesoporous architecture has been investigated. Owing to the necessary annealing step of the mesoporous layer at 500 °C, the behavior of the ALD-TiO₂ layer after annealing in air at various temperatures up to 500 °C has been characterized. The properties of the ALD-TiO₂ after annealing were close to those of SP-TiO₂. The annealing was shown not to affect the optical properties of the ALD-TiO₂ layers of various thicknesses. It tends to homogenize their structural properties (all layers crystallize in the anatase phase). Cyclic voltamperometry showed that the coverage and conformity of as-deposited ALD-TiO₂ was enough to efficiently block the holes for thicknesses as low as 5 nm. The annealing-induced crystallization is accompanied by a diminution of the thickness of the film. The shrinkage probably induces the formation of pinholes in thinner films, reducing their hole-blocking ability.

The homogeneity of both deposition methods has also been assessed by comparing the transmission of the layer over approximately 15×15 cm². SP-TiO₂ was shown to have a rather poor homogeneity across the whole area ascribed to variations in the (manual) deposition process and in the aerolics. Conversely, ALD-TiO₂ exhibited a good homogeneity, which is to correlate with the known assets of the ALD process in term of conformity and homogeneity. It indicates that upscale strategies for perovskite solar cells could greatly benefit from the use of ALD.

The integration of the ALD-TiO₂ layer in working devices has been studied. The structural and morphological properties of the perovskite grown in a mesoporous architecture shows no evident influence of the deposition method of the compact TiO₂ layer. An optimization study on the thickness of the ALD-TiO₂ layer shows

a relatively low influence on the PV parameters for thicknesses lower than 17 nm. For higher thicknesses, the FF decreases which is ascribed to an increase of the series resistance caused by the titania layer. The PV performances of cells based on SP-TiO₂ or on ALD-TiO₂ are comparable with maximum stabilized efficiencies of 19.30% and 19.65% respectively, indicating that ALD is a reliable deposition process. Breaking down the PV parameters has shown that SP-TiO₂ based cells usually have a higher J_{SC} , which the ALD-TiO₂-based cells compensate with an increased reproducibility and FF.

A short study of planar devices based on SP-TiO₂ and ALD-TiO₂ revealed that the mesoporous scaffold is essential to ensure good cell performances. It also hinted toward a more defective interface of the ALD-TiO₂ layer related to the lower V_{OC} of the planar devices.

C.3 Integration of ALD-SnO₂

Planar architectures of perovskite solar cells have also been achieved using ALD-SnO₂ as ETL. The variations of the properties of ALD-SnO₂ upon annealing have been investigated. For a moderate annealing temperature (180 °C), the properties of the SnO₂ do not vary much irrespective of the thickness of the layer. At higher temperatures (from 300 °C), the layer crystallizes into the rutile phase and the thickness of the film shrinks by 20%.

ALD-SnO₂ has been integrated in complete solar devices. The influence of the ALD deposition temperature and of the annealing temperature have been discussed. The variability of the PV parameters is increased for higher deposition temperatures which was ascribed to a reduced homogeneity of the ALD deposition at high temperatures. The deposition of SnO₂ at 100 °C gives reasonably working devices and allows for the deposition of the ETL in soft conditions. Varying the annealing temperature showed an optimum at 180 °C. At higher temperatures, the V_{OC} decreases drastically which – in accordance to the literature – can be ascribed to the start of the phase transition from amorphous to rutile SnO₂.

The cells based only on ALD-SnO₂ displayed a decent J_{SC} (about 20 mA cm⁻²) but a slightly low V_{OC} and a very low FF compared to the literature. To circumvent this issue, a bilayer of ALD-SnO₂/PCBM has been investigated. This bilayer allowed to increase the FF from about 45% up to more than 75%, so that a best efficiency of 16.3% is achieved. However, the deposition of the perovskite on PCBM is hindered by the lower coverage of the perovskite on PCBM, ascribed to the lower wettability of the perovskite on the hydrophobic PCBM. Several strategies have been proposed to solve this issue. The addition of a prewetting step of the PCBM layer with DMF has demonstrated to increase the wettability of the perovskite to a satisfactory level without degrading the performance of the cells.

Finally a study of the influence of the SnO₂ layer in the SnO₂/PCBM bilayer configuration is proposed. Similarly to the results obtained for TiO₂, the thickness has only a little influence up to a threshold thickness (about 15 nm) where series resistance limit the device.

C.4 Passivation of the ZnO/perovskite interface

Finally, the integration of ZnO has been studied. It presents suitable optoelectronic properties to act as the ETL in perovskite solar cell. It nevertheless triggers the degradation of MA-containing perovskite due to acid-base reactions, as reported multiple times in the literature and observed in this dissertation. A passivation strategy based on the grafting of phosphonic acids derivatives has been proposed. Three different molecules have been tested: 2-aminoethylphosphonic acid, 4-aminobenzylphosphonic acid and 4-fluorobenzylphosphonic acid, differing by their spacer (aromatic ring or alkyl chain) and their tail groups (amine group or fluorine). The design of the molecules has been thought so that the grafting on the oxide occurs through the phosphonic group, and the tail groups can cure perovskite surface defects through their coordination with undercoordinated lead. The proposed grafting procedure relies on a dipping step at ambient atmosphere and temperature in non-toxic solvents.

Surface sensitive characterization techniques (contact angle, XPS and ATR-FTIR) have assessed the presence of the molecules at the surface of ZnO and the effectiveness of this deposition procedure. Additional characterization by AR-XPS gave insights on the structure of the grafted layer which has been related to the structure of the molecule. 4-ABzPA and 4-FBzPA formed thin layers, compared to 2-AEPA. Moreover, the 4-FBzPA layer presented a structure close to that of a self-assembled monolayer, with a preferred orientation of the fluorine pointing outwards. This better organization has been ascribed to the conjugation of two effects: $\pi - \pi$ stacking of the benzyl rings which enhances the organisation of the layer, and the low affinity of fluorine towards ZnO which helps keeping the molecules oriented in the same direction. On the other hand the amine-based molecules did not exhibit a specific organization at the surface of ZnO, ascribed to a possible competitive interaction between the amine and phosphonic groups during the grafting process.

The effects of the molecules on the growth of the perovskite have been characterized from a morphological and structural point of view. The perovskite grown on bare ZnO or on ZnO-FBzPA showed a degraded structure and morphology with the appearance of a large PbI_2 phase right after synthesis, indicative of the acid-base degradation process, while the perovskite grown on 2-AEPA displays good features. The lack of effective passivation of 4-FBzPA is ascribed to an incomplete coverage of ZnO. The integration in complete devices confirmed these observations. Cells based on bare ZnO showed very poor PV parameters with a maximum PCE of 2.2%. Cells based on 2-AEPA showed an increased $V_{OC} = 1004 \text{ mV}$ (best cell) indicative of the efficient chemical passivation but a very poor J_{SC} ascribed to an excessive thickness of the layer. Cells based on 4-FBzPA had overall the best PCE of 4.1% due to a higher J_{SC} than the cells based on bare ZnO, but limited by a similar low V_{OC} (around 760 mV) in line with the incomplete coverage of ZnO by 4-FBzPA.

C.5 Bottlenecks to the quick development of new perovskite solar cell architectures

During this thesis, two new materials have been developed by atomic layer deposition for a total of four processes (each material has been developed from two different O sources). Two of these processes have then thoroughly been characterized in full perovskite solar cells devices. In regard of the experience acquired during this three-years process, it appears quite clear that even the adaptation of a synthesis protocol reported in the literature – and in this case of an ALD process – is not straightforward. The specificities of the lab’s conditions, of the reactor and the quality of the batch of precursor all influence the development of new materials. The fact that the properties of the ALD materials can vary in large proportions from group to group (Niemelä et al. (2017); Nazarov et al. (2015)) while using the same precursors supports this observation. From the perspective of the integration in complete devices, the production of meaningful results is hampered by the large variability of the properties of the cells. This variability can be ascribed to several factors:

- The large amount of steps composing the synthesis of a complete device (from the cleaning of the substrates, to the deposition of the various layers and the final contacting), multiplying the sources of variability.
- The huge importance of the interfacial states of the substrate on the quality of deposited layers (especially for the ALD and for the deposition of the perovskite) which vary depending on the lab’s condition (moisture and humidity).
- The numerous degradation processes which can affect the cell (moisture, ionic migration, diffusion of the electrode ...). The individual effects of these mechanisms can be hard to identify, let alone the specific effect investigated during an experiment (for instance changing the thickness of the transport layer).
- Most of the process still rely on manual deposition steps whose quality can vary from batch to batch.

Put together, these factors necessitate a copious amount of samples in order to draw conclusions on a specific experiment, as shown with the ALD-TiO₂ and ALD-SnO₂ integration presented in this work. As stated by Schulz et al. (2019), the recent breakthroughs in perovskite solar cells architectures are most of time empirical, even if the fundamental knowledge on complete devices is slowly building up. The search for efficient charge extraction is an uphill process, for which the matter of band alignment is often regarded as critical. It is complicated to predict the proper architecture from band positions either measured on single layers or computed from simulation, because of the intertwined influences of the substrate and the perovskite absorber on them (Miller et al. (2014)). All these interfacial properties are simultaneously critical to achieve higher efficiencies and stability and difficult to probe without damaging the materials or modifying their properties. In summary, the development and synthesis of new materials – even when backed

with theoretical knowledge and reported processes – can be described as a tedious trial-and-error process, taking time to reach maturity.

C.6 Perspectives

This dissertation opens several perspectives regarding the synthesis, the upscale, the characterization, and the comprehension of devices. From the synthesis point of view, new ETLs can be synthesized by ALD starting from the materials which have been presented. The ALD allows for a controlled doping of thin layers. This can be used in order to tune the electric properties of the ETL (for instance the incorporation of Nb in SnO_2). Nanolaminates of different materials can also be a way to employ the nanometric control of the ALD process, as implemented for instance in Bush et al. (2017) with ZnO and SnO_2 . The newly developed TiO_2 can also find useful applications in conjunction with Al_2O_3 to elaborate efficient nanolaminates for encapsulation purposes. The use of molecules such as those described in Chapter 5 provides an easy way to quickly modify the interface between the ETL and the perovskite and can be adapted to ETL other than ZnO, with more complex molecule designs to tune the chemistry and the electronic properties of the interface. This work has mostly explored the application of ALD thin films deposited *before* the perovskite layer (*e.g.* ETL in n-i-p architectures). However, owing to the soft deposition conditions which can be reached (primary vacuum and $T_{dep} \leq 100^\circ\text{C}$), ALD is compatible for the deposition of thin films *on top* of the perovskite layer (*e.g.* ETL in p-i-n architectures), which can be a promising alternative to the organic charge transport layers usually used on top of the perovskite.

From an upscale perspective, the use of ALD enables the deposition of homogeneous and reproducible layers, which are key parameters to limit electric losses in large scale cells and modules. The adaptability of ALD to a large variety of substrates irrespective of their roughness is also a key asset toward the production of tandem solar cells on Si, since it allows for the deposition of a conformal selective layer even on textured Si. With the quick development of spatial ALD, the development and integration of ALD oxides such as SnO_2 and TiO_2 are also key perspectives to investigate.

Developing a large variety of ETL is essential to get a better understanding of the interplay between the perovskite and the extraction layers. Multiplying the amount of possible ETL (whether it consists in changing the material or the deposition method) gives a wider latitude to elaborate and test models for the transport of carriers across the interfaces in perovskite solar cells, which is identified as one of the bottlenecks to achieve even higher efficiencies. The strengthening of these models also relies on the development of innovative characterization methods to get information on interfacial properties or charge transfer properties. The combination of glow-discharge optical emission spectrometry and XPS can be a powerful tool to investigate the chemical state of an interface buried in a thick layer of perovskite (thick for the XPS, *i.e.* more than a few tens of nm) and decipher the chemical interactions between the perovskite and its substrate in realistic architectures. Finally, the development of new imaging PL methods and models

based on hyperspectral and time resolved fluorescence imaging acquisition is very promising. These techniques present key features beneficial to the understanding of transport phenomena across interfaces: a good spatial, temporal and spectral resolution; a high sensitivity of the photoluminescence to defects; a diversity of possible experimental conditions such as additional light or electric bias, *in operando* observations, ageing in different atmospheres ...

Bibliography

- Aarik, J and A Aidla (1999). “Influence of substrate temperature on atomic layer growth and properties of HfO₂ thin films”. en. In: *Thin Solid Films*, p. 7. DOI: [10.1016/S0040-6090\(98\)01356-X](https://doi.org/10.1016/S0040-6090(98)01356-X).
- Aarik, J. et al. (2000). “Titanium isopropoxide as a precursor for atomic layer deposition: characterization of titanium dioxide growth process”. en. In: *Applied Surface Science* 161(3-4), pp. 385–395. DOI: [10.1016/S0169-4332\(00\)00274-9](https://doi.org/10.1016/S0169-4332(00)00274-9).
- Aarik, J. et al. (2001). “Atomic layer deposition of titanium dioxide from TiCl₄ and H₂O: investigation of growth mechanism”. en. In: *Applied Surface Science* 172(1-2), pp. 148–158. DOI: [10.1016/S0169-4332\(00\)00842-4](https://doi.org/10.1016/S0169-4332(00)00842-4).
- Aghaee, Morteza et al. (2015). “Low temperature temporal and spatial atomic layer deposition of TiO₂ films”. en. In: *Journal of Vacuum Science & Technology A: Vacuum, Surfaces, and Films* 33(4), p. 041512. DOI: [10.1116/1.4922588](https://doi.org/10.1116/1.4922588).
- Ahvenniemi, Esko et al. (2017). “Review Article: Recommended reading list of early publications on atomic layer deposition—Outcome of the “Virtual Project on the History of ALD””. en. In: *Journal of Vacuum Science & Technology A: Vacuum, Surfaces, and Films* 35(1), p. 010801. DOI: [10.1116/1.4971389](https://doi.org/10.1116/1.4971389).
- Akgul, Funda Aksoy et al. (2013). “Structural and electronic properties of SnO₂”. en. In: *Journal of Alloys and Compounds* 579, pp. 50–56. DOI: [10.1016/j.jallcom.2013.05.057](https://doi.org/10.1016/j.jallcom.2013.05.057).
- Ali, Tarek T. et al. (2015). “Effect of Pretreatment Temperature on the Photocatalytic Activity of Microwave Irradiated Porous Nanocrystalline ZnO”. en. In: *New J. Chem.* 39(1), pp. 321–332. DOI: [10.1039/C4NJ01465K](https://doi.org/10.1039/C4NJ01465K).
- An, Qingzhi et al. (2017). “High performance planar perovskite solar cells by ZnO electron transport layer engineering”. en. In: *Nano Energy* 39, pp. 400–408. DOI: [10.1016/j.nanoen.2017.07.013](https://doi.org/10.1016/j.nanoen.2017.07.013).
- Anaraki, Elham Halvani et al. (2016). “Highly efficient and stable planar perovskite solar cells by solution-processed tin oxide”. en. In: *Energy Environ. Sci.* 9(10), pp. 3128–3134. DOI: [10.1039/C6EE02390H](https://doi.org/10.1039/C6EE02390H).
- Anaraki, Elham Halvani et al. (2018). “Low-Temperature Nb-Doped SnO₂ Electron-Selective Contact Yields over 20% Efficiency in Planar Perovskite Solar Cells”. en. In: *ACS Energy Lett.* 3(4), pp. 773–778. DOI: [10.1021/acsenergylett.8b00055](https://doi.org/10.1021/acsenergylett.8b00055).
- Aravindan, V. et al. (2013). “Atomic layer deposited (ALD) SnO₂ anodes with exceptional cycleability for Li-ion batteries”. en. In: *Nano Energy* 2(5), pp. 720–725. DOI: [10.1016/j.nanoen.2012.12.007](https://doi.org/10.1016/j.nanoen.2012.12.007).

- Arora, Neha et al. (2017). “Perovskite solar cells with CuSCN hole extraction layers yield stabilized efficiencies greater than 20%”. en. In: *Science*, eaam5655. DOI: [10.1126/science.aam5655](https://doi.org/10.1126/science.aam5655).
- Ashkenasy, Gonen et al. (2002). “Molecular Engineering of Semiconductor Surfaces and Devices”. en. In: *Acc. Chem. Res.* 35(2), pp. 121–128. DOI: [10.1021/ar990047t](https://doi.org/10.1021/ar990047t).
- Al-Ashouri, Amran et al. (2019). “Conformal monolayer contacts with lossless interfaces for perovskite single junction and monolithic tandem solar cells”. en. In: *Energy Environ. Sci.* 12(11), pp. 3356–3369. DOI: [10.1039/C9EE02268F](https://doi.org/10.1039/C9EE02268F).
- Al-Ashouri, Amran et al. (2020). “Monolithic perovskite/silicon tandem solar cell with > 29% efficiency by enhanced hole extraction”. en. In: *Science* 370(6522), pp. 1300–1309. DOI: [10.1126/science.abd4016](https://doi.org/10.1126/science.abd4016).
- Auger, Pierre (1923). “Sur les rayons beta secondaires produits dans un gaz par des rayons X”. In: *Comptes Rendus de l'Académie des Sciences* 177, pp. 169–171.
- Avis, Christophe et al. (2019). “Amorphous Tin Oxide Applied to Solution Processed Thin-Film Transistors”. en. In: *Materials* 12(20), p. 3341. DOI: [10.3390/ma12203341](https://doi.org/10.3390/ma12203341).
- Aydin, Erkan et al. (2019). “Defect and Contact Passivation for Perovskite Solar Cells”. en. In: *Adv. Mater.*, p. 1900428. DOI: [10.1002/adma.201900428](https://doi.org/10.1002/adma.201900428).
- Azmi, Randi, Wisnu Tanyo Hadmojo, et al. (2018). “High-Efficiency Low-Temperature ZnO Based Perovskite Solar Cells Based on Highly Polar, Non-wetting Self-Assembled Molecular Layers”. en. In: *Adv. Energy Mater.* 8(5), p. 1701683. DOI: [10.1002/aenm.201701683](https://doi.org/10.1002/aenm.201701683).
- Azmi, Randi, Chang-Lyoul Lee, et al. (2018). “Simultaneous Improvement in Efficiency and Stability of Low-Temperature-Processed Perovskite Solar Cells by Interfacial Control”. en. In: *Advanced Energy Materials*, p. 1702934. DOI: [10.1002/aenm.201702934](https://doi.org/10.1002/aenm.201702934).
- Bai, Yu et al. (2014). “Titanium Dioxide Nanomaterials for Photovoltaic Applications”. en. In: *Chem. Rev.* 114(19), pp. 10095–10130. DOI: [10.1021/cr400606n](https://doi.org/10.1021/cr400606n).
- Bakri, A. S. et al. (2017). “Effect of annealing temperature of titanium dioxide thin films on structural and electrical properties”. en. In: Solo, Indonesia, p. 030030. DOI: [10.1063/1.4968283](https://doi.org/10.1063/1.4968283).
- Barreca, Davide et al. (2015). “Fe₂O₃–TiO₂ nanosystems by a hybrid PE-CVD/ALD approach: controllable synthesis, growth mechanism, and photocatalytic properties”. en. In: *CrystEngComm* 17(32), pp. 6219–6226. DOI: [10.1039/C5CE00883B](https://doi.org/10.1039/C5CE00883B).
- Barros, Raquel et al. (2019). “Role of Structure and Composition on the Performances of P-Type Tin Oxide Thin-Film Transistors Processed at Low-Temperatures”. en. In: *Nanomaterials* 9(3), p. 320. DOI: [10.3390/nano9030320](https://doi.org/10.3390/nano9030320).
- Batmunkh, Munkhbayar et al. (2020). “Recent Advances in Perovskite-Based Building-Integrated Photovoltaics”. en. In: *Adv. Mater.* 32(31), p. 2000631. DOI: [10.1002/adma.202000631](https://doi.org/10.1002/adma.202000631).
- Béchu, Solène et al. (2019). “A Challenge for X-Ray Photoelectron Spectroscopy Characterization of Cu(In,Ga)Se₂ Absorbers: the Accurate Quantification of Ga/(Ga + In) Ratio”. en. In: *Thin Solid Films* 669, pp. 425–429. DOI: [10.1016/j.tsf.2018.11.029](https://doi.org/10.1016/j.tsf.2018.11.029).

- Becquerel, Edmond (1839). “Mémoire sur les effets électriques produits sous l’influence des rayons solaires”. In: *Comptes Rendus de l’Académie des Sciences* 9, pp. 561–567.
- Belay, Amare Benor et al. (2012). “Effect of UV-Ozone Exposure on PCBM”. en. In: *IEEE Journal Of Photovoltaics* 2(2), p. 6. DOI: [10.1109/JPHOTOV.2012.2183579](https://doi.org/10.1109/JPHOTOV.2012.2183579).
- Bendavid, A et al. (2000). “Deposition and modification of titanium dioxide thin films by filtered arc deposition”. en. In: *Thin Solid Films*, p. 9. DOI: [10.1016/S0040-6090\(99\)00937-2](https://doi.org/10.1016/S0040-6090(99)00937-2).
- Bercegol, Adrien (2020). “Transport de charge dans le photovoltaïque par imagerie multidimensionnelle de luminescence”. fr. PhD thesis. PSL.
- Bercegol, Adrien, F. Javier Ramos, Amelle Rebai, Thomas Guillemot, Daniel Ory, et al. (2018). “Slow Diffusion and Long Lifetime in Metal Halide Perovskites for Photovoltaics”. en. In: *J. Phys. Chem. C* 122(43), pp. 24570–24577. DOI: [10.1021/acs.jpcc.8b08252](https://doi.org/10.1021/acs.jpcc.8b08252).
- Bercegol, Adrien, F. Javier Ramos, Amelle Rebai, Thomas Guillemot, Jean-Baptiste Puel, et al. (2018). “Spatial Inhomogeneity Analysis of Cesium-Rich Wrinkles in Triple-Cation Perovskite”. en. In: *J. Phys. Chem. C* 122(41), pp. 23345–23351. DOI: [10.1021/acs.jpcc.8b07436](https://doi.org/10.1021/acs.jpcc.8b07436).
- Bercegol, Adrien et al. (2017). “Determination of transport properties in optoelectronic devices by time-resolved fluorescence imaging”. en. In: *Journal of Applied Physics* 122(20), p. 203102. DOI: [10.1063/1.5005164](https://doi.org/10.1063/1.5005164).
- Bercegol, Adrien et al. (2019). “Quantitative Optical Assessment of Photonic and Electronic Properties in Halide Perovskite”. en. In: *Nat Commun* 10(1), p. 1586. DOI: [10.1038/s41467-019-09527-w](https://doi.org/10.1038/s41467-019-09527-w).
- Bercegol, Adrien et al. (2020). “Imaging Electron, Hole, and Ion Transport in Halide Perovskite”. en. In: *J. Phys. Chem. C* 124(22), pp. 11741–11748. DOI: [10.1021/acs.jpcc.9b10876](https://doi.org/10.1021/acs.jpcc.9b10876).
- Berger, P. R. and M. Kim (2018). “Polymer solar cells: P3HT:PCBM and beyond”. en. In: *Journal of Renewable and Sustainable Energy* 10(1), p. 013508. DOI: [10.1063/1.5012992](https://doi.org/10.1063/1.5012992).
- Bisquert, Juan and Emilio J. Juarez-Perez (2019). “The Causes of Degradation of Perovskite Solar Cells”. en. In: *J. Phys. Chem. Lett.* 10(19), pp. 5889–5891. DOI: [10.1021/acs.jpcclett.9b00613](https://doi.org/10.1021/acs.jpcclett.9b00613).
- Bockmeyer, Matthias and Peer Löbmann (2006). “Densification and Microstructural Evolution of TiO₂ Films Prepared by Sol-Gel Processing”. en. In: *Chem. Mater.* 18(18), pp. 4478–4485. DOI: [10.1021/cm052048n](https://doi.org/10.1021/cm052048n).
- Brennan, Thomas P. et al. (2013). “Efficiency enhancement of solid-state PbS quantum dot-sensitized solar cells with Al₂O₃ barrier layer”. en. In: *J. Mater. Chem. A* 1(26), p. 7566. DOI: [10.1039/c3ta10903h](https://doi.org/10.1039/c3ta10903h).
- Brinkmann, Kai Oliver et al. (2020). “Atomic Layer Deposition of Functional Layers in Planar Perovskite Solar Cells”. en. In: *Sol. RRL* 4(1), p. 1900332. DOI: [10.1002/solr.201900332](https://doi.org/10.1002/solr.201900332).
- Brivio, Federico et al. (2014). “Relativistic quasiparticle self-consistent electronic structure of hybrid halide perovskite photovoltaic absorbers”. en. In: *Phys. Rev. B* 89(15), p. 155204. DOI: [10.1103/PhysRevB.89.155204](https://doi.org/10.1103/PhysRevB.89.155204).

- Buckholtz, Gavin A. and Ellen S. Gawalt (2012). “Effect of Alkyl Chain Length on Carboxylic Acid SAMs on Ti-6Al-4V”. In: *Materials* 5(7), pp. 1206–1218. DOI: [10.3390/ma5071206](https://doi.org/10.3390/ma5071206).
- Bush, Kevin A. et al. (2017). “23.6%-efficient monolithic perovskite/silicon tandem solar cells with improved stability”. In: *Nature Energy* 2(4), p. 17009. DOI: [10.1038/nenergy.2017.9](https://doi.org/10.1038/nenergy.2017.9).
- Bush, Kevin A. et al. (2018). “Controlling Thin-Film Stress and Wrinkling during Perovskite Film Formation”. en. In: *ACS Energy Lett.* 3(6), pp. 1225–1232. DOI: [10.1021/acseenergylett.8b00544](https://doi.org/10.1021/acseenergylett.8b00544).
- Cacovich, Stefania et al. (2020). “Light-Induced Passivation in Triple Cation Mixed Halide Perovskites: Interplay between Transport Properties and Surface Chemistry”. en. In: *ACS Appl. Mater. Interfaces* 12(31), pp. 34784–34794. DOI: [10.1021/acsam.0c06844](https://doi.org/10.1021/acsam.0c06844).
- Cao, Jing et al. (2018). “Efficient, Hysteresis-Free, and Stable Perovskite Solar Cells with ZnO as Electron-Transport Layer: Effect of Surface Passivation”. en. In: *Advanced Materials*, p. 1705596. DOI: [10.1002/adma.201705596](https://doi.org/10.1002/adma.201705596).
- Caprioglio, Pietro et al. (2019). “On the Relation between the Open-Circuit Voltage and Quasi-Fermi Level Splitting in Efficient Perovskite Solar Cells”. en. In: *Adv. Energy Mater.* 9(33), p. 1901631. DOI: [10.1002/aenm.201901631](https://doi.org/10.1002/aenm.201901631).
- Ceresa (2018). *Market Study: Titanium Dioxide*.
- Chen, Dazheng et al. (2019). “Efficient planar perovskite solar cells with low-temperature atomic layer deposited TiO₂ electron transport layer and interfacial modifier”. en. In: *Solar Energy* 188, pp. 239–246. DOI: [10.1016/j.solener.2019.06.016](https://doi.org/10.1016/j.solener.2019.06.016).
- Chen, Haoran et al. (2021). “Advances to High-Performance Black-Phase FAPbI₃ Perovskite for Efficient and Stable Photovoltaics”. en. In: *Small Structures* 2(5), p. 2000130. DOI: [10.1002/sstr.202000130](https://doi.org/10.1002/sstr.202000130).
- Chen, Qi et al. (2014). “Controllable Self-Induced Passivation of Hybrid Lead Iodide Perovskites toward High Performance Solar Cells”. en. In: *Nano Lett.* 14(7), pp. 4158–4163. DOI: [10.1021/nl501838y](https://doi.org/10.1021/nl501838y).
- Chen, Ruihao et al. (2019). “High-Efficiency, Hysteresis-Less, UV-Stable Perovskite Solar Cells with Cascade ZnO–ZnS Electron Transport Layer”. en. In: *Journal of the American Chemical Society* 141(1), pp. 541–547. DOI: [10.1021/jacs.8b11001](https://doi.org/10.1021/jacs.8b11001).
- Chen, Xiaobo and Samuel S. Mao (2007). “Titanium Dioxide Nanomaterials: Synthesis, Properties, Modifications, and Applications”. en. In: *Chem. Rev.* 107(7), pp. 2891–2959. DOI: [10.1021/cr0500535](https://doi.org/10.1021/cr0500535).
- Cheng, Yuanhang et al. (2021). “Revealing the Degradation and Self-Healing Mechanisms in Perovskite Solar Cells by Sub-Bandgap External Quantum Efficiency Spectroscopy”. en. In: *Adv. Mater.* 33(3), p. 2006170. DOI: [10.1002/adma.202006170](https://doi.org/10.1002/adma.202006170).
- Chiappim, W. et al. (2016). “Effect of Process Temperature and Reaction Cycle Number on Atomic Layer Deposition of TiO₂ Thin Films Using TiCl₄ and H₂O Precursors: Correlation Between Material Properties and Process Environment”. en. In: *Braz J Phys* 46(1), pp. 56–69. DOI: [10.1007/s13538-015-0383-2](https://doi.org/10.1007/s13538-015-0383-2).
- Choi, Dong-won and Jin-Seong Park (2014). “Highly conductive SnO₂ thin films deposited by atomic layer deposition using tetrakis-dimethyl-amine-tin precursor

- and ozone reactant”. en. In: *Surface and Coatings Technology* 259, pp. 238–243. DOI: [10.1016/j.surfcoat.2014.02.012](https://doi.org/10.1016/j.surfcoat.2014.02.012).
- Choi, Dong-won et al. (2014). “The conducting tin oxide thin films deposited via atomic layer deposition using Tetrakis-dimethylamino tin and peroxide for transparent flexible electronics”. en. In: *Applied Surface Science* 313, pp. 585–590. DOI: [10.1016/j.apsusc.2014.06.027](https://doi.org/10.1016/j.apsusc.2014.06.027).
- Climent-Pascual, Esteban et al. (2016). “Influence of the substrate on the bulk properties of hybrid lead halide perovskite films”. en. In: *J. Mater. Chem. A* 4(46), pp. 18153–18163. DOI: [10.1039/C6TA08695K](https://doi.org/10.1039/C6TA08695K).
- Cocks, G.T. and J.J. Zuckerman (1965). “The Synthesis of Tin(II) Heterocycles Directly from Stannous Oxide”. In: *Inorganic Chemistry* 4(4), pp. 592–593. DOI: [10.1021/ic50026a036](https://doi.org/10.1021/ic50026a036).
- Cook, John et al. (2016). “Consensus on consensus: a synthesis of consensus estimates on human-caused global warming”. en. In: *Environ. Res. Lett.* 11(4), p. 048002. DOI: [10.1088/1748-9326/11/4/048002](https://doi.org/10.1088/1748-9326/11/4/048002).
- Correa Baena, Juan Pablo et al. (2015). “Highly efficient planar perovskite solar cells through band alignment engineering”. en. In: *Energy Environ. Sci.* 8(10), pp. 2928–2934. DOI: [10.1039/C5EE02608C](https://doi.org/10.1039/C5EE02608C).
- Corsini, Francesca and Gianmarco Griffini (2020). “Recent progress in encapsulation strategies to enhance the stability of organometal halide perovskite solar cells”. en. In: *J. Phys. Energy* 2(3), p. 031002. DOI: [10.1088/2515-7655/ab8774](https://doi.org/10.1088/2515-7655/ab8774).
- Coutancier, Damien et al. (2020). “ALD of ZnO:Ti: Growth Mechanism and Application as an Efficient Transparent Conductive Oxide in Silicon Nanowire Solar Cells”. en. In: *ACS Appl. Mater. Interfaces*. DOI: [10.1021/acsami.9b22973](https://doi.org/10.1021/acsami.9b22973).
- Das, Soumen and V. Jayaraman (2014). “SnO₂: A comprehensive review on structures and gas sensors”. en. In: *Progress in Materials Science* 66, pp. 112–255. DOI: [10.1016/j.pmatsci.2014.06.003](https://doi.org/10.1016/j.pmatsci.2014.06.003).
- Database of ALD processes* (2021). URL: <https://www.atomiclimits.com/alddatabase/> (visited on 06/05/2021).
- Davies, Christopher L. et al. (2018). “Impact of the Organic Cation on the Optoelectronic Properties of Formamidinium Lead Triiodide”. en. In: *J. Phys. Chem. Lett.* 9(16), pp. 4502–4511. DOI: [10.1021/acs.jpcllett.8b01628](https://doi.org/10.1021/acs.jpcllett.8b01628).
- De Vos, A. and H. Pauwels (1981). “On the thermodynamic limit of photovoltaic energy conversion”. en. In: *Appl. Phys.* 25(2), pp. 119–125. DOI: [10.1007/BF00901283](https://doi.org/10.1007/BF00901283).
- De Wolf, Stefaan et al. (2014). “Organometallic Halide Perovskites: Sharp Optical Absorption Edge and Its Relation to Photovoltaic Performance”. en. In: *J. Phys. Chem. Lett.* 5(6), pp. 1035–1039. DOI: [10.1021/jz500279b](https://doi.org/10.1021/jz500279b).
- Delamarre, Amaury (2013). “Développement de nouvelles méthodes de caractérisation optoélectroniques des cellules solaires”. PhD thesis. UPMC.
- Delft, J A van et al. (2012). “Atomic layer deposition for photovoltaics: applications and prospects for solar cell manufacturing”. en. In: *Semicond. Sci. Technol.* 27(7), p. 074002. DOI: [10.1088/0268-1242/27/7/074002](https://doi.org/10.1088/0268-1242/27/7/074002).
- Deng, Kaimo et al. (2020). “Modification Engineering in SnO₂ Electron Transport Layer toward Perovskite Solar Cells: Efficiency and Stability”. en. In: *Adv. Funct. Mater.* 30(46), p. 2004209. DOI: [10.1002/adfm.202004209](https://doi.org/10.1002/adfm.202004209).

- Deng, Yuanfu et al. (2016). “The developments of SnO₂/graphene nanocomposites as anode materials for high performance lithium ion batteries: A review”. en. In: *Journal of Power Sources* 304, pp. 81–101. DOI: [10.1016/j.jpowsour.2015.11.017](https://doi.org/10.1016/j.jpowsour.2015.11.017).
- deQuilettes, Dane W. et al. (2016). “Photoluminescence Lifetimes Exceeding 8 μ s and Quantum Yields Exceeding 30% in Hybrid Perovskite Thin Films by Ligand Passivation”. en. In: *ACS Energy Lett.* 1(2), pp. 438–444. DOI: [10.1021/acsenergylett.6b00236](https://doi.org/10.1021/acsenergylett.6b00236).
- deQuilettes, Dane W. et al. (2019). “Charge-Carrier Recombination in Halide Perovskites: Focus Review”. en. In: *Chem. Rev.* 119(20), pp. 11007–11019. DOI: [10.1021/acs.chemrev.9b00169](https://doi.org/10.1021/acs.chemrev.9b00169).
- Dimos, D. and C. H. Mueller (1998). “Perovskite thin films for high-frequency capacitor applications”. en. In: *Annu. Rev. Mater. Sci.* 28(1), pp. 397–419. DOI: [10.1146/annurev.matsci.28.1.397](https://doi.org/10.1146/annurev.matsci.28.1.397).
- Dkhissi, Yasmina et al. (2016). “Stability Comparison of Perovskite Solar Cells Based on Zinc Oxide and Titania on Polymer Substrates”. en. In: *ChemSusChem* 9(7), pp. 687–695. DOI: [10.1002/cssc.201501659](https://doi.org/10.1002/cssc.201501659).
- Dong, Qi et al. (2019). “Defect Passivation by Fullerene Derivative in Perovskite Solar Cells with Aluminum-Doped Zinc Oxide as Electron Transporting Layer”. en. In: *Chem. Mater.*, acs.chemmater.9b01292. DOI: [10.1021/acs.chemmater.9b01292](https://doi.org/10.1021/acs.chemmater.9b01292).
- Dong, Xu et al. (2014). “The Effect of ALD-ZnO Layers on the Formation of CH₃NH₃PbI₃ with Different Perovskite Precursors and Sintering Temperatures”. en. In: *Chem. Commun.* 50(92), pp. 14405–14408. DOI: [10.1039/C4CC04685D](https://doi.org/10.1039/C4CC04685D).
- Dressen, Chris et al. (2020). “Radiative and non-radiative losses by voltage-dependent in-situ photoluminescence in perovskite solar cell current-voltage curves”. en. In: *Journal of Luminescence* 222, p. 117106. DOI: [10.1016/j.jlumin.2020.117106](https://doi.org/10.1016/j.jlumin.2020.117106).
- Egger, David A. et al. (2016). “Hybrid Organic–Inorganic Perovskites on the Move”. en. In: *Acc. Chem. Res.* 49(3), pp. 573–581. DOI: [10.1021/acs.accounts.5b00540](https://doi.org/10.1021/acs.accounts.5b00540).
- EIA (2021). “Levelized Costs of New Generation Resources in the Annual Energy Outlook 2021”. en. In: p. 25.
- Eilers, Paul H. C. (2003). “A Perfect Smoother”. en. In: *Anal. Chem.* 75(14), pp. 3631–3636. DOI: [10.1021/ac034173t](https://doi.org/10.1021/ac034173t).
- Elam, Jeffrey W. et al. (2008). “Atomic layer deposition of tin oxide films using tetrakis(dimethylamino) tin”. en. In: *Journal of Vacuum Science & Technology A: Vacuum, Surfaces, and Films* 26(2), pp. 244–252. DOI: [10.1116/1.2835087](https://doi.org/10.1116/1.2835087).
- Ellmer, Klaus et al. (2008). *Transparent Conductive Zinc Oxide, Basics and Applications in Thin Film Solar Cells*. Springer-Verlag, Berlin Heidelberg. Springer Series in Materials Science 104. ISBN: 978-3-540-73611-0.
- Eperon, Giles E. et al. (2015). “Inorganic caesium lead iodide perovskite solar cells”. en. In: *J. Mater. Chem. A* 3(39), pp. 19688–19695. DOI: [10.1039/C5TA06398A](https://doi.org/10.1039/C5TA06398A).
- Estreicher, Stefan K. et al. (2011). “Activation Energies for Diffusion of Defects in Silicon: The Role of the Exchange-Correlation Functional”. en. In: *Angew. Chem. Int. Ed.* 50(43), pp. 10221–10225. DOI: [10.1002/anie.201100733](https://doi.org/10.1002/anie.201100733).

- Eswar, N.K.R et al. (2019). “Atomic Layer Deposited Photocatalysts: Comprehensive Review on Viable Fabrication Routes and Reactor Design Approaches for Photo – Mediated Redox Reactions”. en. In: *J. Mater. Chem. A* 30. DOI: [10.1039/C9TA04780H](https://doi.org/10.1039/C9TA04780H).
- Fang, Zhigang et al. (1993). “Modeling particle size distributions by the Weibull distribution function”. en. In: *Materials Characterization* 31(3), pp. 177–182. DOI: [10.1016/1044-5803\(93\)90058-4](https://doi.org/10.1016/1044-5803(93)90058-4).
- Feichtenschlager, Bernhard et al. (2011). “Tuning the self-assembled monolayer formation on nanoparticle surfaces with different curvatures: Investigations on spherical silica particles and plane-crystal-shaped zirconia particles”. en. In: *Journal of Colloid and Interface Science* 360(1), pp. 15–25. DOI: [10.1016/j.jcis.2011.03.035](https://doi.org/10.1016/j.jcis.2011.03.035).
- Ferreira da Silva, A. et al. (1996). “Optical Determination of the Direct Bandgap Energy of Lead Iodide Crystals”. en. In: *Appl. Phys. Lett.* 69(13), pp. 1930–1932. DOI: [10.1063/1.117625](https://doi.org/10.1063/1.117625).
- Filip, Marina R. and Feliciano Giustino (2018). “The geometric blueprint of perovskites”. en. In: *Proc Natl Acad Sci USA* 115(21), pp. 5397–5402. DOI: [10.1073/pnas.1719179115](https://doi.org/10.1073/pnas.1719179115).
- Fischer, Andreas et al. (2021). “Thermal atomic layer etching: a review”. In: *Journal of Vacuum Science & Technology A* 39. DOI: [10.1116/6.0000894](https://doi.org/10.1116/6.0000894).
- Fisher, Markus et al. (2021). *International Roadmap for PV*. Tech. rep. 12. VDMA e. V.
- Fournier, Olivier et al. (2021). “Chemical Passivation with Phosphonic Acid Derivatives of ZnO Deposited by Atomic Layer Deposition and Its Influence on the Halide Perovskite Interface”. en. In: *ACS Appl. Energy Mater.* 4(6), pp. 5787–5797. DOI: [10.1021/acsaem.1c00612](https://doi.org/10.1021/acsaem.1c00612).
- Fox, M. (2001). *Optical Properties of Solids*. Oxford University Press: Oxford. ISBN: 9780199573363.
- Fukuda, Kenjiro et al. (2009). “Effects of the alkyl chain length in phosphonic acid self-assembled monolayer gate dielectrics on the performance and stability of low-voltage organic thin-film transistors”. en. In: *Appl. Phys. Lett.* 95(20), p. 203301. DOI: [10.1063/1.3259816](https://doi.org/10.1063/1.3259816).
- Futscher, Moritz H. et al. (2019). “Quantification of ion migration in CH₃NH₃PbI₃ perovskite solar cells by transient capacitance measurements”. en. In: *Mater. Horiz.* 6(7), pp. 1497–1503. DOI: [10.1039/C9MH00445A](https://doi.org/10.1039/C9MH00445A).
- Gao, Wei et al. (1996). “Self-Assembled Monolayers of Alkylphosphonic Acids on Metal Oxides”. en. In: *Langmuir* 12(26), pp. 6429–6435. DOI: [10.1021/la9607621](https://doi.org/10.1021/la9607621).
- Gao, Zhengning and Parag Banerjee (2019). “Review Article: Atomic Layer Deposition of Doped ZnO Films”. en. In: *Journal of Vacuum Science & Technology A* 37(5), p. 050802. DOI: [10.1116/1.5112777](https://doi.org/10.1116/1.5112777).
- Gawalt, Ellen S. et al. (2001). “Self-Assembly and Bonding of Alkanephosphonic Acids on the Native Oxide Surface of Titanium”. en. In: *Langmuir* 17(19), pp. 5736–5738. DOI: [10.1021/la010649x](https://doi.org/10.1021/la010649x).
- GCL's fund raising* (2021). *GCL's fund raising*. URL: <https://www.perovskite-info.com/chinas-gcl-raises-over-15-million-100-mw-mass-production-line-perovskite-solar> (visited on 06/07/2021).

- George, Steven M. (2010). “Atomic Layer Deposition: An Overview”. en. In: *Chemical Reviews* 110(1), pp. 111–131. DOI: [10.1021/cr900056b](https://doi.org/10.1021/cr900056b).
- George, Steven M. et al. (2009). “Surface Chemistry for Molecular Layer Deposition of Organic and Hybrid Organic-Inorganic Polymers”. en. In: *Acc. Chem. Res.* 42(4), pp. 498–508. DOI: [10.1021/ar800105q](https://doi.org/10.1021/ar800105q).
- Gerhard, Marina et al. (2019). “Microscopic insight into non-radiative decay in perovskite semiconductors from temperature-dependent luminescence blinking”. en. In: *Nat Commun* 10(1), p. 1698. DOI: [10.1038/s41467-019-09640-w](https://doi.org/10.1038/s41467-019-09640-w).
- Giordano, Fabrizio et al. (2016). “Enhanced electronic properties in mesoporous TiO₂ via lithium doping for high-efficiency perovskite solar cells”. In: *Nature Communications* 7(1), p. 10379. DOI: [10.1038/ncomms10379](https://doi.org/10.1038/ncomms10379).
- Gitlitz, M.N. and M.K. Moran (2000). “Tin Coumpounds”. In: *Kirk-Othmer Encyclopedia of Chemical Technology*. Vol. 24. John Wiley & Sons, Inc.
- Goldschmidt, V.M. (1926). “Die Gesetze der Krystallochemie”. In: *Die Naturwissenschaften* 21, pp. 477–485. DOI: [10.1007/bf01507527](https://doi.org/10.1007/bf01507527).
- Gong, Xiwen et al. (2019). “Contactless measurements of photocarrier transport properties in perovskite single crystals”. en. In: *Nat Commun* 10(1), p. 1591. DOI: [10.1038/s41467-019-09538-7](https://doi.org/10.1038/s41467-019-09538-7).
- Gu, Shuai et al. (2020). “Tin and Mixed Lead–Tin Halide Perovskite Solar Cells: Progress and their Application in Tandem Solar Cells”. en. In: *Adv. Mater.*, p. 1907392. DOI: [10.1002/adma.201907392](https://doi.org/10.1002/adma.201907392).
- Gu, Xing et al. (2013). “A Solution-Processed Hole Extraction Layer Made from Ultrathin MoS₂ Nanosheets for Efficient Organic Solar Cells”. en. In: *Advanced Energy Materials* 3(10), pp. 1262–1268. DOI: [10.1002/aenm201300549](https://doi.org/10.1002/aenm201300549).
- Guan, Ze-Lei et al. (2010). “Direct determination of the electronic structure of the poly(3-hexylthiophene):phenyl-[6,6]-C₆₀ butyric acid methyl ester blend”. en. In: *Organic Electronics* 11(11), pp. 1779–1785. DOI: [10.1016/j.orgel.2010.07.023](https://doi.org/10.1016/j.orgel.2010.07.023).
- Guo, W. et al. (2010). “Microstructure, optical, and electrical properties of p-type SnO thin films”. en. In: *Appl. Phys. Lett.* 96(4), p. 042113. DOI: [10.1063/1.3277153](https://doi.org/10.1063/1.3277153).
- Habisreutinger, Severin N. et al. (2018). “Hysteresis Index: A Figure without Merit for Quantifying Hysteresis in Perovskite Solar Cells”. en. In: *ACS Energy Letters*, pp. 2472–2476. DOI: [10.1021/acsenergylett.8b01627](https://doi.org/10.1021/acsenergylett.8b01627).
- Hadouchi, Warda et al. (2016). “Zinc Oxide as a Hole Blocking Layer for Perovskite Solar Cells Deposited in Atmospheric Conditions”. en. In: *RSC Advances* 6(72), pp. 67715–67723. DOI: [10.1039/C6RA16865E](https://doi.org/10.1039/C6RA16865E).
- Hair, M.L. and C.P. Tripp (1995). “Alkylchlorosilane reactions at the silica surface”. en. In: *Colloids and Surfaces A: Physicochemical and Engineering Aspects* 105(1), pp. 95–103. DOI: [10.1016/0927-7757\(95\)03298-5](https://doi.org/10.1016/0927-7757(95)03298-5).
- El-Hajje, Gilbert et al. (2016). “Quantification of spatial inhomogeneity in perovskite solar cells by hyperspectral luminescence imaging”. en. In: *Energy & Environmental Science* 9(7), pp. 2286–2294. DOI: [10.1039/C6EE00462H](https://doi.org/10.1039/C6EE00462H).
- Hall, R. N. (1952). “Electron-Hole Recombination in Germanium”. en. In: *Phys. Rev.* 87(2), pp. 387–387. DOI: [10.1103/PhysRev.87.387](https://doi.org/10.1103/PhysRev.87.387).

- Han, Jeong Hwan et al. (2014). “Growth of p-Type Tin(II) Monoxide Thin Films by Atomic Layer Deposition from Bis(1-dimethylamino-2-methyl-2-propoxy)tin and H₂O”. en. In: *Chem. Mater.* 26(21), pp. 6088–6091. DOI: [10.1021/cm503112v](https://doi.org/10.1021/cm503112v).
- Hanson, Eric L. et al. (2003). “Bonding Self-Assembled, Compact Organophosphate Monolayers to the Native Oxide Surface of Silicon”. en. In: *Journal of the American Chemical Society* 125(51), pp. 16074–16080. DOI: [10.1021/ja035956z](https://doi.org/10.1021/ja035956z).
- He, Sisi et al. (2020). “How Far Are We from Attaining 10-Year Lifetime for Metal Halide Perovskite Solar Cells?” en. In: *Materials Science and Engineering: R: Reports* 140, p. 100545. DOI: [10.1016/j.mser.2020.100545](https://doi.org/10.1016/j.mser.2020.100545).
- Heo, Jaeyeong et al. (2010). “Low Temperature Atomic Layer Deposition of Tin Oxide”. en. In: *Chem. Mater.* 22(17), pp. 4964–4973. DOI: [10.1021/cm1011108](https://doi.org/10.1021/cm1011108).
- Hersh, L.S. et al. (1995). “Amine-Reactive Surface Chemistry of Zinc Phosphate Glasses”. en. In: *J. Mater. Res.* 10(8), pp. 2120–2127. DOI: [10.1557/JMR.1995.2120](https://doi.org/10.1557/JMR.1995.2120).
- Hill, Rebecca B. M. et al. (2019). “Phosphonic Acid Modification of the Electron Selective Contact: Interfacial Effects in Perovskite Solar Cells”. en. In: *ACS Applied Energy Materials*, acaem.9b00141. DOI: [10.1021/acsaem.9b00141](https://doi.org/10.1021/acsaem.9b00141).
- Hoke, Eric T. et al. (2015). “Reversible photo-induced trap formation in mixed-halide hybrid perovskites for photovoltaics”. en. In: *Chem. Sci.* 6(1), pp. 613–617. DOI: [10.1039/C4SC03141E](https://doi.org/10.1039/C4SC03141E).
- Hossain, Md. Anower et al. (2020). “Atomic layer deposition enabling higher efficiency solar cells: A review”. en. In: *Nano Materials Science* 2(3), pp. 204–226. DOI: [10.1016/j.nanoms.2019.10.001](https://doi.org/10.1016/j.nanoms.2019.10.001).
- Hotchkiss, Peter J. et al. (2011). “Characterization of Phosphonic Acid Binding to Zinc Oxide”. en. In: *Journal of Materials Chemistry* 21(9), p. 3107. DOI: [10.1039/c0jm02829k](https://doi.org/10.1039/c0jm02829k).
- Hsu, Chia-Hsun et al. (2020). “Effect of Annealing Temperature on Spatial Atomic Layer Deposited Titanium Oxide and Its Application in Perovskite Solar Cells”. en. In: *Nanomaterials* 10(7), p. 1322. DOI: [10.3390/nano10071322](https://doi.org/10.3390/nano10071322).
- Hu, Han et al. (2013). “The Effect of Oxygen Vacancies on Water Wettability of a ZnO Surface”. en. In: *Phys. Chem. Chem. Phys.* 15(39), p. 16557. DOI: [10.1039/c3cp51848e](https://doi.org/10.1039/c3cp51848e).
- Hultqvist, Adam et al. (2021). “SnO_x Atomic Layer Deposition on Bare Perovskite—An Investigation of Initial Growth Dynamics, Interface Chemistry, and Solar Cell Performance”. en. In: *ACS Appl. Energy Mater.* 4(1), pp. 510–522. DOI: [10.1021/acsaem.0c02405](https://doi.org/10.1021/acsaem.0c02405).
- IEA (2020). “Renewables 2020 - Analysis and forecast to 2025”. en. In: p. 172.
- IEA (2021). “Net Zero by 2050 - A Roadmap for the Global Energy Sector”. en. In: p. 224.
- Islam, S Nazrul and John Winkel (2017). “Climate Change and Social Inequality”. en. In: p. 32.
- Jagadish, Chennupati and Stephen Pearton (2006). *Zinc Oxide Bulk, Thin Films and Nanostructures: Processing, Properties and Applications*. Elsevier Science. ISBN: 978-0-08-044722-3.
- Jahn, Ulrike et al. (2018). *Review on infrared and electroluminescence imaging for PV field applications: International Energy Agency Photovoltaic Power Systems*

- Programme: IEA PVPS Task 13, Subtask 3.3: report IEA-PVPS T13-12:2018*. en. International Energy Agency: Paris. ISBN: 978-3-906042-53-4.
- Janocha, E. and C. Pettenkofer (2011). “ALD of ZnO using diethylzinc as metal-precursor and oxygen as oxidizing agent”. en. In: *Applied Surface Science* 257(23), pp. 10031–10035. DOI: [10.1016/j.apsusc.2011.06.133](https://doi.org/10.1016/j.apsusc.2011.06.133).
- Jarzebski, Z. M. and J. P. Morton (1976a). “Physical Properties of SnO₂ Materials: II. Electrical Properties”. en. In: *J. Electrochem. Soc.* 123(9), p. 12. DOI: [10.1149/1.2133090](https://doi.org/10.1149/1.2133090).
- Jarzebski, Z. M. and J. P. Morton (1976b). “Physical Properties of SnO₂ Materials: III . Optical Properties”. en. In: *J. Electrochem. Soc.* 123(10), pp. 333C–346C. DOI: [10.1149/1.2132647](https://doi.org/10.1149/1.2132647).
- Jayalakshmi, G. et al. (2013). “Impact of Thiol and Amine Functionalization on Photoluminescence Properties of ZnO Films”. en. In: *Journal of Luminescence* 140, pp. 21–25. DOI: [10.1016/j.jlumin.2013.02.057](https://doi.org/10.1016/j.jlumin.2013.02.057).
- Jeong, Jaeki et al. (2021). “Pseudo-halide anion engineering for α -FAPbI₃ perovskite solar cells”. en. In: *Nature* 592(7854), pp. 381–385. DOI: [10.1038/s41586-021-03406-5](https://doi.org/10.1038/s41586-021-03406-5).
- Jeong, Seonghwa et al. (2019). “Atomic layer deposition of a SnO₂ electron-transporting layer for planar perovskite solar cells with a power conversion efficiency of 18.3%”. en. In: *Chemical Communications*. DOI: [10.1039/C8CC09557D](https://doi.org/10.1039/C8CC09557D).
- Ji, Jun et al. (2020). “Two-Stage Ultraviolet Degradation of Perovskite Solar Cells Induced by the Oxygen Vacancy-Ti⁴⁺ States”. en. In: *iScience* 23(4), p. 101013. DOI: [10.1016/j.isci.2020.101013](https://doi.org/10.1016/j.isci.2020.101013).
- Jiang, Qi et al. (2016). “Enhanced electron extraction using SnO₂ for high-efficiency planar-structure HC(NH₂)₂PbI₃-based perovskite solar cells”. en. In: *Nature Energy* 2(1), p. 16177. DOI: [10.1038/nenergy.2016.177](https://doi.org/10.1038/nenergy.2016.177).
- Jiang, Qi et al. (2017). “Planar-Structure Perovskite Solar Cells with Efficiency beyond 21%”. en. In: *Adv. Mater.* 29(46), p. 1703852. DOI: [10.1002/adma.201703852](https://doi.org/10.1002/adma.201703852).
- Jiang, Qi et al. (2019). “Surface passivation of perovskite film for efficient solar cells”. en. In: *Nat. Photonics* 13(7), pp. 460–466. DOI: [10.1038/s41566-019-0398-2](https://doi.org/10.1038/s41566-019-0398-2).
- Jin, Chunyan et al. (2015). “Structure and photoluminescence of the TiO₂ films grown by atomic layer deposition using tetrakis-dimethylamino titanium and ozone”. en. In: *Nanoscale Res Lett* 10(1), p. 95. DOI: [10.1186/s11671-015-0790-x](https://doi.org/10.1186/s11671-015-0790-x).
- Johnson, Andrew L. and James D. Parish (2018). “Recent developments in molecular precursors for atomic layer deposition”. In: *Organometallic Chemistry* 42, pp. 1–53. DOI: [10.1039/9781788010672-00001](https://doi.org/10.1039/9781788010672-00001).
- Johnson, Richard W. et al. (2014). “A brief review of atomic layer deposition: from fundamentals to applications”. en. In: *Materials Today* 17(5), pp. 236–246. DOI: [10.1016/j.mattod.2014.04.026](https://doi.org/10.1016/j.mattod.2014.04.026).
- Jošt, Marko et al. (2020). “Monolithic Perovskite Tandem Solar Cells: A Review of the Present Status and Advanced Characterization Methods Toward 30% Efficiency”. en. In: *Adv. Energy Mater.* 10(26), p. 1904102. DOI: [10.1002/aenm.201904102](https://doi.org/10.1002/aenm.201904102).
- Juarez-Perez, Emilio J. et al. (2019). “Degradation Mechanism and Relative Stability of Methylammonium Halide Based Perovskites Analyzed on the Basis

- of Acid–Base Theory”. en. In: *ACS Appl. Mater. Interfaces* 11(13), pp. 12586–12593. DOI: [10.1021/acsami.9b02374](https://doi.org/10.1021/acsami.9b02374).
- Jung, Kwang-Ho et al. (2017). “Solution-Processed SnO₂ Thin Film for Hysteresis-less 19.2% Planar Perovskite Solar Cell”. en. In: *Journal of Materials Chemistry A*. DOI: [10.1039/C7TA08040A](https://doi.org/10.1039/C7TA08040A).
- Kallis, Giorgos et al. (2018). “Research On Degrowth”. en. In: *Annu. Rev. Environ. Resour.* 43(1), pp. 291–316. DOI: [10.1146/annurev-environ-102017-025941](https://doi.org/10.1146/annurev-environ-102017-025941).
- Kane, Evan O. (1963). “Thomas-Fermi Approach to Impure Semiconductor Band Structure”. en. In: *Physical Review* 131(1), pp. 79–88. DOI: [10.1103/PhysRev.131.79](https://doi.org/10.1103/PhysRev.131.79).
- Karwal, Saurabh et al. (2018). “Tailoring nanopore formation in atomic layer deposited ultrathin films”. en. In: *Journal of Vacuum Science & Technology A: Vacuum, Surfaces, and Films* 36(1), 01A103. DOI: [10.1116/1.5003360](https://doi.org/10.1116/1.5003360).
- Kasikov, A et al. (2006). “Refractive index gradients in TiO₂ thin films grown by atomic layer deposition”. In: *J. Phys. D: Appl. Phys.* 39(1), pp. 54–60. DOI: [10.1088/0022-3727/39/1/010](https://doi.org/10.1088/0022-3727/39/1/010).
- Kassir, Mounir et al. (2013). “Surface Modification of TiO₂ Nanoparticles with AHAPS Aminosilane: Distinction Between Physisorption and Chemisorption”. en. In: *Adsorption* 19(6), pp. 1197–1209. DOI: [10.1007/s10450-013-9555-y](https://doi.org/10.1007/s10450-013-9555-y).
- Katahara, John K. and Hugh W. Hillhouse (2014). “Quasi-Fermi level splitting and sub-bandgap absorptivity from semiconductor photoluminescence”. en. In: *Journal of Applied Physics* 116(17), p. 173504. DOI: [10.1063/1.4898346](https://doi.org/10.1063/1.4898346).
- Kavan, Ladislav and Michael Grätzel (1995). “Highly efficient semiconducting TiO₂ photoelectrodes prepared by aerosol pyrolysis”. en. In: *Electrochimica Acta* 40(5), pp. 643–652. DOI: [10.1016/0013-4686\(95\)90400-W](https://doi.org/10.1016/0013-4686(95)90400-W).
- Ke, Weijun, Guojia Fang, et al. (2015). “Low-Temperature Solution-Processed Tin Oxide as an Alternative Electron Transporting Layer for Efficient Perovskite Solar Cells”. en. In: *J. Am. Chem. Soc.* 137(21), pp. 6730–6733. DOI: [10.1021/jacs.5b01994](https://doi.org/10.1021/jacs.5b01994).
- Ke, Weijun, Dewei Zhao, et al. (2015). “Effects of annealing temperature of tin oxide electron selective layers on the performance of perovskite solar cells”. en. In: *J. Mater. Chem. A* 3(47), pp. 24163–24168. DOI: [10.1039/C5TA06574G](https://doi.org/10.1039/C5TA06574G).
- Kegelmann, Lukas (2019). “Entwicklung Ladungsselektiver Kontakte für Effiziente Monolithische Perowskit-Silizium Tandem-Solarzellen Advancing charge selective contacts for efficient monolithic perovskite-silicon tandem solar cells”. de. PhD thesis. Universität Potsdam. DOI: [10.25932/PUBLISHUP-42642](https://doi.org/10.25932/PUBLISHUP-42642).
- Kegelmann, Lukas et al. (2017). “It Takes Two to Tango—Double-Layer Selective Contacts in Perovskite Solar Cells for Improved Device Performance and Reduced Hysteresis”. en. In: *ACS Appl. Mater. Interfaces* 9(20), pp. 17245–17255. DOI: [10.1021/acsami.7b00900](https://doi.org/10.1021/acsami.7b00900).
- Keszthelyi, Tamás et al. (2006). “Investigation of Solid Surfaces Modified by Langmuir-Blodgett Monolayers Using Sum-Frequency Vibrational Spectroscopy and X-ray Photoelectron Spectroscopy”. en. In: *J. Phys. Chem. B* 110(17), pp. 8701–8714. DOI: [10.1021/jp057180p](https://doi.org/10.1021/jp057180p).
- Khenkin, Mark V. et al. (2020). “Consensus statement for stability assessment and reporting for perovskite photovoltaics based on ISOS procedures”. en. In: *Nat Energy* 5(1), pp. 35–49. DOI: [10.1038/s41560-019-0529-5](https://doi.org/10.1038/s41560-019-0529-5).

- Kil, Deok-Sin et al. (2002). “Low-Temperature ALD Growth of SrTiO₃ Thin Films from Sr b-Diketonates and Ti Alkoxide Precursors Using Oxygen Remote Plasma as an Oxidation Source”. en. In: *Chemical Vapor Deposition* 8(5), p. 3. DOI: [10.1002/1521-3862\(20020903\)8:5<195::AID-CVDE195>3.0.CO;2-9](https://doi.org/10.1002/1521-3862(20020903)8:5<195::AID-CVDE195>3.0.CO;2-9).
- Kim, Bumseop et al. (2020). “First-principles identification of the charge-shifting mechanism and ferroelectricity in hybrid halide perovskites”. en. In: *Scientific Reports* 10. DOI: [10.1038/s41598-020-76742-7](https://doi.org/10.1038/s41598-020-76742-7).
- Kim, Hui-Seon et al. (2012). “Lead Iodide Perovskite Sensitized All-Solid-State Submicron Thin Film Mesoscopic Solar Cell with Efficiency Exceeding 9%”. en. In: *Sci Rep* 2(1), p. 591. DOI: [10.1038/srep00591](https://doi.org/10.1038/srep00591).
- Kim, Hyo Yeon et al. (2019). “Phase-controlled SnO₂ and SnO growth by atomic layer deposition using Bis(N-ethoxy-2,2-dimethyl propanamido)tin precursor”. en. In: *Ceramics International* 45(4), pp. 5124–5132. DOI: [10.1016/j.ceramint.2018.09.263](https://doi.org/10.1016/j.ceramint.2018.09.263).
- Kim, Hyungjun (2011). “Characteristics and applications of plasma enhanced-atomic layer deposition”. en. In: *Thin Solid Films* 519(20), pp. 6639–6644. DOI: [10.1016/j.tsf.2011.01.404](https://doi.org/10.1016/j.tsf.2011.01.404).
- Kim, Jae-Kwan and Ji-Myon Lee (2017). “Wet Chemical Etching of ZnO Films Using NH_x-based(NH₄)₂CO₃ and NH₄OH Alkaline Solution”. en. In: *J Mater Sci* 52(22), pp. 13054–13063. DOI: [10.1007/s10853-017-1409-7](https://doi.org/10.1007/s10853-017-1409-7).
- Kirchartz, Thomas et al. (2016). “Impact of Photon Recycling on the Open-Circuit Voltage of Metal Halide Perovskite Solar Cells”. en. In: *ACS Energy Lett.* 1(4), pp. 731–739. DOI: [10.1021/acsenergylett.6b00223](https://doi.org/10.1021/acsenergylett.6b00223).
- Kirchartz, Thomas et al. (2020). “Photoluminescence-Based Characterization of Halide Perovskites for Photovoltaics”. en. In: *Adv. Energy Mater.*, p. 1904134. DOI: [10.1002/aenm.201904134](https://doi.org/10.1002/aenm.201904134).
- Knapas, Kjell and Mikko Ritala (2013). “In Situ Studies on Reaction Mechanisms in Atomic Layer Deposition”. en. In: *Critical Reviews in Solid State and Materials Sciences* 38(3), pp. 167–202. DOI: [10.1080/10408436.2012.693460](https://doi.org/10.1080/10408436.2012.693460).
- Knöfel, Christina et al. (2009). “Study of Carbon Dioxide Adsorption on Mesoporous Aminopropylsilane-Functionalized Silica and Titania Combining Microcalorimetry and in Situ Infrared Spectroscopy”. en. In: *J. Phys. Chem. C* 113(52), pp. 21726–21734. DOI: [10.1021/jp907054h](https://doi.org/10.1021/jp907054h).
- Knoops, H.C.M. et al. (2015). “Atomic Layer Deposition”. en. In: *Handbook of Crystal Growth*. Elsevier, pp. 1101–1134. DOI: [10.1016/B978-0-444-63304-0.00027-5](https://doi.org/10.1016/B978-0-444-63304-0.00027-5).
- Ko, Yohan et al. (2017). “Electrodeposition of SnO₂ on FTO and its Application in Planar Heterojunction Perovskite Solar Cells as an Electron Transport Layer”. en. In: *Nanoscale Res Lett* 12(1), p. 498. DOI: [10.1186/s11671-017-2247-x](https://doi.org/10.1186/s11671-017-2247-x).
- Kojima, Akihiro et al. (2009). “Organometal Halide Perovskites as Visible-Light Sensitizers for Photovoltaic Cells”. en. In: *Journal of the American Chemical Society* 131(17), pp. 6050–6051. DOI: [10.1021/ja809598r](https://doi.org/10.1021/ja809598r).
- Koushik, Dibyashree et al. (2017). “High-efficiency humidity-stable planar perovskite solar cells based on atomic layer architecture”. In: *Energy Environ. Sci.* 10(1), pp. 91–100. DOI: [10.1039/C6EE02687G](https://doi.org/10.1039/C6EE02687G).

- Krücke-meier, Lisa et al. (2021). “Understanding Transient Photoluminescence in Halide Perovskite Layer Stacks and Solar Cells”. en. In: *Adv. Energy Mater.* 11(19), p. 2003489. DOI: [10.1002/aenm.202003489](https://doi.org/10.1002/aenm.202003489).
- Kumari, M. Aruna et al. (2018). “Fullerene derivatives: A review on perovskite solar cells”. en. In: *mat express* 8(5), pp. 389–406. DOI: [10.1166/mex.2018.1449](https://doi.org/10.1166/mex.2018.1449).
- Kwoka, M. et al. (2005). “XPS study of the surface chemistry of L-CVD SnO₂ thin films after oxidation”. en. In: *Thin Solid Films* 490(1), pp. 36–42. DOI: [10.1016/j.tsf.2005.04.014](https://doi.org/10.1016/j.tsf.2005.04.014).
- Kwon, Hannah et al. (2019). “Towards efficient and stable perovskite solar cells employing non-hygroscopic F4-TCNQ doped TFB as the hole-transporting material”. en. In: *Nanoscale* 11(41), pp. 19586–19594. DOI: [10.1039/C9NR05719F](https://doi.org/10.1039/C9NR05719F).
- Kykyneshi, Robert et al. (2011). “Transparent Conducting Oxides Based on Tin Oxide”. en. In: *Handbook of Transparent Conductors*. Ed. by David S. Ginley. Springer US: Boston, MA, pp. 171–191. DOI: [10.1007/978-1-4419-1638-9_6](https://doi.org/10.1007/978-1-4419-1638-9_6).
- Lacher, Sebastian et al. (2011). “Molecular and Supramolecular Control of the Work Function of an Inorganic Electrode with Self-Assembled Monolayer of Umbrella-Shaped Fullerene Derivatives”. en. In: *J. Am. Chem. Soc.* 133(42), pp. 16997–17004. DOI: [10.1021/ja2067675](https://doi.org/10.1021/ja2067675).
- Lambert, Johann Heinrich (1760). *Photometria sive de mensura et gradibus luminis, colorum et umbrae*.
- Lange, Ilja et al. (2014). “Tuning the Work Function of Polar Zinc Oxide Surfaces using Modified Phosphonic Acid Self-Assembled Monolayers”. en. In: *Advanced Functional Materials* 24(44), pp. 7014–7024. DOI: [10.1002/adfm.201401493](https://doi.org/10.1002/adfm.201401493).
- Lange, Ilja et al. (2015). “Zinc Oxide Modified with Benzyolphosphonic Acids as Transparent Electrodes in Regular and Inverted Organic Solar Cell Structures”. en. In: *Appl. Phys. Lett.* 106(11), p. 113302. DOI: [10.1063/1.4916182](https://doi.org/10.1063/1.4916182).
- Lasher, Gordon and Frank Stern (1964). “Spontaneous and Stimulated Recombination Radiation in Semiconductors”. en. In: *Physical Review* 133(2A), A553–A563. DOI: [10.1103/PhysRev.133.A553](https://doi.org/10.1103/PhysRev.133.A553).
- Le Tulzo, Harold (2018). “Exploration de procédés tout-ALD via la synthèse de couches minces à base de sulfures et d’oxydes pour l’élaboration de cellules photovoltaïques de type CIGS”. PhD thesis. PSL Research University.
- Le Tulzo, Harold et al. (2019). “Toward an All-Atomic Layer Deposition (ALD) Process for Cu(In,Ga)(S,Se)₂ (CIGS)-Type Solar Cell”. en. In: *Solar Energy Materials and Solar Cells* 200, p. 109965. DOI: [10.1016/j.solmat.2019.109965](https://doi.org/10.1016/j.solmat.2019.109965).
- Lee, M. M. et al. (2012). “Efficient Hybrid Solar Cells Based on Meso-Superstructured Organometal Halide Perovskites”. en. In: *Science* 338(6107), pp. 643–647. DOI: [10.1126/science.1228604](https://doi.org/10.1126/science.1228604).
- Lee, Mikyung et al. (2011). “Wettability Control of ZnO Nanoparticles for Universal Applications”. en. In: *ACS Appl. Mater. Interfaces* 3(9), pp. 3350–3356. DOI: [10.1021/am2004762](https://doi.org/10.1021/am2004762).
- Lee, Sang-Won et al. (2016). “UV Degradation and Recovery of Perovskite Solar Cells”. en. In: *Scientific Reports* 6(1). DOI: [10.1038/srep38150](https://doi.org/10.1038/srep38150).
- Lee, Sang-Won et al. (2020). “Historical Analysis of High-Efficiency, Large-Area Solar Cells: Toward Upscaling of Perovskite Solar Cells”. en. In: *Adv. Mater.* 32(51), p. 2002202. DOI: [10.1002/adma.202002202](https://doi.org/10.1002/adma.202002202).

- Lee, Yonghui et al. (2018). “Efficient Planar Perovskite Solar Cells Using Passivated Tin Oxide as an Electron Transport Layer”. en. In: *Advanced Science*, p. 1800130. DOI: [10.1002/advs.201800130](https://doi.org/10.1002/advs.201800130).
- Leys, Christophe et al. (2013). “Detecting outliers: Do not use standard deviation around the mean, use absolute deviation around the median”. en. In: *Journal of Experimental Social Psychology* 49(4), pp. 764–766. DOI: [10.1016/j.jesp.2013.03.013](https://doi.org/10.1016/j.jesp.2013.03.013).
- Li, Daiyu et al. (2021). “A Review on Scaling Up Perovskite Solar Cells”. en. In: *Adv. Funct. Mater.* 31(12), p. 2008621. DOI: [10.1002/adfm.202008621](https://doi.org/10.1002/adfm.202008621).
- Li, Hui and Wei Zhang (2020). “Perovskite Tandem Solar Cells: From Fundamentals to Commercial Deployment”. en. In: *Chem. Rev.* 120(18), pp. 9835–9950. DOI: [10.1021/acs.chemrev.9b00780](https://doi.org/10.1021/acs.chemrev.9b00780).
- Li, Ning et al. (2016). “Hydrophilic Modification of Polyvinylidene Fluoride Membranes by ZnO Atomic Layer Deposition using Nitrogen Dioxide/Diethylzinc Functionalization”. en. In: *Journal of Membrane Science* 514, pp. 241–249. DOI: [10.1016/j.memsci.2016.04.072](https://doi.org/10.1016/j.memsci.2016.04.072).
- Li, Xiong et al. (2016). “A vacuum flash-assisted solution process for high-efficiency large-area perovskite solar cells”. en. In: *Science* 353(6294), pp. 58–62. DOI: [10.1126/science.aaf8060](https://doi.org/10.1126/science.aaf8060).
- Li, Yi et al. (2015). “Mesoporous SnO₂ nanoparticle films as electron-transporting material in perovskite solar cells”. en. In: *RSC Adv.* 5(36), pp. 28424–28429. DOI: [10.1039/C5RA01540E](https://doi.org/10.1039/C5RA01540E).
- Liang, Jia et al. (2016). “All-Inorganic Perovskite Solar Cells”. en. In: *J. Am. Chem. Soc.* 138(49), pp. 15829–15832. DOI: [10.1021/jacs.6b10227](https://doi.org/10.1021/jacs.6b10227).
- Liang, Xinhua et al. (2009). “Low-Temperature Atomic Layer-Deposited TiO₂ Films with Low Photoactivity”. en. In: *Journal of the American Ceramic Society* 92(3), pp. 649–654. DOI: [10.1111/j.1551-2916.2009.02940.x](https://doi.org/10.1111/j.1551-2916.2009.02940.x).
- Liao, Kejun et al. (2020). “Hot-Casting Large-Grain Perovskite Film for Efficient Solar Cells: Film Formation and Device Performance”. en. In: *Nano-Micro Lett.* 12(1), p. 156. DOI: [10.1007/s40820-020-00494-2](https://doi.org/10.1007/s40820-020-00494-2).
- Liao, Kung-Ching et al. (2010). “Designed Organophosphonate Self-Assembled Monolayers Enhance Device Performance of Pentacene-Based Organic Thin-Film Transistors”. en. In: *Adv. Mater.* 22(28), pp. 3081–3085. DOI: [10.1002/adma.201001310](https://doi.org/10.1002/adma.201001310).
- Liao, Yusen et al. (2015). “Amine-Functionalized ZnO Nanosheets for Efficient CO₂ Capture and Photoreduction”. en. In: *Molecules* 20(10), pp. 18847–18855. DOI: [10.3390/molecules201018847](https://doi.org/10.3390/molecules201018847).
- Lin, Qianqian et al. (2018). “Hybrid Perovskites: Prospects for Concentrator Solar Cells”. en. In: *Adv. Sci.* 5(4), p. 1700792. DOI: [10.1002/advs.201700792](https://doi.org/10.1002/advs.201700792).
- Lin, Renxing et al. (2019). “Monolithic all-perovskite tandem solar cells with 24.8% efficiency exploiting comproportionation to suppress Sn(II) oxidation in precursor ink”. en. In: *Nat Energy* 4(10), pp. 864–873. DOI: [10.1038/s41560-019-0466-3](https://doi.org/10.1038/s41560-019-0466-3).
- Lin-Vien, Daimay et al. (1991a). “Aromatic and Heteroaromatic Rings”. en. In: *The Handbook of Infrared and Raman Characteristic Frequencies of Organic Molecules*. Elsevier, pp. 277–306. DOI: [10.1016/B978-0-08-057116-4.50023-7](https://doi.org/10.1016/B978-0-08-057116-4.50023-7).

- Lin-Vien, Daimay et al. (1991b). “Compounds Containing —NH₂, —NHR, and —NR₂ Groups”. en. In: *The Handbook of Infrared and Raman Characteristic Frequencies of Organic Molecules*. Elsevier, pp. 155–178. DOI: [10.1016/B978-0-08-057116-4.50016-X](https://doi.org/10.1016/B978-0-08-057116-4.50016-X).
- Lin-Vien, Daimay et al. (1991c). “Organophosphorus Compounds”. en. In: *The Handbook of Infrared and Raman Characteristic Frequencies of Organic Molecules*. Elsevier, pp. 263–276. DOI: [10.1016/B978-0-08-057116-4.50022-5](https://doi.org/10.1016/B978-0-08-057116-4.50022-5).
- Liu, Jie et al. (2020). “The diverse passivation effects of fullerene derivative on hysteresis behavior for normal and inverted perovskite solar cells”. en. In: *Journal of Power Sources* 461, p. 228156. DOI: [10.1016/j.jpowsour.2020.228156](https://doi.org/10.1016/j.jpowsour.2020.228156).
- Liu, Xianghong et al. (2015). “High-rate amorphous SnO₂ nanomembrane anodes for Li-ion batteries with a long cycling life”. en. In: *Nanoscale* 7(1), pp. 282–288. DOI: [10.1039/C4NR04903A](https://doi.org/10.1039/C4NR04903A).
- Liu, Xu et al. (2018). “Exploring Inorganic Binary Alkaline Halide to Passivate Defects in Low-Temperature-Processed Planar-Structure Hybrid Perovskite Solar Cells”. en. In: *Adv. Energy Mater.* 8(20), p. 1800138. DOI: [10.1002/aenm.201800138](https://doi.org/10.1002/aenm.201800138).
- Liu, Zhengzheng et al. (2020). “Advances in inorganic and hybrid perovskites for miniaturized lasers”. en. In: *Nanophotonics* 9(8), pp. 2251–2272. DOI: [10.1515/nanoph-2019-0572](https://doi.org/10.1515/nanoph-2019-0572).
- Liu, Zhifa et al. (2019). “Open-Circuit Voltages Exceeding 1.26 V in Planar Methylammonium Lead Iodide Perovskite Solar Cells”. en. In: *ACS Energy Lett.* 4(1), pp. 110–117. DOI: [10.1021/acseenergylett.8b01906](https://doi.org/10.1021/acseenergylett.8b01906).
- Löckinger, Johannes et al. (2018). “TiO₂ as intermediate buffer layer in Cu(In,Ga)Se₂ solar cells”. en. In: *Solar Energy Materials and Solar Cells* 174, pp. 397–404. DOI: [10.1016/j.solmat.2017.09.030](https://doi.org/10.1016/j.solmat.2017.09.030).
- Longo, Roberto C. et al. (2013). “Monolayer Doping via Phosphonic Acid Grafting on Silicon: Microscopic Insight from Infrared Spectroscopy and Density Functional Theory Calculations”. en. In: *Adv. Funct. Mater.* 23(27), pp. 3471–3477. DOI: [10.1002/adfm.201202808](https://doi.org/10.1002/adfm.201202808).
- Lopez-Varo, Pilar et al. (2017). “Effects of Ion Distributions on Charge Collection in Perovskite Solar Cells”. In: *ACS Energy Lett.* 2(6), pp. 1450–1453. DOI: [10.1021/acseenergylett.7b00424](https://doi.org/10.1021/acseenergylett.7b00424).
- Lushtinetz, Regina et al. (2007). “Infrared Spectra of Alkylphosphonic Acid Bound to Aluminium Surfaces”. en. In: *Macromol. Symp.* 254(1), pp. 248–253. DOI: [10.1002/masy.200750837](https://doi.org/10.1002/masy.200750837).
- Lv, Yifan et al. (2018). “Low-Temperature Atomic Layer Deposition of Metal Oxide Layers for Perovskite Solar Cells with High Efficiency and Stability under Harsh Environmental Conditions”. en. In: *ACS Appl. Mater. Interfaces* 10(28), pp. 23928–23937. DOI: [10.1021/acssami.8b07346](https://doi.org/10.1021/acssami.8b07346).
- Mackus, Adriaan J. M. et al. (2018). “Synthesis of Doped, Ternary, and Quaternary Materials by Atomic Layer Deposition: A Review”. en. In: *Chemistry of Materials* 31(4), pp. 1142–1183. DOI: [10.1021/acs.chemmater.8b02878](https://doi.org/10.1021/acs.chemmater.8b02878).
- Malygin, Anatolii A. et al. (2015). “From V. B. Aleskovskii’s “Framework” Hypothesis to the Method of Molecular Layering/Atomic Layer Deposition”. en.

- In: *Chem. Vap. Deposition* 21(10-11-12), pp. 216–240. DOI: [10.1002/cvde.201502013](https://doi.org/10.1002/cvde.201502013).
- Mani, Gopinath et al. (2008). “Stability of Self-Assembled Monolayers on Titanium and Gold”. en. In: *Langmuir* 24(13), pp. 6774–6784. DOI: [10.1021/la8003646](https://doi.org/10.1021/la8003646).
- Markvart, Tom and Luis Castañer (2018). “Semiconductor Materials and Modeling”. en. In: *McEvoy’s Handbook of Photovoltaics*. Elsevier, pp. 29–57. DOI: [10.1016/B978-0-12-809921-6.00002-1](https://doi.org/10.1016/B978-0-12-809921-6.00002-1).
- Mathews, Ian et al. (2019). “Technology and Market Perspective for Indoor Photovoltaic Cells”. en. In: *Joule* 3(6), pp. 1415–1426. DOI: [10.1016/j.joule.2019.03.026](https://doi.org/10.1016/j.joule.2019.03.026).
- Mazzolini, Piero et al. (2016). “Controlling the Electrical Properties of Undoped and Ta-Doped TiO₂ Polycrystalline Films via Ultra-Fast-Annealing Treatments”. en. In: *Adv. Electron. Mater.* 2(3), p. 1500316. DOI: [10.1002/aelm.201500316](https://doi.org/10.1002/aelm.201500316).
- McDermott, Joseph E. et al. (2007). “Organophosphonate Self-Assembled Monolayers for Gate Dielectric Surface Modification of Pentacene-Based Organic Thin-Film Transistors: A Comparative Study”. en. In: *J. Phys. Chem. A* 111(49), pp. 12333–12338. DOI: [10.1021/jp075177v](https://doi.org/10.1021/jp075177v).
- Meadows, Donella H. and Club of Rome, eds. (1972). *The Limits to growth: a report for the Club of Rome’s project on the predicament of mankind*. Universe Books: New York. ISBN: 978-0-87663-165-2.
- Meitner, Lise (1922). “Über die Entstehung der beta-Strahl-Spektren radioaktiver Substanzen”. In: *Zeitschrift für Physik* 9(1), pp. 131–144.
- Meng, Xiangbo (2017). “An Overview of Molecular Layer Deposition for Organic and Organic-Inorganic Hybrid Materials: Mechanisms, Growth Characteristics, and Promising Applications”. en. In: *J. Mater. Chem. A* 5, pp. 18326–18378. DOI: [10.1039/C7TA04449F](https://doi.org/10.1039/C7TA04449F).
- Meyer, J. et al. (2009). “Reliable thin film encapsulation for organic light emitting diodes grown by low-temperature atomic layer deposition”. en. In: *Appl. Phys. Lett.* 94(23), p. 233305. DOI: [10.1063/1.3153123](https://doi.org/10.1063/1.3153123).
- Miller, Elisa M. et al. (2014). “Substrate-controlled band positions in CH₃NH₃PbI₃ perovskite films”. In: *Phys. Chem. Chem. Phys.* 16(40), pp. 22122–22130. DOI: [10.1039/C4CP03533J](https://doi.org/10.1039/C4CP03533J).
- Miyata, Atsuhiko et al. (2015). “Direct measurement of the exciton binding energy and effective masses for charge carriers in organic–inorganic tri-halide perovskites”. en. In: *Nature Phys* 11(7), pp. 582–587. DOI: [10.1038/nphys3357](https://doi.org/10.1038/nphys3357).
- Monteiro, Jorge H. S. K. (2020). “Recent Advances in Luminescence Imaging of Biological Systems Using Lanthanide(III) Luminescent Complexes”. en. In: *Molecules* 25(9), p. 2089. DOI: [10.3390/molecules25092089](https://doi.org/10.3390/molecules25092089).
- Mote, Vd et al. (2012). “Williamson-Hall analysis in estimation of lattice strain in nanometer-sized ZnO particles”. en. In: *J Theor Appl Phys* 6(1), p. 6. DOI: [10.1186/2251-7235-6-6](https://doi.org/10.1186/2251-7235-6-6).
- Mullings, Marja N. et al. (2013). “Tin oxide atomic layer deposition from tetrakis(dimethylamino)tin and water”. en. In: *Journal of Vacuum Science & Technology A: Vacuum, Surfaces, and Films* 31(6), p. 061503. DOI: [10.1116/1.4812717](https://doi.org/10.1116/1.4812717).

- Murakami, Motohiko et al. (2012). “A perovskitic lower mantle inferred from high-pressure, high-temperature sound velocity data”. en. In: *Nature* 485(7396), pp. 90–94. DOI: [10.1038/nature11004](https://doi.org/10.1038/nature11004).
- Nam, Sooji et al. (2012). “Effects of direct solvent exposure on the nanoscale morphologies and electrical characteristics of PCBM-based transistors and photovoltaics”. en. In: *J. Mater. Chem.* 22(12), p. 5543. DOI: [10.1039/c2jm15260f](https://doi.org/10.1039/c2jm15260f).
- Nazarov, D V et al. (2015). “Atomic layer deposition of tin dioxide nanofilms: a review”. en. In: *Reviews on Advances Materials Science* 40, pp. 262–275. DOI: [10.1116/1.4972554](https://doi.org/10.1116/1.4972554).
- Niemelä, Janne-Petteri et al. (2017). “Titanium dioxide thin films by atomic layer deposition: a review”. en. In: *Semicond. Sci. Technol.* 32(9), p. 093005. DOI: [10.1088/1361-6641/aa78ce](https://doi.org/10.1088/1361-6641/aa78ce).
- Noel, Nakita K. et al. (2014). “Enhanced Photoluminescence and Solar Cell Performance via Lewis Base Passivation of Organic–Inorganic Lead Halide Perovskites”. In: *ACS Nano* 8(10), pp. 9815–9821. DOI: [10.1021/nm5036476](https://doi.org/10.1021/nm5036476).
- Norris, Michael R. and Brandi M. Cossairt (2015). “CdSe on a Mesoporous Transparent Conducting Oxide Scaffold as a Photocathode”. en. In: *J. Mater. Chem. A* 3(28), pp. 14585–14591. DOI: [10.1039/C5TA03910J](https://doi.org/10.1039/C5TA03910J).
- Onclin, Steffen et al. (2005). “Engineering Silicon Oxide Surfaces Using Self-Assembled Monolayers”. en. In: *Angew. Chem. Int. Ed.* 44(39), pp. 6282–6304. DOI: [10.1002/anie.200500633](https://doi.org/10.1002/anie.200500633).
- Openlearning, Aalto (2021). *ALD: brief introduction to ALD*. URL: <https://openlearning.aalto.fi/mod/page/view.php?id=7632>.
- Ory, Daniel et al. (2020). “Optical and recombination properties of dislocations in cast-mono silicon from short wave infrared luminescence imaging”. en. In: *Journal of Applied Physics* 127(6), p. 063102. DOI: [10.1063/1.5140245](https://doi.org/10.1063/1.5140245).
- Oxford PV (2021). *Oxford PV*. URL: <https://www.oxfordpv.com/news/oxford-pv-hits-new-world-record-solar-cell> (visited on 06/07/2021).
- Özgür, ü. et al. (2005). “A Comprehensive Review of ZnO Materials and Devices”. en. In: *Journal of Applied Physics* 98(4), p. 041301. DOI: [10.1063/1.1992666](https://doi.org/10.1063/1.1992666).
- Pan, Xiaoyang et al. (2013). “Defective TiO₂ with oxygen vacancies: synthesis, properties and photocatalytic applications”. en. In: *Nanoscale* 5(9), p. 3601. DOI: [10.1039/c3nr00476g](https://doi.org/10.1039/c3nr00476g).
- Paniagua, Sergio A. et al. (2008). “Phosphonic Acid Modification of Indium-Tin Oxide Electrodes: Combined XPS/UPS/Contact Angle Studies”. en. In: *J. Phys. Chem. C* 112(21), pp. 7809–7817. DOI: [10.1021/jp710893k](https://doi.org/10.1021/jp710893k).
- Paniagua, Sergio A. et al. (2016). “Phosphonic Acids for Interfacial Engineering of Transparent Conductive Oxides”. en. In: *Chem. Rev.* 116(12), pp. 7117–7158. DOI: [10.1021/acs.chemrev.6b00061](https://doi.org/10.1021/acs.chemrev.6b00061).
- Pari, Baraneedharan et al. (2013). “Recent Advances in SnO₂ Based Photo Anode Materials for Third Generation Photovoltaics”. In: *MSF* 771, pp. 25–38. DOI: [10.4028/www.scientific.net/MSF.771.25](https://doi.org/10.4028/www.scientific.net/MSF.771.25).
- Park, Helen Hejin (2021a). “Inorganic Materials by Atomic Layer Deposition for Perovskite Solar Cells”. en. In: *Nanomaterials* 11(1), p. 88. DOI: [10.3390/nano11010088](https://doi.org/10.3390/nano11010088).

- Park, Helen Hejin (2021b). “Transparent Electrode Techniques for Semitransparent and Tandem Perovskite Solar Cells”. In: *Electronic Materials Letters* 17(1), pp. 18–32. DOI: [10.1007/s13391-020-00259-4](https://doi.org/10.1007/s13391-020-00259-4).
- Parsons, Gregory N. and Robert D. Clark (2020). “Area-Selective Deposition: Fundamentals, Applications, and Future Outlook”. en. In: *Chem. Mater.* 32(12), pp. 4920–4953. DOI: [10.1021/acs.chemmater.0c00722](https://doi.org/10.1021/acs.chemmater.0c00722).
- Parsons, Gregory N. et al. (2011). “Progress and future directions for atomic layer deposition and ALD-based chemistry”. en. In: *MRS Bull.* 36(11), pp. 865–871. DOI: [10.1557/mrs.2011.238](https://doi.org/10.1557/mrs.2011.238).
- Pazos-Outon, L. M. et al. (2016). “Photon recycling in lead iodide perovskite solar cells”. en. In: *Science* 351(6280), pp. 1430–1433. DOI: [10.1126/science.aaf1168](https://doi.org/10.1126/science.aaf1168).
- Peng, Jun et al. (2017). “Interface passivation using ultrathin polymer–fullerene films for high-efficiency perovskite solar cells with negligible hysteresis”. en. In: *Energy Environ. Sci.* 10(8), pp. 1792–1800. DOI: [10.1039/C7EE01096F](https://doi.org/10.1039/C7EE01096F).
- Perkins, Craig L. (2009). “Molecular Anchors for Self-Assembled Monolayers on ZnO: A Direct Comparison of the Thiol and Phosphonic Acid Moieties”. en. In: *The Journal of Physical Chemistry C* 113(42), pp. 18276–18286. DOI: [10.1021/jp906013r](https://doi.org/10.1021/jp906013r).
- Pham, Hoai Phuong et al. (2017). “Characterization of Ag-Doped p-Type SnO Thin Films Prepared by DC Magnetron Sputtering”. en. In: *Journal of Nanomaterials* 2017, pp. 1–6. DOI: [10.1155/2017/8360823](https://doi.org/10.1155/2017/8360823).
- Ponzoni, Andrea (2020). “Morphological Effects in SnO₂ Chemiresistors for Ethanol Detection: A Review in Terms of Central Performances and Outliers”. en. In: *Sensors* 21(1), p. 29. DOI: [10.3390/s21010029](https://doi.org/10.3390/s21010029).
- Poodt, Paul et al. (2012). “Spatial atomic layer deposition: A route towards further industrialization of atomic layer deposition”. en. In: *Journal of Vacuum Science & Technology A: Vacuum, Surfaces, and Films* 30(1), p. 010802. DOI: [10.1116/1.3670745](https://doi.org/10.1116/1.3670745).
- Pore, Viljami et al. (2011). “Atomic Layer Deposition of Antimony and its Compounds Using Dechlorosilylation Reactions of Tris(triethylsilyl)antimony”. en. In: *Chem. Mater.* 23(2), pp. 247–254. DOI: [10.1021/cm102904f](https://doi.org/10.1021/cm102904f).
- Pörtner, H.-O. et al. (2019). *IPCC, 2019: IPCC Special report on the ocean and cryosphere in a changing climate*. Tech. rep.
- Puurunen, Riikka L. (2014). “A Short History of Atomic Layer Deposition: Tuomo Suntola’s Atomic Layer Epitaxy”. en. In: *Chem. Vap. Deposition* 20(10-11-12), pp. 332–344. DOI: [10.1002/cvde.201402012](https://doi.org/10.1002/cvde.201402012).
- Quiñones, Rosalynn et al. (2014). “Investigation of Phosphonic Acid Surface Modifications on Zinc Oxide Nanoparticles under Ambient Conditions”. en. In: *Thin Solid Films* 565, pp. 155–164. DOI: [10.1016/j.tsf.2014.06.057](https://doi.org/10.1016/j.tsf.2014.06.057).
- Quiñones, Rosalynn et al. (2017). “Study of Perfluorophosphonic Acid Surface Modifications on Zinc Oxide Nanoparticles”. en. In: *Materials* 10(12), p. 1363. DOI: [10.3390/ma10121363](https://doi.org/10.3390/ma10121363).
- Rahtu, Antti and Mikko Ritala (2002). “Reaction Mechanism Studies on Titanium Isopropoxide-Water Atomic Layer Deposition Process”. en. In: *Chemical Vapor Deposition* 8(1). DOI: [10.1021/LA026357T](https://doi.org/10.1021/LA026357T).

- Raiford, James A. et al. (2020). “Applications of atomic layer deposition and chemical vapor deposition for perovskite solar cells”. en. In: *Energy Environ. Sci.* 13(7), pp. 1997–2023. DOI: [10.1039/DOEE00385A](https://doi.org/10.1039/DOEE00385A).
- Rau, U. et al. (2004). “Resistive limitations to spatially inhomogeneous electronic losses in solar cells”. en. In: *Appl. Phys. Lett.* 85(24), pp. 6010–6012. DOI: [10.1063/1.1835536](https://doi.org/10.1063/1.1835536).
- Rau, Uwe (2007). “Reciprocity relation between photovoltaic quantum efficiency and electroluminescent emission of solar cells”. en. In: *Phys. Rev. B* 76(8), p. 085303. DOI: [10.1103/PhysRevB.76.085303](https://doi.org/10.1103/PhysRevB.76.085303).
- Ritala, Mikko and Jaakko Niinistö (2009). “Industrial Applications of Atomic Layer Deposition”. en. In: *ECS Trans.* 25(8), pp. 641–652. DOI: [10.1149/1.3207651](https://doi.org/10.1149/1.3207651).
- Robinson, S. J. et al. (1994). “Departures from the principle of superposition in silicon solar cells”. en. In: *Journal of Applied Physics* 76(12), pp. 7920–7930. DOI: [10.1063/1.357902](https://doi.org/10.1063/1.357902).
- Rongwei Zhang et al. (2009). “Enhanced Electrical Properties of Anisotropic Conductive Adhesive With π -Conjugated Self-Assembled Molecular Wire Junctions”. en. In: *IEEE Trans. Comp. Packag. Technol.* 32(3), pp. 677–683. DOI: [10.1109/TCAPT.2009.2012720](https://doi.org/10.1109/TCAPT.2009.2012720).
- Roosbroeck, W. van and W. Shockley (1954). “Photon-Radiative Recombination of Electrons and Holes in Germanium”. en. In: *Phys. Rev.* 94(6), pp. 1558–1560. DOI: [10.1103/PhysRev.94.1558](https://doi.org/10.1103/PhysRev.94.1558).
- Rose, G. (1840). “Ueber einige neue Mineralien des Urals”. In: *Journal für Praktische Chemie* 19(1), pp. 459–468.
- Ross, Robert T. (1967). “Some Thermodynamics of Photochemical Systems”. en. In: *The Journal of Chemical Physics* 46(12), pp. 4590–4593. DOI: [10.1063/1.1840606](https://doi.org/10.1063/1.1840606).
- Saha, Jewel Kumer et al. (2020). “Significant improvement of spray pyrolyzed ZnO thin film by precursor optimization for high mobility thin film transistors”. en. In: *Sci Rep* 10(1), p. 8999. DOI: [10.1038/s41598-020-65938-6](https://doi.org/10.1038/s41598-020-65938-6).
- Saint-André, Simón et al. (2021). “TiO₂ nanotubes antireflection coating design for GaAs solar cells”. en. In: *Solar Energy Materials and Solar Cells* 230, p. 111201. DOI: [10.1016/j.solmat.2021.111201](https://doi.org/10.1016/j.solmat.2021.111201).
- Saliba, Michael et al. (2016). “Cesium-Containing Triple Cation Perovskite Solar Cells: Improved Stability, Reproducibility and High Efficiency”. en. In: *Energy & Environmental Science* 9(6), pp. 1989–1997. DOI: [10.1039/C5EE03874J](https://doi.org/10.1039/C5EE03874J).
- Saliba, Michael et al. (2018). “How to Make over 20% Efficient Perovskite Solar Cells in Regular (n-i-p) and Inverted (p-i-n) Architectures”. In: *Chem. Mater.* 30(13). Publisher: American Chemical Society, pp. 4193–4201. DOI: [10.1021/acs.chemmater.8b00136](https://doi.org/10.1021/acs.chemmater.8b00136).
- Sanchez, Sandy et al. (2018). “Flash Infrared Annealing for Antisolvent-Free Highly Efficient Perovskite Solar Cells”. en. In: *Advanced Energy Materials*, p. 1702915. DOI: [10.1002/aenm.201702915](https://doi.org/10.1002/aenm.201702915).
- Sandmann, Alice et al. (2015). “Interaction of L-Cysteine with ZnO: Structure, Surface Chemistry, and Optical Properties”. en. In: *Langmuir* 31(21), pp. 5701–5711. DOI: [10.1021/la504968m](https://doi.org/10.1021/la504968m).

- Scheer, Roland and H. W. Schock (2011). *Chalcogenide photovoltaics: physics, technologies, and thin film devices*. OCLC: ocn664325819. Wiley-VCH: Weinheim, Germany. ISBN: 978-3-527-31459-1.
- Schulz, Philip et al. (2019). “Halide Perovskites: Is It All about the Interfaces?” en. In: *Chem. Rev.* 119(5), pp. 3349–3417. DOI: [10.1021/acs.chemrev.8b00558](https://doi.org/10.1021/acs.chemrev.8b00558).
- Schutt, Kelly et al. (2019). “Overcoming Zinc Oxide Interface Instability with a Methylammonium-Free Perovskite for High-Performance Solar Cells”. en. In: *Advanced Functional Materials* 29(47). DOI: [10.1002/adfm.201900466](https://doi.org/10.1002/adfm.201900466).
- Shallcross, R. Clayton et al. (2019). “Impact of Titanium Dioxide Surface Defects on the Interfacial Composition and Energetics of Evaporated Perovskite Active Layers”. en. In: *ACS Appl. Mater. Interfaces* 11(35), pp. 32500–32508. DOI: [10.1021/acsami.9b09935](https://doi.org/10.1021/acsami.9b09935).
- Sharma, Asha et al. (2009). “Tailoring the Work Function of Indium Tin Oxide Electrodes in Electrophosphorescent Organic Light-Emitting Diodes”. en. In: *Journal of Applied Physics* 105(8), p. 084507. DOI: [10.1063/1.3095492](https://doi.org/10.1063/1.3095492).
- Shen, Heping et al. (2018). “In situ recombination junction between p-Si and TiO₂ enables high-efficiency monolithic perovskite/Si tandem cells”. en. In: *Sci. Adv.* 4(12), eaau9711. DOI: [10.1126/sciadv.aau9711](https://doi.org/10.1126/sciadv.aau9711).
- Sheng, Jiazhen et al. (2018). “Review Article: Atomic layer deposition for oxide semiconductor thin film transistors: Advances in research and development”. en. In: *Journal of Vacuum Science & Technology A* 36(6), p. 060801. DOI: [10.1116/1.5047237](https://doi.org/10.1116/1.5047237).
- Shi, Yue-Jie et al. (2017). “Optical Constants and Band Gap Evolution with Phase Transition in Sub-20-nm-Thick TiO₂ Films Prepared by ALD”. en. In: *Nanoscale Res Lett* 12(1), p. 243. DOI: [10.1186/s11671-017-2011-2](https://doi.org/10.1186/s11671-017-2011-2).
- Shockley, W. and W. T. Read (1952). “Statistics of the Recombinations of Holes and Electrons”. en. In: *Phys. Rev.* 87(5), pp. 835–842. DOI: [10.1103/PhysRev.87.835](https://doi.org/10.1103/PhysRev.87.835).
- Shockley, William and Hans J. Queisser (1961). “Detailed Balance Limit of Efficiency of p–n Junction Solar Cells”. en. In: *Journal of Applied Physics* 32(3), pp. 510–519. DOI: [10.1063/1.1736034](https://doi.org/10.1063/1.1736034).
- Slotcavage, Daniel J. et al. (2016). “Light-Induced Phase Segregation in Halide-Perovskite Absorbers”. en. In: *ACS Energy Letters* 1(6), pp. 1199–1205. DOI: [10.1021/acsenergylett.6b00495](https://doi.org/10.1021/acsenergylett.6b00495).
- Smecca, Emanuele et al. (2013). “Spectroscopic and Theoretical Study of the Grafting Modes of Phosphonic Acids on ZnO Nanorods”. en. In: *J. Phys. Chem. C* 117(10), pp. 5364–5372. DOI: [10.1021/jp308983p](https://doi.org/10.1021/jp308983p).
- Smits, Edsger C. P. et al. (2008). “Bottom-up organic integrated circuits”. en. In: *Nature* 455(7215), pp. 956–959. DOI: [10.1038/nature07320](https://doi.org/10.1038/nature07320).
- Snaith, Henry J. et al. (2009). “Charge Generation and Photovoltaic Operation of Solid-State Dye-Sensitized Solar Cells Incorporating a High Extinction Coefficient Indolene-Based Sensitizer”. en. In: *Adv. Funct. Mater.* 19(11), pp. 1810–1818. DOI: [10.1002/adfm.200801751](https://doi.org/10.1002/adfm.200801751).
- Song, Jiaying et al. (2017). “Highly Efficient and Stable Low-Temperature Processed ZnO Solar Cells with Triple Cation Perovskite Absorber”. en. In: *Journal of Materials Chemistry A* 5(26), pp. 13439–13447. DOI: [10.1039/C7TA03331A](https://doi.org/10.1039/C7TA03331A).

- Song, Miao et al. (2020). “Phase transformations among TiO₂ polymorphs”. en. In: *Nanoscale* 12(45), pp. 23183–23190. DOI: [10.1039/D0NR06226J](https://doi.org/10.1039/D0NR06226J).
- Soto-Montero, Tatiana et al. (2020). “Pressing challenges of halide perovskite thin film growth”. en. In: *APL Materials* 8(11), p. 110903. DOI: [10.1063/5.0027573](https://doi.org/10.1063/5.0027573).
- Staerz, Anna et al. (2020). “SnO₂: The most important base material for semiconducting metal oxide-based materials”. en. In: *Tin Oxide Materials*. Elsevier, pp. 345–377. DOI: [10.1016/B978-0-12-815924-8.00012-8](https://doi.org/10.1016/B978-0-12-815924-8.00012-8).
- Stefik, Morgan et al. (2012). “Transparent, Conducting Nb:SnO₂ for Host–Guest Photoelectrochemistry”. en. In: *Nano Lett.* 12(10), pp. 5431–5435. DOI: [10.1021/nl303101n](https://doi.org/10.1021/nl303101n).
- Stolterfoht, Martin et al. (2019). “Voltage-Dependent Photoluminescence and How It Correlates with the Fill Factor and Open-Circuit Voltage in Perovskite Solar Cells”. en. In: *ACS Energy Lett.* 4(12), pp. 2887–2892. DOI: [10.1021/acsenergylett.9b02262](https://doi.org/10.1021/acsenergylett.9b02262).
- Stolterfoht, Martin et al. (2020). “How To Quantify the Efficiency Potential of Neat Perovskite Films: Perovskite Semiconductors with an Implied Efficiency Exceeding 28%”. en. In: *Adv. Mater.* 32(17), p. 2000080. DOI: [10.1002/adma.202000080](https://doi.org/10.1002/adma.202000080).
- Stott, P. (2016). “How climate change affects extreme weather events”. en. In: *Science* 352(6293), pp. 1517–1518. DOI: [10.1126/science.aaf7271](https://doi.org/10.1126/science.aaf7271).
- Sun, Chong et al. (2014). “Surface modification with EDTA molecule: A feasible method to enhance the adsorption property of ZnO”. en. In: *Journal of Physics and Chemistry of Solids* 75(6), pp. 726–731. DOI: [10.1016/j.jpcs.2014.01.016](https://doi.org/10.1016/j.jpcs.2014.01.016).
- Sun, Shaodong et al. (2019). “Amorphous TiO₂ nanostructures: synthesis, fundamental properties and photocatalytic applications”. en. In: *Catal. Sci. Technol.* 9(16), pp. 4198–4215. DOI: [10.1039/C9CY01020C](https://doi.org/10.1039/C9CY01020C).
- Sun, Xiaoyu et al. (2019). “Research Status of Antireflection Film Based on TiO₂”. In: *IOP Conf. Ser.: Mater. Sci. Eng.* 490, p. 022074. DOI: [10.1088/1757-899X/490/2/022074](https://doi.org/10.1088/1757-899X/490/2/022074).
- Sutanto, Albertus A. et al. (2021). “2D/3D perovskite engineering eliminates interfacial recombination losses in hybrid perovskite solar cells”. In: *Chem.* DOI: [10.1016/j.chempr.2021.04.002](https://doi.org/10.1016/j.chempr.2021.04.002).
- Tailor, Naveen Kumar et al. (2020). “Recent progress in morphology optimization in perovskite solar cell”. en. In: *J. Mater. Chem. A* 8(41), pp. 21356–21386. DOI: [10.1039/D0TA00143K](https://doi.org/10.1039/D0TA00143K).
- Tang, H. et al. (1994). “Electrical and optical properties of TiO₂ anatase thin films”. en. In: *Journal of Applied Physics* 75(4), pp. 2042–2047. DOI: [10.1063/1.356306](https://doi.org/10.1063/1.356306).
- Tian, Liang et al. (2015). “Undoped TiO₂ and nitrogen-doped TiO₂ thin films deposited by atomic layer deposition on planar and architected surfaces for photovoltaic applications”. en. In: *Journal of Vacuum Science & Technology A: Vacuum, Surfaces, and Films* 33(1), 01A141. DOI: [10.1116/1.4904025](https://doi.org/10.1116/1.4904025).
- Tress, Wolfgang (2017). “Metal Halide Perovskites as Mixed Electronic–Ionic Conductors: Challenges and Opportunities—From Hysteresis to Memristivity”. en. In: *The Journal of Physical Chemistry Letters* 8(13), pp. 3106–3114. DOI: [10.1021/acs.jpcllett.7b00975](https://doi.org/10.1021/acs.jpcllett.7b00975).

- Trost, Sara et al. (2015). “Tin Oxide (SnO_x) as Universal “Light-Soaking” Free Electron Extraction Material for Organic Solar Cells”. en. In: *Advanced Energy Materials* 5(17), p. 1500277. DOI: [10.1002/aenm.201500277](https://doi.org/10.1002/aenm.201500277).
- Trupke, T. et al. (2012). “Photoluminescence Imaging for Photovoltaic Applications”. en. In: *Energy Procedia* 15, pp. 135–146. DOI: [10.1016/j.egypro.2012.02.016](https://doi.org/10.1016/j.egypro.2012.02.016).
- Tsarev, Sergey and Pavel A. Troshin (2020). “Surface Modification of ZnO Electron Transport Layer with Thermally Evaporated WO_3 for Stable Perovskite Solar Cells”. en. In: *Synthetic Metals* 269, p. 116547. DOI: [10.1016/j.synthmet.2020.116547](https://doi.org/10.1016/j.synthmet.2020.116547).
- Tseng, Zong-Liang et al. (2016). “Surface Engineering of ZnO Electron Transporting Layer via Al Doping for High Efficiency Planar Perovskite Solar Cells”. en. In: *Nano Energy* 28, pp. 311–318. DOI: [10.1016/j.nanoen.2016.08.035](https://doi.org/10.1016/j.nanoen.2016.08.035).
- Tsin, Fabien et al. (2015). “Electrodeposition of ZnO Window Layer for an All-Atmospheric Fabrication Process of Chalcogenide Solar Cell”. en. In: *Sci Rep* 5(1), p. 8961. DOI: [10.1038/srep08961](https://doi.org/10.1038/srep08961).
- Tsukazaki, Atsushi et al. (2005). “Repeated temperature modulation epitaxy for p-type doping and light-emitting diode based on ZnO”. en. In: *nature materials* 4, p. 5. DOI: [10.1038/nmat1284](https://doi.org/10.1038/nmat1284).
- Turren-Cruz, Silver-Hamill et al. (2018). “Enhanced charge carrier mobility and lifetime suppress hysteresis and improve efficiency in planar perovskite solar cells”. en. In: *Energy & Environmental Science*. DOI: [10.1039/C7EE02901B](https://doi.org/10.1039/C7EE02901B).
- Tynell, Tommi and Maarit Karppinen (2014). “Atomic layer deposition of ZnO: a review”. en. In: *Semicond. Sci. Technol.*, p. 16. DOI: [10.1088/0268-1242/29/4/043001](https://doi.org/10.1088/0268-1242/29/4/043001).
- Ulman, Abraham (1996). “Formation and Structure of Self-Assembled Monolayers”. en. In: *Chem. Rev.* 96(4), pp. 1533–1554. DOI: [10.1021/cr9502357](https://doi.org/10.1021/cr9502357).
- Ulman, Abraham and Raymond P. Scaringe (1992). “On the formation of ordered two-dimensional molecular assemblies”. en. In: *Langmuir* 8(3), pp. 894–897. DOI: [10.1021/la00039a025](https://doi.org/10.1021/la00039a025).
- Ulman, Abraham et al. (1989). “Packing and molecular orientation of alkanethiol monolayers on gold surfaces”. en. In: *Langmuir* 5(5), pp. 1147–1152. DOI: [10.1021/la00089a003](https://doi.org/10.1021/la00089a003).
- Unger, E. L. et al. (2014). “Hysteresis and transient behavior in current–voltage measurements of hybrid-perovskite absorber solar cells”. en. In: *Energy Environ. Sci.* 7(11), pp. 3690–3698. DOI: [10.1039/C4EE02465F](https://doi.org/10.1039/C4EE02465F).
- Urbach, Franz (1953). “The Long-Wavelength Edge of Photographic Sensitivity and of the Electronic Absorption of Solids”. en. In: *Physical Review* 92(5), pp. 1324–1324. DOI: [10.1103/PhysRev.92.1324](https://doi.org/10.1103/PhysRev.92.1324).
- Vericat, C et al. (2010). “Self-assembled monolayers of thiols and dithiols on gold: new challenges for a well-known system”. en. In: p. 30. DOI: [10.1039/B907301A](https://doi.org/10.1039/B907301A).
- Viirola, H and L Niinistö (1994). “Controlled growth of tin dioxide thin films by atomic layer epitaxy”. en. In: *Thin Solid Films* 249(2), pp. 144–149. DOI: [10.1016/0040-6090\(94\)90752-8](https://doi.org/10.1016/0040-6090(94)90752-8).
- Wallwork, Mark L. et al. (2001). “Complex Chemical Force Titration Behavior of Amine-Terminated Self-Assembled Monolayers”. en. In: *Langmuir* 17(4), pp. 1126–1131. DOI: [10.1021/la000870u](https://doi.org/10.1021/la000870u).

- Wang, Changlei et al. (2016). “Low-temperature plasma-enhanced atomic layer deposition of tin oxide electron selective layers for highly efficient planar perovskite solar cells”. en. In: *J. Mater. Chem. A* 4(31), pp. 12080–12087. DOI: [10.1039/C6TA04503K](https://doi.org/10.1039/C6TA04503K).
- Wang, Dong et al. (2020). “A bilayer TiO₂/Al₂O₃ as the mesoporous scaffold for enhanced air stability of ambient-processed perovskite solar cells”. en. In: *Mater. Adv.* 1(6), pp. 2057–2067. DOI: [10.1039/D0MA00562B](https://doi.org/10.1039/D0MA00562B).
- Wang, Feng et al. (2018). “Defects Engineering for High-Performance Perovskite Solar Cells”. en. In: *npj Flex Electron* 2(1), p. 22. DOI: [10.1038/s41528-018-0035-z](https://doi.org/10.1038/s41528-018-0035-z).
- Wang, Jinghui et al. (2017). “Controlled synthesis of Sn-based oxides via a hydrothermal method and their visible light photocatalytic performances”. en. In: *RSC Adv.* 7(43), pp. 27024–27032. DOI: [10.1039/C7RA04041E](https://doi.org/10.1039/C7RA04041E).
- Wang, Junke et al. (2019). “Insights into Fullerene Passivation of SnO₂ Electron Transport Layers in Perovskite Solar Cells”. en. In: *Adv. Funct. Mater.*, p. 13. DOI: [10.1002/adfm.201905883](https://doi.org/10.1002/adfm.201905883).
- Wang, Sanjun et al. (2020). “Structural, electronic, and optical properties of cubic formamidinium lead iodide perovskite: a first-principles investigation”. en. In: *RSC Adv.* 10(54), pp. 32364–32369. DOI: [10.1039/D0RA06028C](https://doi.org/10.1039/D0RA06028C).
- Wang, Shi et al. (2018). “High-air-flow-velocity assisted intermediate phase engineering for controlled crystallization of mixed perovskite in high efficiency photovoltaics”. en. In: *J. Mater. Chem. A* 6(19), pp. 8860–8867. DOI: [10.1039/C8TA02144A](https://doi.org/10.1039/C8TA02144A).
- Wang, Tianyi et al. (2017). “Indirect to direct bandgap transition in methylammonium lead halide perovskite”. en. In: *Energy Environ. Sci.* 10(2), pp. 509–515. DOI: [10.1039/C6EE03474H](https://doi.org/10.1039/C6EE03474H).
- Wei, Jing et al. (2016). “Suppressed hysteresis and improved stability in perovskite solar cells with conductive organic network”. en. In: *Nano Energy* 26, pp. 139–147. DOI: [10.1016/j.nanoen.2016.05.023](https://doi.org/10.1016/j.nanoen.2016.05.023).
- Weinreich, Wenke et al. (2013). “Structural properties of as deposited and annealed ZrO₂ influenced by atomic layer deposition, substrate, and doping”. en. In: *Journal of Vacuum Science & Technology A: Vacuum, Surfaces, and Films* 31(1), 01A119. DOI: [10.1116/1.4765047](https://doi.org/10.1116/1.4765047).
- Whitfield, P. S. et al. (2016). “Structures, Phase Transitions and Tricritical Behavior of the Hybrid Perovskite Methyl Ammonium Lead Iodide”. en. In: *Scientific Reports* 6(1). DOI: [10.1038/srep35685](https://doi.org/10.1038/srep35685).
- Williamson, G. and W Hall (1953). “X-ray line broadening from filed aluminium and wolfram”. In: *Acta Metallurgica* 1, pp. 22–31. DOI: [10.1016/0001-6160\(53\)90006-6](https://doi.org/10.1016/0001-6160(53)90006-6).
- Wolff, Christian M. et al. (2019). “Nonradiative Recombination in Perovskite Solar Cells: The Role of Interfaces”. en. In: *Adv. Mater.* 31(52), p. 1902762. DOI: [10.1002/adma.201902762](https://doi.org/10.1002/adma.201902762).
- Wolff, Christian M. et al. (2020). “Perfluorinated Self-Assembled Monolayers Enhance the Stability and Efficiency of Inverted Perovskite Solar Cells”. en. In: *ACS Nano*, acsnano.9b03268. DOI: [10.1021/acsnano.9b03268](https://doi.org/10.1021/acsnano.9b03268).

- Won, Jong Hyeon et al. (2020). “Effect of Oxygen Source on the Various Properties of SnO₂ Thin Films Deposited by Plasma-Enhanced Atomic Layer Deposition”. en. In: *Coatings* 10(7), p. 692. DOI: [10.3390/coatings10070692](https://doi.org/10.3390/coatings10070692).
- Wood, Christopher et al. (2012). “Binding Modes of Fluorinated Benzyolphosphonic Acids on the Polar ZnO Surface and Impact on Work Function”. en. In: *J. Phys. Chem. C* 116(36), pp. 19125–19133. DOI: [10.1021/jp3050725](https://doi.org/10.1021/jp3050725).
- Wright, Adam D. et al. (2016). “Electron–phonon coupling in hybrid lead halide perovskites”. en. In: *Nat Commun* 7(1), p. 11755. DOI: [10.1038/ncomms11755](https://doi.org/10.1038/ncomms11755).
- Wu, Y. et al. (2013). “Enhanced Doping Efficiency of Al-Doped ZnO by Atomic Layer Deposition Using Dimethylaluminum Isopropoxide as an Alternative Aluminum Precursor”. en. In: *Chem. Mater.* 25(22), pp. 4619–4622. DOI: [10.1021/cm402974j](https://doi.org/10.1021/cm402974j).
- Wu, Yongzhen et al. (2014). “Highly compact TiO₂ layer for efficient hole-blocking in perovskite solar cells”. en. In: *Applied Physics Express* 7(5), p. 052301. DOI: [10.7567/APEX.7.052301](https://doi.org/10.7567/APEX.7.052301).
- Wurfel, P (1982). “The chemical potential of radiation”. en. In: *Journal of Physics C: Solid State Physics* 15(18), pp. 3967–3985. DOI: [10.1088/0022-3719/15/18/012](https://doi.org/10.1088/0022-3719/15/18/012).
- Würfel, Peter (2005). *Physics of solar cells: from principles to new concepts*. en. Wiley-VCH: Weinheim. ISBN: 978-3-527-40428-5.
- Xia, Hua-Rong et al. (2015). “Hydrothermal synthesis of organometal halide perovskites for Li-ion batteries”. en. In: *Chem. Commun.* 51(72), pp. 13787–13790. DOI: [10.1039/C5CC05053G](https://doi.org/10.1039/C5CC05053G).
- Xiang, Wanchun and Wolfgang Tress (2019). “Review on Recent Progress of All-Inorganic Metal Halide Perovskites and Solar Cells”. en. In: *Adv. Mater.* 31(44), p. 1902851. DOI: [10.1002/adma.201902851](https://doi.org/10.1002/adma.201902851).
- Xie, Qi et al. (2008). “Growth Kinetics and Crystallization Behavior of TiO₂ Films Prepared by Plasma Enhanced Atomic Layer Deposition”. en. In: *Journal of The Electrochemical Society* 155(9), p. 5. DOI: [10.1149/1.2955724](https://doi.org/10.1149/1.2955724).
- Xu, Jixian et al. (2015). “Perovskite–fullerene hybrid materials suppress hysteresis in planar diodes”. en. In: *Nature Communications*, p. 8. DOI: [10.1038/ncomms8081](https://doi.org/10.1038/ncomms8081).
- Yang, Bin (2020). “Applications of Titania Atomic Layer Deposition in the Biomedical Field and Recent Updates”. en. In: *AJBSR* 8(6), pp. 465–468. DOI: [10.34297/AJBSR.2020.08.001321](https://doi.org/10.34297/AJBSR.2020.08.001321).
- Yang, Jinli et al. (2015). “Origin of the Thermal Instability in CH₃NH₃PbI₃ Thin Films Deposited on ZnO”. en. In: *Chemistry of Materials* 27(12), pp. 4229–4236. DOI: [10.1021/acs.chemmater.5b01598](https://doi.org/10.1021/acs.chemmater.5b01598).
- Yang, Lili et al. (2015). “Effects of Interface Modification with Self-Assembled Monolayers on the Photovoltaic Performance of CdS Quantum Dots Sensitized Solar Cells”. en. In: *Electrochimica Acta* 164, pp. 38–47. DOI: [10.1016/j.electacta.2015.02.190](https://doi.org/10.1016/j.electacta.2015.02.190).
- Yang, Liyan et al. (2018). “Restrained light-soaking and reduced hysteresis in perovskite solar cells employing a helical perylene diimide interfacial layer”. en. In: *Journal of Materials Chemistry A* 6(22), pp. 10379–10387. DOI: [10.1039/C8TA02584C](https://doi.org/10.1039/C8TA02584C).

- Yang, Woon Seok et al. (2017). “Iodide management in formamidinium-lead-halide-based perovskite layers for efficient solar cells”. In: *Science* 356(6345), pp. 1376–1379. DOI: [10.1126/science.aan2301](https://doi.org/10.1126/science.aan2301).
- Yang, Xinbo et al. (2016). “High-Performance TiO₂-Based Electron-Selective Contacts for Crystalline Silicon Solar Cells”. en. In: *Adv. Mater.* 28(28), pp. 5891–5897. DOI: [10.1002/adma.201600926](https://doi.org/10.1002/adma.201600926).
- Yang, Yuqian et al. (2020). “Suppressing Vacancy Defects and Grain Boundaries via Ostwald Ripening for High-Performance and Stable Perovskite Solar Cells”. en. In: *Adv. Mater.* 32(7), p. 1904347. DOI: [10.1002/adma.201904347](https://doi.org/10.1002/adma.201904347).
- Yin, W.-J. et al. (2019). “Oxide Perovskites, Double Perovskites and Derivatives for Electrocatalysis, Photocatalysis, and Photovoltaics”. en. In: *Energy Environ. Sci.* 12, pp. 442–462. DOI: [10.1039/C8EE01574K](https://doi.org/10.1039/C8EE01574K).
- Yin, Wan-Jian et al. (2015). “Halide perovskite materials for solar cells: a theoretical review”. en. In: *J. Mater. Chem. A* 3(17), pp. 8926–8942. DOI: [10.1039/C4TA05033A](https://doi.org/10.1039/C4TA05033A).
- Yin, Xin et al. (2019). “Novel NiO Nanoforest Architecture for Efficient Inverted Mesoporous Perovskite Solar Cells”. en. In: *ACS Appl. Mater. Interfaces* 11(47), pp. 44308–44314. DOI: [10.1021/acsami.9b15820](https://doi.org/10.1021/acsami.9b15820).
- Yu, Ing-Song et al. (2013). “Surface Passivation and Antireflection Behavior of ALD on n-Type Silicon for Solar Cells”. en. In: *International Journal of Photoenergy* 2013, pp. 1–7. DOI: [10.1155/2013/431614](https://doi.org/10.1155/2013/431614).
- Zardetto, V. et al. (2017). “Atomic layer deposition for perovskite solar cells: research status, opportunities and challenges”. en. In: *Sustainable Energy & Fuels* 1(1), pp. 30–55. DOI: [10.1039/C6SE00076B](https://doi.org/10.1039/C6SE00076B).
- Zardetto, V. et al. (2018). “Atmospheric Pressure Spatial ALD Layer for Ambient, Thermally and Light Stable p-i-n Planar Perovskite Solar Cells”. en. In: *2018 IEEE 7th World Conference on Photovoltaic Energy Conversion (WCPEC) (A Joint Conference of 45th IEEE PVSC, 28th PVSEC & 34th EU PVSEC)*. IEEE: Waikoloa Village, HI, pp. 3514–3517. DOI: [10.1109/PVSC.2018.8548089](https://doi.org/10.1109/PVSC.2018.8548089).
- Zhang, Bingjuan et al. (2020). “NiO/Perovskite Heterojunction Contact Engineering for Highly Efficient and Stable Perovskite Solar Cells”. en. In: *Adv. Sci.* 7(11), p. 1903044. DOI: [10.1002/advs.201903044](https://doi.org/10.1002/advs.201903044).
- Zhang, Dezhong et al. (2019). “Surface Chlorination of ZnO for Perovskite Solar Cells with Enhanced Efficiency and Stability”. en. In: *Sol. RRL* 3(8), p. 1900154. DOI: [10.1002/solr.201900154](https://doi.org/10.1002/solr.201900154).
- Zhang, Jiahuan et al. (2018). “Optimizing the efficiency of perovskite solar cells by a sub-nanometer compact titanium oxide electron transport layer”. en. In: *Nano Energy* 49, pp. 230–236. DOI: [10.1016/j.nanoen.2018.04.042](https://doi.org/10.1016/j.nanoen.2018.04.042).
- Zhang, Jing et al. (2020). “Critical review of recent progress of flexible perovskite solar cells”. en. In: *Materials Today* 39, pp. 66–88. DOI: [10.1016/j.mattod.2020.05.002](https://doi.org/10.1016/j.mattod.2020.05.002).
- Zhang, Peng et al. (2017). “Perovskite Solar Cells with ZnO Electron-Transporting Materials”. en. In: *Advanced Materials*, p. 1703737. DOI: [10.1002/adma.201703737](https://doi.org/10.1002/adma.201703737).
- Zhang, Wenzhi et al. (2016). “Structure, Stability and Electrochromic Properties of Polyaniline Film Covalently Bonded to Indium Tin Oxide Substrate”. en. In:

BIBLIOGRAPHY

- Applied Surface Science* 367, pp. 542–551. DOI: [10.1016/j.apsusc.2016.01.041](https://doi.org/10.1016/j.apsusc.2016.01.041).
- Zhong, Yu et al. (2020). “Role of PCBM in the Suppression of Hysteresis in Perovskite Solar Cells”. en. In: *Adv. Funct. Mater.*, p. 9. DOI: [10.1002/adfm.201908920](https://doi.org/10.1002/adfm.201908920).
- Zhou, Weiran et al. (2017). “Successive surface engineering of TiO₂ compact layers via dual modification of fullerene derivatives affording hysteresis-suppressed high-performance perovskite solar cells”. en. In: *J. Mater. Chem. A* 5(4), pp. 1724–1733. DOI: [10.1039/C6TA07876A](https://doi.org/10.1039/C6TA07876A).
- Zhu, Tao et al. (2019). “Interfacial Engineering through Chloride-Functionalized Self-Assembled Monolayer for High-Performance Perovskite Solar Cells”. en. In: *ACS Appl. Mater. Interfaces*, acsami.9b18034. DOI: [10.1021/acsami.9b18034](https://doi.org/10.1021/acsami.9b18034).

Appendix

A.1 Experimental

A.1.1 Device preparation

Annealing procedure. The as-deposited ALD-thin films are annealed in a Nabertherm furnace. The temperature is increased at a rate of $1100\text{ }^{\circ}\text{C h}^{-1}$ until the set temperature, where it plateaus for 20 min, before being allowed to cool down without assistance.

Synthesis of a baseline perovskite solar cell. FTO-coated glass (Solems) is etched using Zn powder and HCl (0.1 M). Substrates are cleaned by ultrasonication in RBS detergent solution (2 vol%), IPA and acetone, then dried under N_2 flow. The compact TiO_2 layer is deposited by spray pyrolysis at $450\text{ }^{\circ}\text{C}$ from a solution containing 0.6 mL of titanium diisopropoxide bis(acetyl acetonate) (75% in 2-propanol), 0.4 mL of acetyl acetone in 9 mL of IPA and oxygen as carrier gas. The mp- TiO_2 layer is deposited using a solution of commercial 30NR-D (Dyesol) diluted in absolute ethanol (1:7 in wt. respectively), and annealed up to $500\text{ }^{\circ}\text{C}$ according to a recipe described elsewhere (Bercegol, Ramos, Rebai, Guillemot, Ory, et al. (2018)). The hot substrates are transferred in the glovebox. The perovskite solution consists of 1.10M PbI_2 , 0.20M PbBr_2 , 1.00M FAI and 0.20M MABr dissolved in a solvent mixture of DMF:DMSO (4:1 in v/v). After stirring, the perovskite solution is deposited by spin coating. $35\text{ }\mu\text{L}$ of solution are deposited during a first plateau at 2000 rpm. The chlorobenzene antisolvent is deposited during a second plateau at 6000 rpm. The film is then annealed at $100\text{ }^{\circ}\text{C}$ for 30 min. The HTL is deposited by spin coating in the glovebox. The solution consists in Spiro-OMeTAD dissolved in chlorobenzene (100 mg mL^{-1}) and doped with FK209, Li-TFSI and ${}^t\text{Bp}$ (5%, 50% and 330% molar concentration relative to Spiro-OMeTAD respectively). $35\text{ }\mu\text{L}$ of this solution is spun at 3000 rpm for 25 s. Finally, 100 nm of Au are evaporated at 0.01 nm s^{-1} (10 nm) and 0.1 nm s^{-1} (90 nm) in a Plassys MEB550SL evaporator.

ALD of ZnO. The substrates were transferred into a BENEQ TFS-200 ALD reactor for the deposition of 10 or 50 nm of zinc oxide. The deposition was performed according to a process described elsewhere (Le Tulzo et al. (2019)).

A.1.2 Characterization techniques

Contact angle. The wettability of the surfaces was assessed by contact angle measurements on a Krüss DSA 10 MK2 apparatus. Sessile drop method was used with 10 μL DI water droplets. For sake of reliability, each measurement was performed on at least three distinct samples every second for ten seconds and then averaged.

Cyclic voltamperometry. The working electrode consists in a TCO covered by the investigated ETL. The contact area between the electrolyte and the working electrode is delimited by a mask of determined area. The electrolyte consists in a solution of potassium hexacyanoferrate (III) (0.1 mol L^{-1}) and potassium hexacyanoferrate (II) (0.1 mol L^{-1}). The redox couple $[\text{Fe}(\text{CN})_6]^{3-} / [\text{Fe}(\text{CN})_6]^{4-}$ has a standard redox potential of 0.356 V vs. the standard hydrogen electrode. A SCE is chosen as reference electrode, and a Pt electrode as counter electrode. The voltage sweep rate is fixed at 20 mV s^{-1} .

EQE. The external quantum efficiency was measured on an Oriel IQE 200 setup at room temperature. The measurements were performed from 300 nm to 800 nm with a 10 nm resolution.

ATR-FTIR. ATR-FTIR spectra were recorded using a Bomem MB100 FTIR spectrometer equipped with a liquid nitrogen-cooled MCT photovoltaic detector. The measurement chamber was purged with N_2 45 min prior to measurement. The Si prisms used as a substrate for the experiments were of typical size $15 \times 14 \times 0.5 \text{ mm}^3$, with a 45° angle, providing a number of ~ 14 useful reflections. The data were acquired with a 4 cm^{-1} resolution over 200 consecutive scans. The displayed spectra are plotted as absorbance (computed using the natural logarithm) and treated with an asymmetric least square smoother for the baseline subtraction as described by Eilers (2003).

Hall effect. Hall effect measurements were performed on an ECOPIA HMS-5000 system with a 0.556 T permanent magnet. The measurements were averaged on at least three samples.

J–V characteristics. Solar cell efficiencies were evaluated under 1 sun (100 mW cm^{-2}) simulated sunlight using an Oriel AAA solar simulator from Newport equipped with a Xenon lamp. The light intensity was calibrated using a certified Si reference diode from Newport. Current voltage (J–V) curves (scan speed: 20 mV s^{-1}) as well as stabilized efficiencies (PCE averaged between 3 min and 5 min at MPP) of perovskite solar cells were measured with an Arkeo measurement system from Cicci research.

QCM. In situ QCM measurements were acquired with a Colnatec Eon-LT monitor system, using an HT quartz crystal covered by an aluminum alloy (6 MHz initial oscillation frequency) located on the cover lid of the reactor. Measurements were done after a stabilization time of 1 h to reach a uniform and constant

A.2 Additional information on characterization techniques

temperature in the whole reaction chamber ($\Delta T = \pm 1.5^\circ\text{C}$). The mass gains are determined from the frequency variation using the Sauerbrey law.

SEM. SEM was used to observe the different layers with a Merlin VP Compact scanning electron microscope (SEM) provided by Zeiss. The cross sections were done with a simple cleaving tool, and a C metallization is performed with a Denton desk V metallizer.

Spectrophotometry. Transmittance and reflectance spectra were obtained using an Agilent Cary 5000 UV-vis-NIR spectrophotometer equipped with an Agilent diffuse reflectance accessory. The direct and indirect band gaps were determined with the Tauc plot method, *e.g.* as the intercept of the linear fit of $(\alpha h\nu)^{1/r}$ with the abscissa around the absorption edge ($r = 1/2$ for direct band gap, $r = 2$ for indirect band gap).

XRD, GI-XRD and XRR. XRD measurements are performed on a PanAnalytical Empyrean diffractometer with copper K alpha radiation ($\lambda = 1.5406 \text{ \AA}$) in Bragg-Brentano configuration. A dedicated modulus is added to carry out GIXRD and XRR. For GI-XRD measurements, the incidence angle was fixed at 0.4° , except for [Chapter 5](#), where it was varied from 0.2° to 1.2° . The FWHM was used as broadening parameter in the Williamson-Hall plot analysis. XRR measurements were fitted with the XPert Reflectivity software.

XPS and AR-XPS. XPS and AR-XPS analyses were carried out with a Thermo Electron K-Alpha⁺ spectrometer using a monochromatic Al-K α X-Ray source (1486.6 eV). The resolution of the binding energy is 0.1 eV. In depth measurements were done after bombardment with Ar⁺ clusters at 500 eV. AR-XPS experiments consist of tilting the considered sample from 0 to 60° (step of 10°) to perform non-destructive depth profiling by modifying the detection angle. The calibration of the spectrometer was performed according to Thermo Fisher procedure. The X-Ray spot size was 400 μm for a depth probed in the range of 10 nm. High energy resolution spectra were acquired using a Constant Analyzer Energy mode of 10 eV and 0.05 eV as energy step size. Data were processed using the Thermo Fisher scientific Avantage data system.

A.2 Additional information on characterization techniques

A.2.1 Principle of the cyclic voltametry

This section aims at explaining the peculiar shape of the voltamograms acquired with semiconducting electrodes.

First the case of a conducting electrode is considered, and its voltamogram is presented in [Figure A.1.a](#). As the potential is varied, the concentration

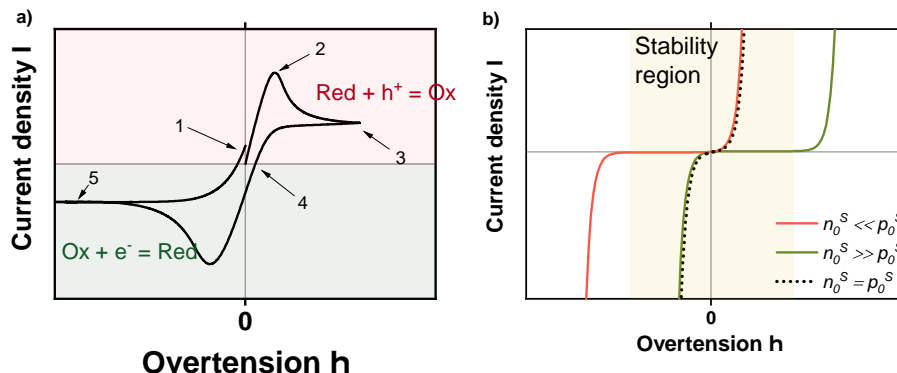


Figure A.1: a) Basic features of a cyclic voltamogram on a conductive electrode. η is the overpotential applied vs. the open circuit voltage of the circuit. The situation at the reference points 1 to 5 is detailed in the text. b) Naive sketch of a voltamogram with an electrode coated with a semiconductor function of its relative surface concentration in electron n_0^S and hole p_0^S . The colored area figures the stability region of the electrolyte. The diffusion of species in the electrolyte is not considered.

of the species of interest (here the Ox/Red redox couple) is dictated by Nernst equation:

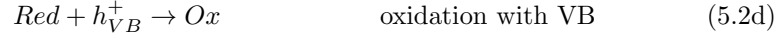
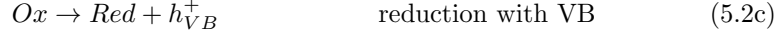
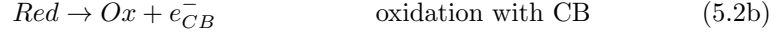
$$E = E^0 + \frac{RT}{nF} \cdot \log \left(\frac{a_{Ox}}{a_{Red}} \right) \quad (5.1)$$

where E^0 is the standard potential of the redox couple, R is the gas constant, T the temperature, n the amount of electrons involved in the half-reaction, F the Faraday constant, and a_X is the chemical activity of species X . When the potential η is increased (point 1), the reaction moves towards the formation of Fe^{3+} , *i.e.* the oxidation of Fe^{2+} , and an anodic current ($I > 0$) is created by the motion of the charges. A depletion in Red is created in the vicinity of the working electrode, and the width of this region increases as the potential increases, up to the point where the peak anodic current is reached (point 2). Here, the width of the depletion region in the electrolyte slows the diffusion of Red coming from the bulk electrolyte to fuel the oxidation reaction, and the current decreases, limited by the diffusion (point 3). When the scanning direction is reversed, the oxidation is less favored at the working electrode down to the point where the reduction current is majority (point 4). This whole dynamic explain the "duck-shape" in the $\eta > 0$ region. The same yields for the $\eta < 0$ region, only in this region the reduction is majority and the diffusion of the reducing species from the bulk of the electrolyte to the surface of the electrode limits the cathodic current (point 5).

When the working electrode is coated with a semiconductor, the situation changes. Due to the existence of forbidden energy states inside the gap of the semiconductor, the electronic exchanges happening during the oxydo-reduction reactions can only occur between the solution and the conduction band (electrons are exchanged) or the valence band (holes are exchanged). The elementary charge

A.2 Additional information on characterization techniques

transfer reactions read:



At equilibrium, the net current between the conduction band (resp. the valence band) and the electrolyte must be zero. An equilibrium exchange current J_C^0 (resp. J_V^0) can thus be defined as the current resulting from the exchange of electron from the electrolyte to the CB (resp. VB) or equally from the CB (resp. VB) to the electrolyte as:

$$J_C^0 = qk_1n_S^0[Ox] \quad (5.3a)$$

$$J_V^0 = qk_2p_S^0[Red] \quad (5.3b)$$

where k_1 and k_2 are the reaction rate constants in Equation (5.2a) and Equation (5.2d) respectively, n_S^0 and p_S^0 are the electron and hole surface concentrations at equilibrium, and [Ox] and [Red] are the concentrations of the oxidizing and reducing agents. When an overpotential η is applied, the current-tension characteristic can be described as:

$$J = \underbrace{J_V^0 \left(\exp\left(\frac{q\eta}{kT}\right) - 1 \right)}_{\text{oxidation current}} - \underbrace{J_C^0 \left(\exp\left(-\frac{q\eta}{kT}\right) - 1 \right)}_{\text{reduction current}} \quad (5.4)$$

The characteristic hence consists in two diodes of opposite direction. The reduction with the CB dominates the $\eta < 0$ region, while the oxidation with the VB dominates the $\eta > 0$ region. For an n-type semiconductor, $n_S^0 \gg p_S^0$ which implies that $J_C^0 \gg J_V^0$. Hence, higher voltages are required to drive the oxidation reactions (corresponding to the semiconductor being in inversion regime) (Figure A.1.b). These voltages are practically not reached in the cyclic voltammetry to avoid the degradation of the electrolyte, and only the $\eta < 0$ "duck" subsists.

A.2.2 Statistical analysis of the distribution of the perovskite grain size

This section aims at describing the methodology employed to estimate the mean size of the perovskite grain from SEM images, and at outlining the limits of these estimations. To ease the reasoning, Figure 3.6 is reproduced here (Figure A.2). Once the contours of the grains are enhanced (Figure A.2.c,d), ImageJ is used to measure the area of each grain.

The data are binned in intervals of 25 nm so that each interval is populated enough to allow for a consistent analysis. In both cases, the distribution is peaked around a mean value but is asymmetric with a longer tail towards larger grains. The distribution was modeled by a Weibull law which is superimposed on Figure A.2.c,d. Its probability density function is given by Equation (5.5):

$$f(x; \lambda, k) = \begin{cases} 0 & x < 0 \\ \frac{k}{\lambda} \left(\frac{x}{\lambda}\right)^{k-1} e^{-(x/\lambda)^k} & 0 \leq x \end{cases} \quad (5.5)$$

A.2 Additional information on characterization techniques

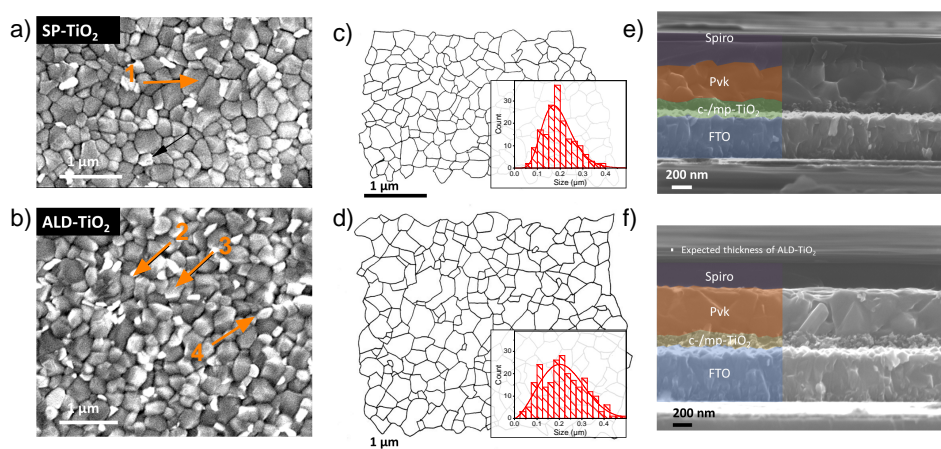


Figure A.2: Morphology of the perovskite on SP-TiO₂ (a,c,e) and ALD TiO₂ (b,d,f). a,b) Top surface SEM micrographs of the perovskite (magnification 25k). c,d) Contours of the grain boundaries for statistical analysis. The associated grain size distributions are given in the insets, fitted with a Weibull distribution. e,f) Cross sectional images with identification of the constitutive layers.

where λ and k are respectively the scale and shape factors of the distribution. Please note that the use of a Weibull distribution is not based on a theoretical justification, but is rather an empirical mean to model the grain size, as used in Z. Fang et al. (1993).

These results should be considered carefully for several reasons. 1) The size of a grain is defined here as the square-root of the measured area. This would be true if there were only square-shaped grains in the films which is not the case. However, since the shape of the grains is quite isotropic, the absolute values of the sizes should not be taken as real *per se*, but the mean size of a sample relative to another one has a meaning. 2) Both PbI₂ and perovskite grains are counted. If the attribution of a grain to one of these two sets can be quite easy (for instance grain 1 is clearly associated to the perovskite while grain 2 is associated to PbI₂), the labeling of other grains is less certain (*e.g.* grains 3 or 4). This uncertainty could be lifted if SEM images were combined with an EDS map. Such analysis was not performed in this study. Even if the grains were precisely sorted, the lead iodide grains lay mostly on top of the perovskite grains, which blurs the determination of the precise outlines of perovskite grains. Having that in mind, the low size tail of the distribution is probably slightly overestimated (PbI₂ grains are included) and the differences observed in the distributions are not significant enough to evidence a change in the morphology of the perovskite.

A.3 Additional experimental data

A.3.1 Fitting parameters of the PL spectra

Table A.1: Fitted parameters of the PL spectra presented in chapter 3 by the generalized Planck law. T and αd are set at 298 K and 20 respectively.

	Glass	SP-TiO ₂	ALD-TiO ₂
E_g (eV)	1.640	1.658	1.659
γ (meV)	62	67	66
θ (-)	2	2	2
$\Delta\mu$ (eV)	1.218	1.221	1.219
qV_{OV}^{rad} (eV)	1.418	1.437	1.436
PLQY (%)	0.041	0.023	0.022
Relative error (%)	3	2	3

A.3.2 Mean PV parameters of the cells based on ALD-TiO₂ and SP-TiO₂

Table A.2: PV parameters of five separate batches comparing cells based on ALD-TiO₂ or SP-TiO₂. The quantities are given for forward (roman font) and reverse (italic font) scans at 20 mV s⁻¹. The value and the uncertainty for each parameter are given as the median and MAD of the dataset respectively. The number of cells and the nature of the c-TiO₂ layer are given in the second column.

	Nb of cells	V _{OC} (mV)	J _{SC} (mA cm ⁻²)	FF (%)	PCE (%)
1	4	1069 ± 7	21.3 ± 0.2	72.2 ± 1.3	16.5 ± 0.5
	ALD	<i>1075 ± 7</i>	<i>21.4 ± 0.2</i>	<i>73.4 ± 0.2</i>	<i>16.9 ± 0.6</i>
	5	1070 ± 13	21.8 ± 0.1	59.6 ± 7.4	12.0 ± 0.3
	SP	<i>1080 ± 1</i>	<i>21.9 ± 0.1</i>	<i>74.4 ± 0.2</i>	<i>17.6 ± 0.1</i>
2	6	1099 ± 1	22.6 ± 0.1	73.0 ± 1.0	18.2 ± 0.3
	ALD	<i>1102 ± 1</i>	<i>22.5 ± 0.1</i>	<i>76.4 ± 1.0</i>	<i>18.9 ± 0.3</i>
	4	1080 ± 2	23.0 ± 0.1	70.8 ± 2.1	17.7 ± 0.5
	SP	<i>1084 ± 2</i>	<i>22.9 ± 0.1</i>	<i>73.9 ± 2.2</i>	<i>18.5 ± 0.5</i>
3	12	1021 ± 13	18.8 ± 0.2	61.1 ± 2.4	12.1 ± 0.5
	ALD	<i>1026 ± 11</i>	<i>18.6 ± 0.3</i>	<i>76.2 ± 0.9</i>	<i>14.6 ± 0.4</i>
	4	1001 ± 26	19.2 ± 0.1	59.5 ± 3.2	11.5 ± 1.1
	SP	<i>1005 ± 23</i>	<i>19.0 ± 0.2</i>	<i>74.6 ± 1.4</i>	<i>14.5 ± 0.8</i>
4	12	1055 ± 5	21.6 ± 0.2	68.7 ± 1.1	15.9 ± 0.2
	ALD	<i>1046 ± 10</i>	<i>21.5 ± 0.2</i>	<i>77.4 ± 8.7</i>	<i>17.7 ± 0.3</i>
	4	1034 ± 5	21.5 ± 0.2	65.5 ± 3.3	14.9 ± 0.7
	SP	<i>1023 ± 10</i>	<i>21.7 ± 0.2</i>	<i>77.4 ± 1.1</i>	<i>17.5 ± 0.5</i>
5	7	1056 ± 24	21.8 ± 0.4	61.4 ± 0.1	13.8 ± 1.5
	ALD	<i>1048 ± 18</i>	<i>21.6 ± 0.5</i>	<i>77.5 ± 5.7</i>	<i>12.7 ± 1.8</i>
	3	1072 ± 25	22.0 ± 0.5	71.5 ± 0.1	16.9 ± 0.8
	SP	<i>1069 ± 26</i>	<i>21.5 ± 0.5</i>	<i>62.1 ± 2.5</i>	<i>15.6 ± 0.2</i>

A.3.3 FTIR spectra of the free molecules

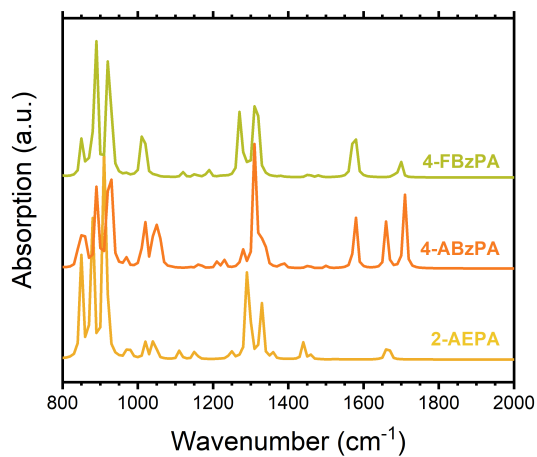


Figure A.3: DFT simulation of the FTIR spectra of the free molecules 2-AEPA, 4-ABzPA and 4-FBzPA, computed by P.Baranek.

A.3.4 Transmission spectra of Ref-pvk and AEPA-pvk

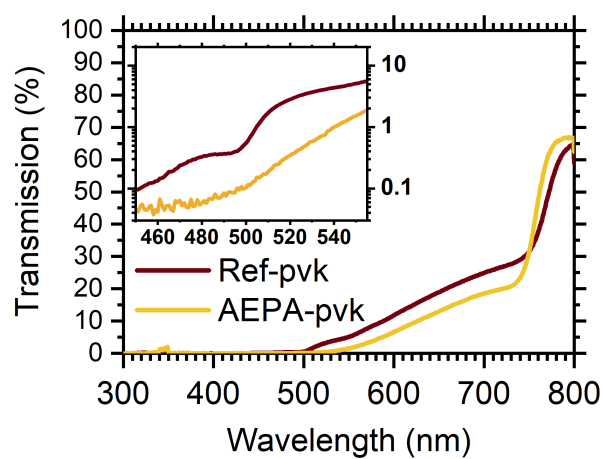


Figure A.4: Transmission spectrum of fresh Ref-pvk and AEPA-pvk. The inset is a magnification in log-scale of the PbI₂ absorption region.

A.4 List of conferences and publications

A.4.1 List of publications

Quantitative optical assessment of photonic and electronic properties in halide perovskite, *A. Bercegol, D. Ory, D. Suchet, S. Cacovich, **O. Fournier**, J. Rousset, L. Lombez*, Nat. Comm., 2019, DOI: 10.1038/s41467-019-09527-w.

ALD of ZnO:Ti: Growth Mechanism and Application as an Efficient Transparent Conductive Oxide in Silicon Nanowire Solar Cells, *D. Coutancier, S.T. Zhang, S. Bernardini, **O. Fournier**, T. Mathieu-Pennober, F. Donsanti, M. Tchernycheva, M. Foldyna, N. Schneider*, ACS App. Mat. Int., 2020, DOI: 10.1021/ac-sami.9b22973.

Chemical passivation of ZnO by phosphonic acid derivatives and its influence on halide perovskite interface, ***O. Fournier**, C. Darin-Bapaume, D. Messou, M. Bouttemy, P. Schulz, F. Ozanam, L. Lombez, J. Rousset, N. Schneider*, ACS Appl. En. Mat., 2021, DOI: 10.1021/acsaem.1c00612

A.4.2 List of international conferences

ICANS (2019): Chemical and Optoelectrical Modification of the Electron Transport Layer/Perovskite Interface Using Self Assembled Monolayers for Photovoltaic Devices, ***O. Fournier**, C. Darin Bapaume, D. Messou, J. Alvarez, L. Lombez, S. Béchu, M. Bouttemy, P. Schulz, N. Schneider, J. Rousset* (oral presentation)

MRS Fall (2019): Effect of the Integration of a Self-Assembled Monolayer in Perovskite Solar Cell on Passivation and Extraction, ***O. Fournier**, C. Darin Bapaume, D. Messou, J. Alvarez, L. Lombez, M. Bouttemy, P. Schulz, N. Schneider, J. Rousset* (oral presentation)

A.4.3 List of national conferences

RAFALD(2018): Versatile Perovskite Solar Cell Encapsulation by Low-Temperature ALD- Al_2O_3 with Long-Term Stability Improvement, *F. J. Ramos, T. Maindron, S. Béchu, A. Rebai, M. Frégnaux, M. Bouttemy, **O. Fournier**, J. Rousset, P. Schulz, N. Schneider* (poster)

RAFALD (2019): Integration of Titanium Oxide Deposited by ALD as Electron Transport Layer in Perovskite Solar Cells, ***O. Fournier**, E. Garel, A. Crisci, A. Mantoux, L. Lombez, J. Rousset, E. Blanquet, N. Schneider* (poster)

RAFALD (2019): Chemical and Optoelectrical Modification of ZnO deposited by Atomic Layer Deposition Using Self Assembled Monolayers for Perovskite Based Photovoltaic Devices, ***O. Fournier**, C. Darin-Bapaume, D. Messou, M. Bouttemy, P. Schulz, F. Ozanam, L. Lombez, J. Rousset, N. Schneider* (oral presentation)

Résumé des travaux de thèse

Introduction

Au cours des 50 dernières années - et encouragé par la publication de plusieurs rapports (tels que Meadows and Rome (1972)) - le concept de transition énergétique (ou crise énergétique) a gagné en importance dans la sphère politique, ainsi que dans l'opinion publique en réaction aux crises pétrolières consécutives et, plus récemment, au nombre croissant de rapports et d'études soulignant l'impact global de l'économie moderne, basée sur les combustibles fossiles, sur l'environnement. Après plusieurs années de recherches et de débats, il est désormais admis que le changement climatique observé, caractérisé par une augmentation progressive de la température globale (d'où l'appellation trompeuse de "réchauffement climatique"), est de nature anthropique, appuyé un large consensus dans la communauté scientifique (Cook et al. (2016)). Le changement climatique anthropique n'agit pas seulement à l'échelle évidente du climat, avec l'augmentation des événements climatiques extrêmes (tels que les vagues de chaleur, les sécheresses, les incendies de forêt, les tempêtes... Stott (2016)) ou la fonte accélérée de la cryosphère (Pörtner et al. (2019)). Il affecte également des questions d'ordre social et environnemental plus larges. Par exemple, l'impact du changement climatique sur les inégalités sociales est une question persistante aussi bien à l'échelle mondiale (entre les pays) qu'à l'échelle locale (au sein d'un pays, Islam and Winkel (2017)). Une prise de conscience globale des questions complexes liées au changement climatique s'est manifestée. Du côté des gouvernements, elle s'est traduite, entre autres, par l'organisation de la Conférence annuelle des Nations Unies sur le Changement Climatique ou la constitution du Groupe d'experts Intergouvernemental sur l'Evolution du Climat (GIEC). La multiplication des initiatives citoyennes - telles que les actions menées et les rapports fournis par des organisations non gouvernementales, ou l'organisation de manifestations en faveur de l'environnement (récemment : Fridays for Future ou les marches pour le climat) - montre également l'intérêt croissant de la population civile pour cette question. Ces efforts communs sans précédent soulignent l'urgence d'aborder les questions liées au changement climatique. Le GIEC fait régulièrement rapport sur divers sujets liés au changement climatique et fournit des conseils et des recommandations aux décideurs politiques. Il a produit en 2018 le "rapport spécial sur le réchauffement planétaire de 1,5°C" qui décrit les conséquences d'une augmentation de la température mondiale de 1,5°C ainsi que les mesures nécessaires pour limiter l'augmentation de la température à 1,5°C. L'une des principales conclusions est que, dans un scénario de *statu quo*, cet objectif serait dépassé avant

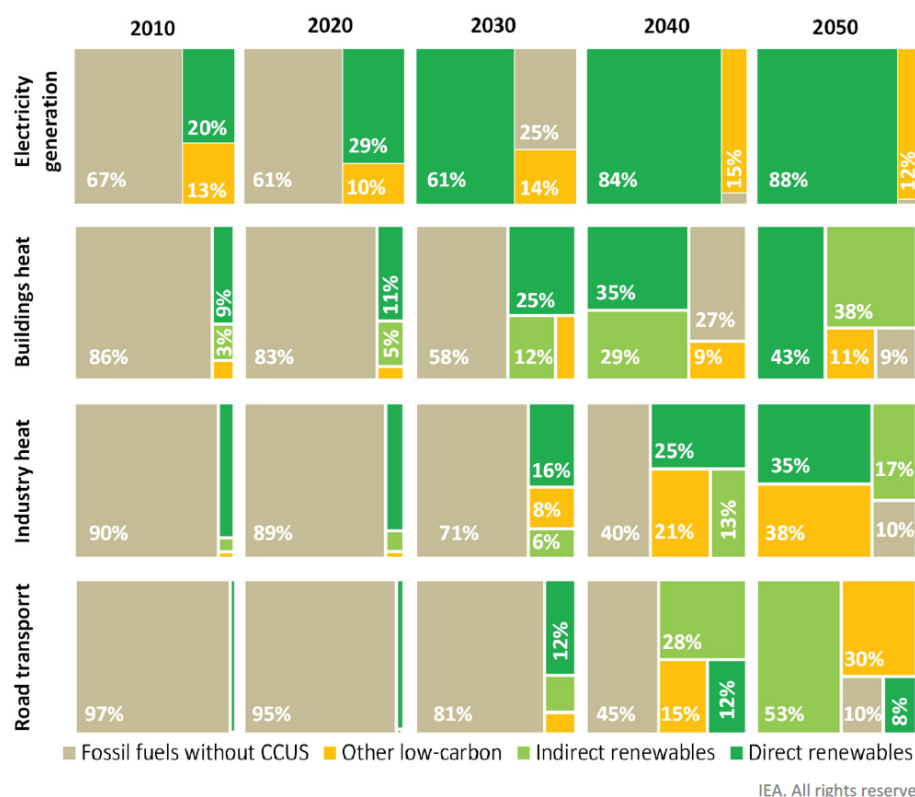


Figure R.1: Part des combustibles dans la consommation totale d'énergie pour certaines applications dans le scénario d'émissions nettes nulles. Notes : Énergies renouvelables indirectes = utilisation de l'électricité et du chauffage urbain produits par des énergies renouvelables. Autres énergies bas-carbone = énergie nucléaire, installations équipées de CCUS, hydrogène et carburants à base d'hydrogène bas-carbone. Adapté de IEA (2021).

2050. Suivre l'objectif fixé par les accords de Paris en 2015 - par lequel les pays ont convenu de "parvenir à un équilibre entre les émissions anthropiques par les sources et les absorptions par les puits de gaz à effet de serre dans la seconde moitié du siècle" - ne serait pas non plus suffisant et conduirait à une augmentation de 3°C d'ici 2100. Pour limiter l'augmentation de la température à 1,5°C, il faudrait essentiellement réduire les émissions nettes de CO₂ et atteindre une émission nette nulle d'ici 2050.

Cet objectif ambitieux - mais crucial - implique de réévaluer la façon dont la production et l'utilisation de l'énergie sont conçues. En préparation de la 26^e conférence des parties à la convention-cadre des Nations unies sur les changements climatiques, l'Agence Internationale de l'Énergie (AIE) a fourni une feuille de route indiquant les actions et les politiques à entreprendre pour atteindre effectivement l'objectif d'émission nette zéro (NZE) d'ici 2050 (IEA (2021)). Il est intéressant de noter que le rapport encourage explicitement une baisse immédiate des investissements dans les combustibles fossiles afin de limiter leur utilisation au strict

nécessaire, en combinaison avec la capture, l'utilisation et le stockage du carbone (CCUS). Le scénario NZE s'articule autour de plusieurs piliers : l'augmentation de l'efficacité énergétique, le changement des comportements et le développement de l'électrification, des énergies renouvelables, des technologies basées sur l'hydrogène, de la bioénergie et du CCUS. Les trois premiers piliers permettraient incidemment une diminution de la consommation totale d'énergie de 412EJ (1 EJ = 1018 J) en 2020 à 344EJ en 2050, soit un taux de croissance annuel moyen de -0,6%/an. Cette diminution de la consommation d'énergie n'entraverait pas nécessairement la croissance du produit intérieur brut (PIB) (même si des scénarios alternatifs sont discutés ailleurs dans le cadre de la théorie de la décroissance, Kallis et al. (2018)) en raison d'une diminution concomitante de l'intensité énergétique (considérée comme la quantité d'énergie nécessaire pour créer 1 point de PIB). Un aspect essentiel du NZE réside dans le changement du paradigme actuel de la production d'énergie avec un transfert progressif d'une production basée sur les combustibles fossiles vers une production d'énergie renouvelable dans tous les secteurs, comme le montre la [Figure R.1](#). La part des énergies renouvelables dans le bouquet énergétique du NZE devrait passer de 29% en 2020 à 88% en 2050, principalement grâce à l'augmentation de la capacité des centrales solaires photovoltaïques (PV) et éoliennes. Pour atteindre ces objectifs ambitieux, la capacité annuelle installée doit être multipliée par 5 et par 3 respectivement en 2030 par rapport aux capacités installées en 2020 (de 134 GW en 2020 à 630 GW en 2030 pour le solaire PV, de 114 GW en 2020 à 390 GW en 2030 pour l'éolien), et rester à ce niveau jusqu'en 2050.

Le solaire PV a le potentiel de concurrencer les sources d'énergie conventionnelles et renouvelables actuelles et donc de répondre à ces attentes. La pénétration du PV sur le marché de l'énergie est actuellement stimulée par d'importants ajouts nets de capacité en Chine, aux États-Unis et en Europe, qui représentent plus de 50% de la capacité ajoutée (IEA (2020)). D'autres marchés (notamment en Inde et au Moyen-Orient) devraient se développer et contribuer à l'augmentation de la capacité annuelle installée. Cependant, le développement de l'énergie solaire photovoltaïque dépend toujours fortement des réglementations et des politiques locales. Un rapport récent de l'Agence d'Information sur l'Énergie montre que la production d'énergie solaire photovoltaïque est l'une des sources d'énergie les plus attrayantes sur le plan économique, juste après la géothermie (EIA (2021)), avec un coût moyen de l'électricité (LCOE) de 30,43 2020-USD par MWh pour les ressources entrant en service en 2026 à grande échelle (incluant les crédits d'impôts). Des LCOE aussi bas peuvent être atteints grâce à la diminution constante des prix de vente des modules à mesure que la livraison cumulée de modules augmente. La courbe d'apprentissage est présentée [Figure R.2.a](#). Le taux d'apprentissage de 23,8% jusqu'en 2006 a augmenté de 40% depuis 2006, ce qui favorise l'accélération de l'intégration du solaire PV dans le mix énergétique mondial. La diminution des coûts du PV grâce aux économies de production de masse est un moyen de rendre le PV plus attractif. Une autre façon d'y parvenir est d'augmenter l'efficacité des modules, ce qui accroît la production potentielle d'électricité par unité de surface. Selon les prévisions de la 12^e édition de la feuille de route internationale pour le PV (ITRPV), le marché du PV sera encore fortement dominé par les cellules au Si basées sur une jonction p-n diffusée et passivée (PERC/PERL/PERT/TOPCON),

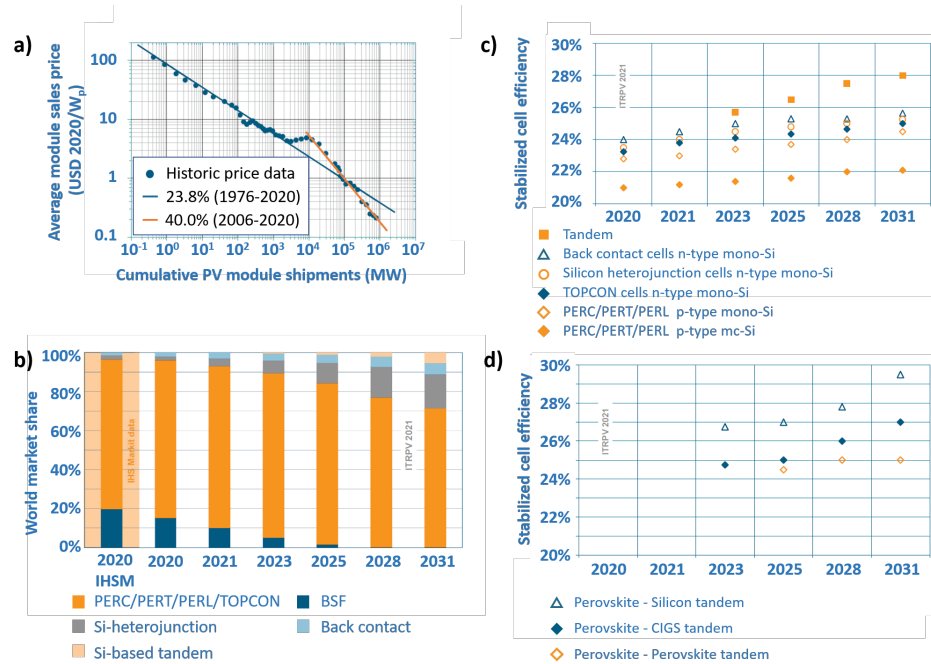


Figure R.2: Projection de l’ITRPV sur le marché des modules solaires PV. a) Courbe d’apprentissage du prix de vente des modules photovoltaïques en fonction des expéditions cumulées de modules PV. b) Composition prévue du marché des modules PV en termes de technologie. c) Efficacités prévues des modules photovoltaïques produits en série en fonction de la technologie. d) Efficacités prévues des modules photovoltaïques produits en série pour diverses technologies tandem. Adapté de Fisher et al. (2021).

représentant encore plus de 70% de la part de marché en 2031 (Figure R.2.b). En fonction de la technologie Si considérée, les rendements actuels des modules en production de masse varient entre 21% et 24%, et devraient plafonner à 25,5% d’ici 2031 (Figure R.2.c). Une autre façon d’augmenter l’efficacité des modules consiste à développer des technologies tandem. Ces types de modules consistent en différentes cellules solaires empilées les unes sur les autres, dans le but de récolter le rayonnement solaire de manière plus efficace. Le lecteur est invité à consulter H. Li and Wei Zhang (2020) pour plus de détails sur cette question. L’ITRPV prévoit l’introduction de modules solaires tandem sur le marché dès 2023, avec un rendement de départ d’environ 25,5%, qui passera à plus de 28% en 2031 (augmentation relative de +12% par rapport aux simples jonctions Si) (Figure R.2.d). Selon les prévisions de l’ITRPV, toutes les technologies tandem industrielles prometteuses reposent sur une cellule supérieure à base de pérovskite (Fisher et al. (2021)). D’autres solutions basées sur des technologies CuInGaSe₂ (CIGS) ou III-V sur silicium à large bande interdite sont en cours de développement à l’échelle du laboratoire, mais manquent encore en termes d’efficacité de conversion ou de rentabilité économique.

Les cellules solaires à base de pérovskite sont une technologie révolutionnaire

en couche mince dont le développement a été extrêmement rapide : le rendement des cellules à l'échelle du laboratoire a été rapporté pour la première fois en 2009 à 3,8% (Kojima et al. (2009)), et a depuis régulièrement augmenté pour atteindre 25,5% en 2021 (J. Jeong et al. (2021)). Le développement de la production à l'échelle industrielle de modules pérovskites (en configuration tandem ou simple jonction) a rapidement suivi, soutenu par l'émergence de start up dédiées (Oxford PV, Saule Technology...) et les récents investissements massifs des fabricants de PV (15 millions de dollars levés par GCL pour le développement d'une ligne de production de masse *GCL's fund raising* (2021)). Cette classe de matériaux est basée sur une chimie hybride organique-inorganique et englobe une grande variété de matériaux. Leurs propriétés opto-électriques peuvent être ajustées en fonction de l'application souhaitée, allant des cellules à faible bande interdite pour les jonctions simples flexibles aux cellules à grande bande interdite pour les cellules supérieures en tandem. Les cellules solaires à base de pérovskite peuvent être développées à basse température (généralement $\leq 200^\circ\text{C}$) par une grande variété de procédés, et présentent une tolérance intéressante aux défauts. En dehors de ces formidables atouts, un certain nombre de questions doivent encore être réglées pour exploiter le plein potentiel de cette technologie. Les principaux défis consistent en :

- (i) la poursuite de l'optimisation de l'architecture des cellules pour atteindre des rendements encore plus élevés (limite théorique autour de 30%, selon la composition de la pérovskite) ;
- (ii) minimiser les pertes pendant la transition des cellules à l'échelle du laboratoire aux modules commerciaux ;
- (iii) assurer la stabilité des cellules pour répondre aux attentes normatives.

Cette thèse se concentre sur la synthèse et la caractérisation d'une couche constitutive d'une cellule solaire pérovskite (PSC) appelée couche de transport d'électrons (ETL, ou contact sélectif de type n). Cette couche est généralement un oxyde à large bande interdite – largement abordé dans ce manuscrit – ou une couche organique semi-conductrice. Le dépôt chimique en phase vapeur à flux alternés (ALD) a été choisi pour synthétiser ces contacts sélectifs. Il présente plusieurs atouts au regard des défis évoqués précédemment. L'ALD est une technique de dépôt qui est déjà utilisée à l'échelle industrielle (aidant à la résolution du défi (ii)). Elle permet de déposer dans des conditions douces ($P \sim 1\text{mbar}$, $T \leq 200^\circ\text{C}$) des couches très fines mais conformes avec un contrôle possiblement sub-nanométrique de leur épaisseur, tout en assurant une bonne homogénéité des couches. De plus, la composition du film peut être finement contrôlée (contribuant à relever les défis (i) et (iii)). La synthèse (ALD et réalisation de la cellule) et la plupart des caractérisations des cellules ont été réalisées à l'Institut Photovoltaïque d'Île-de-France (IPVF, Palaiseau, France). Des caractérisations complémentaires ont été effectuées à l'Institut Lavoisier de Versailles (Versailles, France) et au Laboratoire de Physique de la Matière Condensée (Palaiseau, France).

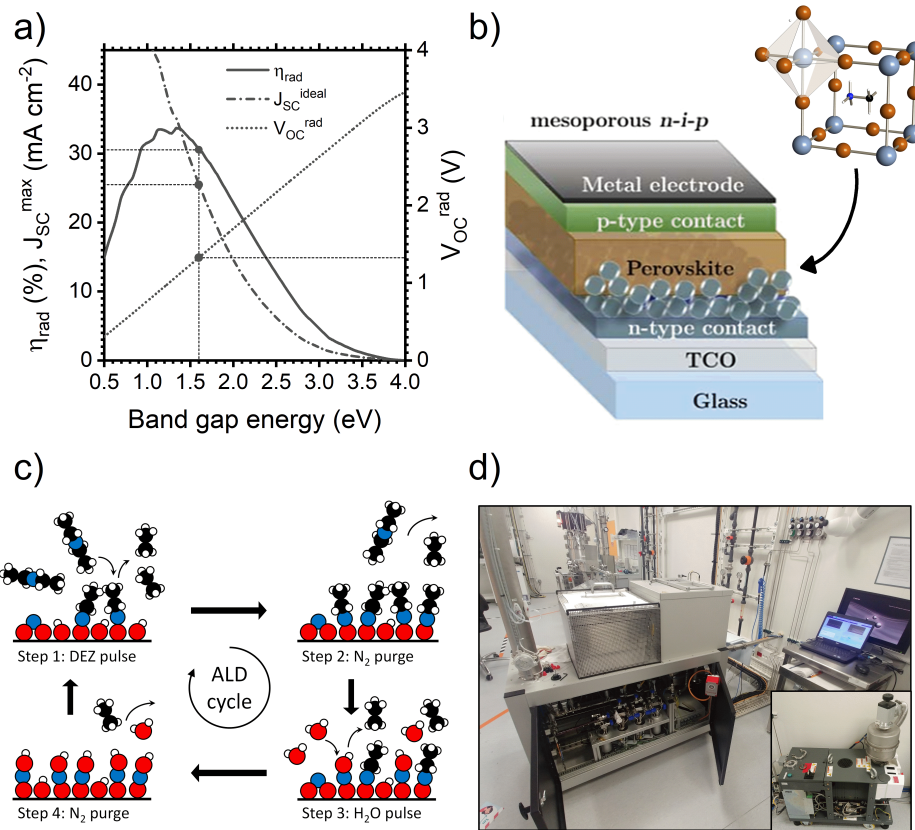


Figure R.3: a) Limites théoriques des paramètres PV d'une simple jonction dans la limite de Shockley-Queisser. Les valeurs limites pour un semiconducteur de gap 1.6 eV sont reportés sur les ordonnées. b) Architecture classique mésoporeuse d'une cellule solaire à base de pérovskite, et structure cristalline cubique d'une pérovskite (adapté de Kegelmann (2019)). c) Représentation schématique d'un cycle ALD entre le diéthyl Zn et H₂O pour former du ZnO. d) Photographie du réacteur Beneq TFS-200 utilisé durant cette thèse. L'insert est une photographie de la pompe.

Chapitre 1 : Introduction Générale

Dans ce chapitre d'introduction, les principes de base de la physique des cellules solaires tels que la génération et le recombinaison de charges dans un semiconducteur ont été présentés. A partir de considérations thermodynamiques, les paramètres ultimes d'un convertisseur PV et d'une cellule solaire à simple jonction ont été déterminés (Figure R.3.a). Ces derniers servent à estimer dans quelle mesure les dispositifs réels s'écartent de leurs performances optimales, et aident à identifier les limitations de la cellule.

Les principales propriétés de la pérovskite hybride organique-inorganique ont

été discutées. Les propriétés opto-électriques de ces matériaux ont été comparées à celles d'autres semi-conducteurs et leurs variations en fonction de la composition chimique de la pérovskite ont été discutées. En raison de la bonne absorption, de la faible énergie des excitons et de la longueur de diffusion des porteurs de l'ordre du μm , les matériaux pérovskites sont appropriés pour être intégrés dans des architectures à couches minces (Figure R.3.b). Malgré les multiples atouts des cellules solaires à pérovskite, des défis restent à relever (montée en gamme, stabilité, augmentation de l'efficacité) pour favoriser l'entrée des dispositifs solaires à base de pérovskite sur le marché mondial.

Enfin, les grands principes du procédé ALD ont été présentés sur la base de l'exemple prototypique du dépôt de ZnO à partir de DEZ et de H₂O (Figure R.3.c). La définition des différentes étapes des cycles ALD a été expliquée et la notion de réactions de surface autolimitées a été illustrée. L'évolution des représentations schématiques de l'ALD au fil des années a également été présentée et a permis d'appréhender les subtilités du procédé, au-delà de la conception naïve de dépôt "couche atomique par couche atomique". Les procédés émergents dérivés du processus ALD (par exemple l'ALD spatial, l'ALD sélective et la gravure ALE) ont également été présentés et soulignent la diversité des applications des techniques ALD. Les spécificités du réacteur Beneq TFS-200 – et notamment le moyen de transporter des précurseurs de faible volatilité – ont enfin été présentées (Figure R.3.d).

Chapitre 2 : Méthodes et procédés

Le développement du TiO₂ et SnO₂ par ALD en utilisant diverses combinaisons de précurseurs a été présenté. Ces matériaux n'étaient pas connus à l'IPVF au début de la thèse et ont nécessité une optimisation minutieuse du processus de déposition pour obtenir des recettes performantes. Pour chaque matériau, un précurseur pour l'espèce métallique (tetrakis(diméthylamino)Sn - TDMASn, Ti tetra(isopropoxide) - TTIP) et deux précurseurs pour l'oxygène (H₂O et H₂O₂) ont été étudiés. En raison de la faible volatilité des précurseurs organométalliques utilisés, le transport de ces précurseurs de leur réservoir à la chambre de réaction a été optimisé en combinant un chauffage du réservoir et un transport des précurseurs assisté par gaz (en utilisant N₂).

Le processus ALD a été reconnu comme tel par des études de microbalance à quartz pour toutes les combinaisons de précurseurs grâce à l'identification des réactions de surface auto-limitantes. Pour le TiO₂, une fenêtre ALD avec H₂O est trouvée entre 100°C et 210°C, alors qu'aucune fenêtre ALD évidente n'a pu être déterminée avec H₂O₂. Pour le SnO₂, il n'y avait de fenêtre ALD dans aucun cas, mais l'épaisseur déposée par cycle (GPC) en fonction de la température de dépôt du procédé H₂O était plus élevée que celle du procédé H₂O₂.

La caractérisation des films déposés avec le TTIP a révélé dans les deux cas la formation d'un film de TiO₂ dont la stoechiométrie a été confirmée par des mesures de spectroscopie des photoélectrons X (XPS). Une différence notable réside dans la forme du spectre haute résolution C1s, qui peut indiquer une

contamination différente du film en fonction du couple de précurseurs utilisé (soit dû à une contamination de surface, soit dû à une contamination par des fragments de précurseurs ALD). Lors de la croissance à partir de H_2O_2 , le film déposé est un matériau amorphe à large bande interdite (3,6eV) avec une bonne transparence dans le domaine visible. Lorsqu'il est crû à partir de H_2O , le film déposé a des propriétés similaires mais passe de la phase amorphe à la phase anatase à partir d'une épaisseur spécifique (18 nm à 200°C). En ce qui concerne les caractérisations du procédé et du matériau, la température de dépôt du TTIP/ H_2O a été fixée à 200°C (GPC = 0,35Å/cycle), tandis que celle du procédé TTIP/ H_2O_2 a été fixée à 100°C (GPC = 0,7Å/cycle).

La caractérisation du film déposé avec TDMASn a montré de grandes différences en fonction de la source d'oxygène utilisée. L'utilisation de H_2O donne un matériau de type p faiblement dopé avec une bande interdite optique étroite (2,6eV), relativement résistif et avec des propriétés structurales proches de celles de la phase romarchite de SnO , ne convenant pas à l'application prévue comme couche de transport de charge. L'utilisation de H_2O_2 permet d'obtenir un matériau de type n, avec une bande interdite plus large (4,2eV), garantissant une excellente transmission dans le domaine visible, et des propriétés structurales proches de celles de la phase rutile du SnO_2 . Ce dernier film a été étudié par XPS, qui révèle une contamination du film par des ligands DMA et des groupes -OH, et confirme la stœchiométrie SnO_2 du film. En ce qui concerne les caractérisations du procédé et du matériau, la température de dépôt a été fixée à 100°C pour le procédé TDMASn/ H_2O_2 (GPC = 1,8Å/cycle).

Chapitre 3 : Intégration du TiO_2 par ALD

L'intégration de l'ALD- TiO_2 comme substitut à la couche compacte traditionnelle de TiO_2 déposée par pyrolyse d'aérosol (SP- TiO_2) dans une architecture mésoporeuse a été étudiée (Figure R.4.a). En raison de l'étape nécessaire de recuit de la couche mésoporeuse à 500°C, le comportement de la couche ALD- TiO_2 après recuit à l'air à différentes températures jusqu'à 500°C a été caractérisé. Les propriétés de l'ALD- TiO_2 après recuit étaient proches de celles du SP- TiO_2 . Le recuit n'a pas affecté les propriétés optiques des couches ALD- TiO_2 de différentes épaisseurs. Il tend à homogénéiser leurs propriétés structurales (toutes les couches cristallisent dans la phase anatase). La voltampérométrie cyclique a montré que la couverture et la conformité de l'ALD- TiO_2 tel que déposé étaient suffisantes pour bloquer efficacement les trous pour des épaisseurs aussi faibles que 5nm. La cristallisation induite par le recuit est accompagnée d'une réduction de l'épaisseur du film. Celle-ci induit probablement la formation de piqûres dans les films plus fins, réduisant ainsi leur capacité à bloquer les trous.

L'homogénéité des deux méthodes de dépôt a également été évaluée en comparant la transmission de la couche sur environ 15x15 cm² (Figure R.4.b). Le SP- TiO_2 s'est avéré avoir une homogénéité plutôt mauvaise sur cette surface, attribuée à des variations dans le processus de dépôt (manuel) et dans l'aérolique. À l'inverse, le TiO_2 ALD a montré une bonne homogénéité, ce qui est à corrélérer avec les atouts connus du procédé ALD en terme de conformité et d'homogénéité. Cela indique

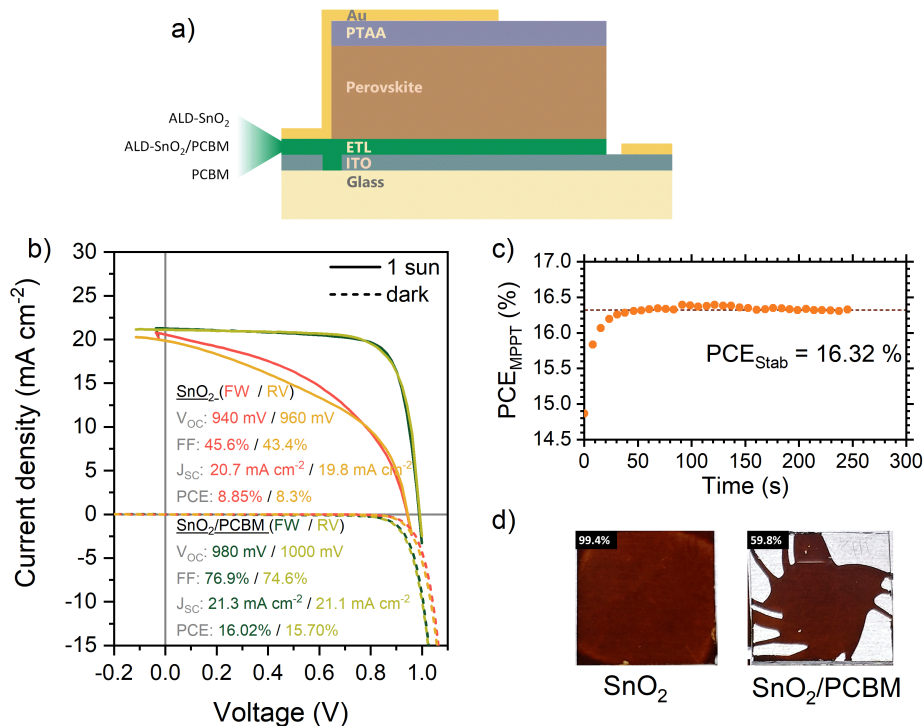


Figure R.5: a) Représentation schématique de l'architecture de cellules utilisée lors de l'étude de l'ALD-SnO₂. b) Caractéristiques IV sous illumination (1 soleil) et dans le noir de la meilleure cellule basée sur ALD-SnO₂ et de la meilleure cellule basée sur SnO₂/PCBM. c) Efficacité de conversion stabilisée sous une illumination d'un soleil pour la meilleure cellule basée sur une bichouche SnO₂/PCBM. d) Différence de couverture de la pérovskite sur un substrat de SnO₂ ou de SnO₂/PCBM.

ALD-TiO₂ était plus défectueuse, ce qui explique le faible V_{OC} des dispositifs planaires avec du ALD-TiO₂.

Chapitre 4 : Intégration du SnO₂ par ALD

Des architectures planaires de cellules solaires à base de pérovskite ont également été réalisées à l'aide d'ALD-SnO₂ comme ETL (Figure R.5.a). Les variations des propriétés de l'ALD-SnO₂ lors du recuit ont été étudiées. Pour une température de recuit modérée (180°C), les propriétés du SnO₂ ne varient pas beaucoup, quelle que soit l'épaisseur de la couche. A des températures plus élevées (à partir de 300°C), la couche cristallise en phase rutile et l'épaisseur du film diminue de 20%.

L'ALD-SnO₂ a été intégré dans des dispositifs solaires complets. L'influence de la température de dépôt ALD et de la température de recuit a été discutée. La variabilité des paramètres PV est accrue pour des températures de dépôt plus élevées, ce qui a été attribué à une homogénéité réduite du dépôt ALD à haute température. Le dépôt de SnO₂ à 100°C donne des dispositifs fonctionnant raisonnablement et

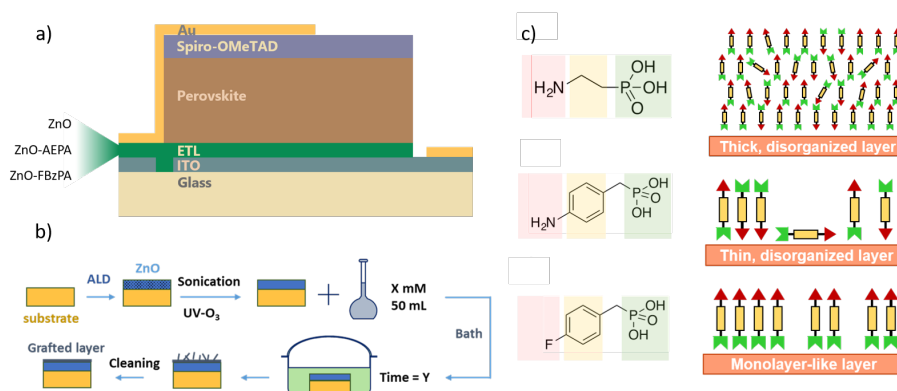


Figure R.6: a) Représentation schématique de l'architecture de cellules utilisée lors de l'étude de l'ALD-ZnO. b) Représentation schématique du procédé de greffage développé durant la thèse. c) Formule développée des trois molécules étudiées et représentation schématique de l'organisation de la couche greffée à la surface du ZnO pour chaque molécule.

permet le dépôt de l'ETL dans des conditions douces. La variation de la température de dépôt a montré un optimum à 180°C. A des températures plus élevées, le V_{OC} diminue drastiquement ce qui - conformément à la littérature - peut être attribué au début de la transition de phase du SnO_2 amorphe au rutile.

Les cellules basées uniquement sur l'ALD- SnO_2 ont montré un J_{SC} raisonnable (environ 20 mA cm^{-2}) mais un V_{OC} légèrement bas et un FF très bas par rapport à la littérature. Pour résoudre ce problème, une bicouche composée d'ALD- SnO_2 et de PCBM a été étudiée. Cette bicouche a permis d'augmenter le FF d'environ 45% à plus de 75%, de sorte qu'un meilleur rendement de 16,3% est atteint (Figure R.5.b,c). Cependant, le dépôt de la pérovskite sur le PCBM est entravé par la moins bonne couverture de la pérovskite sur le PCBM, attribuée à une moins bonne mouillabilité de la pérovskite sur le PCBM hydrophobe (Figure R.5.d). Plusieurs stratégies ont été proposées pour répondre à ce problème. L'ajout d'une étape de pré-mouillage de la couche de PCBM avec du DMF a permis d'augmenter la mouillabilité de la pérovskite à un niveau satisfaisant sans dégrader les performances des cellules.

Enfin, une étude de l'influence de l'épaisseur de la couche de SnO_2 dans la configuration bicouche SnO_2/PCBM est proposée. De manière similaire aux résultats obtenus pour le TiO_2 , l'épaisseur n'a qu'une faible influence jusqu'à une épaisseur seuil (environ 15nm) où la résistance série limite le dispositif.

Chapitre 5 : Passivation de l'interface ZnO/pérovskite

Enfin, l'intégration du ZnO a été étudiée (Figure R.6.a). Le ZnO possède des propriétés optoélectroniques adéquates pour servir d'ETL dans une cellule solaire à pérovskite, mais tend à déclencher une dégradation rapide de pérovskite contenant du MA par des réactions acide-base, comme rapporté de multiples fois dans la littérature et observé dans cette thèse. Une stratégie de passivation basée sur le greffage de dérivés d'acides phosphoniques a été proposée. Trois

molécules différentes ont été testées : l'acide 2-aminoéthylphosphonique, l'acide 4-aminobenzylphosphonique et l'acide 4-fluorobenzylphosphonique, différant par leur espaceur (cycle aromatique ou chaîne alkyle) et leurs groupes de queue (groupe amine ou fluor). La conception des molécules a été pensée de manière à ce que le greffage sur l'oxyde se fasse par le biais du groupe phosphonique, et que les groupes de queue puissent remédier aux défauts de surface de la pérovskite grâce à leur coordination avec le plomb sous-coordonné. La procédure de greffage proposée repose sur une étape de trempage à atmosphère et température ambiantes dans des solvants non toxiques (Figure R.6.b).

Des techniques de caractérisation sensibles à la surface (angle de contact, XPS et ATR-FTIR) ont permis d'évaluer la présence des molécules à la surface du ZnO et l'efficacité de cette procédure de dépôt. Une caractérisation supplémentaire par ARXPS a donné un aperçu de la structure de la couche greffée qui a été reliée à la structure de la molécule (Figure R.6.c). Le 4-ABzPA et le 4-FBzPA ont formé des films très minces, par rapport au 2-AEPA. De plus, la couche de 4-FBzPA a présenté une structure proche de celle d'une monocouche auto-assemblée, avec une orientation préférentielle du fluor vers l'extérieur. Cette meilleure organisation a été attribuée à deux effets : l'empilement $\pi - \pi$ des cycles benzyle qui renforce l'organisation de la couche, et la faible affinité du fluor envers le ZnO qui permet de maintenir les molécules orientées dans la même direction. D'autre part, les molécules à base d'amine n'ont pas montré une organisation spécifique à la surface du ZnO, attribuée à une possible interaction compétitive entre les groupes amine et phosphonique pendant le processus de greffage.

Les effets des molécules sur la croissance de la pérovskite ont été caractérisés d'un point de vue morphologique et structurel. La pérovskite déposée sur du ZnO ou sur du ZnO-FBzPA a montré une structure et une morphologie dégradées avec l'apparition d'une phase de PbI_2 juste après la synthèse, caractéristique du processus de dégradation acido-basique, alors que la pérovskite déposée sur du 2-AEPA présente de bonnes caractéristiques. Le manque de passivation efficace du 4-FBzPA est attribué à une couverture incomplète de ZnO. L'intégration dans des dispositifs complets a confirmé ces observations. Les cellules basées sur le ZnO ont montré des paramètres PV très faibles avec un PCE maximum de 2.2%. Les cellules basées sur le 2-AEPA ont montré une augmentation du $V_{OC} = 1004$ mV (meilleure cellule) indiquant une passivation chimique efficace mais un J_{SC} très faible attribué à une épaisseur excessive de la couche de molécules. Les cellules basées sur le 4-FBzPA ont eu globalement les meilleures efficacités (4.1% au maximum) en raison d'un J_{SC} plus élevé que les cellules basées sur le ZnO, mais limité par un V_{OC} comparable (environ 760 mV) en accord avec la couverture incomplète du ZnO par le 4-FBzPA.

Conclusion

L'objectif de cette thèse était de développer et de caractériser des couches inorganiques de transport d'électrons pour des applications de cellules solaires à bas de pérovskite. Deux matériaux – SnO_2 et TiO_2 – ont été développés par ALD à l'IPVF et intégrés dans différentes architectures de cellules solaires à base de

pérovskite (architectures mésoporeuses ou planaires). L'effet d'une modification de l'interface entre le ZnO et la pérovskite par de petites molécules organiques a également été étudié. Les principaux résultats liés à ces sujets ont été résumés dans les sections précédentes. Ce travail a aussi été l'occasion de questionner l'efficacité et les limites de la méthodologie employée, et d'ainsi identifier les obstacles au développement rapide d'une nouvelle architecture de cellules solaires à base de pérovskite. Au cours de cette thèse, deux nouveaux matériaux ont été développés par ALD pour un total de quatre procédés (chaque matériau a été développé à partir de deux sources d'O différentes). Deux de ces procédés ont ensuite été caractérisés de manière approfondie dans des dispositifs complets de cellules solaires. Au regard de l'expérience acquise au cours de ces trois ans, il apparaît clairement que même l'adaptation d'un protocole de synthèse rapporté dans la littérature - dans ce cas d'un procédé ALD - n'est pas simple. Les spécificités des conditions du laboratoire, du réacteur et de la qualité du lot de précurseur influencent tous le développement du nouveau matériau. Le fait que les propriétés des matériaux ALD puissent varier dans de grandes proportions d'un groupe à l'autre (Niemelä et al. (2017); Nazarov et al. (2015)) tout en utilisant les mêmes précurseurs soutient ce constat. Du point de vue de l'intégration dans des dispositifs complets, la production de résultats significatifs est entravée par la grande variabilité des propriétés des cellules. Cette variabilité peut être attribuée à plusieurs facteurs :

- le grand nombre d'étapes composant la synthèse d'un dispositif complet (du nettoyage des substrats au dépôt des différentes couches et à la mise en contact finale), multipliant les sources de variabilité.
- l'importance considérable des états interfaciaux du substrat sur la qualité des couches déposées (surtout pour l'ALD et pour le dépôt de la pérovskite) qui varient en fonction des conditions du laboratoire (humidité notamment).
- les nombreux processus de dégradation qui peuvent affecter la cellule (humidité, migration ionique, diffusion de l'électrode...).
- Les effets individuels de ces mécanismes peuvent être difficiles à identifier, pouvant cacher l'effet spécifique étudié au cours d'une expérience (par exemple la modification de l'épaisseur de la couche de transport).
- la plupart du procédé de synthèse repose encore sur des étapes de dépôt manuel dont la qualité peut varier d'un lot à l'autre.

Pris ensemble, ces facteurs nécessitent donc de produire une quantité importante d'échantillons afin de pouvoir tirer des conclusions fiables sur une expérience spécifique, comme le montrent les intégrations d'ALD-TiO₂ et d'ALD-SnO₂ présentées dans ce travail. Comme indiqué par Schulz et al. (2019), les récentes avancées effectuées dans les architectures de cellules solaires à base de pérovskite sont la plupart du temps empiriques, même si les connaissances fondamentales sur les dispositifs complets s'accumulent lentement. L'optimisation de l'extraction des charges est un processus difficile, pour lequel la question de l'alignement des bandes est souvent considérée comme critique. Il est toutefois compliqué de prédire l'architecture appropriée à partir des positions des bandes mesurées sur des couches simples ou calculées par simulation, en raison de l'influence conjuguée du substrat et de

l'absorbeur pérovskite sur ces positions de bandes (Miller et al. (2014)). Toutes ces propriétés interfaciales sont critiques pour atteindre des efficacités et une stabilité plus élevées, mais difficiles à sonder sans endommager les matériaux ou en modifier les propriétés. En résumé, le développement et la synthèse de nouveaux matériaux - même s'ils s'appuient sur des connaissances théoriques et des procédés rapportés - peuvent être décrits comme un processus fastidieux d'essais et d'erreurs, qui prend du temps pour atteindre la maturité.

Perspectives

Cette thèse ouvre plusieurs perspectives concernant la synthèse, la mise à l'échelle industrielle, la caractérisation et la compréhension des dispositifs. Du point de vue de la synthèse, de nouveaux ETLs peuvent être synthétisés par ALD à partir des matériaux qui ont été présentés. L'ALD permet un dopage contrôlé des couches minces. Ceci peut être utilisé afin de modifier les propriétés électriques de l'ETL (par exemple l'incorporation de Nb dans le SnO_2). Des nanolaminés de différents matériaux peuvent également être un moyen d'utiliser le contrôle nanométrique du processus ALD, comme cela a été mis en œuvre par Bush et al. (2017) avec ZnO et SnO_2 . Le TiO_2 nouvellement développé peut également trouver une application utile en conjonction avec de l' Al_2O_3 pour élaborer des nanolaminés efficaces à des fins d'encapsulation. L'utilisation de molécules telles que celles décrites au chapitre 5 fournit un moyen facile de modifier rapidement l'interface entre l'ETL et la pérovskite et peut être adaptée à d'autres ETL que le ZnO , avec des conceptions de molécules plus complexes pour ajuster la chimie et les propriétés électroniques de l'interface. Ce travail a principalement exploré l'application des films minces d'ALD déposés avant la couche de pérovskite (par exemple, l'ETL dans les architectures n-i-p). Cependant, en raison des conditions de dépôt douces qui peuvent être atteintes (vide primaire et $T_{\text{dep}} \leq 100^\circ\text{C}$), l'ALD est compatible avec le dépôt de films minces par-dessus la couche de pérovskite (par exemple l'ETL dans les architectures p-i-n), ce qui peut constituer une alternative prometteuse aux couches extractrices organiques habituellement utilisés au-dessus de la pérovskite.

Dans une perspective de passage à l'échelle industrielle, l'utilisation de l'ALD permet le dépôt de couches homogènes et reproductibles, qui sont des paramètres clés pour limiter les pertes électriques dans les cellules et modules à grande échelle. L'adaptabilité de la technologie ALD à une grande variété de substrats, quelle que soit leur rugosité, est également un atout essentiel pour la production de cellules solaires tandem sur Si, puisqu'elle permet le dépôt d'une couche sélective conforme, même sur du Si texturé. Avec le développement rapide de l'ALD spatiale, le développement et l'intégration d'oxydes ALD tels que le SnO_2 et le TiO_2 par cette méthode de dépôt sont également des perspectives clés à étudier.

Il est essentiel d'élargir le catalogue d'ETL disponibles afin de mieux comprendre l'interaction entre la pérovskite et les couches d'extraction, qu'il s'agisse de changer le matériau ou la méthode de dépôt. Ceci donne une plus grande latitude pour élaborer et tester des modèles pour le transport des porteurs de charge à travers les interfaces dans les cellules solaires à pérovskite, qui est identifié comme l'un des

freins pour atteindre des rendements encore plus élevés. Le renforcement de ces modèles repose également sur le développement de méthodes de caractérisation innovantes pour obtenir des informations sur les propriétés interfaciales ou les propriétés de transfert de charges. La combinaison de la spectrométrie d'émission optique à décharge lumineuse (GD-OES) et de l'XPS peut être un outil puissant pour étudier l'état chimique d'une interface enfouie dans une couche épaisse de pérovskite (épaisse pour l'XPS, c'est-à-dire plus de quelques dizaines de nm) et décrypter les interactions chimiques entre la pérovskite et son substrat dans des architectures réalistes. Enfin, le développement de nouvelles méthodes et modèles d'imagerie PL basés sur l'acquisition d'images de fluorescence hyperspectrales et résolues en temps est très prometteur. Ces techniques présentent des caractéristiques clés bénéfiques à la compréhension des phénomènes de transport à travers les interfaces : une bonne résolution spatiale, temporelle et spectrale ; une haute sensibilité de la photoluminescence aux défauts ; une diversité de conditions expérimentales possibles telles qu'un biais lumineux ou électrique supplémentaire, des observations in operando, un vieillissement dans différentes atmosphères...

RÉSUMÉ

L'intérêt éveillé par les cellules solaires à base de pérovskite dans la communauté photovoltaïque (PV) est allé grandissant ces 10 dernières années, dû notamment aux excellentes propriétés opto-électroniques de ces matériaux, à la diversité de leurs applications potentielles et à leur attractivité économique. Cette technologie est attendue sur le marché du PV d'ici 2023, mais certains défis tels que la stabilité des cellules ou le passage à l'échelle industrielle restent à relever afin de garantir son industrialisation. Une stratégie consiste à optimiser les couches extractrices de charges qui doivent garantir une bonne sélectivité vis-à-vis des porteurs de charge et assurer une bonne interface avec la pérovskite. Le dépôt chimique en phase vapeur à flux alternés (*Atomic Layer Deposition* – ALD) est une méthode de dépôt industrielle permettant la synthèse de nombreux matériaux. Les films minces déposés par ALD sont denses, homogènes, sans piqûres, conformes, et leur épaisseur et leur composition peuvent être contrôlées à l'échelle nanométrique. L'ALD apparaît donc comme un candidat idéal pour déposer ces couches extractrices de charges. Cette thèse s'est intéressée au développement et à la caractérisation de divers oxydes par ALD. Le SnO₂ et le TiO₂ ont été développés à l'Institut Photovoltaïque d'Île-de-France (IPVF) à partir de deux procédés pour chaque matériau. A partir des caractérisations des couches minces obtenues, un procédé a été retenu pour chaque matériau en vue d'une intégration dans un dispositif PV en tant que couches inorganiques extractrices d'électrons. L'intégration d'une couche compacte de TiO₂-ALD (15 nm) dans une architecture mésoporeuse a été démontrée, et ses propriétés comparées à la couche compacte standard déposée par pyrolyse d'aérosol. Des efficacités de conversion comparables (19%) ont été atteintes, ainsi qu'une meilleure homogénéité engendrant une meilleure reproductibilité des résultats; ce moyen de dépôt est maintenant utilisé pour les cellules de référence à l'IPVF. L'intégration du SnO₂-ALD est aussi présentée. Une couche de 10 nm de SnO₂ a montré des efficacités moyennes dues à un déficit dans le facteur de forme. L'ajout d'une couche organique a résolu ce problème et a permis d'atteindre des performances de 16%. Enfin, la modification de ZnO-ALD par des dérivés de l'acide phosphonique a été étudiée. L'organisation des molécules à la surface du ZnO, puis leur effet sur la croissance de la pérovskite ont été détaillés, mais les résultats de cellules complètes restent très faibles.

MOTS CLÉS

Pérovskite halogénée, cellule solaire, atomic layer deposition, couche inorganique extractrice d'électrons, interfaces, greffage, photovoltaïque.

ABSTRACT

Perovskite solar cells have sparked a large interest in the photovoltaic community in the last 10 years due to their expedient optoelectrical properties, their vast scope of applications and their economical attractiveness. They are expected to reach the market by 2023, but challenges have to be tackled first, among which upscale and stability issues. To do so, a strategy is to work on the charge transport layers. They need to ensure a high selectivity towards one charge carrier, and have a good interface. Atomic layer deposition (ALD) is an industrial deposition technique which allows for the synthesis of a large variety of materials. ALD layers are dense, homogeneous, conformal, pinhole-free and their thickness and composition can be controlled at the nano-scale. ALD hence appears as an ideal candidate to deposit the charge extraction layers. This thesis focuses on the development and on the characterization of various oxides by ALD. SnO₂ and TiO₂ have been developed at the Institut Photovoltaïque d'Île-de-France (IPVF) with two different processes for each material. Their properties in regard of an integration in perovskite solar cells as inorganic electron transport layers have been explored, and one process for each material has been chosen. The advantageous integration of a 15 nm-thick ALD-TiO₂ layer has been demonstrated as compact blocking layer in a mesoporous architecture, and compared to a blocking layer deposited by spray pyrolysis. Similar power conversion efficiencies (PCE) up to 19% have been achieved, with a higher homogeneity of the ALD layer leading to a better reproducibility of the results now used in the baseline production at IPVF. The integration of ALD-SnO₂ in planar structures is also discussed. The 10 nm-thick layer alone was found to give mediocre efficiencies due to a lack of fill factor. The addition of an organic interlayer solved this issue allowing for PCE up to 16%. Finally an analysis of the interface between ALD-ZnO modified by phosphonic acid derivatives and a perovskite absorber is proposed. The organization of the molecules at the surface of ZnO and their impact on the perovskite have been determined, but the performances of full devices are poor.

KEYWORDS

Halide perovskite, solar cells, atomic layer deposition, inorganic electron transport layer, interfaces, grafting, photovoltaics.